EMBRITTLEMENT AND FLOW LOCALIZATION OF REACTOR STRUCTURE MATERIALS

Xianglin Wu, Xiao Pan, James F. Stubbins

University of Illinois at Urbana-Champaign

103 S. Goodwin Avenue, Urbana, IL 61801

Phone: (217)333-6474, Email: jstubbin@uiuc.edu

Final Report

TABLE OF CONTENTS

EXECUTIVE SUMMARY

The project "Embrittlement and Flow Localization of Reactor Structural Materials" is funded by the DOE Nuclear Engineering Education Research program with the grant number DE-FG07-02ID14337 starting from June 2002 to June 2005. The Principle Investigation, Prof. James F. Stubbins, and three graduate students, Xianglin Wu, Xiao Pan and Meimei Li, are involved in this project. More than ten journal article have been published or being preparation and one Ph.D. has been awarded, two Ph.D. in progress based on this reward. This project is divided into three phases; the annual reports have been submitted every year. During the first year, the creep-fatigue behavior for CuCrZr has been analyzed and the tensile data shared by our national lab colleagues are discussed. The critical stress concept was established based on the first year's work. For the second year, more details about the critical stress of irradiated materials were carried out and the temperature dependence of critical stress and its impact and explanation are carried in detail. In the third year, the focus was put in the microstructural analysis of flow localization of reactor structural materials. The novel technique of electron backscattering diffraction has been utilized for the competing mechanism between mechanical twinning and dislocation-based planar slip. X-ray diffraction technique was used for the materials textural analysis. Finite element analysis has been extensively applied for this project. The finite element analysis has been used to verify the tensile results and microstructural examination. Based on the good agreement of experimental study and finite element analysis, the technique is used to predict the mechanical behavior of reactor structural materials in irradiation circumstance. The simulation provided insight for the nuclear engineering design.

CHAPTER 1   INTRODUCTION

There has been a long and continuing effort to understand the influence of exposure to irradiation on reactor structure materials. In current Light Water Reactors (LWRs) and advanced fission reactor arena, this research covers a wide variety of materials that are found in and around the fuel, core and containment of nuclear fission reactor systems. Type 316L (LN) austenitic stainless steel has served as component structure material for current LWRs and Accelerator Driven System (ADS) for a long term and it is of continuing interest as candidate structure material for International Thermonuclear Experimental Reactor (ITER) and Generation IV reactors conceptual designs due, in large part, to their combination of acceptable strength and excellent ductility to resist brittle fracture by plastic deformation.

Most materials experts are familiar with the embrittlement issue with reactor pressure vessel steels that occurs at relatively low dpa (displacements per atom) levels: typically less than 0.1 dpa. This concern has dominated reactor safety analysis for the past three or more decades. More recently cladding and core internal materials have risen to similar levels of concern due to their loss of ductility with exposure to radiation, but typically at much higher dose levels: greater than 1 dpa. Most core internal components are fabricated from austenitic alloys, principally from Type 316L or Type 304L stainless steels. Cladding materials are typically Zr-based alloys: the Zircalloy series or Zirlo. These three alloy types represent body-centered cubic (bcc), face-centered cubic (fcc) and hexagonal close-packed (hcp) crystal structures, the later two of which were assumed to be relatively immune from plastic instabilities. Certain irradiation conditions lead to the development of a damage microstructure where plastic flow is limited to very small volumes or regions of material, as opposed to the general plastic flow in unexposed materials. This process is referred to as *flow localization* or *plastic instability* [1-12]. This process results in a fracture mode

that appears to be brittle since only small volumes of the material are able to deform through plastic flow. Even though there is extensive plastic flow in the small, confined regions, deformation essentially results in brittle fracture since very little energy is required to induce fracture. This loss of ductility typically exhibits itself through two major changes in the tensile behavior: (1) an elevated yield strength which is argued to be explained by "barrier" mechanism [13-15] accompanied by (2) very low uniform elongation under tensile loading conditions. The tensile response is characterized by a sharp increase in yield strength, and a quick transition to channel or other localized flow at the onset of plastic deformation. This means that the ultimate tensile strength, and thus, uniform elongation is reached very quickly once the material yields. Uniform elongation values often drop below 1% while total elongations may be higher due to local ductility in the vicinity of plastic flow initiation. In the past, much of the effort to understand flow localization concentrated on this dislocation pinning and path clearing phenomena. These phenomena clearly account for the large increases in yield strength.

Recent researches [16-19], however, show that the flow localization problem is associated more closely with the final stages of tensile deformation rather than the initial stage. In fact, despite irradiation exposure, the plastic flow behavior of a material is always approximately (within experimental error) the same up to the point of plastic instability. In the true stress-strain curves, the true stress for plastic instability (necking) is approximately constant regardless of the external irradiation level, and designated here as the "*critical stress*". This critical stress is directly correlated to the linear hardening property of materials and can be obtained from the tensile property of unirradiated materials because of its irradiation insensitivity. This value can also be concluded from the linear relationship between uniform elongation and yield stress in case of the shortage of full data set. It is noticed that the plastic flow exhibits a uniform behavior for various

6

irradiation levels before the onset of plastic instability for all irradiation conditions. Therefore, the controlling microstructural mechanism for flow localization should be working for both unirradiated and irradiated materials and could include deformation-induced twinning and large scale planar slip in addition to the cleared channel flow due to the irradiation-induced defect microstructure. This insight provides an advantage in studying the final stages of flow localization, since the point of instability occurs at the same true stress level for both irradiated and unirradiated materials. Thus the controlling mechanism can be studied directly from unirradiated material.

Limited studies [20] have been carried out at moderate irradiation temperatures typical of LWR core internal temperatures. A major conclusion of these lower temperature radiation studies is that 316L and 304L stainless steels experience a ductility minimum in the temperature range of 150 to 400°C when irradiated to doses as low as 1 dpa, precisely the temperature range and irradiation conditions where they are used in current LWR's and new, advanced sodium and lead/lead-bismuth cooled fast reactor designs. Although the critical stress is insensitive to the irradiation environment, it has strong dependence on the test temperatures. From room temperature to the vicinity of 200°C, there is a significant drop of critical stress and thereafter, it falls into a plateau. The capacity of strain hardening is determined by the margin between critical stress and yield strength and the yield strength is relatively temperature insensitive. Therefore, the difference between critical stress and yield strength is very small even at very low dose level in the moderate temperature range and it explains the ductility minimum in the temperature range of 150-350°C observed by Robertson *et al.* [20].

Electron backscattered diffraction (EBSD) technique was applied to analyze crystallography and texture evolution during tensile loading. Mechanic twinning and planar slip are believed to be

the competing mechanisms controlling the flow localization. Deformation twinning system can be activated as an additional deformation mechanism when the true stress is larger than the critical twinning stress. Stacking fault energy is an important factor controlling the critical twinning stress for twinning activation and it has strong temperature dependence. This temperature dependence of stacking fault energy causes the temperature dependence of critical twinning stress and therefore determines the temperature dependence of controlling mechanism for flow localization: mechanic twinning dominates the low temperature deformation and planar slip controls the high temperature deformation. Texture analysis was also performed during the tensile loading and grain re-orientation was studied. It is indicated that during the tensile loading, the grains are re-orientating to the vicinity of Brass (2 <112>) and Goss ({110} <100>) type textures which are believed to be the preferred deformation orientation for face-centered cubic materials.

Notch strengthening analysis of 316L stainless steel was carried out using electron backscatter diffraction (EBSD) and the finite element method (FEM) techniques. The influence of exposure to irradiation was examined by employing irradiated tensile properties in the FEM analyses. The major issue of interest is the possibility that low ductility, often found following irradiation exposure, will translate into low notch toughness. It was found that notch depth plays an important role in notch strengthening and mechanical properties degradation. Differences in notch depth and shape result in various sizes of plastic deformation and twinning zones. Experimental results and FEM modeling results correlate well over the range of notch conditions examined here. It is found that notch ductility and plastic deformation can be highly localized for irradiated materials, exacerbating the flow localization problem. Thus the influence of irradiation exposure can also lead to flow localization problems with components with notches or stress concentrators.

CHAPTER 2   BACKGROUND

The applications of 316L austenitic stainless steel for International Thermonuclear Experimental Reactor, Accelerator Driven System and concept designs of Generation IV reactor are addressed in this chapter. A literature review covering tensile property and its temperature dependence, hardening mechanism, radiation effects, microstructure analysis and notch strengthening mechanism is presented. Fundamental concepts and recently progress on the studies of flow localization are discussed.

2.1   Application of 316L stainless steel in advanced nuclear applications

316L stainless steel has been widely used in the current LWR systems and it is a promising candidate structure material for many advanced nuclear applications such as ITER, ADS and Gen IV reactors. The purpose of ITER program is to develop a large-scale magnetic fusion device capable of demonstrating fusion "breakeven" and its commercial operation. The building site has been decided to be in France and the first plasma should be possible by the end of 2016. It will be a critical step for the commercial operation of fusion reactor and ultimate clean resolution for future energy demand.

The modular removable design of ITER double-walled vacuum vessel is shown in Figure 2-1a [21]. It is lined with blanket modules, diverter cassettes, diagnostic sensors and port plugs for heating antennae, limiters, diagnostics and test blanket modules which are mechanically attached to the vacuum vessel. Since these plasma facing components experience most of the heat, radiation damage and plasma vibrating, the selection of materials and its combination become one of the key issues of ITER design. Copper alloys are considered as candidate materials for heat sink application due to their excellent heat conductivity. Dispersion strengthening and

precipitation hardening are use to increase the strength of copper as long as keeping the electrical and thermal conductivity. Beryllium, tungsten and carbon fibre composites are selected as plasma-facing materials because of their high melting temperatures. 316L (LN) stainless steel is used for vacuum vessel and ports, blanket shield modules, thin walled tubes for first wall, cooling manifolds and divertor body due to its high strength and good irradiation resistance.

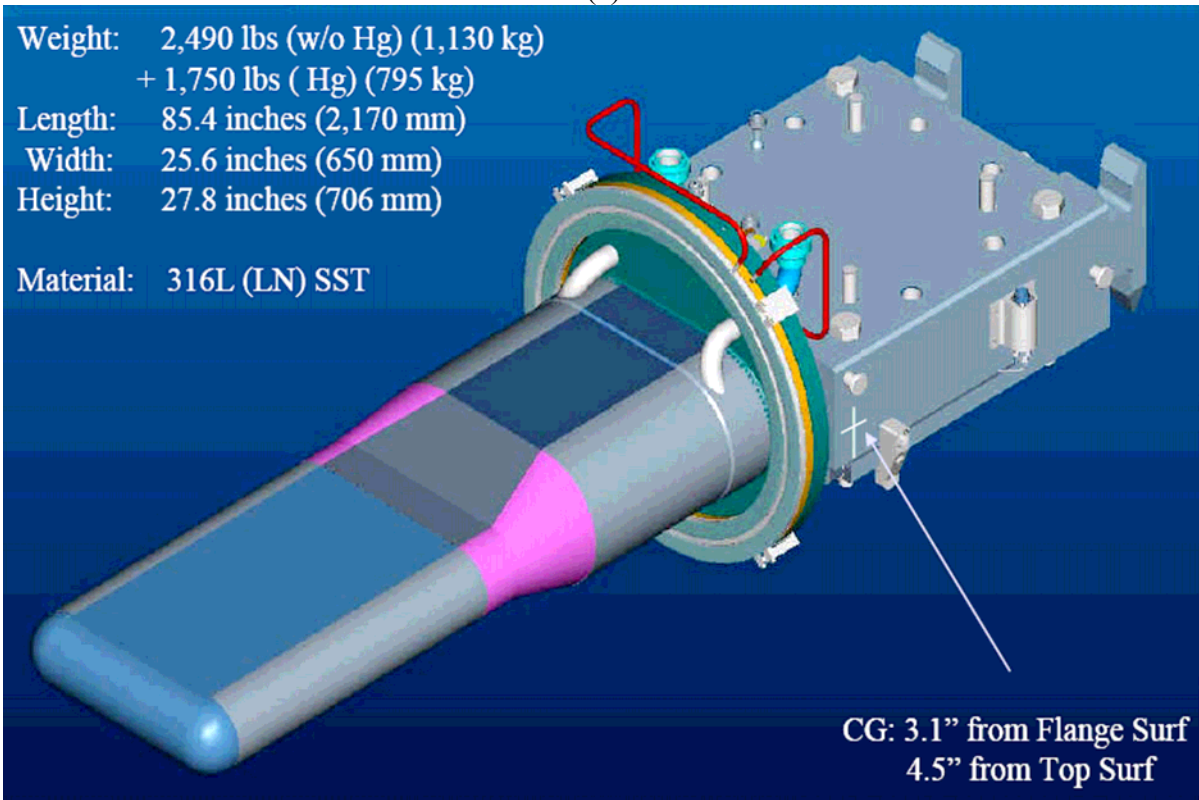316L austenitic stainless steel is also widely used in ADS and concept designs of Gen IV reactors. The Spallation Neutron Source (SNS) is an accelerator-based neutron source being built in Oak Ridge, Tennessee, by the U.S. Department of Energy. The SNS will provide the most intense pulsed neutron beams in the world for scientific research and industrial development. At a total cost of $1.4 billion, construction began in 1999 and will be completed in 2006. 316L stainless steel is selected as structure and container material for the Spallation Neutron Source project. The target module is shown in Figure 2-1b [22] and the target material is mercury.

The 11th Generation IV International Forum (GIF) members have selected six concepts to develop in order to meet the technology goals for new nuclear systems. GIF members believe developing these concepts will achieve long-term benefits so nuclear energy can play an essential role worldwide. Generation IV nuclear energy systems are future, next-generation technologies that will compete in all markets with the most cost-effective technologies expected to be available over the next three decades. Comparative advantages include reduced capital cost, enhanced nuclear safety, minimal generation of nuclear waste, and further reduction of the risk of weapons materials proliferation. Generation IV systems are intended to be responsive to the needs of a broad range of nations and users. The purpose of Gen IV is to develop nuclear energy systems that would be available for worldwide deployment by 2030 or earlier. The Forum's 11 members are Argentina, Brazil, Canada, Euroatom, France, Japan, South Korea, South Africa, Switzerland,

United Kingdom, and the United States. The final Generation IV Systems selected in 2002 are: Gas-Cooled Fast Reactor (GFR): features a fast-neutron-spectrum, helium-cooled reactor and closed fuel cycle; Very-High-Temperature Reactor (VHTR): a graphite-moderated, helium-cooled reactor with a once-through uranium fuel cycle; Supercritical-Water-Cooled Reactor (SCWR): a high-temperature, high-pressure water-cooled reactor that operates above the thermodynamic critical point of water; Sodium-Cooled Fast Reactor (SFR): features a fast-spectrum, sodium-cooled reactor and closed fuel cycle for efficient management of actinides and conversion of fertile uranium; Lead-Cooled Fast Reactor (LFR): features a fast-spectrum lead of lead/bismuth eutectic liquid metal-cooled reactor and a closed fuel cycle for efficient conversion of fertile uranium and management of actinides; Molten Salt Reactor (MSR): produces fission power in a circulating molten salt fuel mixture with an epithermal-spectrum reactor and a full actinide recycle fuel cycle. Sodium-cooled fast reactor and Lead/Lead-Bismuth cooled fast reactor are two of six concept designs of Gen IV reactors. These two reactors are expected to operate in the moderate temperature range and 316L stainless steel is selected as candidate material for structure applications.

Central Solenoid
Outer Intercoil Structure
Toroidal Field Coil
Poloidal Field Coil
Machine Gravity Supports

Blanket Module
Vacuum Vessel
Cryostat
Port Plug (ICHeating)
Divertor
Torus Cryopump

(a)

Weight: 2,490 lbs (w/o Hg) (1,130 kg)
+ 1,750 lbs (Hg) (795 kg)
Length: 85.4 inches (2,170 mm)
Width: 25.6 inches (650 mm)
Height: 27.8 inches (706 mm)

Material: 316L (LN) SST

CG: 3.1" from Flange Surf
4.5" from Top Surf

(b)

Figure 2-1 The applications of 316L stainless steel in advanced nuclear applications: (a) view of ITER design [21] and (b) view of SNS target module [22].

2.2   Literature review on the radiation embrittlement of 316L stainless steel

2.2.1   Tensile properties of engineering materials

During the engineering service, materials typically suffer from the tensile loading. Attentions have been paid to the tensile behavior of materials for a long term. A typical material engineering stress-strain curve with mechanic property parameters is shown in Figure 2-2 [2].
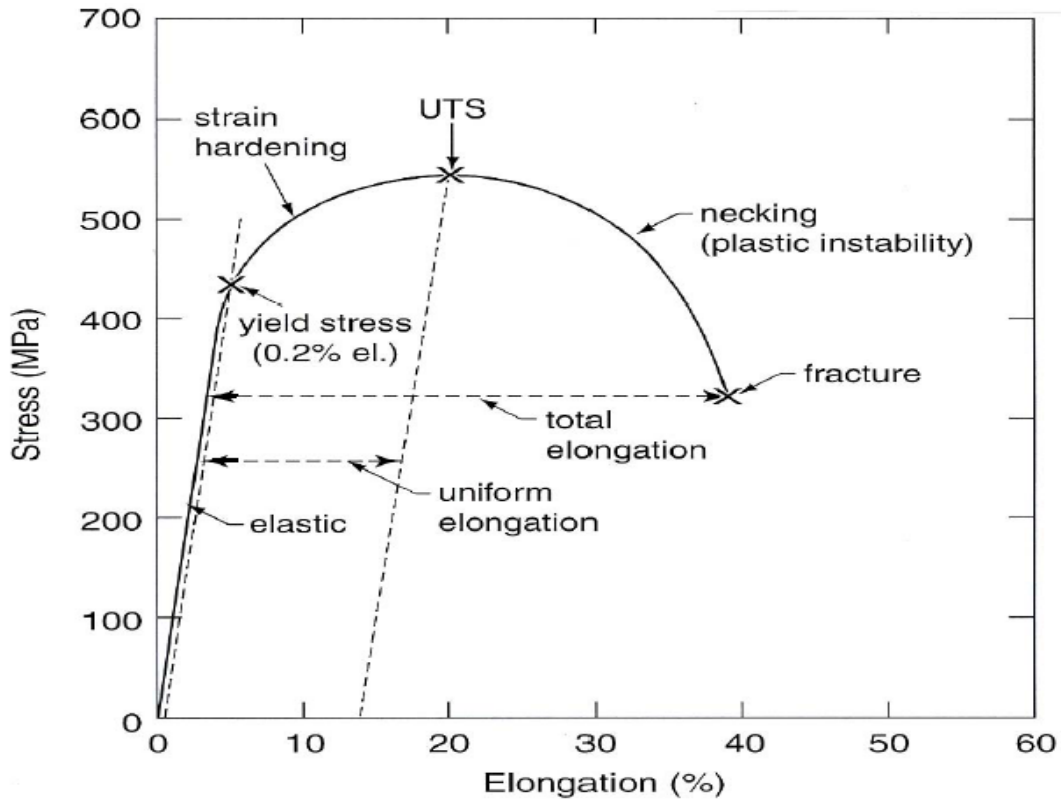

Figure 2-2 Typical tensile engineering stress-strain curve [2].

It is well known that engineering stress and engineering strain are defined as

$$S = \frac{P}{A_0}$$

$$e = \frac{l - l_0}{l}$$

Here P is the load, A_0 is the original area of the specimen and l_0 is the original gage length of the specimen. During tensile loading, Materials initially elastically deformed and this process is reversible. However, once the yield point is overcome, the plastic deformation mechanism starts to operate and this process is "remembered", the stress and strain damages are residued in the materials. Even if the material is unloaded and loaded again, it will not yield at previous point and, instead, the yielding starts at the "remembered stress". In the plastic deformation arena, the concepts of true stress and true strain are introduced to characterize the real stress and strain state of the material. True stress is defined as the load P divided by the instantaneous area A:

$$\sigma = \frac{P}{A}$$

And the strain can be computed by integrating from the original length to the instantaneous length:

$$\varepsilon = \int_{l_0}^{l} \frac{dL}{L}$$

The correlation between true and engineering stress-strain can be written as:

$$\varepsilon_t = Ln(1 + e)$$

$$\sigma_t = S * (1 + e) \quad [23]$$

2.2.2   Microstructure damage induced by irradiation

14

It is well accepted that the macroscopic mechanical property changes by irradiation for 316L austenitic stainless steel are directly correlated with the development of irradiation induced microstructure damage [2, 5, 6, 24-31]. Radiation damage has been a long term concern in the nuclear industry and it includes precipitates, voids, bubbles, dislocation loops and networks *etc.*

2.2.2.1 Precipitates

Precipitates are thermally introduced and it will result in a variety of second phase formation including MC, M_6C and $M_{23}C_6$ carbides. Figure 2-3 illustrates the response of precipitates evolution with temperature and dose along with the dose dependence of $\sqrt{Nd}$. It is clearly indicated that with a higher temperature transformation, a lower density of larger precipitates hence a lower peak value of $\sqrt{Nd}$ is resulted [14].
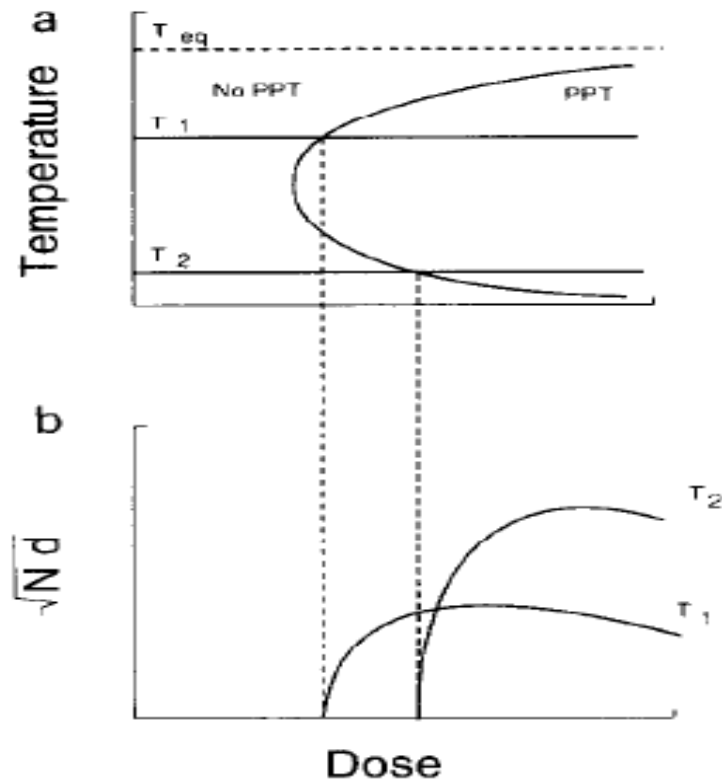

Figure 2-3 Temperature and dose dependence of precipitation [14]

15

2.2.2.2   Nucleation of bubbles

Bubbles are primarily helium and hydrogen filled gas cavity in irradiated materials. In high energy (Mev) irradiation environment such as Spallation and fusion environment, the helium and hydrogen production reaction is prone to be activated. Vacancies are absorbed by helium and hydrogen to form bubbles. The bubbles grow by absorbing helium/hydrogen gas and vacancies after nucleation. Models [24, 32-34] of bubble formation suggest that the nucleation dose decreases with decreasing irradiation temperature and the density of bubble has a saturation with the increasing irradiation level, as shown in Figure 2-4.

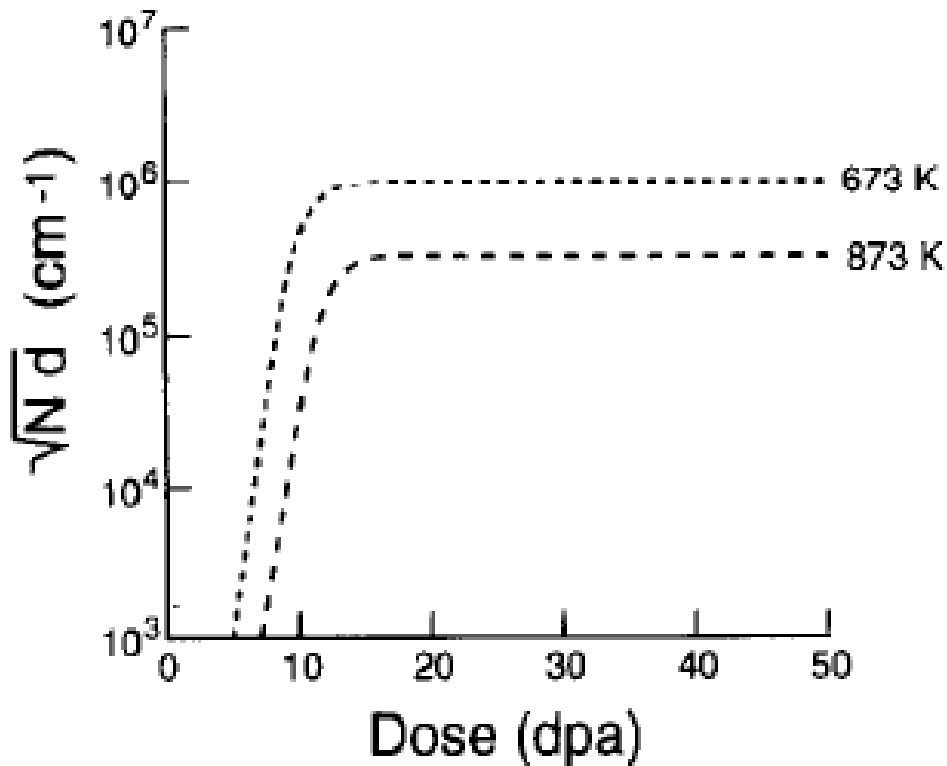
Figure 2-4 Evolution of bubble density in irradiated materials [24, 32-34]

2.2.2.3   Voids formation

After the combinations of bubbles and vacancies and the overcame of a critical value of radius of the bubble, bubbles will become unstable and grow as voids [24, 32-34]. The

approximate void evolution is shown in Figure 2-5. It is evident that with a fixed irradiation level, the void density increases with the decreasing of irradiation temperature while the void size is a positive function of irradiation temperatures. The dose dependence of $\sqrt{Nd}$ is also indicated in the figure, and again, it shows a saturation trend after certain dose level.
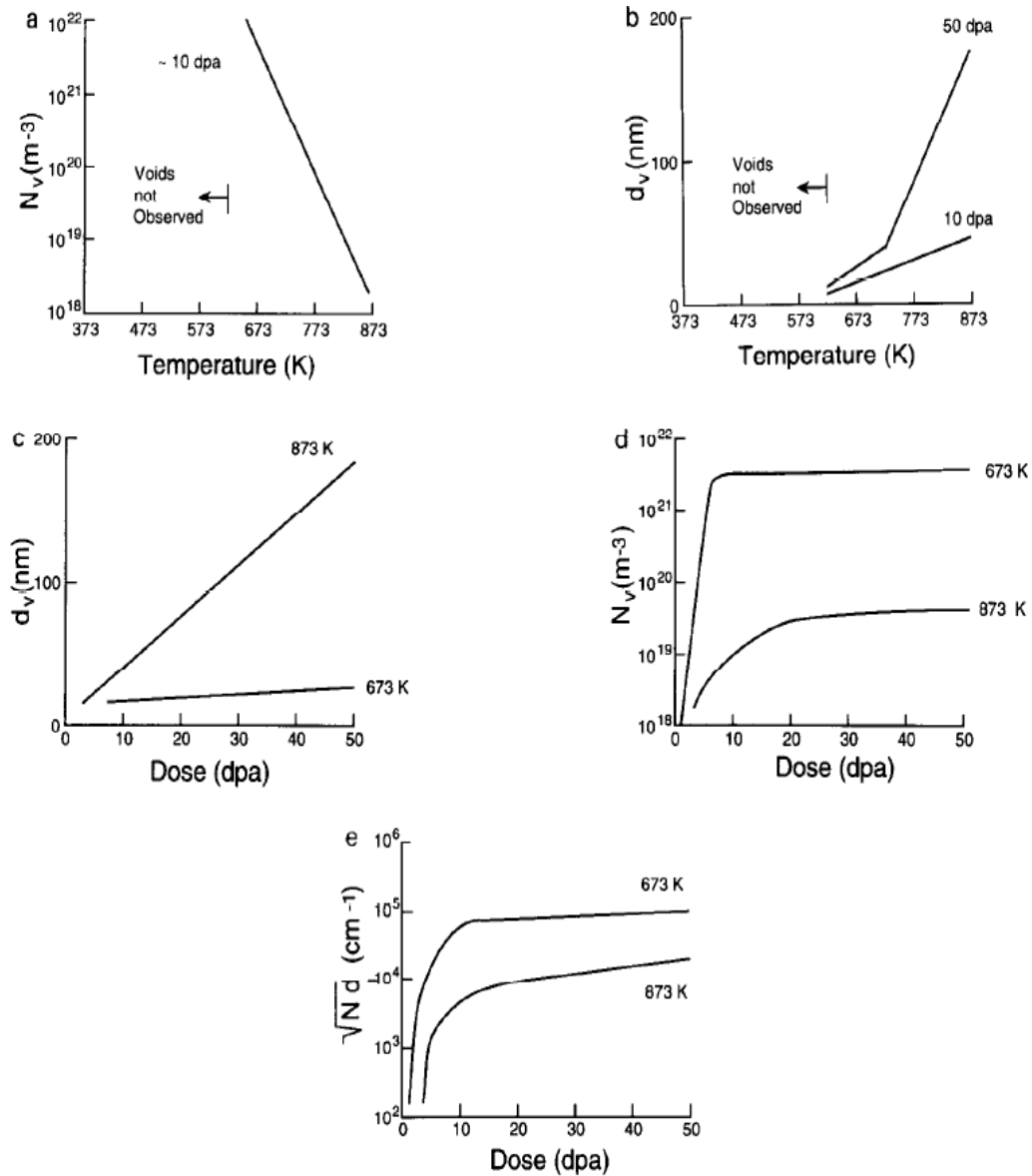
Figure 2-5 Dose and temperature dependence of void density. (a) temperature dependence of void density; (b) temperature dependence of void size; (c) variation of void size with dose and temperature; (d) variation of void density with dose and temperature and (e) variation of $\sqrt{Nd}$ with dose and temperature [24, 32-34].

2.2.2.4 Dislocation network and its density evolution

"Black dot" is a common observed microstructure in the irradiated materials. It can be identified as faulted, interstitial type tiny dislocation loops. These loops can expand by net self-interstitial absorption and eventually become indistinguishable from originally presented dislocation networks. The production and growth of network dislocations are dose dependent. The density of dislocations is sensitive to the environment irradiation level. The dose dependence of dislocation density is shown in Figure 2-6 [35, 36]. It is evident that with the increasing of irradiation dose and after certain level, the density of dislocation falls into saturation. It indicates an approximate balance between dislocation production and recovery. The temperature dependence of dislocation density is also indicated. It is believed that the saturation level is relatively insensitive to the heat treatment and inherent material composition [24, 37]
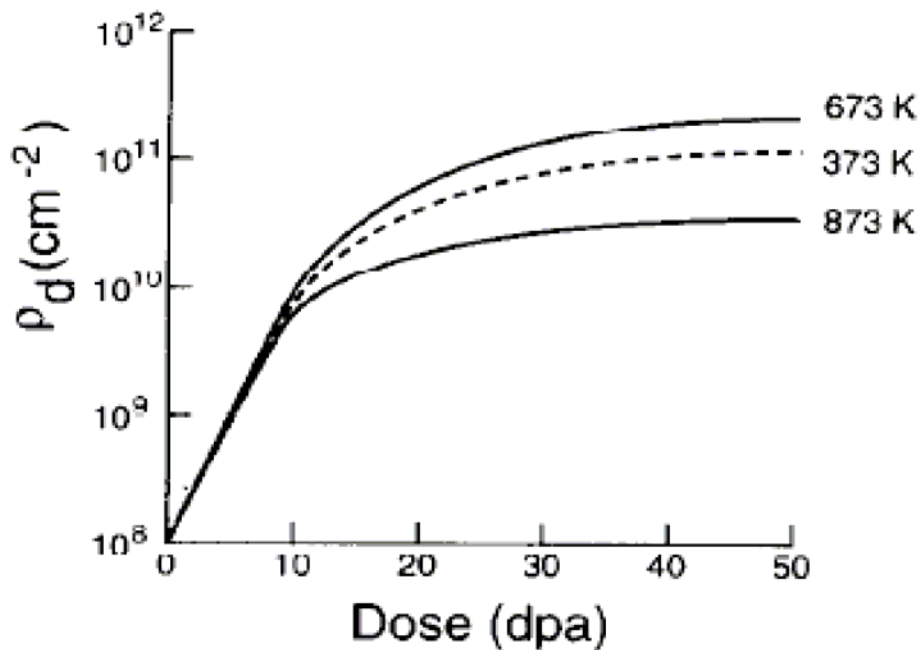
Figure 2-6 Dose and temperature dependence of network dislocation density [24, 37]

2.2.3   Irradiation induced mechanic property changes

2.2.3.1   Yield strength and "barrier" mechanism

18

It is now well accepted that there is an increase on yield strength of engineering materials like steels after exposure to irradiation environment[15, 35, 38-41]. This dose dependence of yield strength is believed to be correlated with the irradiated induced microstructure damage. A number of models based on the dispersed "barrier" hardening mechanism have been carried out to predict the changes of yield strength after irradiation [14, 15, 42]. The change of yield stress can be expressed in terms of the required stress to move a dislocation through a field of obstacles of strength α and average inter-obstacle spacing l as:

$$\Delta\sigma_y = M\alpha\mu b / l = \begin{cases} M\alpha\mu b\sqrt{Nd} \ldots\ldots obstacles \\ M\alpha\mu b\sqrt{\rho_d} \ldots dislocations \end{cases}$$

Here, the average discrete obstacle spacing l is assumed to be equal to be the inverse of $\sqrt{Nd}$ due to most of irradiation-induced defects are relatively strong obstacles [43, 44] and the average dislocation spacing is proportional to the square root of dislocation density, *e.g.* $\sqrt{\rho_d}$. For other parameters used in this equation, μ is the shear modulus of matrix material, b is the Burgers vector and M is the factor relating shear stress on a slip plane to the uniaxial stress to activate the slip stress, M is believed to be a value in the range of $\sqrt{3}$ to 3 [45]. All these barriers are divided into three groups: Voids and large precipitates are included as Orowan barriers with high barrier strength and α approaching 1; Frank loops and small MC precipitates are regards as barriers with moderate strengths and small bubbles, loops and dislocation networks are grouped into small strength barriers. Then the yield stress of irradiated materials is equal to the yield stress before irradiation plus the change. The total change due to all kinds of obstacles and dislocations can be written as:

$$\Delta\sigma_{tot} = \sqrt{\sum_i (\Delta\sigma_{SR,i})^2} + \Delta\sigma_{LR}$$

Here SR means short range and LR means long range. Typically, the dislocations are regarded as long range obstacles and other irradiation-induced obstacles like void, precipitates *etc.* are treated as short range ones. Figure 2-7 [25] shows the schematically description of change of yield stress with dose from the contributions of aforementioned obstacles.
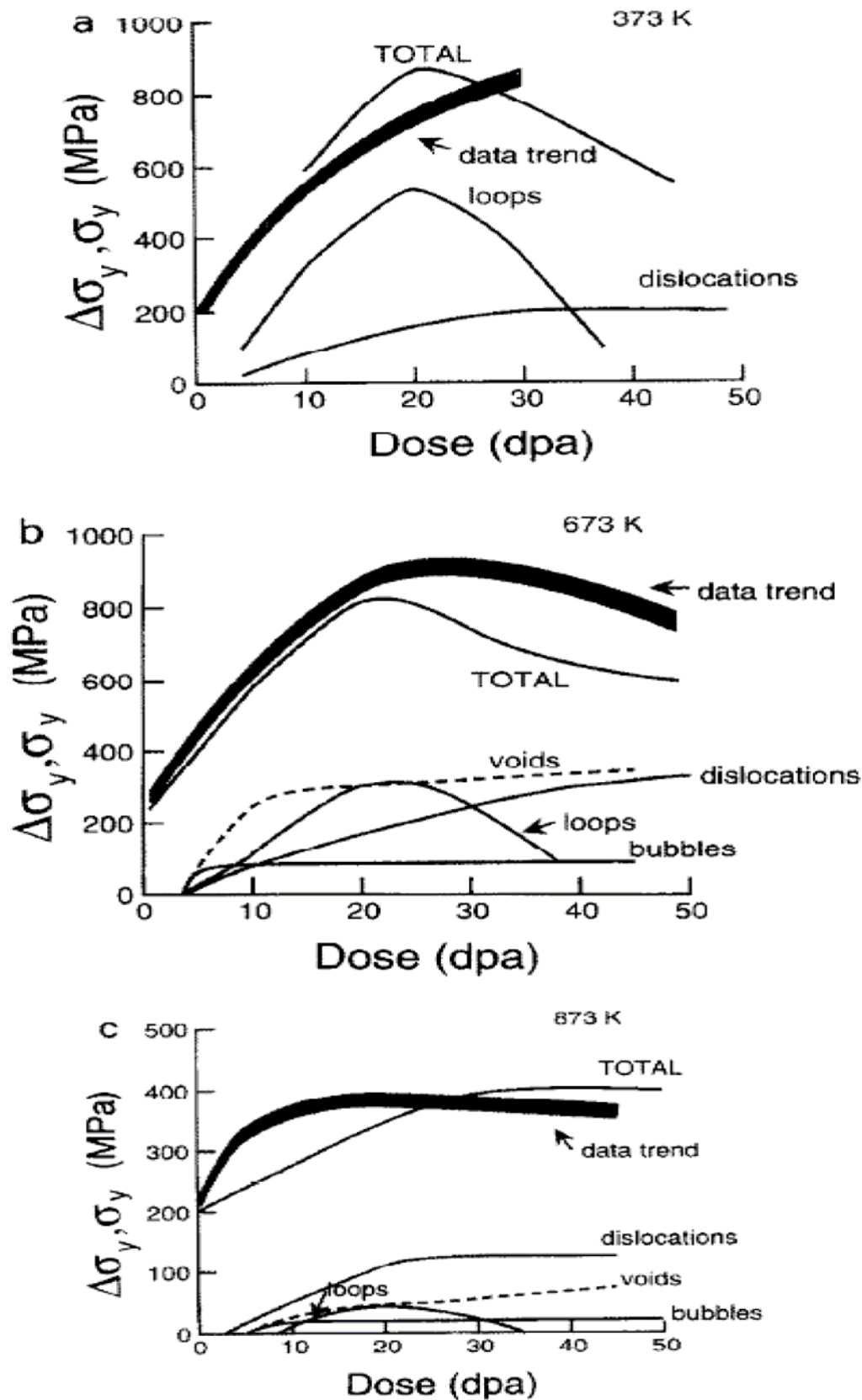
Figure 2-7 Dose and temperature dependence of yield stress change and its contributions [25]

2.2.3.2 Uniform elongation and ductility

The engineering materials suffer from the ductility loss after exposure to irradiation environment. The loss of uniform ductility is believed to be attributed to the interactions between dislocations and irradiation-induced defects. Instead of leading to dislocation multiplication and plastic-induced martensitic formation by interaction between dislocations and obstacles in unirradiated materials, the same process in irradiated materials may lead to barriers elimination or weakness [25, 36, 46-50]. Several possible mechanisms for this elimination or weakness are presented in Figure 2-8 [25]. Strudel and Washburn [47] argued that the interactions of the Schockley partial with the faulted loop produces a helical segment on the original dislocation and eliminates the loop, which is shown in Figure 2-8a. Foreman and Sharp [48] proposed that the intersection between a mobile dislocation and a prismatic loop provides an possibility for the loop to glide on itself and merge to part of the glide dislocation, Figure 2-8b indicates this process. Figure 2-8c, which shows the model of Gelles [36], also describes the interaction between glide dislocation and fault loop could eliminate the fault and incorporate the loop as part of the dislocation. And in the end, Figure 2-8d [36, 46, 49, 50] shows how the small voids being sheared into two dislocations, which leads to no dislocation multiplication and a smaller α obstacle.
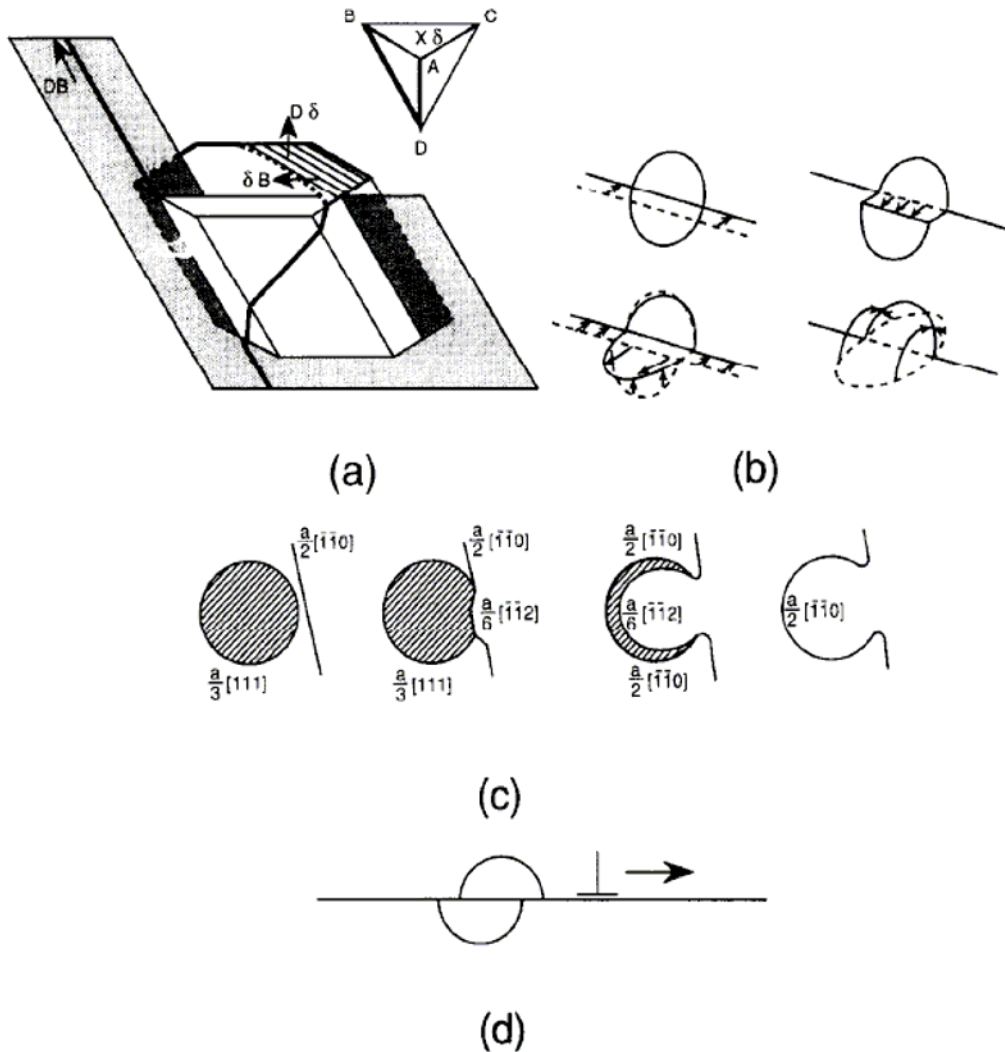
Figure 2-8 Work softening and flow localization: (a) mechanism of Strudel and Washburn, (b) mechanism of Foreman and Sharp, (c) mechanism of Gelles and (d) mechanism of void interaction [36, 46, 49, 50]

Since the interaction between dislocations and irradiation-induced microstructure damage, there is a strong dependence of uniform elongation on the dose and also temperature. The latter can be somehow correlated to the temperature dependence of irradiation-induced defect as reviewed in previous sections. The dose and temperature dependence of uniform elongation are shown in Figure 2-9 [25]. It is clearly evident that with the increasing of irradiation dose, the uniform elongation will drop to a lowest point. It is noteworthy to point out that the uniform elongation for the solution annealed material suffers the ductility minimum in the moderate

temperature range. This phenomena will discussed in this study and an argument explaining it will
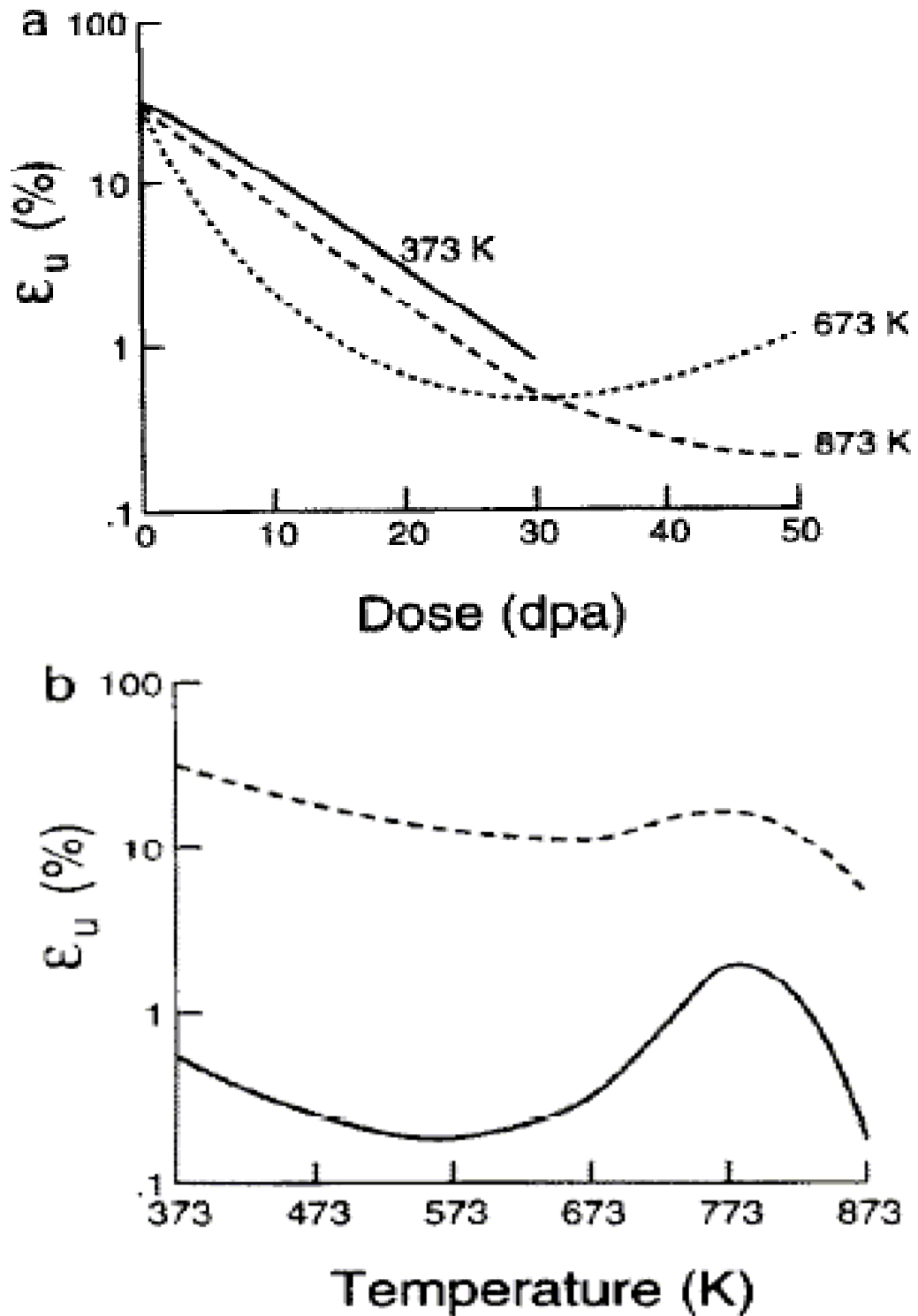
be proposed.

Figure 2-9 Dose and temperature dependence of uniform elongation [25]

2.2.4   Recent developments on the tensile properties of 316L stainless steel for nuclear applications

With the development of International Thermonuclear Experimental Reactor, Accelerator Driven System and Generation IV concept design, extensive investigations have been carried out in recent years on the irradiation effects of 316L stainless steel in Spallation[2, 3, 7-12, 31, 32, 51-59], fission and fusion [60-66] environments. In this section, the recent developments of researches on irradiated 316L stainless steel will be briefly reviewed. It is well accepted that the tensile properties of 316L stainless steel have a strong dependence on the irradiation level. With the increasing of the dose level, the yield strength is enhanced and there is a severe reduction of uniform ductility. The typical tensile curves for irradiated 316L stainless steel are shown in Figure 2-10 [11].
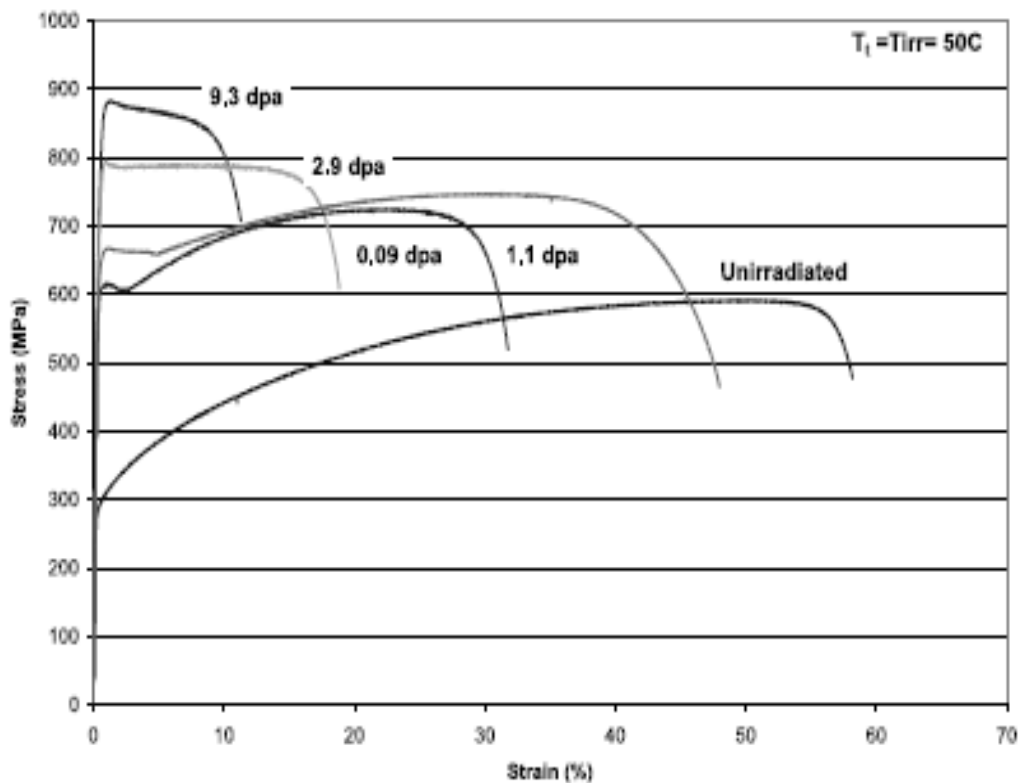

Figure 2-11 Engineering stress-strain curves for 316L stainless steel after irradiation to Spallation environment [11]

The increase of yield strength after exposure to irradiation environment is reported everywhere. It seems the yield strength reaches a saturation value after certain dose value, which is consistent with the saturation of density of irradiation-induced defects. The dose dependence of yield strength for fusion and Spallation applications are reviewed here respectively in Figure 2-12 [20] and Figure 2-13 [11]. The loss of ductility is also shown in Figure 13 and Figure 14 [20].
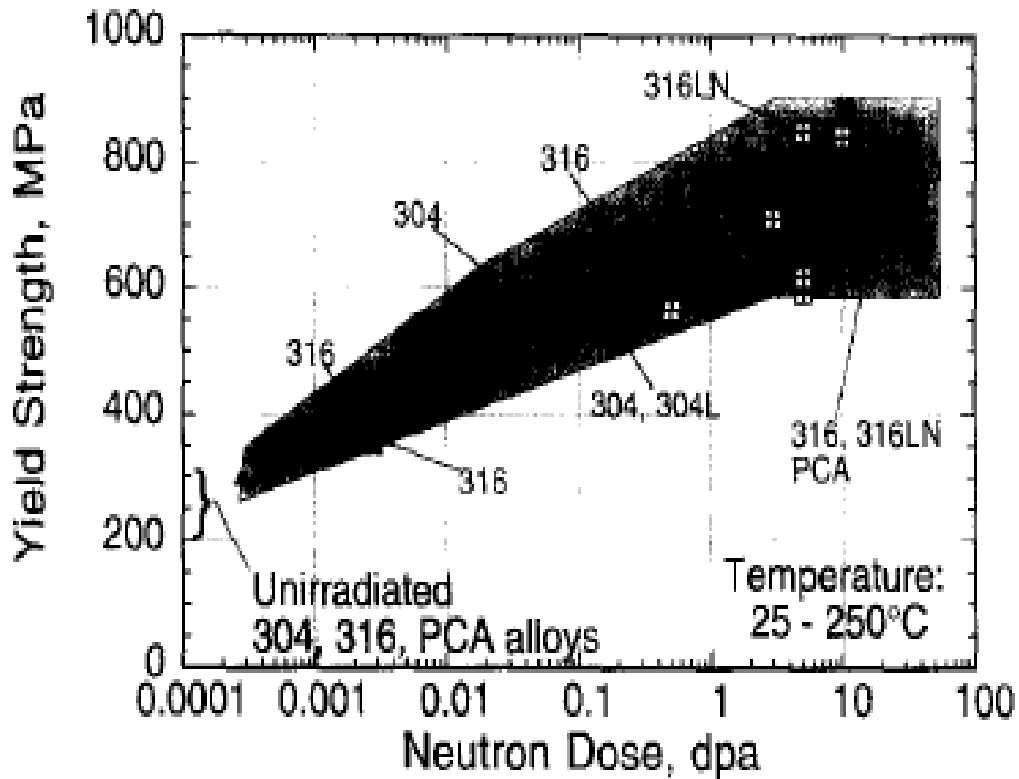

Figure 2-12 Dose dependence of yield strength for 316L and 304L stainless steel [20]
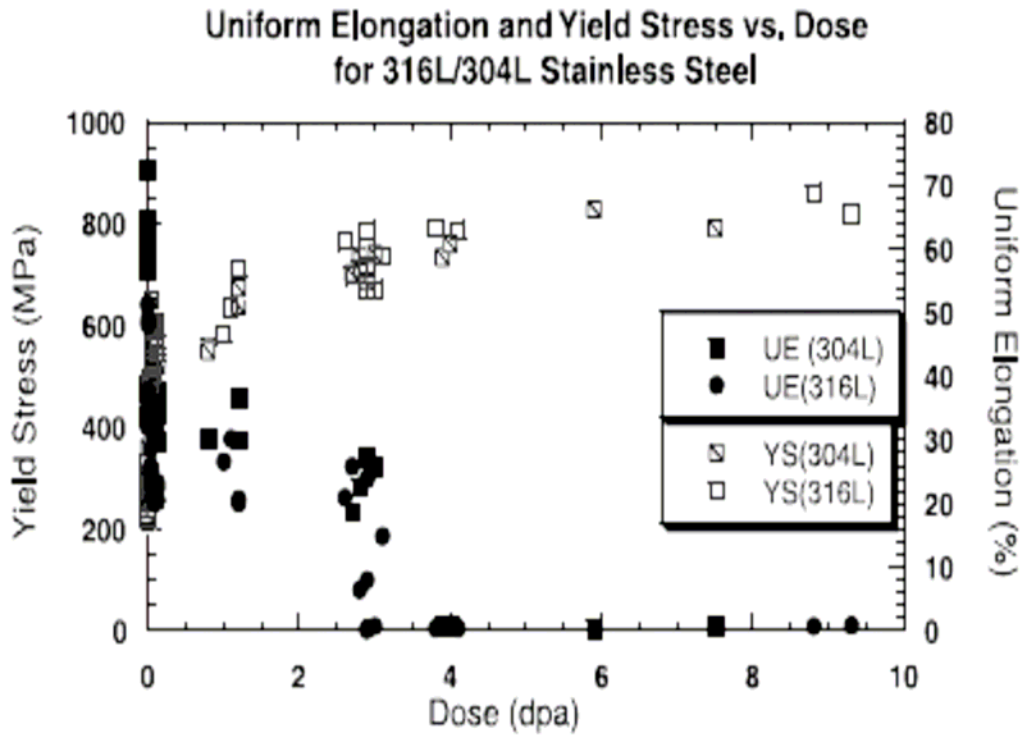
Figure 2-13 Dose dependence of yield strength and uniform elongation for 316L and 304L stainless steel irradiated in LANSCE [11].
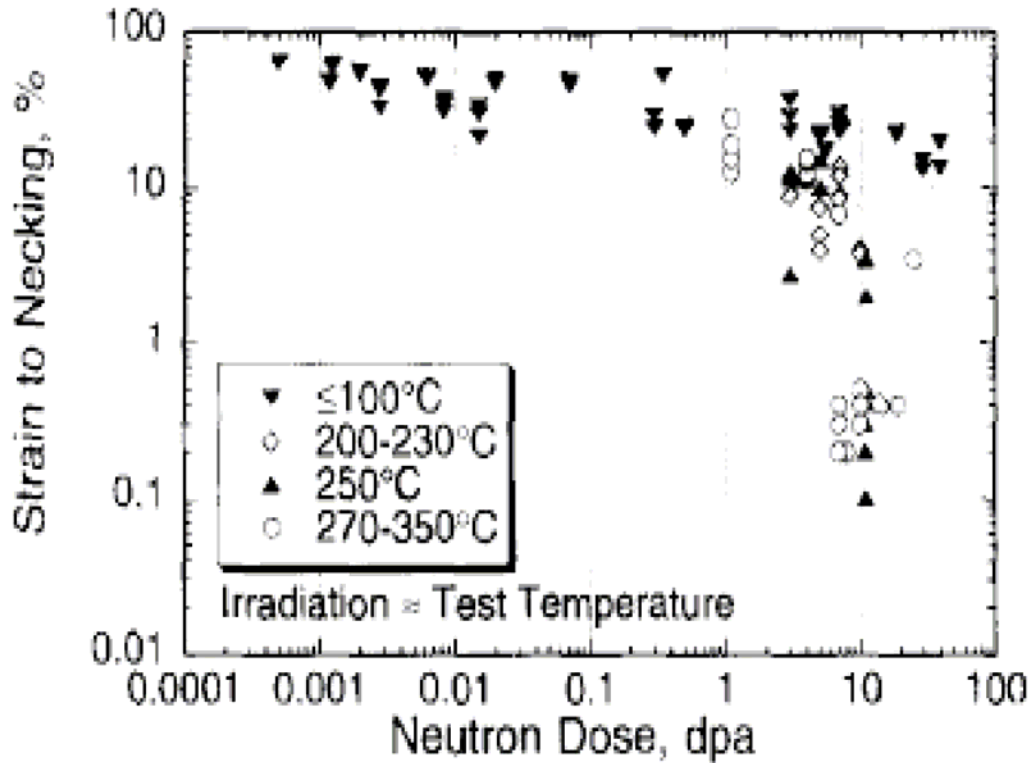

Figure 2-14 Strain to Necking as a function of dose and temperature [20]

2.2.5   Strain hardening behavior of structure materials

As mentioned in the previous section, when a stress exceeding the original yield strength is applied on structure materials, plastic deformation will dominate and this process is irreversible. The induced stress is residued and strengthens the materials. This strengthening is called "strain hardening". The degree of plastic deformation can be conveniently expressed as percent cold work, defined as:

$$\%CW = \frac{A_0 - A_f}{A_0} \times 100$$

Where A_0 is the original cross-sectional area and A_f is the final cross-sectional area. Due to the strain hardening process, the yield and tensile strength will increase with increasing cold work while the ductility will decrease. An annealing heat treatment may remove the effects of strain hardening.

The response of strain hardening is given by the strain-hardening coefficient n, which is the slope of the plastic portion of the true stress-true strain curve. The plastic portion of true stress-strain can be fitted by the power law as:

$$\sigma_t = K\varepsilon_t^n$$

Where the strength coefficient, K, and the strain hardening exponent, n, are both materials properties. The strain-hardening coefficient n is an inherent material property and different material shows different hardening capability. 316L stainless steel typically shows a value of 0.4 to 0.5 for strain-hardening coefficient. Materials with a low strain-hardening coefficient respond a poor work hardening capability. Other equations have been developed with similar relationships to model the strain hardening process in materials, such as, $\sigma_t = A + B\varepsilon_t^n$ for austenitic stainless steel and other engineering materials [67]. A series of researches have been carried out for

28

straining hardening of materials. Thompson *et al.* [68] argued the grain size dependence of strain or work hardening capability of polycrystalline materials. Byun, Lee, Asgari, Copley *etc.* [29, 69-71] discussed the strain hardening controlling mechanism from the aspects of microstructure characteristic and investigated the dependence on dislocation dissociation and stacking fault energy. Extensive studies are also performed on the correlation of the strain hardening to temperature and strain rates [72-74]. Several physically and phenomenologically based models have been developed to describe the strain hardening process and its dependence on temperature and strain rates for face centered cubic and body centered cubic crystals such as Johnson-Cook model [75], Zerilli-Armstrong model [76], Bodner-Partom model [77] and Khan-Huang model [78]. For an instant, John-Cook model is expressed for true stress in terms of true strain, strain rate and temperature as:

$$\sigma = (A + B\varepsilon^n)(1 + C\ln(\dot{\varepsilon}^*))(1 - T^{*m})$$

The strengthening of materials by strain hardening is well accepted to be the result of interactions: 1. between dislocations and obstacles and 2: among dislocations themselves. When a stress greater than the yield strength is applied, dislocations starts to slip until encountering obstacles that pin the ends of the dislocation line. During this process, more and more dislocation loops will be produced and this is called Frank-Read source. This dislocation multiplication process increases the density of dislocations and thereafter increases the interaction among dislocations and obstacles and themselves. Larger external stress then is required to move the dislocation and the material is strengthened [23]. The obstacles that restrict the movement of dislocation and promote the strain hardening include particles, twinning bands, dislocation partials, dislocation channels *etc.* The details will be introduced in the microstructure section.

29

The strain hardening capacity of reactor structure materials is strongly sensitive to environmental irradiation exposure. After exposure to irradiation environment, there is a sharp increase in the value of yield strength while the strain hardening capability is severely reduced. Figure 2-15 and Figure 2-16 [79] show the dose dependent of strain hardening of face centered cubic EC316LN stainless steel and body centered cubic 9Cr-2WVTa Ferritic/Martensitic steel respectively. Both the unirradiated materials tested at room temperature and higher temperature show much larger strain hardening capability than the materials after irradiation and tested at the same temperatures, *e.g.* 1.87 dpa for EC316LN stainless steel and 2.53 dpa for 9Cr-2WVTa Ferritic/Martensitic steel.
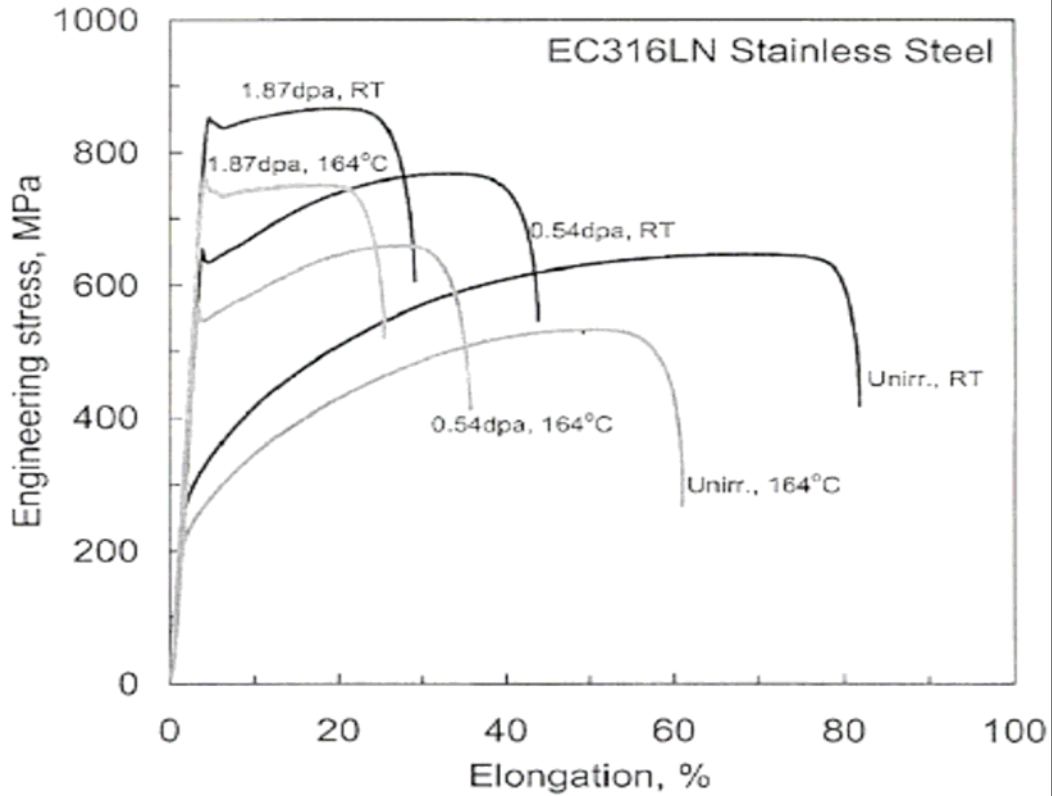
Figure 2-15 The dose dependence of strain hardening capability of EC316LN stainless steel [79].
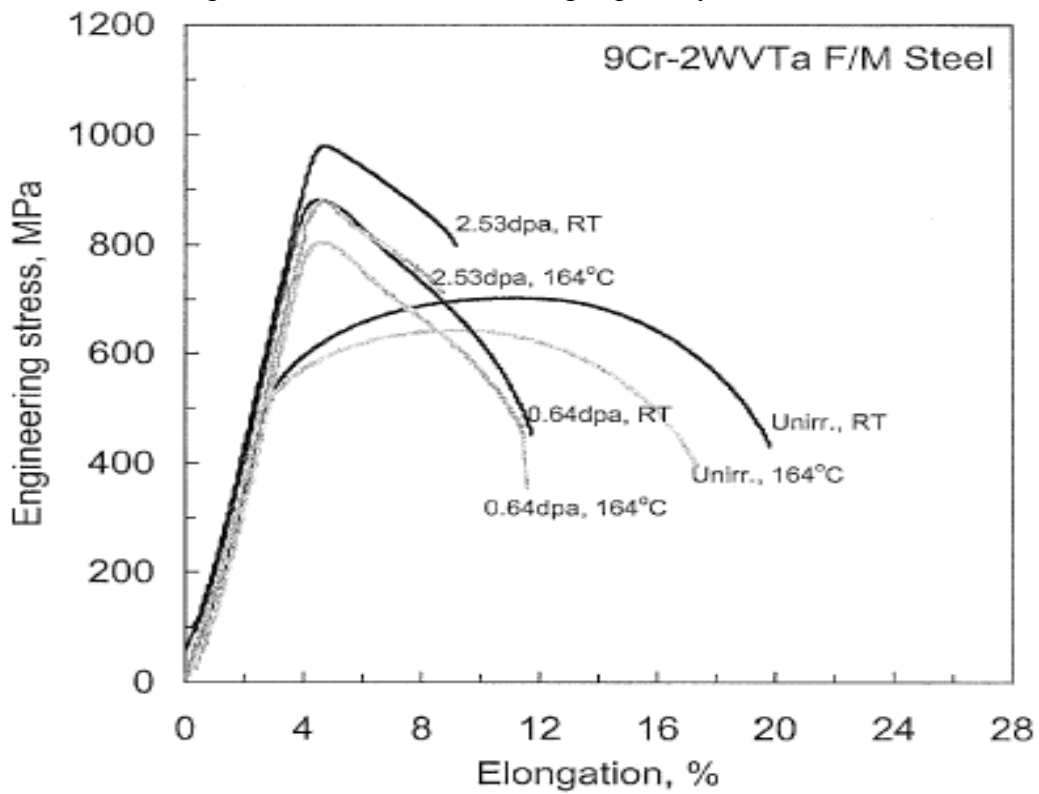

Figure 2-16 The dose dependence of strain hardening capability of 9Cr-2WVTa Ferritic/Martensitic steel [79]

31

2.3 Temperature dependence of Flow localization of 316L stainless steel

316L austenitic stainless steel has been selected a candidate structure material for ITER, ADS and Gen IV reactors, which operate at the moderate temperature range. It is a major concern of the temperature dependence of the mechanical properties of austenitic stainless steel exposed to an irradiation environment. Robertson *et al.* [28, 80, 81] reported that both the yield strength and the uniform elongation have temperature dependence. Similar observation is also reported by Kohyama *et al.* [65]. The temperature dependence of yield strength is plotted in Figure 2-17 [28] and Figure 2-18 [65] and the dependence of uniform elongation is plotted in Figure 2-19 [65].
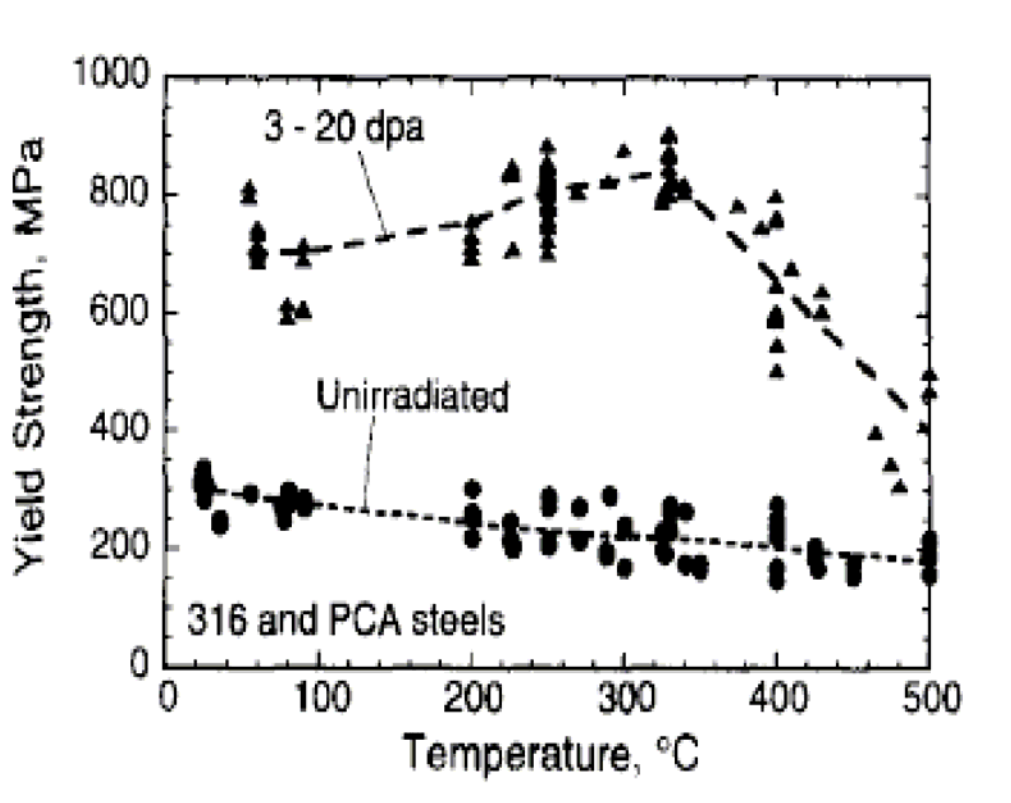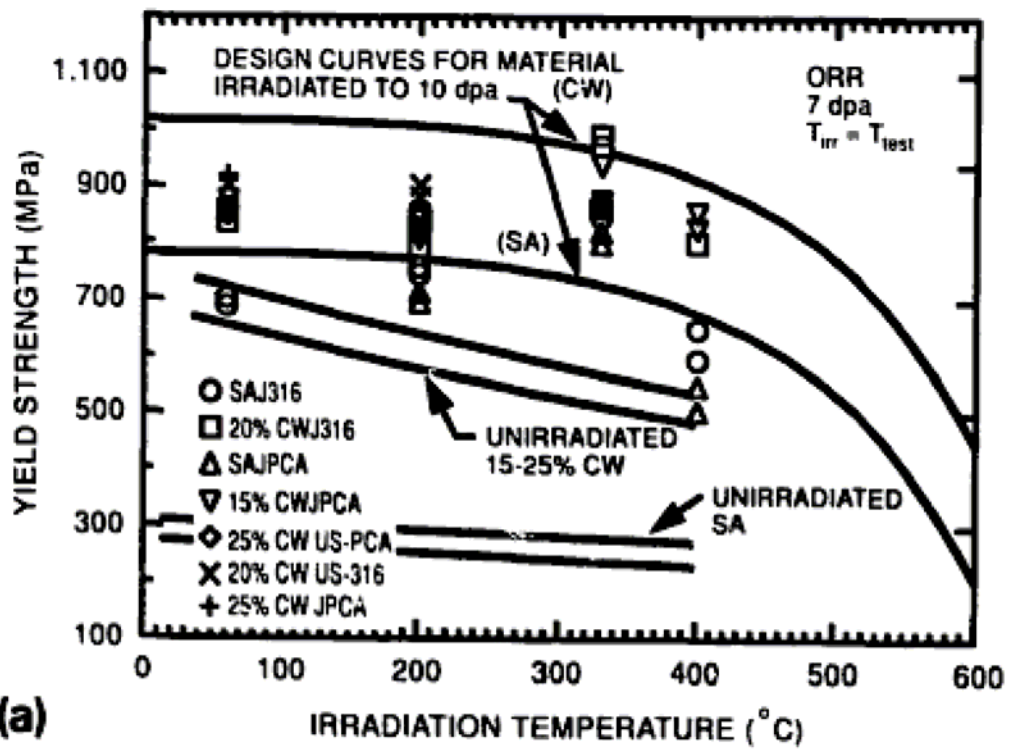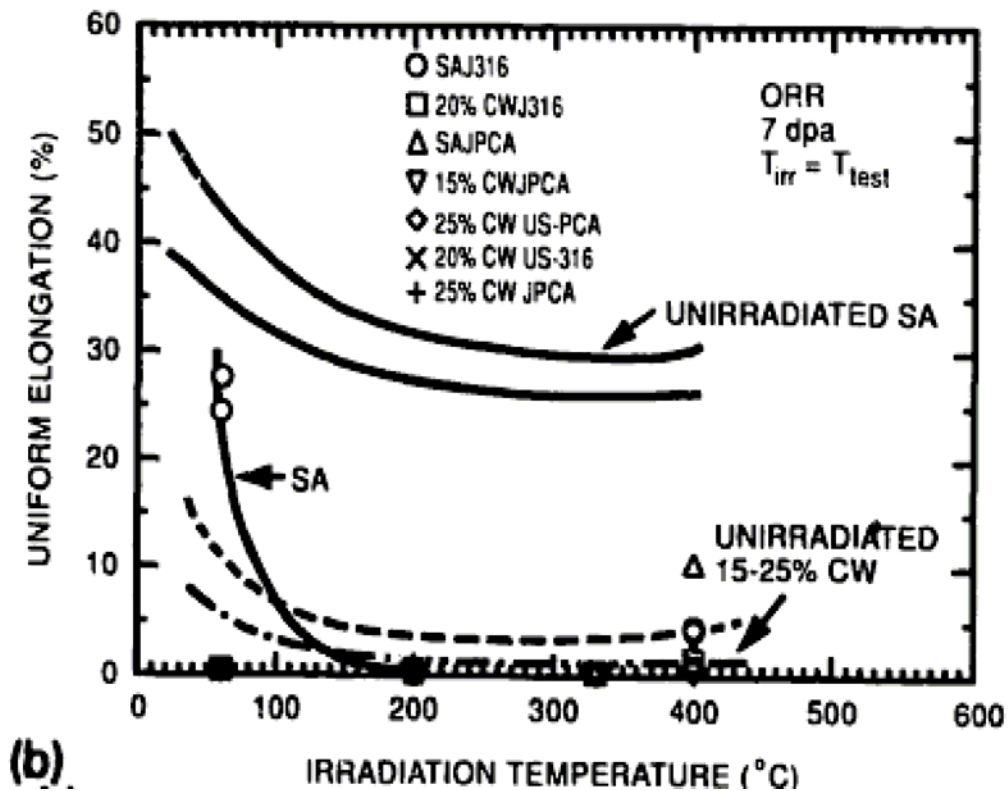

Figure 2-17 Temperature dependence of yield strength of 316 stainless steel by Robertson [28]

Figure 2-18 Temperature dependence of yield strength of 316 stainless by Kohyama [65]

Figure 2-19 Temperature dependence of uniform elongation of 316 stainless by Kohyama [65]

Robertson *et al.* [28] also reported that at low temperatures below 100°C, even at a relatively high dose condition (> 30dpa), the materials still remain certain ductility (STN > 5%) while at intermediate temperatures, even at very low irradiation level, the loss of ductility is very severe. The curve is shown as Figure 2-20 [28]. More details and explanations will be discussed later.
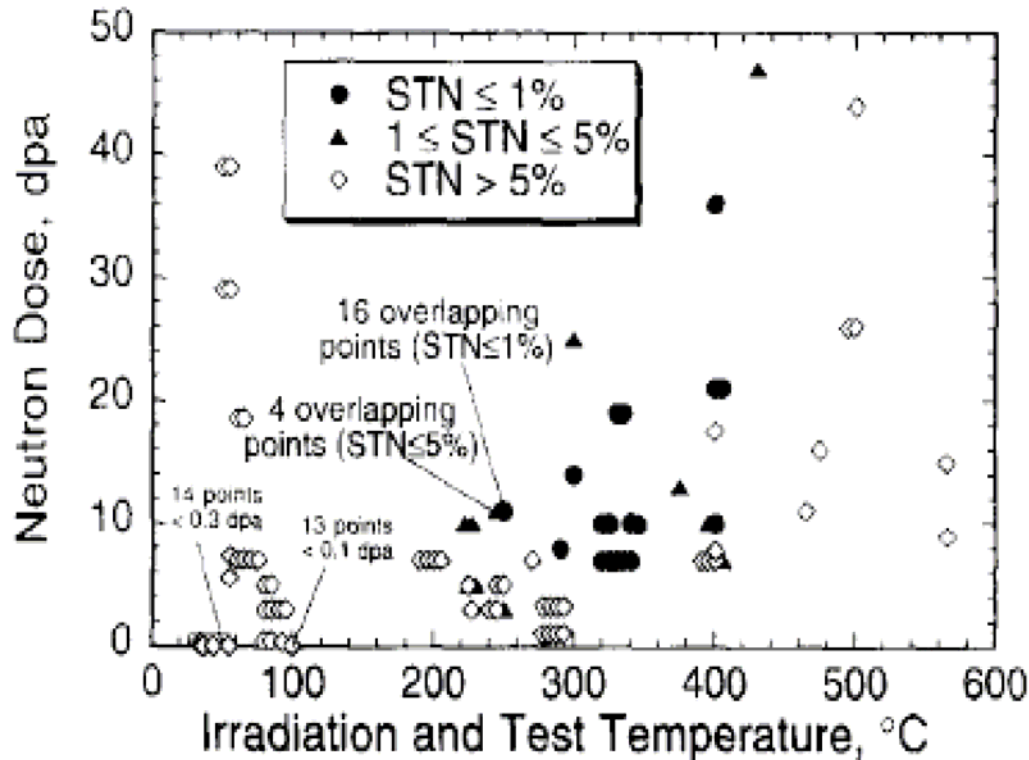
Figure 2-20 Strain to Necking as a function of neutron dose and temperature for 316 stainless [28]

2.4   Microstructure analysis during tensile loading for irradiated and unirradiated 316L stainless steel

2.4.1   Dislocation-based slip mechanism

Slip is resulted from the gliding of many dislocations. In the mode of dislocation glide, the dislocation only moves in the surface with both dislocation line and Burgers vector. Slip is the most common manifestation of plastic deformation in crystalline solids. To minimize the Peierls stress, slip predominantly occurs on the planes with maximum atomic density. The close-packed

orientation which has the lowest energy is the preferred slip direction. For face centered cubic, the preferred slip system is {111} <110>. The movement of screw dislocations are tended to be confined in certain crystallographic planes (plane family), however, they can switch from one plane to another one in the same plane family [82]. For an instant, in face centered cubic, screw dislocations can move from one {111} type plane to another. This process is defined as cross slip which is indicated in Figure 2-21 [83]:

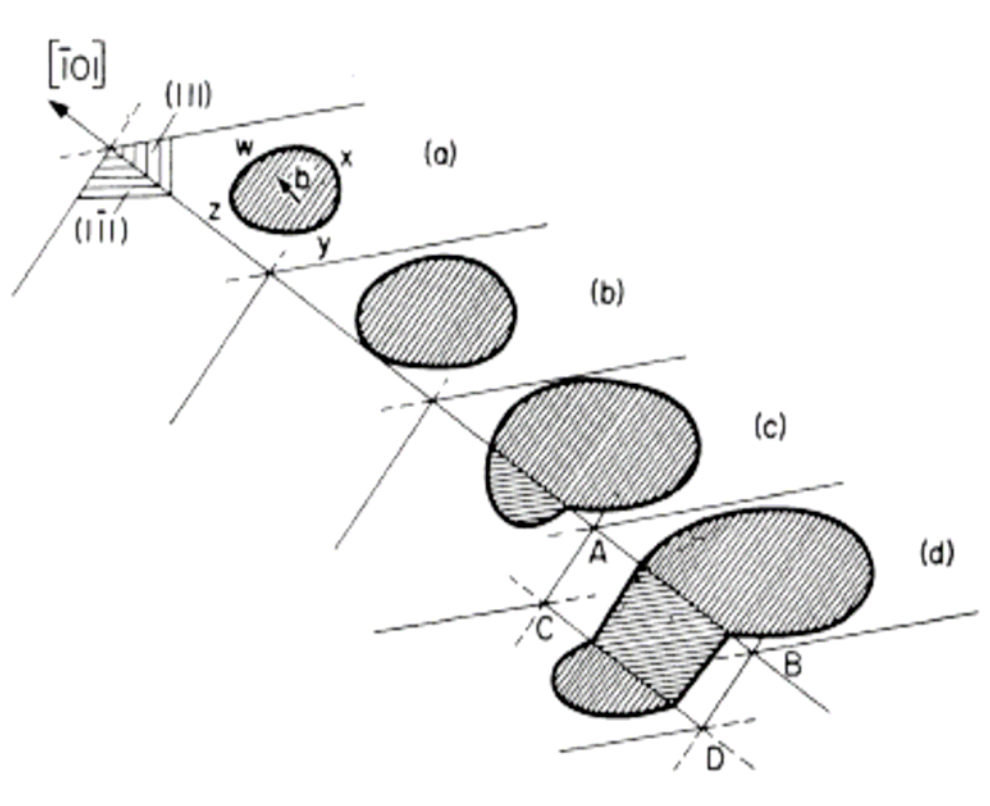Figure 2-21 Cross slip in a face centered cubic crystal [83]

The onset of plastic deformation in a single crystal is determined by the critical shear stress acting on the incipient slip plane, which is call critical resolved shear stress. This stress can be expressed as:

$$\tau_{CRSS} = \frac{P}{A_0}\cos\lambda\cos\vartheta = \frac{P}{A_0}\cdot(Schmidt.Factor)$$

The Schmidt factor represents an orientation factor.

2.4.2   Partial dislocation dissociation and stacking fault

The stacking sequence of close packed face centered cubic can be presented by ABCABCABC.... During the movement of layers to produce a displacement in the slip direction, the B layer atoms will first move to the nearby C site along the "valley" and then to the new B site instead of moving directly to another B site. Thus the unit lattice displacement b_1 is achieved by two movements of b_2 and b_3. In another word, the perfect dislocation with Burger vector of b_1 is dissociated into two partial dislocations b_2 and b_3. This process is expressed in the following equation:

$$b_1 \rightarrow b_2 + b_3$$

$$\text{Or } \frac{1}{2} <110> \rightarrow \frac{1}{6} <211> + \frac{1}{6} <12\bar{1}> \quad [83]$$

This perfect dislocation dissociation process is energy favorable which can be shown by $b_1^2 = \frac{a^2}{2} > b_2^2 + b_3^2 = \frac{a^2}{6} + \frac{a^2}{6} = \frac{a^2}{3}$. This dislocation dissociation process is shown in Figure 2-22 [69]. With the existing of dislocation dissociation or stacking fault, the cross slip is more difficult to achieve because a partial vector only lies in one {111} plane and an individual Shockley partial cannot cross slip. The stacking fault energy provides a force per unit length of line to combine the partial dislocations. The relationship between the stacking fault separation and stacking fault energy is approximately estimated as $d = \frac{Gb^2}{4\pi\gamma}$ [83].
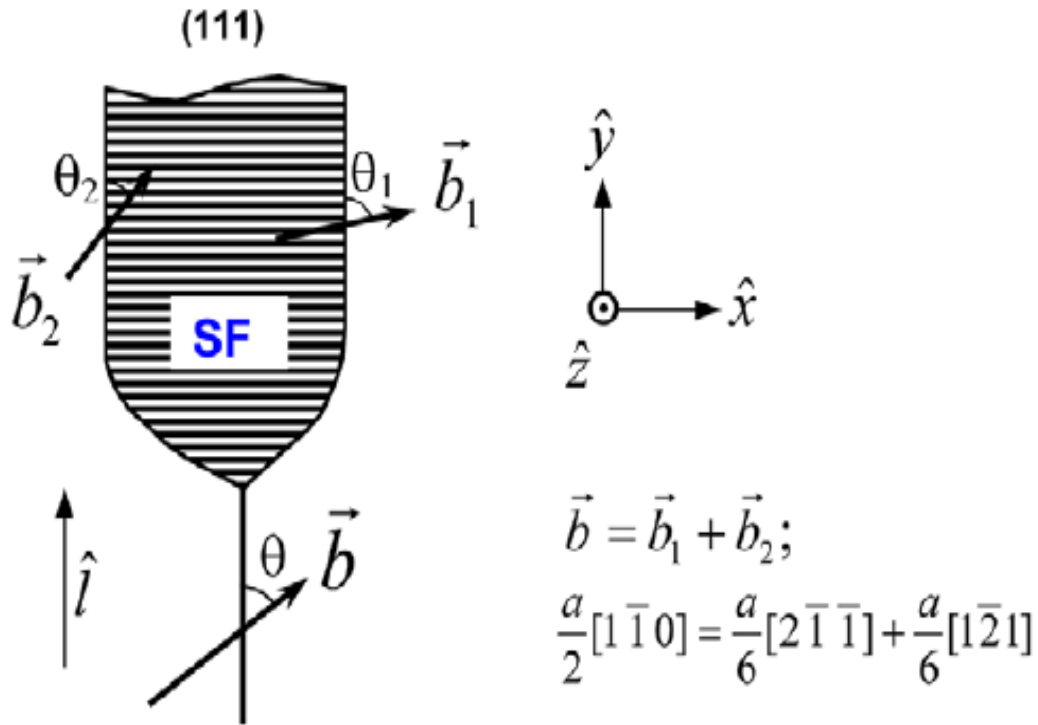
Figure 2-22 Dissociation of perfect dislocation in {111} plane into two Schockley partial dislocations [69]

2.4.3   Mechanical twinning

The deformation twinning is referred as the mirror structure induced by the homogeneous shape deformation. As shown in Figure 2-23 [82], the twinning process is essentially a rotation of the lattice in the twin producing a mirror image of those in the un-twinned material. The twinned area is rotated to another orientation; and on the contrast, the planar slip keeps the orientation of slipped regions remains unchanged. As mentioned in the previous section, the face centered cubic materials and hexagonal close-packed materials show a stacking sequence of close packed atoms. The stacking sequence is ABCABCABC… in face centered cubic materials. The twinning process causes an error in the planar stacking sequence: From -ABCABCABCABC- to $ABCAB\overline{C}BACBA$, which constitutes a twinning boundary. In this arrangement of stacking sequence, there consists of a stacking fault $B\overline{C}B$. The formation of twins is closed associated with the stacking fault [83].
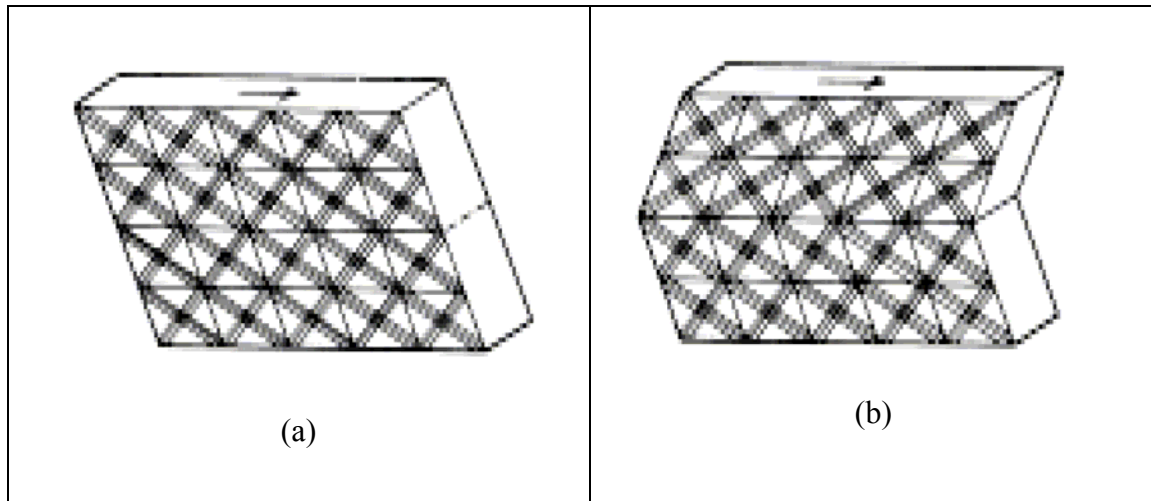
Figure 2-23 Shape change in solid cube by shear stress: (a) undistorted cube and (b) twinned shape [82]

There have been extensive studies on the effect of mechanic twinning on the plastic deformation of HCP and FCC materials [84-96]. Twinning process is prone to be activated in the materials with low stacking fault energy. In FCC materials, most of the twins are very thin comparing to the ones in HCP materials. Twinning bands, as well as the stacking fault, function as the barriers to the planar slip and hence promote the strain hardening ability of engineering materials.

2.4.4   Recent development of microstructure evolution for 316L stainless after irradiation

In the materials development for Advanced Driven System such as the Spallation Neutron Source developing in Oak Ridge National Laboratory and the concept designs of Generation IV reactors, a series of tests are carrying out in the high flux isotope reactor (HFIR) at ORNL and Los Alamos Neutron Science Center (LANSCE) at LANL. Extensive investigations have been performed on the microstructure evolution for irradiated 316L stainless steel. The microstructure characteristic of as-irradiated 316L stainless steel is shown in Figure 2-24 [30]. Small black dots, large interstitial-type faulted Frank loops and un-faulted loops can be identified. The sample was

irradiated to 10 dpa at 200°C. Bubble and loop microstructures for 316LN stainless steel irradiated with He are shown in Figure 2-25 [29].

With the development of plastic deformation, the mechanic twinning and dislocation channeling are introduced as addition deformation mechanisms. The plastic deformation process is dominated by dislocation channeling deformation. These microstructure characteristics are shown in Figure 2-26 [29] and Figure 2-27[29].
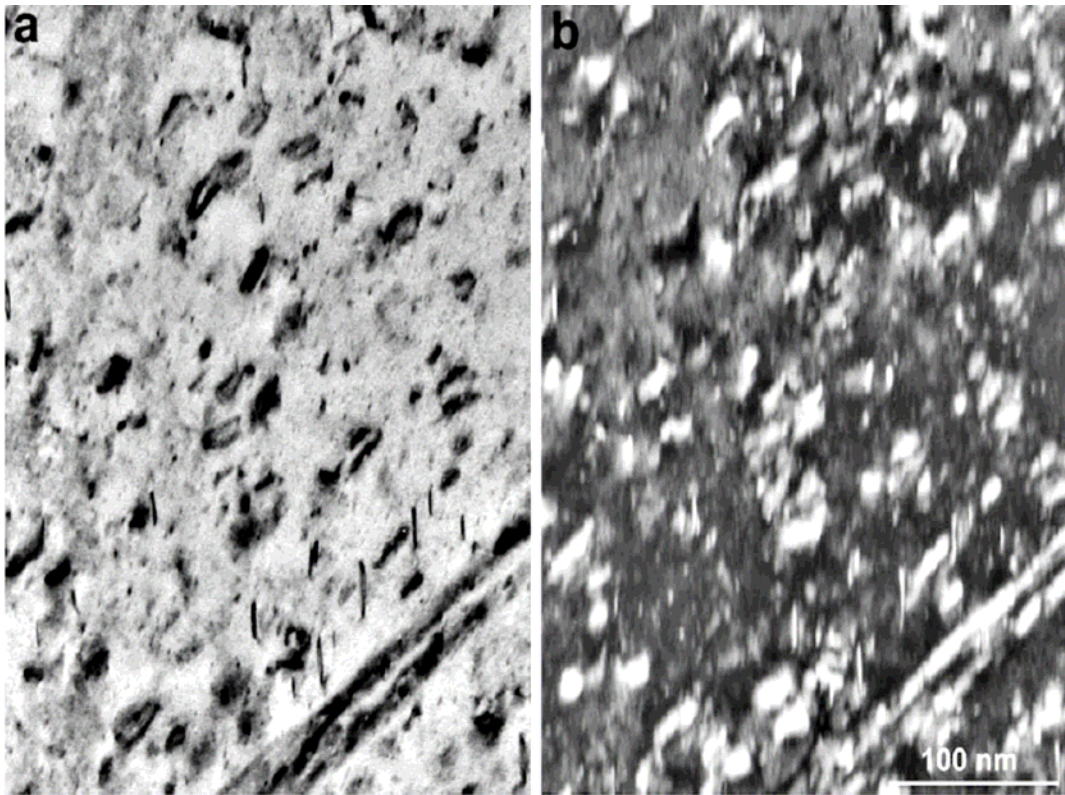
Figure 2-24 Microstructure characteristic for 316L stainless steel irradiated to 10 dpa at 200°C (Bright and dark field microscopy) [30]
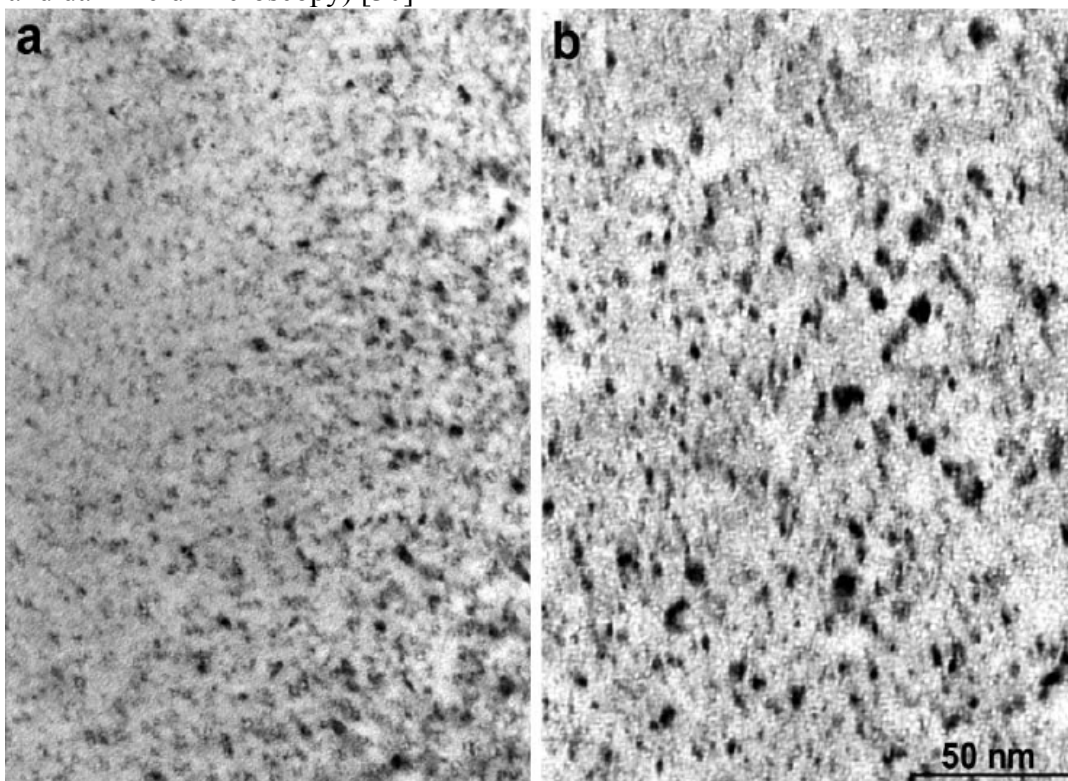
Figure 2-25 Bubble and loops microstructures for 316LN stainless steel irradiated with He to 3.75 and 7.5 dpa at 200°C [29]

Figure 2-26 The formation of twinning bands after deformed to 10%: (a) 10 dpa (b) 7.5 dpa and (c) cleared channels are shown [29]

Figure 2-27 Twinning bands (a), Stacking fault fringes (b) and defects reduced channels (c) [29]

2.5   Notch strengthening and fracture mechanism of 316L stainless steel

2.5.1   Notch strengthening mechanism

Notch strengthening has been a long term concern in nuclear industry because of the wide application of structure materials in joints, pipes *etc.* 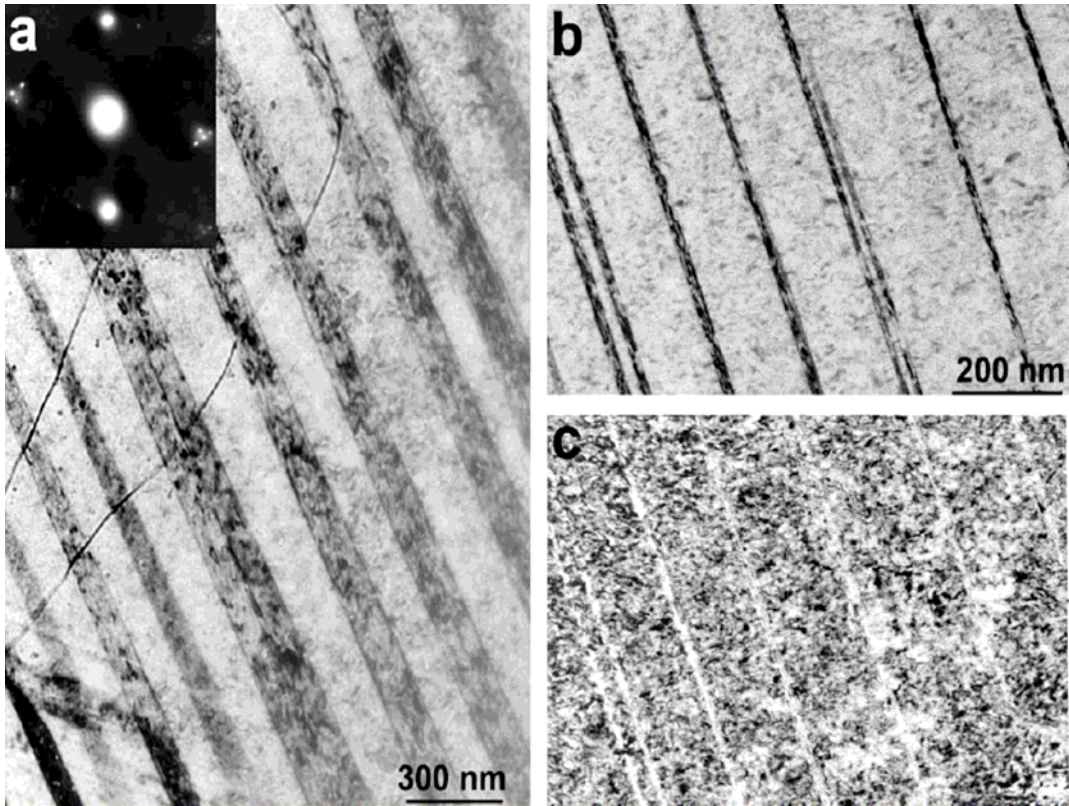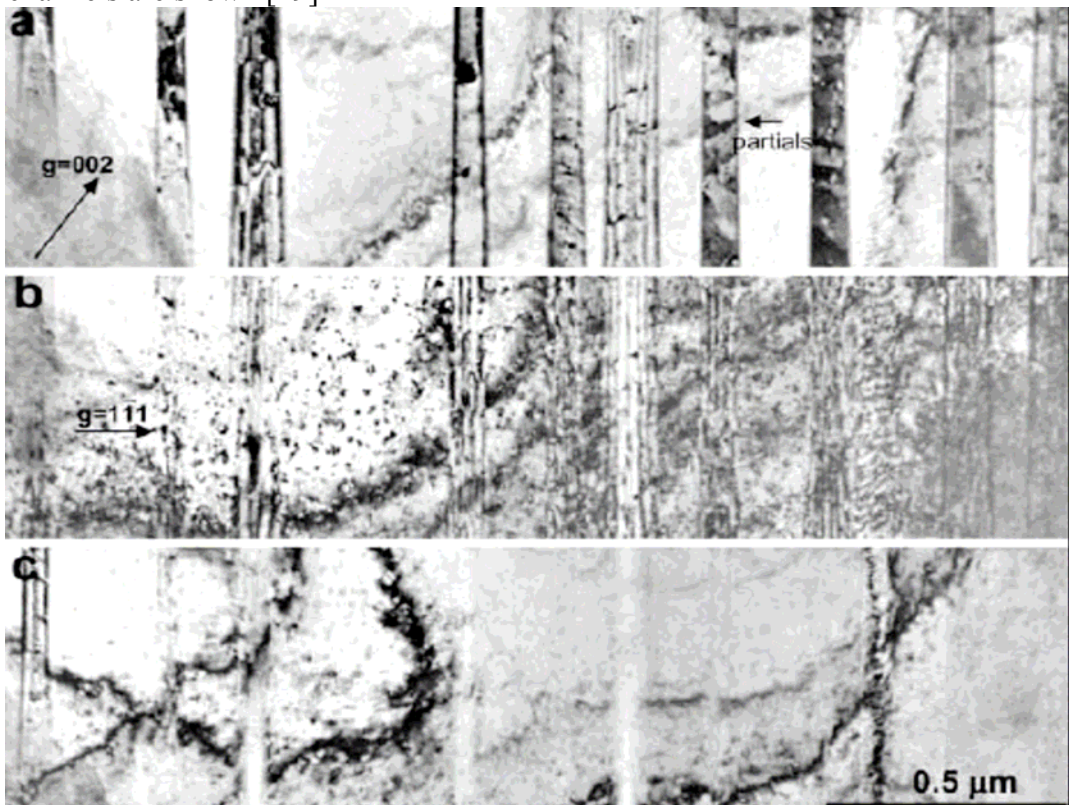The jointing portion of different component or pipe corner may cause strong locally stress concentration. This kind of stress concentration will initiate cracks and cause the failure of structure component, especially in the case of irradiation induced materials embritterment. The notch strengthening effects can be characterized by the stress concentration factor. The maximum stress at the notch tip is express as:

$$\sigma_{max} = \sigma_a (1 + \frac{2a}{b})$$

$$\text{And} \quad k_t = \frac{\sigma_{max}}{\sigma_a}$$

In the case of circle notch, this factor is 3 (a=b)

The expressions for other notch geometry can be also found in the reference [82].

2.5.2   Intergranular and transgranular fracture

Transgranular fracture and intergranular fracture are two major fracture paths observed in metals and alloys. In the following, transgranular ductile fracture, transgranular brittle fracture and intergranular fracture will be discussed.

Ductile transgranular fracture is very common in many ductile metallic metals, which results from microvoid coalescence. The fracture of ductile materials can be divided into three aspects: void nucleation, void growth and void coalesce [82].   Under local stress concentrations, plasticity-induced voids always nucleate at indigenous nucleation sites such as inclusions, second-phases and grain boundaries by particle cracking and interface decohension between

particles and matrix. Void growth results from cavity enlargement by localized plastic deformation. Coalescence is the plastic instability between voids and eventually results fracture [97]. The model proposed by Gurson [98-100] and developed by Tvergaard and Needleman [101-107] is widely used to characterize this process since it provides a quantitative explanation for void nucleation and growth.

Brittle transgranular fracture, also called cleavage fracture, usually occurs when plastic deformation becomes very difficult or plastic deformation is inhibited [82]. This typically occurs when certain dislocation slip directions are highly favored, such as those made from atoms with highly directional bonds or with low symmetry. Low temperatures, high strain rates, large grain sizes and high yield strengths usually favor this deformation mode. For austenitic stainless steel, the favored slip direction and plane are <110> on {111} [82], though fcc metals and alloys are usually much less susceptible to this deformation and fracture mode than metals and alloys with other crystal structures.

Intergranular fracture is typically the result of sustained loading at elevated temperature or in aggressive environments [82]. Conditions favorable to intergranular fracture are the presence of certain phases on grain boundaries, thermal treatments resulting in segregation of certain impurities to grain boundaries, action of certain environments and combination of stress and high temperature [97]. Fracture energies are always low due to the relative weakness of the grain boundaries which control the process.

CHAPTER 3   FLOW LOCALIZATION OF FACE CENTERED CUBIC MATERIALS

3.1   Overview

Type 316L stainless steel has been the most widely employed austenitic steel for irradiation applications. Despite limitations in thermal conductivity, swelling resistance, and resistance to stress corrosion cracking, this alloy has been used extensively in past nuclear applications and is slated for continued use in advanced nuclear systems including the Spallation Neutron Source (SNS) and the ITER fusion device.   The appeal of this material is that it is highly fabricable, weldable, and maintains reasonable ductility and fracture toughness in most applications. It has also been the basis for the development of low swelling and swelling resistant austenitic steel alloys. Low carbon versions, 316L austenitic stainless steel, and low carbon with nitrogen additions versions, 316LN stainless steel, have been developed to address stress corrosion cracking problems by reduction of carbon content, or replacement of carbon with nitrogen. Because of its widespread use as a structural alloy in a variety of nuclear applications, the mechanical stability of type 316L stainless steel as a function of radiation exposure has been a major point of concern. This alloy is susceptible to the development of very low tensile ductility due to irradiation in the temperature range of 150 to 400ºC [20]. This limitation is now well documented and shows that in a wide variety of 316 stainless steel and modified 316 stainless steel alloys, tensile ductility falls below 1% uniform elongation after doses as low as a few dpa in this temperature range. This process is often characterized as *flow localization* since the materials neck shortly after reaching their yield point in tensile loading. Because of the importance of this process to materials applications, ductility loss due to irradiation exposure has resulted in a large number of studies designed to understand the relationship between radiation-induced microstructural changes and their impact on materials

elastic and plastic flow properties. These studies have concentrated on the dislocation multiplication, pinning and flow processes. These phenomena are typically used to model yield properties and flow processes just after yield.

3.2　　Experiments and data sources

In this study, the processes of radiation-induced loss of uniform tensile elongation and flow localization in 316L stainless steel were examined. Two major studies on flow localization effects 316L stainless steel irradiated in fission spectra, one by Pawel-Robertson and co-workers [20] and a second recent study by Farrell, Byun and Hashimoto [6] were employed. In addition, a recent study on tensile properties of 316L stainless steel following exposure to a spallation-type neutron and proton irradiation spectrum were analyzed [11]. The distinction between these two types of irradiation spectra is important due to major differences in the amounts of He and H produced in addition to the displacement damage. For the studies of Pawel-Roberson *et al.* [20], neutron energy spectrum tailored reactor irradiations were performed to produce He/dpa ratios of around 10 appm He/dpa [20]. The other fission exposures produced a He/dpa ratio of on the order of 1 appm He/dpa or greater depending primarily on the neutron energy spectrum, the Ni content and the levels of B impurities [2]. The spallation environment experiments, which in most cases included irradiation along the direct beam irradiation direction where proton irradiation accompanied the neutron irradiation, produced He/dpa ratios in the range of ~40 appm He/dpa in SNS [5] to ~50 appm [108] He/dpa in LANSCE, depending on the relative numbers and energies of protons and neutrons [11, 109]. In addition, substantial amounts of H are also produced in this spectrum and can be retained in the material following irradiation exposure [11]. It is also known that H storage can develop in typical fission reactor spectra, especially when large levels of He are also produced [110].

3.3   Dose dependence of mechanic property and the concept of critical stress

Studies of loss of ductility in austenitic alloys have been on-going for over forty years. In austenitic stainless steels, this process is most apparent at intermediate temperatures, typically between 50 and 400ºC depending on the irradiation conditions. It is found that even small irradiation doses, on the order of a few dpa, are sufficient to reduce material uniform elongation to less than 1%. Figure 3-1 shows selected engineering stress – engineering strain curves for 316L stainless steel taken from the work of Maloy *et al.* [11]. The figure compares the tensile response for unirradiated and similar irradiation conditions at two tensile test temperatures, 50°C and 164ºC. The tendency toward higher yield strengths and very low values of uniform elongation with irradiation dose is clear. For doses of around 8 dpa, the material shows uniform elongations of less than 1%. Perhaps a more striking feature of the curves is the strong temperature dependence of the tensile behavior. Even for the unirradiated conditions, a change in test temperature from 50 to 164ºC results in a major change in uniform elongation from a value of around 60% at 50ºC to a level of around 40% at 164ºC. For the 2.9 dpa irradiated case, the initial deformation is similar at 50 and 164ºC, but the material then fails at low uniform and total elongations at 164ºC. At 50ºC, the material continues to strain harden following the initial deformation behavior. By 8.8 dpa, the material is brittle and necks just following yield for both test temperatures, though even the necking deformation is different between the two cases.
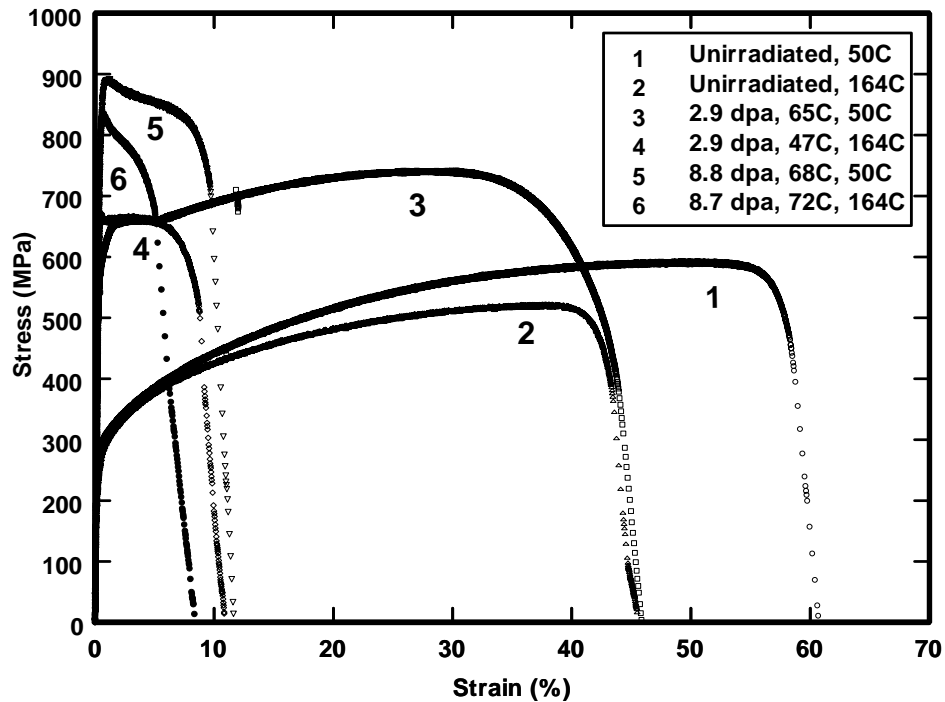
Figure 3-1 Engineering stress-strain curves for 316L SS tested at 50 or 164°C [11].

For irradiation applications, it is normal to consider the changes in yield strength and uniform elongation as a function of dose. Figure 3-2 shows the dose response of 316 stainless steel following the studies of Pawel-Robertson *et al.* [20], and Farrell, Byun and Hashimoto [6] and Malloy *et al.* [11]. Only selected data from these studies are plotted here for clarity in the figure. The data from Farrell *et al.* [6] are plotted as the average values from multiple tests at each dose and tested at room temperature. Averaged data for 25°C tensile tests from the studies of Pawel-Robertson *et al.*[20] are also shown. All available data points from the Malloy *et al.* study [11] are shown. The figure indicates that within moderate limits, the radiation-induced increases in yield strengths are similar in all cases (this will be examined in detail later), whereas the uniform elongation response has a strong temperature dependence.
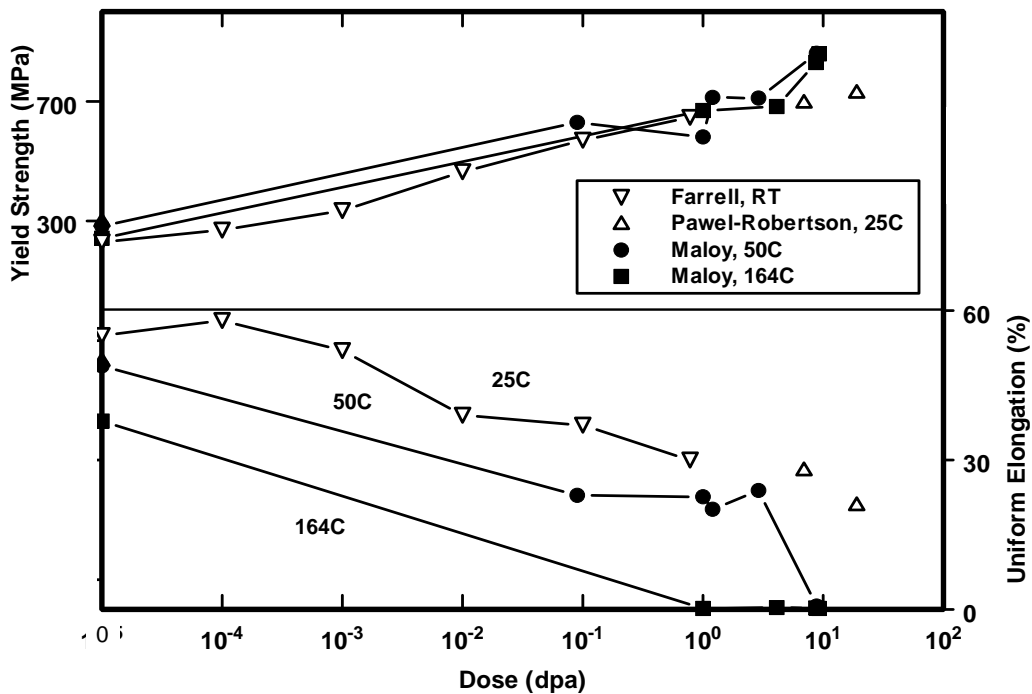
47

Figure 3-2 The relationship between irradiation exposure dose and yield strength and uniform elongation for type 316 SS [6, 11, 20].

In addition to the strong temperature dependence, there seems to be a strong correlation between the increase in yield strength and decrease in uniform elongation. In Figure 3-3, uniform elongation is shown as a function of yield strength for all of the data in the Pawel-Robertson studies [20] and for the Farrell, Byun and Hashimoto study [6]. The Pawel-Robertson data at 25°C are shown with a least squares linear fit, as are the Farrell *et al.* [6] data. While there are slight differences in the data sets, the fits are remarkably similar, with nearly the same slope. The Pawel-Robertson data at 400°C were also fit with a linear least squares fit. This fit seems to be a reasonable representation the all of the data from those studies at temperatures between 200 and 400°C. The curve also seems to be a reasonable fit to the data from the Farrell et al. study for specimens tested ate 288°C. The strong difference in temperature dependence of the two sets of curves, the ones near room temperature and the ones between 200 and 400°C, is apparent.
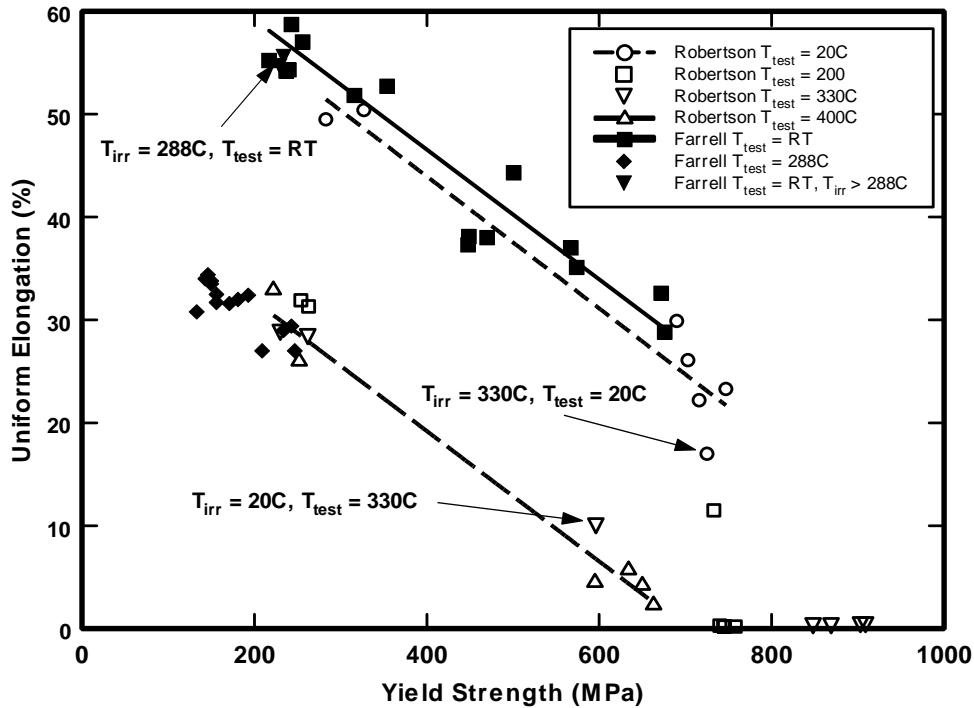
Figure 3-3 The relationship between uniform elongation and yield strength for 316 stainless steel [6, 20].

Figure 3-3 also indicates that the tensile test temperatures play a more important role in the tensile response than does the irradiation temperature. Three data points that were tensile tested at a temperature different than the irradiated temperature are indicated. These points are best associated with the tensile properties trends according to test temperature rather than irradiation temperature.

Figure 3-4 show the data from the Maloy *et al.* studies [11] with the data trends from Figure 3-3. Again there is strong temperature dependence in the tensile response between tests performed at 50°C and at 164°C. One data point at 25°C is also shown. The data trends show a different slope than those in Figure 3-3. This seems to be a result of the differences in yield strengths of the starting materials. In fact, the point of near zero uniform elongation for the 164°C tests intersects the yield strength axis at nearly the same point as that from the Pawel-Robertson studies at about 700 MPa.

The tensile tests at 50ºC indicate that an intersection of the line with the yield strength axis falls at about 900 MPa.
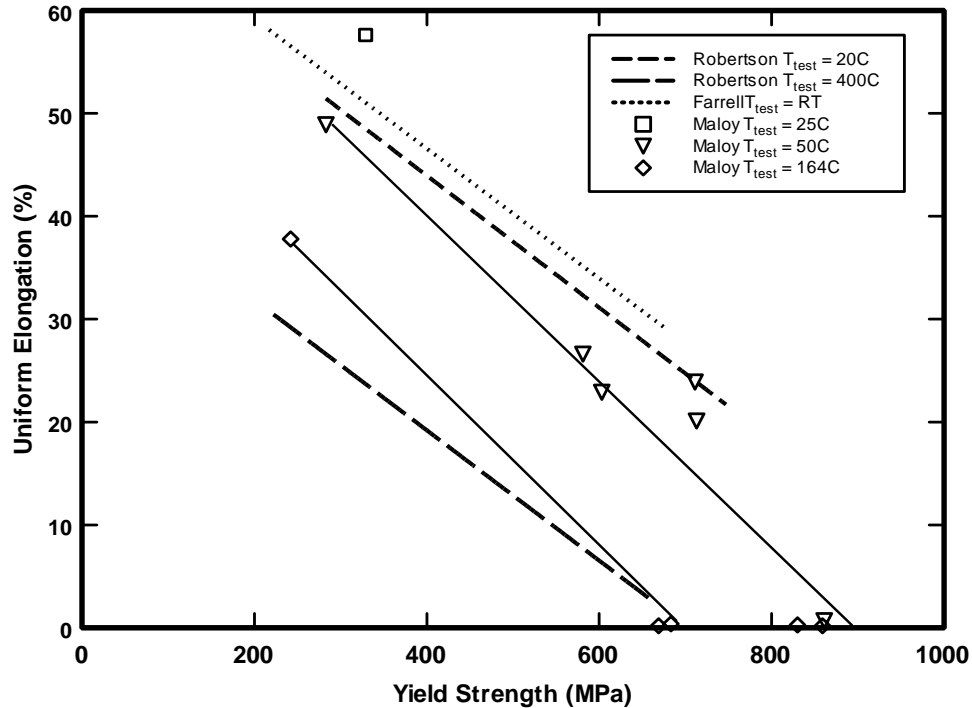

Figure 3-4   Uniform elongation versus yield strength for 316L SS irradiated in a spallation particle spectrum and tested at 50 or 164ºC [6].   The data for Maloy et al. [11] are compared to the data trends in Figure 3-3.

The intersection of the yield strength – uniform elongation trend curves with the yield strength axis defines a critical stress at which flow localization takes place upon yielding. This point is consistent with the true stress level at necking for all tensile curves regardless of radiation damage level. The true stress – true strain curves for the Maloy *et al.* [11] tensile tests are shown in Figure 3-5 for 50ºC and in Figure 3-6 for 164ºC.   Figure 3-5 shows that the true stress to necking is approximately 900 MPa at 50ºC and about 700 MPa at 164ºC, which are the same as the intersection points of the trend curves with the yield strength axis for those two temperatures in Figures 3-3 and 3-4. The true stress-strain relationships for EC316LN stainless steel are also shown in Figure 3-7.
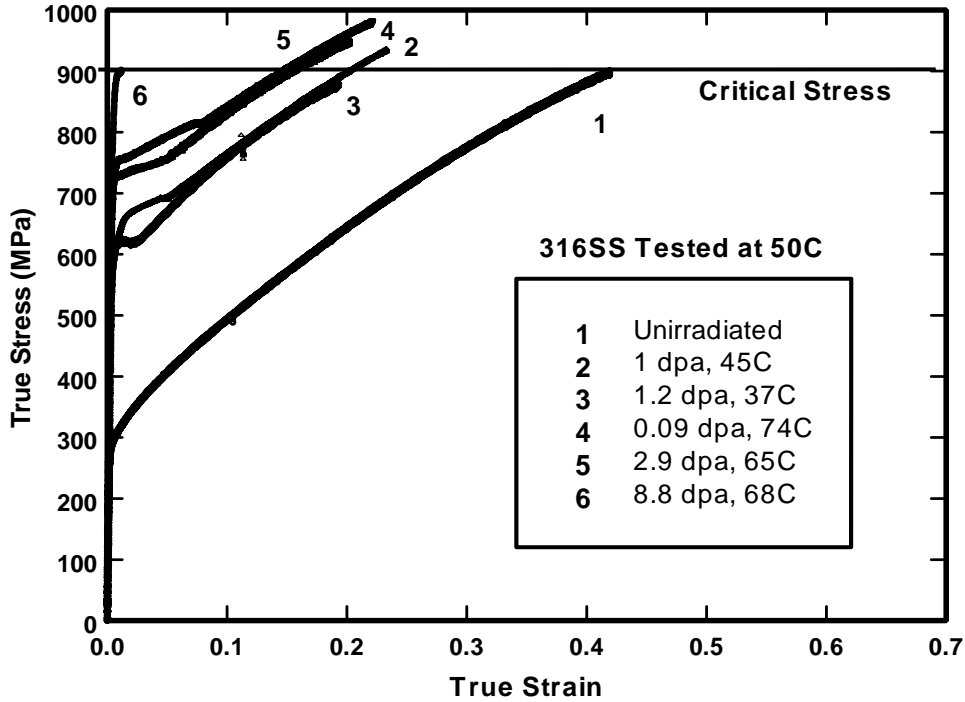
Figure 3-5 True stress-strain plot for 316L SS irradiated tested at 50ºC. The irradiation doses and temperatures are indicated in the legend [11].
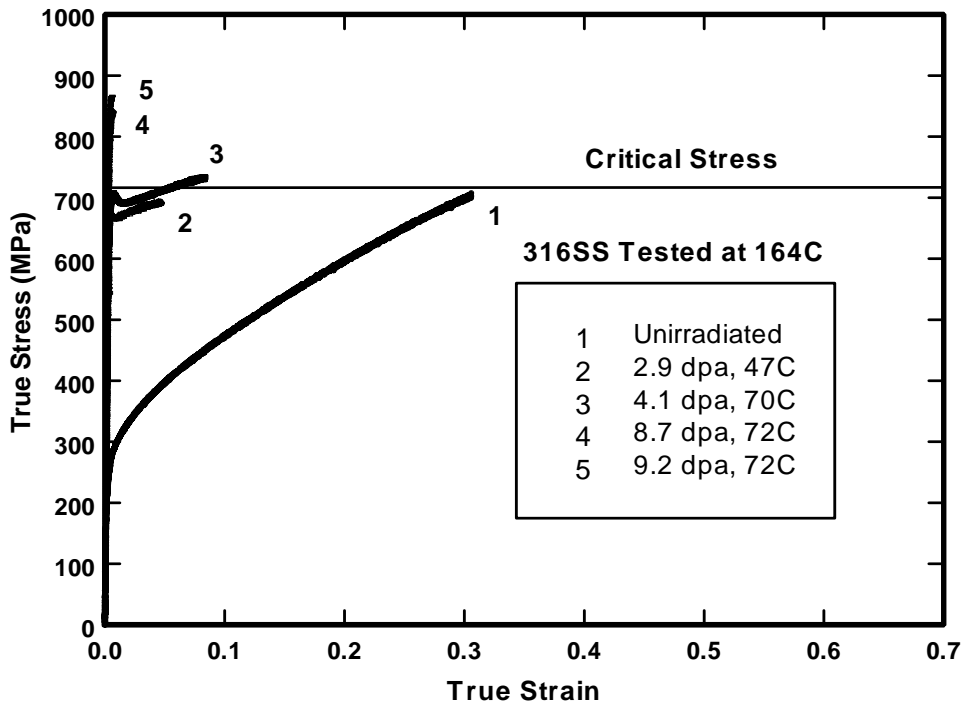

Figure 3-6 True stress-strain plot for 316L SS irradiated tested at 164ºC. The irradiation doses and temperatures are indicated in the legend [11].
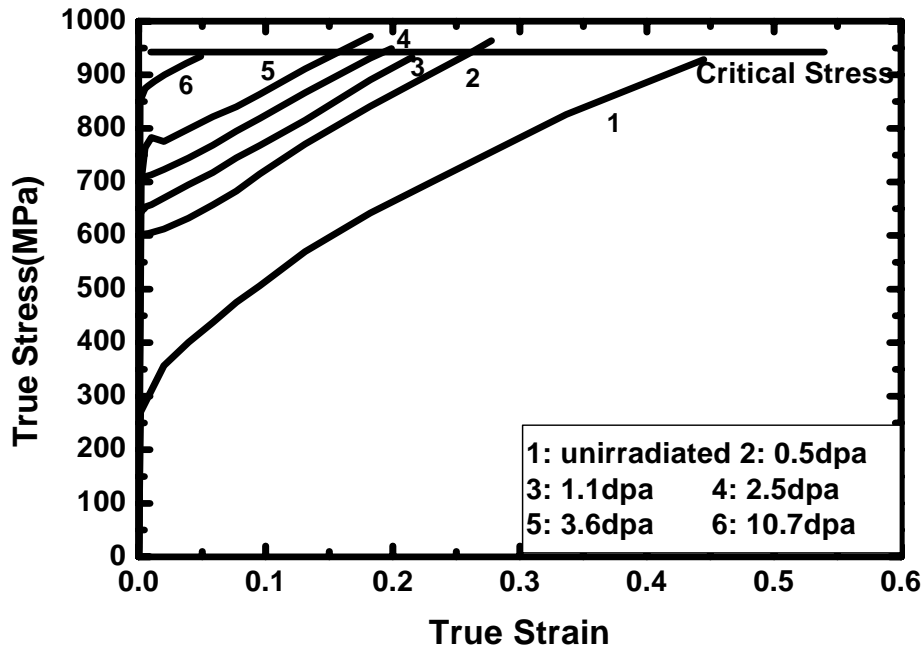
Figure 3-7 The true stress-strain tensile curves are shown for EC316LN SS tested at room temperature [6]

From the results presented above, it appears that the true stress at the onset of necking is a material property and not a function of radiation-induced defect microstructure, dislocation multiplication mechanisms or strain hardening behavior. The critical stress is reasonably insensitive to irradiation conditions. The curves from Byun and Farrell [6] at room temperature show a critical stress limit of around 950 MPa. The data from Maloy *et al.* [11] show a critical stress limit of between 900 and 950 MPa at 50°C and a level of around 700 MPa at 164°C.

3.4   Critical stress for other FCC materials

In addition to 316L stainless steel, other FCC metals are found to show the same property. One of the earliest efforts to characterize this loss of ductility in FCC metals [111] reported room temperature tensile properties for Au and Ni following various levels of irradiation exposure in

RTNS-II. Those results are re-plotted here in Figure 3-9 to Figure 3-11 in terms of true stress and true strain rather than engineering stress-strain. The figures show the curves up to the end of uniform elongation. In addition, room temperature tensile results from OFHC Cu irradiated in a fission neutron spectrum [112] are also plotted in terms of true stress and true strain. All three materials are shown on similar scales to allow direct comparison. These three FCC materials represent a spectrum of flow properties with major differences in yield strength, strain hardening behavior, and ductility. Nevertheless, in each case there is an apparent upper, critical stress limit where necking starts and uniform elongation ends. In the case of OFHC Cu, a limit of around 300 MPa is found for all conditions apart from the lowest dose irradiated condition, which seems to have broken prematurely. In Ni, the limit for all of the irradiated conditions is around 350 MPa, but the unirradiated condition shows a somewhat higher limit of just above 400 MPa. In Au, a critical stress limit of 160 MPa is found for all conditions apart from the highest irradiation condition which does, however, experience a yield drop (and possible necking) at exactly that stress level.
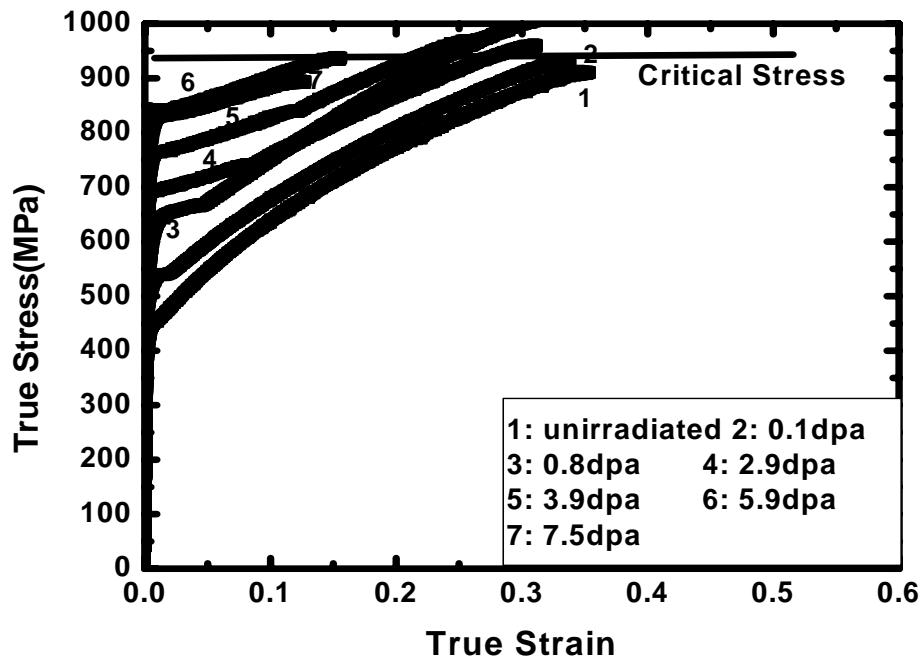
Figure 3-8 The true stress-strain tensile curves are shown for 304L tested at 50ºC [11]
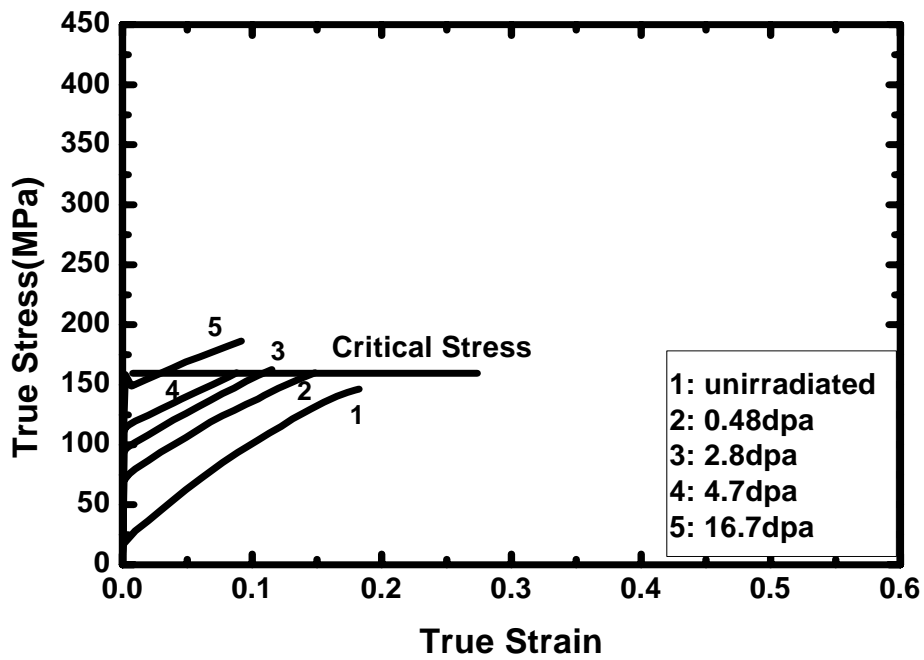

Figure 3-9 The true stress-strain tensile curves are shown for pure Au irradiated in RTNS-II with DT neutrons [111]
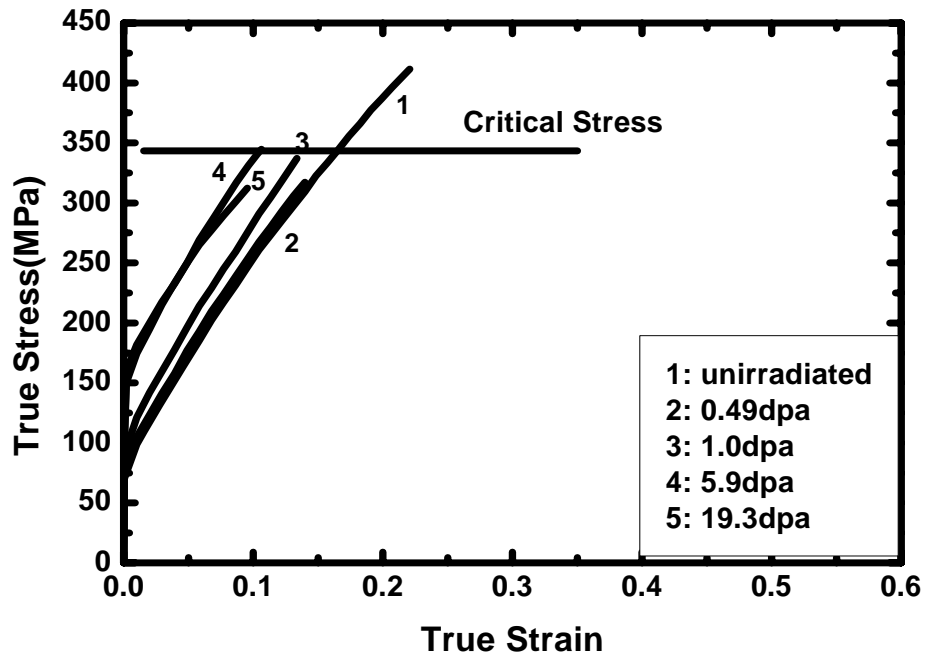
Figure 3-10 The true stress-strain tensile curves are shown for pure Ni irradiated in RTNS-II with DT neutrons [111]
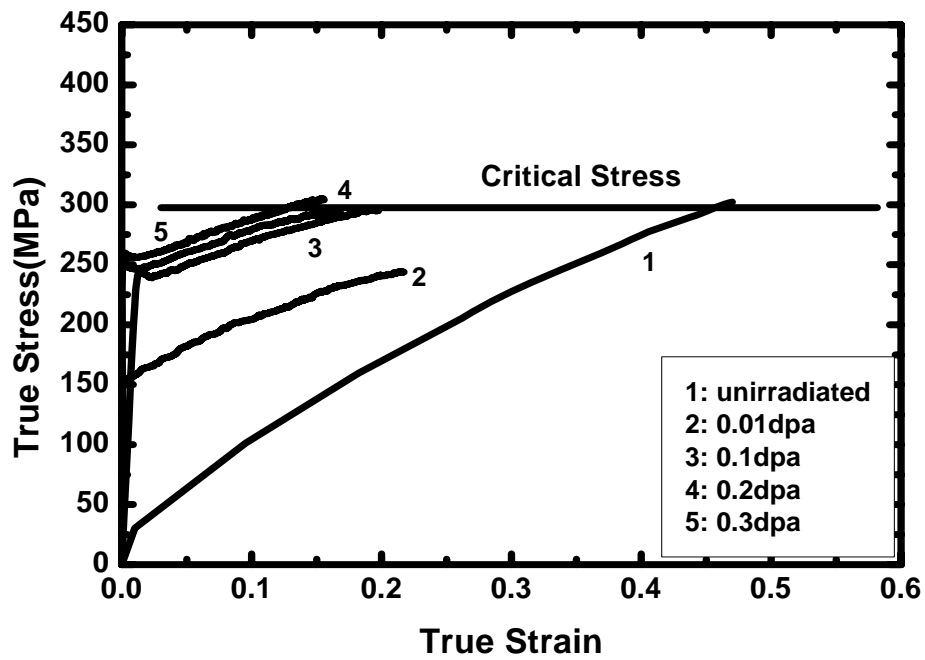

Figure 3-11 The true stress-strain tensile curves are shown for OFHC-Cu irradiated in DR-2 with a fission neutron spectrum [112]

As the linear correlation between uniform elongation and yield strength of 316 stainless steel shown in Figures 3-3 and 3-4, Figure 3-12 shows yield strength and uniform elongation data from the Ni, Au, and Cu tensile tests shown in Figure 3-9 to Figure 3-11. Data in Figure 3-12 were selected to include only the tensile tests results with the measured. In addition, the critical stress is indicated on the yield strength axis at zero uniform elongation, consistent with observations of the tendency for flow localization at yield once the yield strength reaches the critical stress. Here it is apparent that a nearly linear relationship exists between the yield strength and the uniform elongation. The intercept of the trend lines with the yield strength axis (i.e. the x-axis) provides a good estimate of the critical stress level. This is the yield strength level at which the material will neck at yield, and thus exhibited zero uniform elongation. In irradiation studies, it is possible to elevate the yield strength above this critical limit. In those cases, the specimen will also neck at yield.
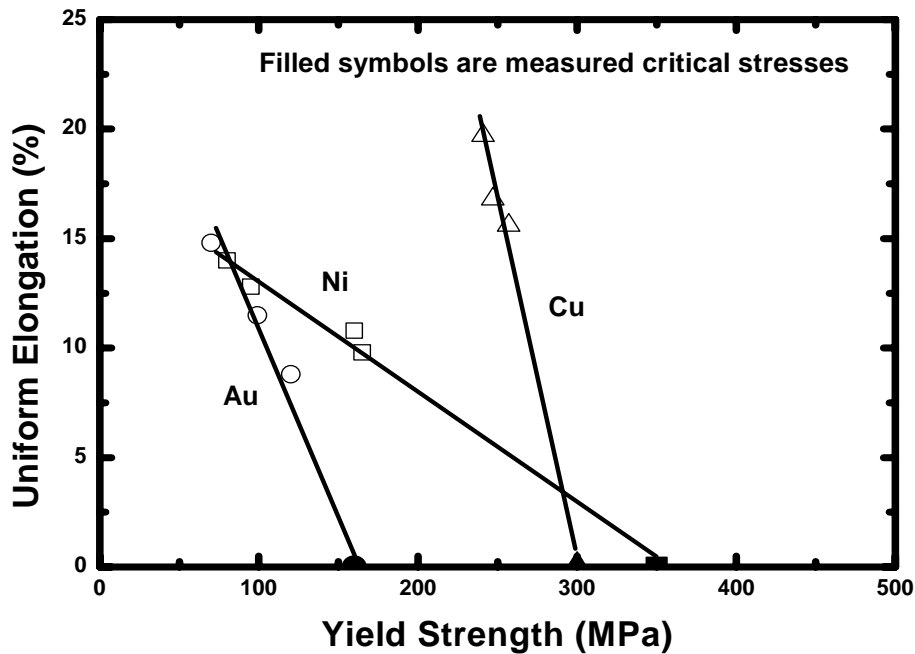
Figure 3-12 The uniform tensile elongation versus the yield strength is shown for the Ni, Au, and Cu conditions shown in Figures 3-9 to 3-11

It is commonly observed that increases in material yield strength with irradiation result in a reduction of uniform elongation. In the cases examined here, there is a nearly direct correlation between these two properties, which is there is a decrease in uniform elongation that is inversely proportion to the increase of yield strength. In all of the preceding cases, there is also a critical stress level at which uniform elongation stops and necking starts. This level seems to be independent of irradiation condition for the materials examined here. In the current cases, the full tensile curves are available to examine the precise strain hardening behavior leading to the end of uniform tensile elongation. In many cases, the full tensile curves are not available for analysis. In the absence of full tensile curve data it is possible to develop a reasonable estimate of the critical stress level using only the yield strength and uniform elongation data. This was shown to be useful for analyzing a broad number of type 316 stainless steel alloys. Here it is apparent that a nearly linear relationship exists between the yield strength and the uniform elongation. The intercept of the trend lines with the yield strength axis (i.e. the x-axis) provides a good estimate of the critical stress level. This is the yield strength level at which the material will neck at yield, and thus exhibited zero uniform elongation. In irradiation studies, it is possible to elevate the yield strength above this critical limit. In those cases, the specimen will also neck at yield. Examples of this deformation behavior can be seen in Figure 3-6 for 316L stainless steel tensile tested at 164C.

CHAPTER 4 TEMPERATURE DEPENDENCE OF FLOW LOCALIZATION FOR FACE CENTERED CUBIC MATERIALS

4.1 Overview of temperature dependence and experiments

Studies of loss of ductility in metallic alloys during irradiation have received considerable attention since the earliest studies on irradiation effects in materials. Face centered cubic (FCC) metals and alloys have shown the best resistance to radiation-induced ductility loss at ambient and intermediate irradiation temperatures. In order to investigate the radiation effects in austenitic stainless steel, data from irradiated 300 series stainless steels from ORNL, LANL and PNNL are analyzed. The geometry of LANL's specimen is referred to Figures 4-1. The 316L and 304L specimens were irradiated from 30 to 120ºC up to 12 dpa. The specimen thicknesses are 0.25 and 0.75mm and the specimens are in the annealed form without further heat treatment [12]. The dimensions of specimen are shown as Figure 4-1 [11]. The experiments at LANL were performed at temperatures of 20, 22, 50, 80 and 164 ºC.
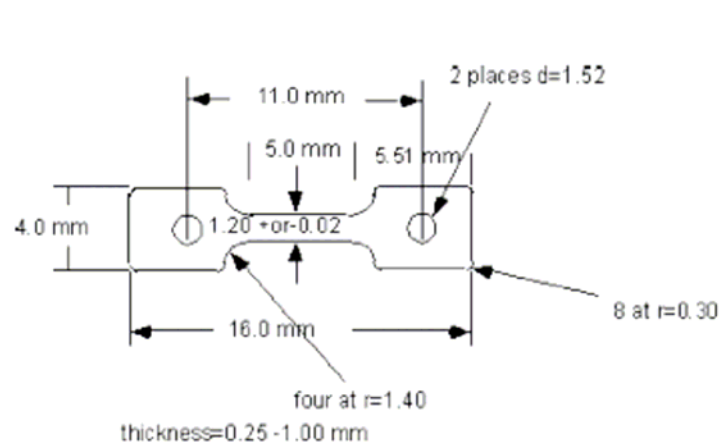

Figure 4-1 Dimensions of specimens used in the LANL experiments [11, 12]

Several earlier studies from ORNL were also employed, but these studies reported only major tensile properties following irradiation, and did not include full tensile curves. The ORNL

specimens were irradiated in fission reactor, usually in HFIR, and the specimens of LANL were irradiated in a spallation spectrum with very high energy neutrons and protons at the LANCE Irradiation facility with source protons at 800 MeV. Because of the very high energy of the initial proton beam, the spallation irradiation spectrum is very hard, and produces large amounts of H and He through transmutation reactions. Some H is also implanted from the incident proton beam or through spallation protons incident on the material specimens. These elements can also affect the irradiation response of the material. Table 4-1 shows the details of the sources of data.

Table 4-1 Sources of Tensile Data

Data Type	Sources of Data
Unirradiated 316L Stainless Steel: annealed and cold worked	This Study
Unirradiated and Irradiated 316L and 304L Stainless Steel	LANL and ORNL
OFHC-Cu	PNNL
Ni and Au	A. Okada [111]

Tensile tests were also performed in this study on unirradiated 316L stainless steel in Advanced Materials Testing and Evaluation Laboratory (AMTEL) in University of Illinois at Urbana-Champaign. The temperature range is from room temperature to 600 ℃ and the cross-head speed is 0.005 mm/s. Two sets experiments were carried out: one is cold worked 316L stainless steel and the other is annealed 316L stainless steel. Figure 4-2 shows the engineering stress-strain curves for 316L stainless steel from RT to 600° C. These curves indicate that the

testing temperatures have a significant impact on the materials ductility. The true stress- strain

curves for the materials tested in this study are shown in Figure 4-3. More details about the

temperature dependence of the tensile response will be discussed later in this study.
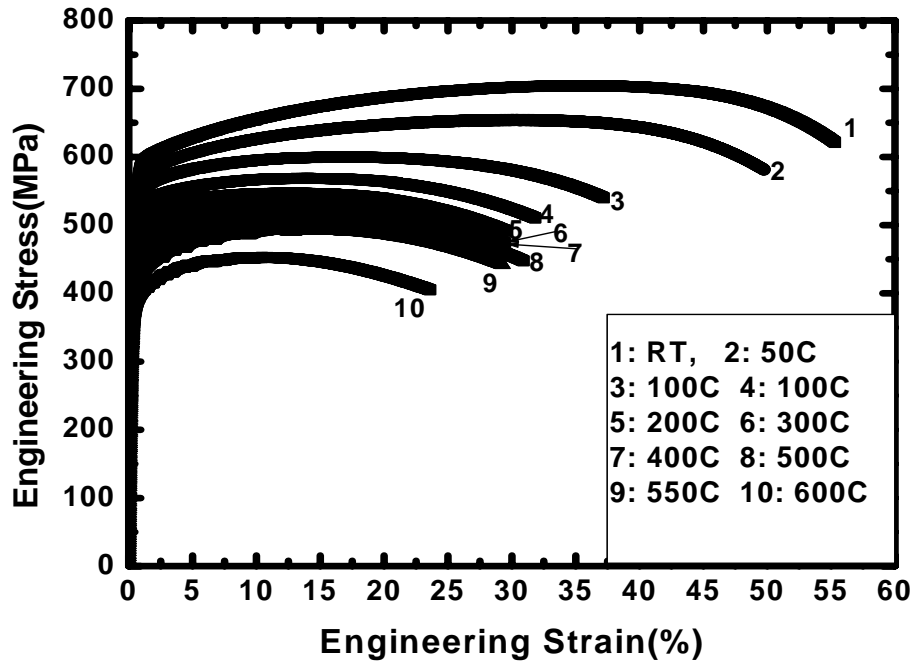

Figure 4-2 Engineering stress-strain relationship for unirradiated 316L stainless steel tested at temperature from 20 to 600° C
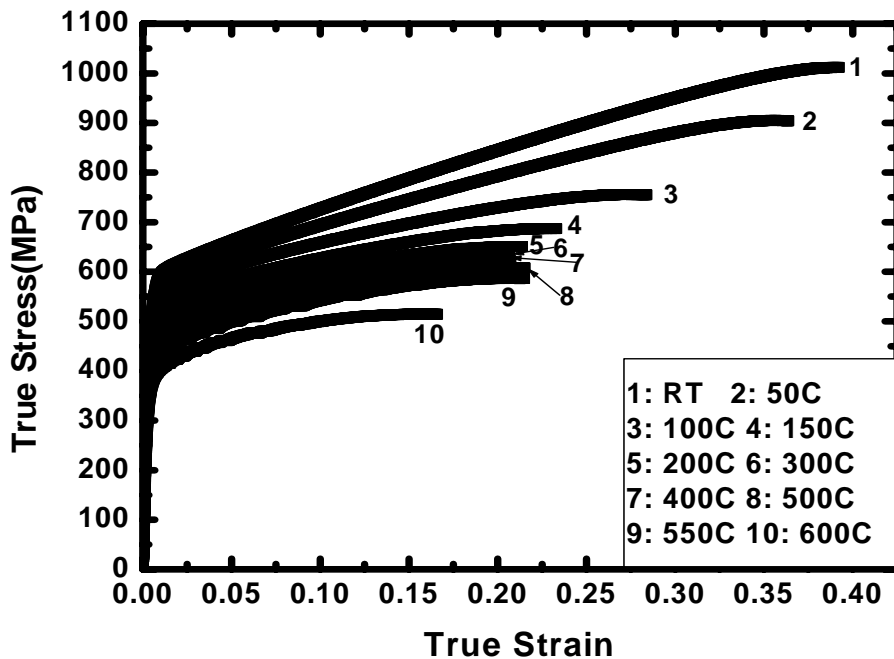
Figure 4-3 True stress-strain relationship for unirradiated 316L stainless steel tested at temperature from 20 to 600° C

4.2   Shift method and linear hardening

Figure 4-4 indicates the same data re-plotted according to a method suggested by Byun and

Farrell [6] so that the curves are shifted proportional to their increase in yield strength. This

approach makes it more obvious that the final portions of the curves all exhibit essentially the

same strain hardening behavior prior to necking. Even in the case of Ni, where the tensile curve

for the unirradiated specimen shows a larger uniform elongation, all of the strain hardening curves

superimpose. It is also notable that the last segments of the strain hardening curves are nearly

linear. All three of these materials exhibit three stages to the tensile behavior: linear elastic

deformation, post-yield strain hardening, and a final linear strain hardening portion leading to

necking. In several cases, the irradiated material does not show the intermediate strain hardening

behavior; rather elastic yield is followed by direct linear hardening until necking. The values of

the linear strain hardening slopes are given in Table 4-2 along with the critical stress limits. In the cases where there is no intermediate strain hardening phase, the values of the intercept are a good approximation of the material yield point.

TABLE 4-2— Critical Stress and Linear Strain Hardening values for Ni, Au and Cu

Material	Critical Stress, MPa	Linear Strain Hardening: $\sigma = A_0 + A_1\varepsilon^1$, MPa
Ni	350	$\sigma = 95.777 + 1536.4\varepsilon^1$
Au	160	$\sigma = 37.507 + 623\varepsilon^1$
Cu	300	$\sigma = 78.811 + 484.84\varepsilon^1$
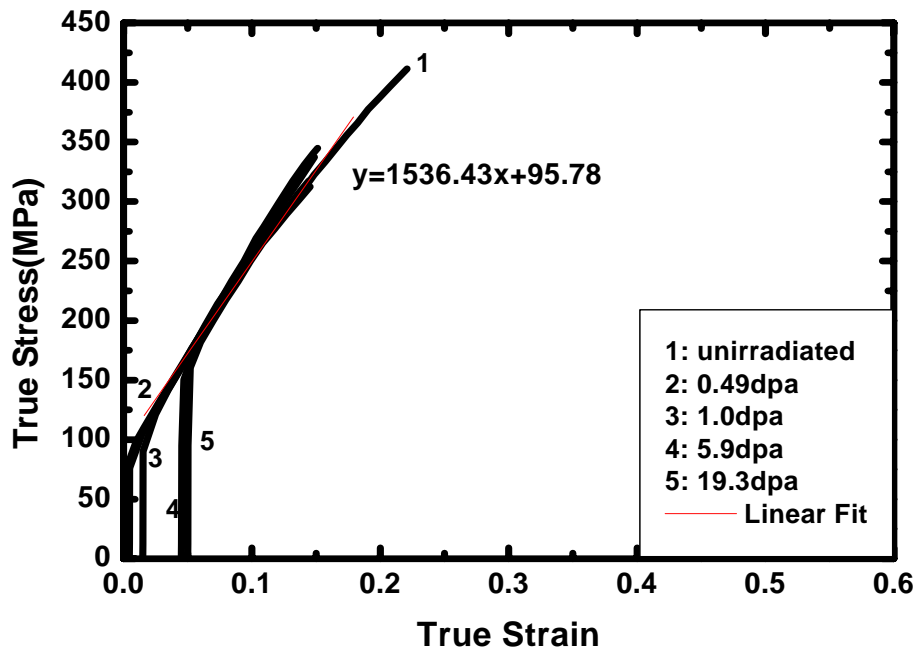
(a)
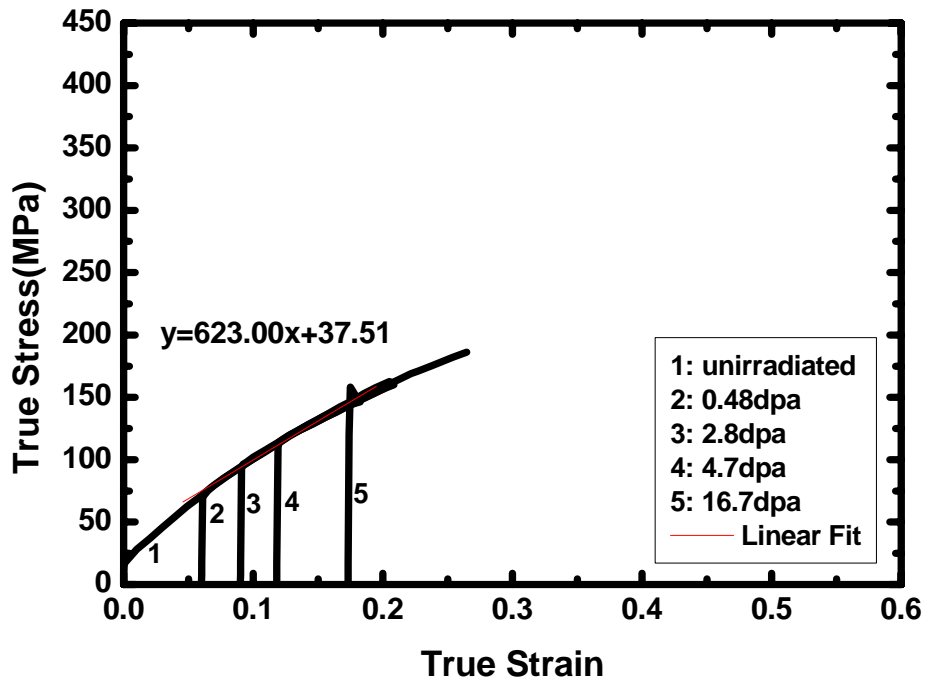
(b)
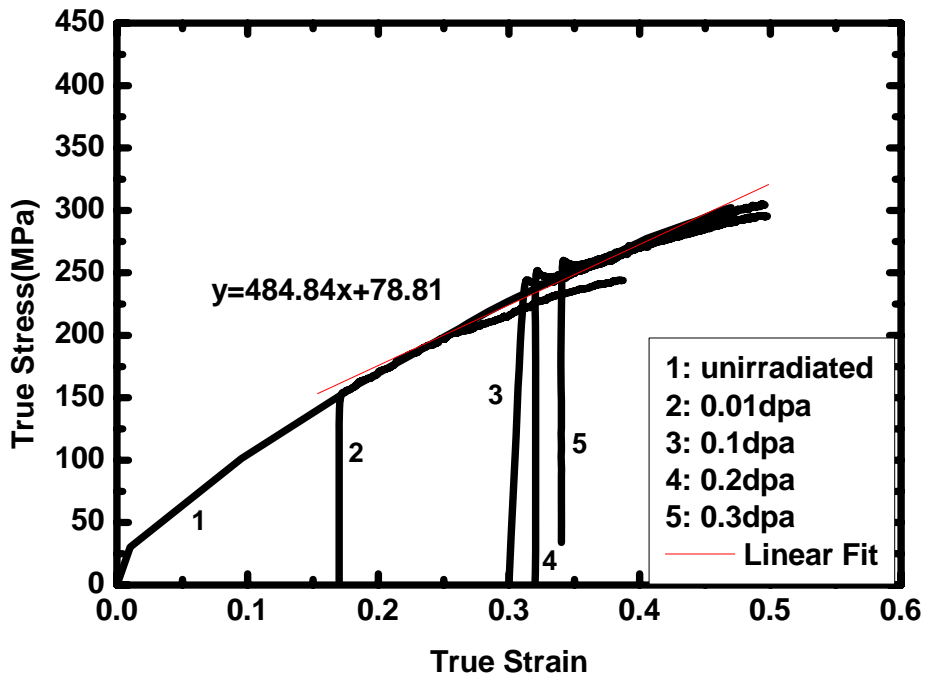
(c)

Figure 4-4   The true stress-strain tensile curves are shown for (a) Ni [111], (b) Au [111], and (c) Cu [112] with the curves shifted proportional to the irradiation-induced increases in yield strength. The fit to the linear strain hardening region is shown.

4.3   Temperature dependence of critical stress for 316L stainless steel

The tensile behavior of the type 300 series stainless steel alloys following irradiation is of direct concern for a number of practical applications. Several recent and past studies have examined this behavior, primarily though direct reporting of engineering tensile properties as a function of dose [6, 11, 20, 79]. Earlier work in the previous section indicated that a useful interpretation of the data could be obtained by plotting the uniform elongation as a function of the yield stress. In most cases, this yields a linear relation between the two values which intercepts the yield strength axis (i.e. at zero uniform elongation) at or very near the critical stress level. This approach is useful when limited tensile data are available. However, as the analysis for the three unalloyed FCC metals indicates, more useful information can be obtained from the full stress-strain curve, particularly plotted in terms of true stress - true strain. Certain of these curves are available for Type 316 stainless steel and Type 304 stainless steel at various temperature and irradiation conditions.
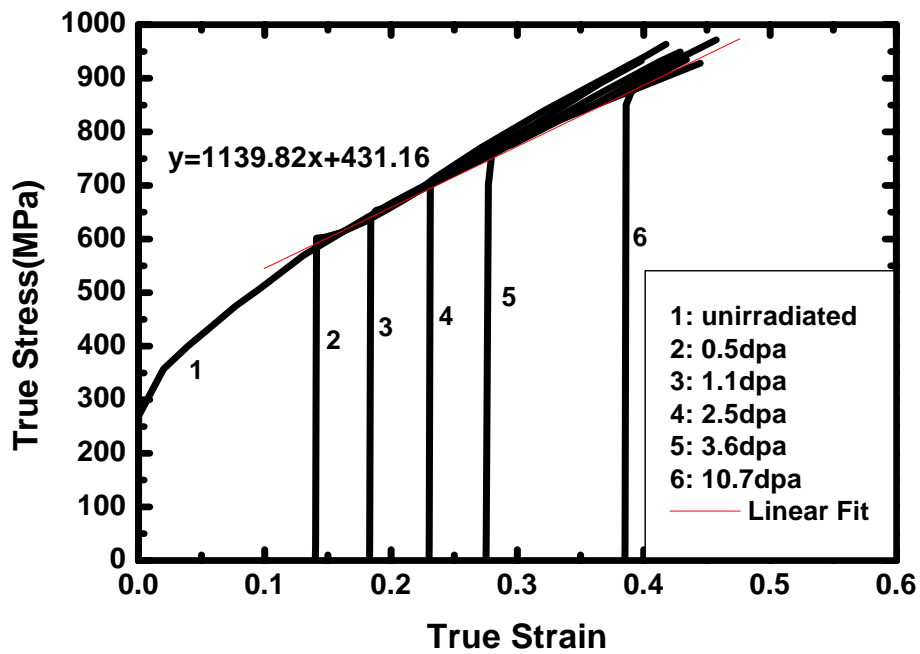
Data from Byun and Farrell [6] for EC 316LN stainless steel tensile tested at room temperature, and data from Maloy *et al.* [11, 12] at tensile test temperatures of 50 for 316L stainless steel and 304L stainless steel, and 164C for 316L stainless steel were used to better examine the flow localization process. Figures 3-5 to 3-7 indicate true stress – true strain curves for various type 316L stainless steels at three test temperatures [6, 11, 12, 51]. It is clear that an upper limit to the stress which leads to necking is found in all three cases. This critical stress is reasonably insensitive to irradiation conditions. The curves from Byun and Farrell [6, 51] at room temperature show a critical stress limit of around 950 MPa. The data from Maloy *et al.* [11, 12] show a critical stress limit of between 900 and 950 MPa at 50ºC and a level of around 700 MPa at 164ºC.   Earlier studies [17] show that this critical stress limit is apparently very sensitive to test

temperature as the temperature increase above room temperature, and relatively insensitive to test temperature between about 200 and 400ºC.

The curves shown in Figures 3-5 to 3-7 are re-plotted according to the method of Byun and Farrell [79] in Figure 4-5 for the same sets of alloy and test conditions. Again, it is apparent that the final stages of the strain hardening behavior are well represented by a linear fit. The irradiated conditions show a sharp transition from linear elastic behavior to linear plastic behavior, whereas the unirradiated conditions show an intermediate strain hardening phase. Nevertheless, the final stages of plastic flow behavior prior to necking are essentially the same for the unirradiated and irradiated materials conditions. The values for these linear strain hardening curves are given in Table 4-3.

TABLE 4-3— Critical Stress and Linear Strain Hardening values for 316 SS

T (ºC)	Critical Stress, MPa	Linear Strain Hardening: $\sigma = A_0 + A_1\varepsilon^1$, (MPa)
20	~950	$\sigma = 408.34 + 1262.9\varepsilon^1$
50	~950	$\sigma = 394.37 + 1241.8\varepsilon^1$
164	~700	$\sigma = 380.94 + 1066.1\varepsilon^1$

(a)

y=1241.85x+394.37

1: unirradiated
2: 0.09dpa
3: 1.0dpa
4: 1.2dpa
5: 2.9dpa
6: 8.8dpa
—— Linear Fit

(b)

y=1041.03x+387.55

1: unirradiated
2: 2.9dpa
3: 4.1dpa
—— Linear Fit
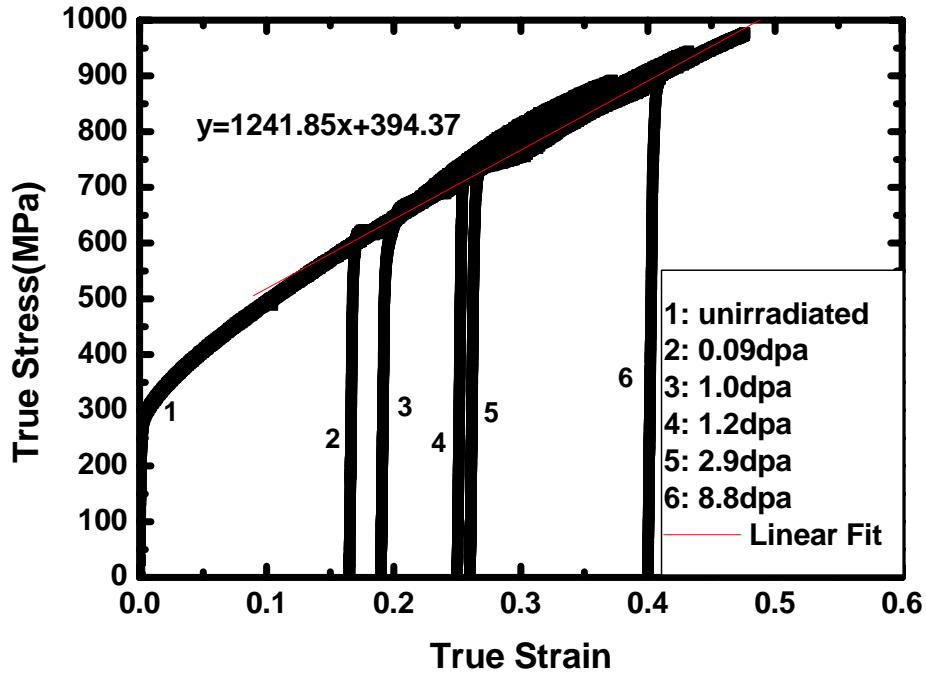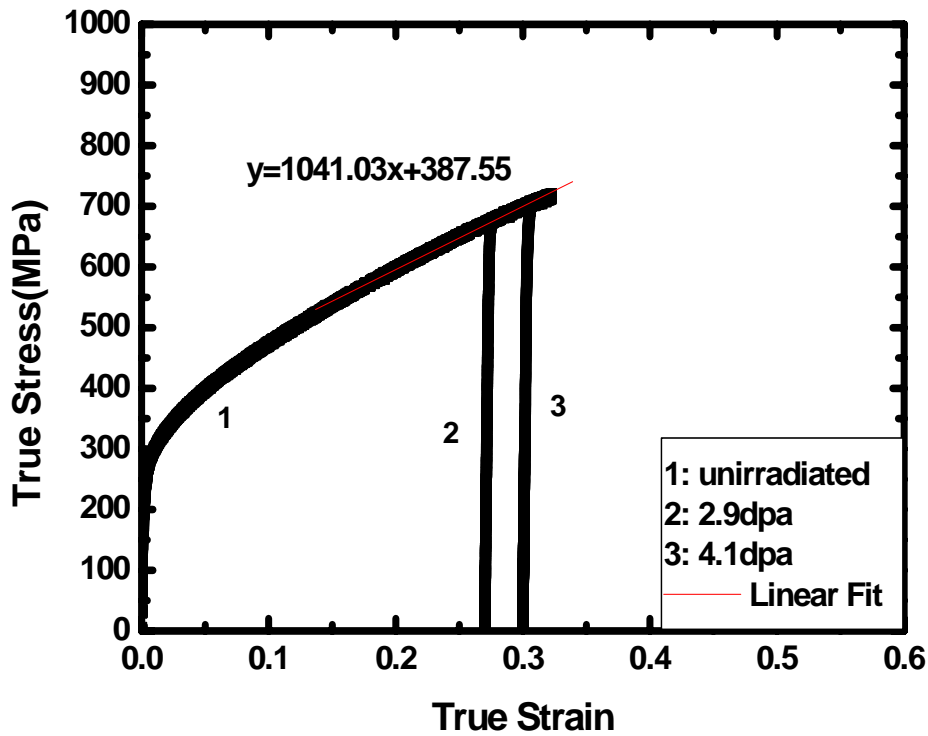
(c)

Figure 4-5   The true stress-strain tensile curves are shown for (a) ECN 316SS tested at room temperature [51], (b) 316L SS tested at 50°C [11], and (c) 316L SS tested at 164°C [11] with the curves shifted proportional to the irradiation-induced increases in yield strength. The fit to the linear strain hardening region is shown.

Figure 4-6 shows a comparison of the 316L stainless steel and 304L stainless steel both irradiated under similar conditions at 50C by Maloy [11, 12]. The difference in the materials yield strength is apparent as is the more pronounced upper yield phenomenon for the irradiated 304L SS. There is also more apparent scatter in the final hardening behavior for the 304L SS, than is seen in most of the other materials examined here. Nevertheless, the critical stress level is very nearly the same for both materials at this temperature. The critical stress is approximately 950 MPa for both materials.
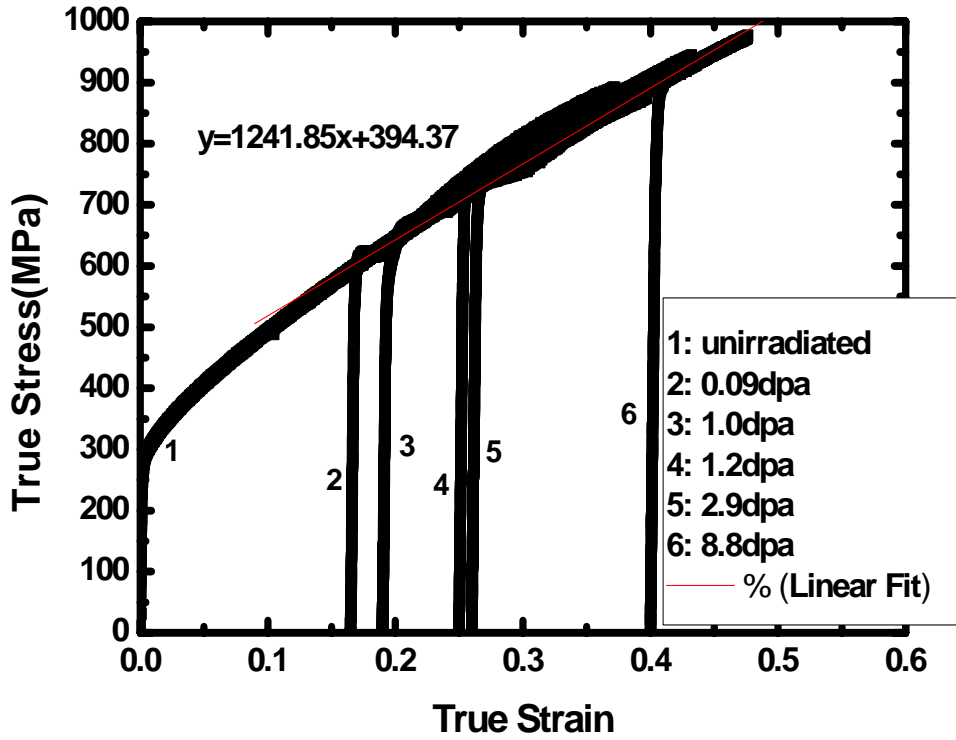
(a)
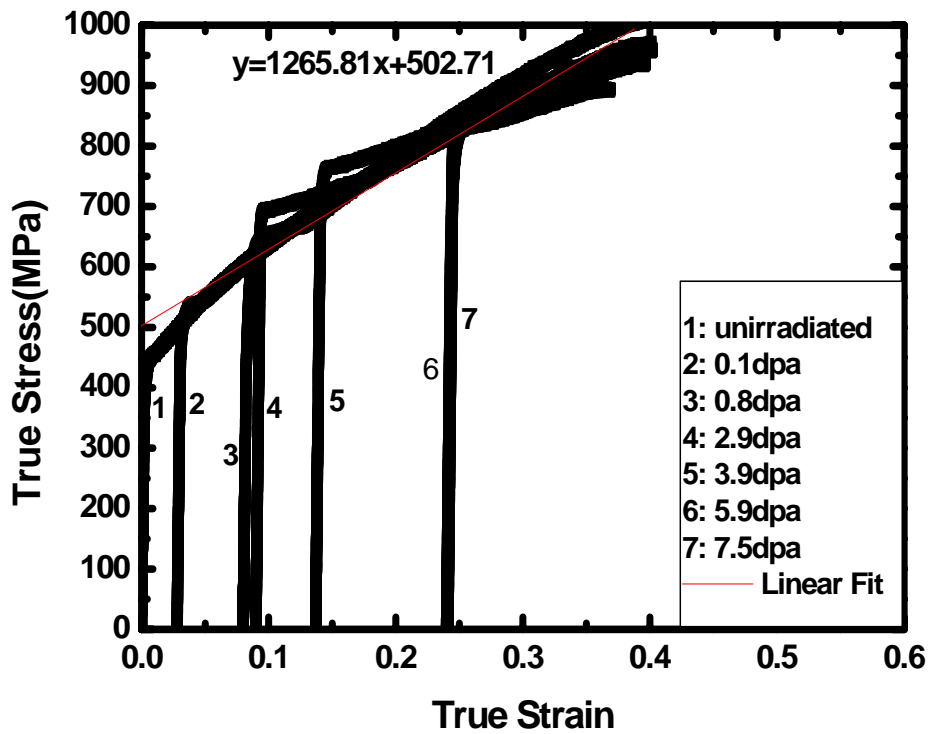
(b)

Figure 4-6   The true stress-strain tensile curves are shown for (a) 316L SS tested at 50°C [11], and (b) 304 SS tested at 50°C [11] with the curves shifted proportional to the irradiation-induced increases in yield strength. The fit to the linear strain hardening region is shown.

CHAPTER 5   THE CONTROLLING MICROSTRUCTURE OF FLOW LOCALIZATION FOR 316L STAINLESS STEEL

5.1   Overview

Previous chapters indicate that regardless of the irradiation level, the true stress for the onset of plastic instability (necking) is approximately constant, defined as the "*critical stress*". In other words, the true stress to failure is an inherent material property rather than a function of irradiation-induced defect microstructure or strain hardening behavior. Limited studies of the tensile behavior of 300-series stainless steels following irradiation exposure have been carried out at intermediate temperatures in the past. A major conclusion by Robertson *et al.* [20] is that the 316L stainless steel could suffer a minimum ductility in the range of 150 to 350°C even at the irradiation levels as low as 1 dpa. This temperature range and irradiation conditions are typical of several current nuclear systems including Spallation Neutron Source (SNS), current Light Water Reactors (LWRs) and some Generation IV reactor concepts designs. Past efforts to understand flow localization concentrated primarily on dislocation pinning and channeling effects. Several models based on the "barrier" mechanism have been proposed to explain the large increase in yield strength. However, current research shows that the flow localization process is more closely associated with the final stage of tensile deformation instead of the initial stage. From the shifting curves, it could be observed that the plastic flow exhibits a uniform behavior for various irradiation levels before the onset of plastic instability for all irradiation conditions. Therefore, the controlling microstructural mechanism for flow localization should be working for both unirradiated and irradiated materials and could include deformation-induced twinning and large scale planar slip in addition to the cleared channel flow due to the irradiation-induced defect microstructure. This insight provides an advantage in studying the final stages of flow localization,

since the point of instability occurs at the same true stress level for both irradiated and unirradiated materials. Thus the controlling mechanism can be studied directly from unirradiated material.

5.2 Experiments

The material studied here was annealed 316L austenitic stainless steel with nominal composition given in Table 5-1. The tensile tests were carried out at 100, 200 and 400°C. These testes were interrupted at low strain level, moderate strain level and uniform elongation for each temperature. The interrupted points were determined using the hardening rate curve from the tensile test ended at the onset of necking. Thereafter, the specimens are sliced symmetrically from the centerline and very fine vibratory polished with 20nm colloidal silica to be examined using the JEOL 7000F SEM with electron backscattered diffraction (EBSD).

Table 5-1
Composition for 316L stainless steel

Material	Composition (wt. %)										
	C	Co	Cr	Cu	Mn	Mo	N	Ni	P	S	Si
316L SS	0.20	0.155	16.847	0.322	1.755	2.214	0.039	10.234	0.027	0.002	0.388

5.3 Strain hardening and the impact of stacking fault energy on the twinning

Both the hardening rates ($\frac{d\sigma}{d\varepsilon}$) and true stress ($\sigma$) versus true strain ($\varepsilon$) for materials tested from room temperature to 400°C are plotted in Figure 5-1 to correlate the mechanic property change and microstructure evolution. It is clearly noticeable from the hardening rate curve of room temperature that in the first hardening stage, the hardening rate drops dramatically in the true strain range of 0.025. This quick drop is believed to be the result of the initial dislocation multiplication. Thereafter, the curve falls in a pseudo-plateau area. The onset of this

plateau is argued to be the trigger for activation of twinning deformation system [96, 113] in the materials with low stacking fault energy (SFE) and deformed at proper condition. However, this pseudo-plateau cannot be noticed in the hardening rate curves for the materials deformed at higher temperatures from 100 to 400°C. After the initial drop, the downward curves are becoming steeper with the increasing of temperature. And finally, those hardening curves will intercept with true stress and this intercepting point is the index of the onset of plastic instability, *i.e.* critical stress. The ending points of interrupted testes are also indicated in Figure 5-1. The first interrupted point for each case is the ending of the first dropping stage, which is about 4% in engineering strain. The activation of twinning systems is believed to be associated with the width of Shockley partial which depends largely on the stacking fault energy (SFE). SFE is a positive function of temperature for many FCC materials. Above 200°C, the SFE is too high to allow the twinning mechanism to activate. This effect will be discussed in the following sections.
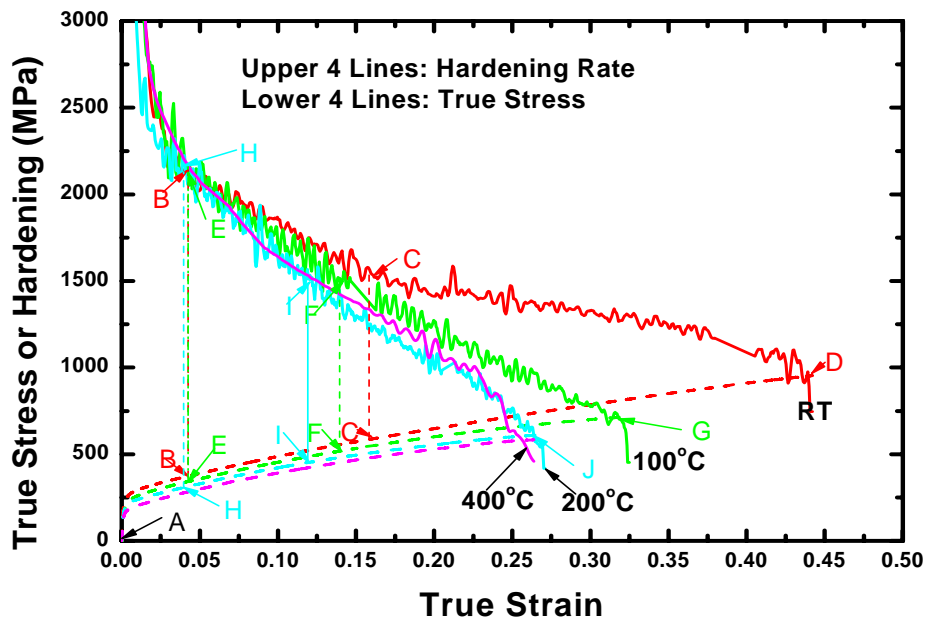

Figure 5-1   The strain hardening rate (upper curves) and true stress-strain curve (lower curves) for annealed 316L SS tested at room temperature; the interrupted points are indicated.

5.4   Phase transform during plastic deformation

Figure 5-2 shows the phase transfer from face-centered cubic to body-centered cubic during the plastic deformation at room temperature. The phase comparison between fcc and bcc for the sample at the onset of necking is shown in Figure 4a. At this point, the bcc portion is still a minor part and most of the grains are still fcc structure. However, after the materials are deformed to final failure, the grains are greatly elongated and there is a severe phase transform from fcc to bcc. The portion of grains with bcc phase can be as high as 50% as shown in Figure 4b. This means although there may be certain phase transform during strain hardening process, the mechanism of phase transform may not have a great impact on the materials plastic deformation before the onset of necking and it should play an important role in the necking process. Then it can be reasonably concluded that there should exist other microstructural deformation mechanisms controlling the flow localization of low stacking fault fcc materials like 316L stainless steel. The lamellar structure is also noticeable in the heavily deformed sample.
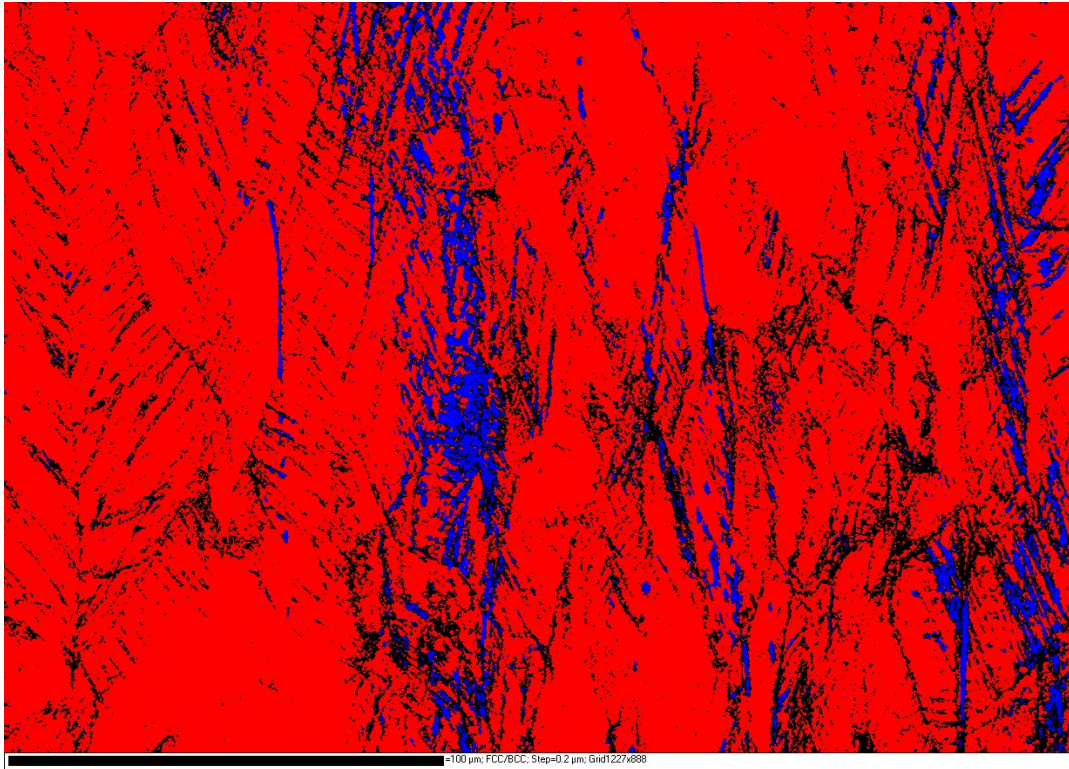
$100 \mu m$ (a)
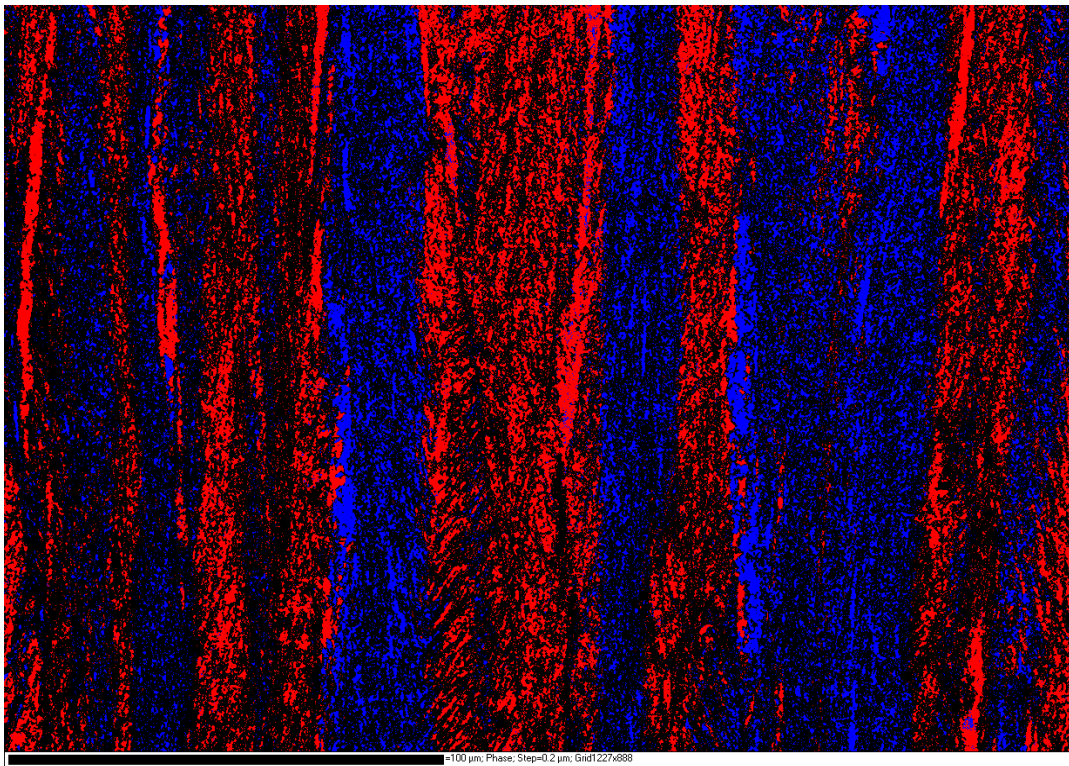

$100 \mu m$ (b)

Figure 5-2   Phase transform is shown here for room temperature test: (a), at the onset of necking and (b), after failure; color red represents fcc phase and blue is bcc phase.

5.5   The competing mechanism between mechanical twinning and planar slip

One aspect of the microstructural processes that controls the flow localization process can be identified by examining the relevant materials deformation modes as a function of temperature. Figure 5-3 shows the deformation microstructure of 316L stainless steel undeformed and deformed to the critical stress point (i.e. to approximately the UTS, just prior to the onset of necking), from room temperature to 200°C. The undeformed specimen has equiaxed grain in all grain orientations. The grain structure following uniform plastic strain to the point of necking shows a grain structure that is elongated in the direction of the applied stress. The room temperature deformed specimen has extensive twinning whereas the 100°C specimen shows much less twinning. At the higher test temperature of 200°C, twinning is completely absent. It is noted that in the room temperature and 100°C cases, twinning occurs in the grains with preferred crystal orientations. The specimen tested at room temperature to the point of plastic instability also shows extensive twin intersection which is believed to be the cause of rapid drop of strain hardening rate and the onset of flow localization.
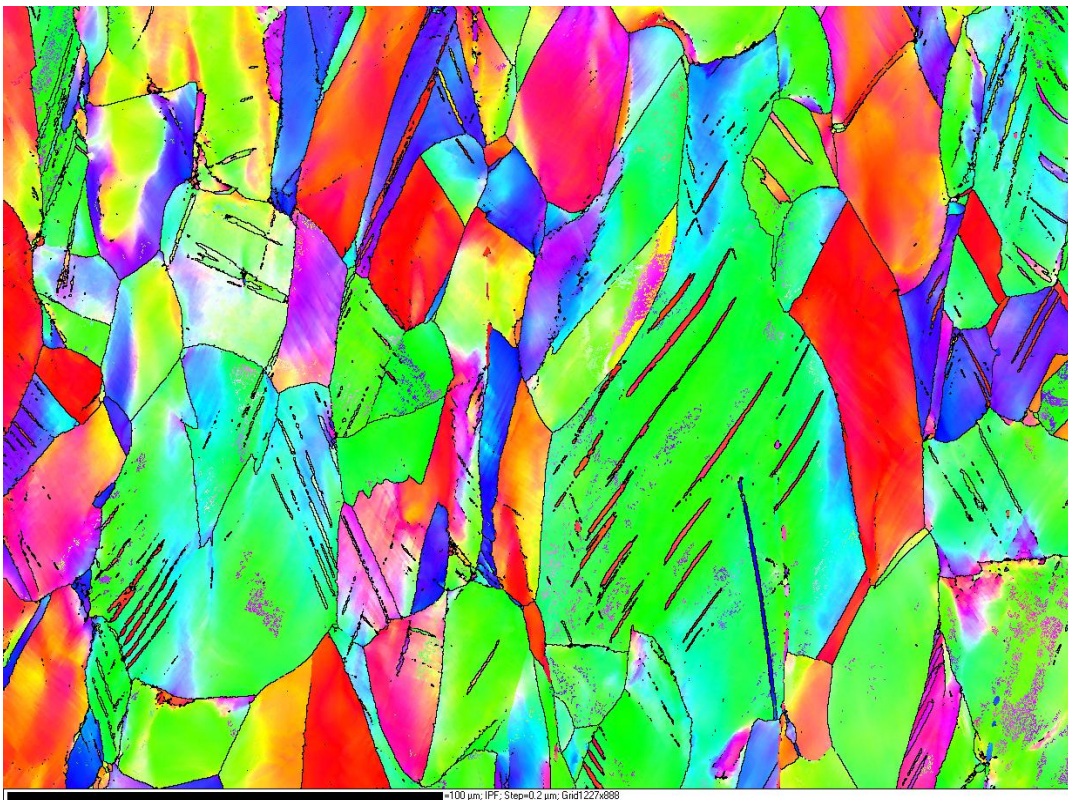
$100 \mu m$ (a)

$100 \mu m$ (b)
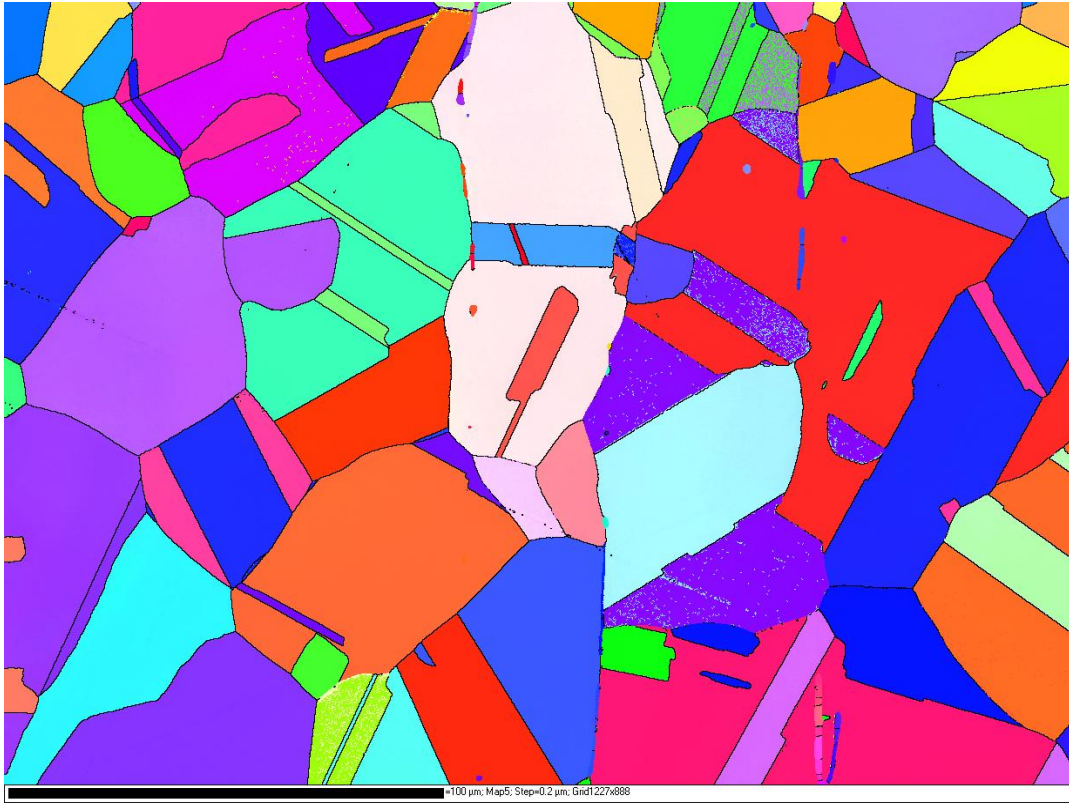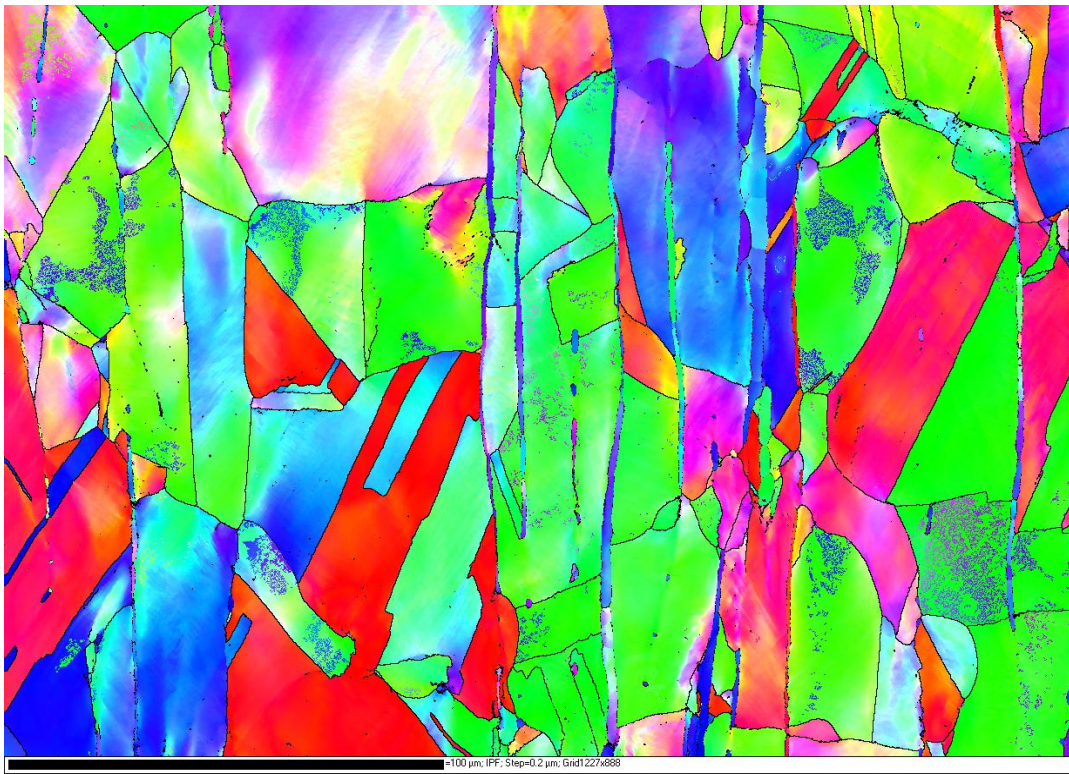

$100 \mu m$ (c)
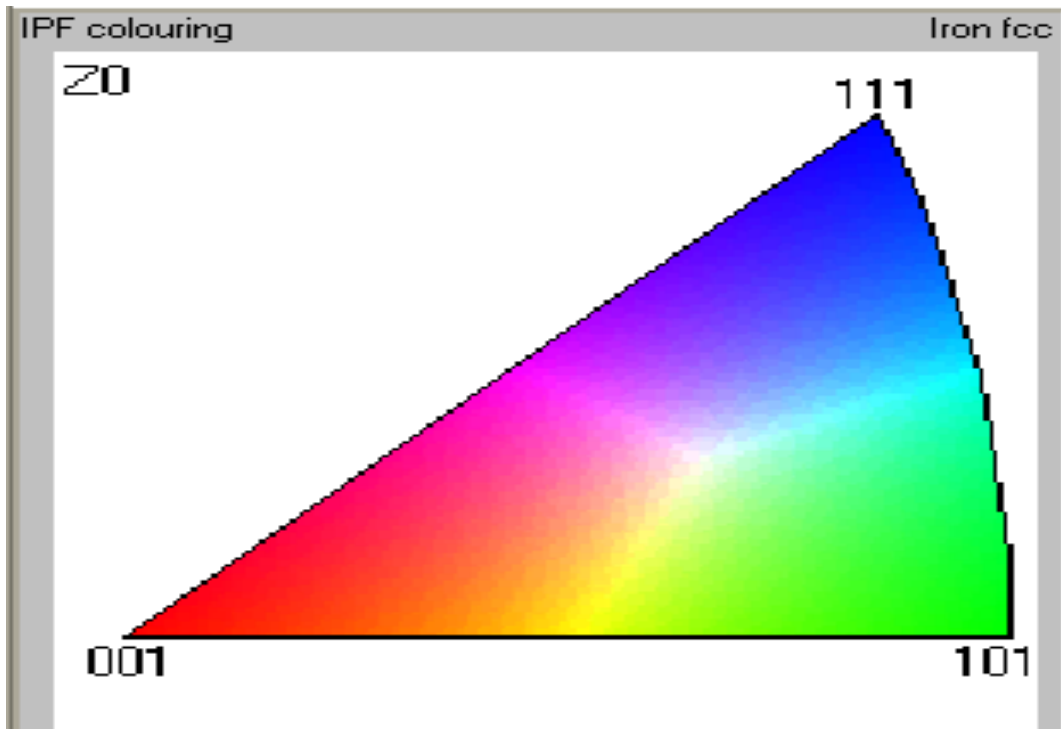
$100\mu m$ (d)

(e)

Figure 5-3   SEM with EBSD pictures show the twinning structure and crystal orientation for (a) undeformed and deformed to the point of uniform elongation at (b) RT, (c) 100ºC and (d) 200ºC; (e) shows the legend for crystal orientation.

Figures 5-4, 5-5and 5-6 show the EBSD patterns for specimen strained to different strain levels from room temperature to 200°C respectively. For the undeformed materials, the grains are still equiaxed. No deformation can be observed and the orientation in each grain is uniform. Figures 5-4b to 5-4d indicate the microstructure evolution for the materials tested at room temperature and interrupted at different strain levels. Plastic deformation can be observed in the EBSD pattern of B. The orientations in some grains are not uniform anymore and misorientation lines (grey lines) can be observed. The twinning system is still not initiated because the true stress is less than the critical twinning stress. When the specimens are strained to the moderate strain level as shown in Figure 5-4c, the twinning is clearly evident in the {110} grains and the density of these textures is clearly increased, which means the grains are re-oriented to the vicinity of brass-type texture. This occurrence of mechanical twinning and grain re-orientation are consistent with texture analysis in the previous section. Furthermore, when the material is loaded to uniform elongation, the twinning systems are greatly developed and the interceptions of twinning systems are introduced. This development of twinning systems and introduction of interception of twinning are believed to be related with the final plastic instability. Figure 5-5e to Figure 5-5g show the microstructure evolution EBSD patterns for the materials tested at 100°C and Figure 5-6h to Figure 5-6j for 200°C. Rather than the room temperature case, twinning can only be observed in the specimen tested at 100°C and strained to uniform elongation. From above statements, it can be concluded that: (1) There must be different deformation modes dominating low temperatures and high temperatures deformations respectively; (2) Twinning plays an important role in the plastic deformation for the materials operated in the low temperature environments. These conclusions are also consistent with the hardening rates curves shown in Figure 5-1 that after the initial quick drop of the hardening rate, the room temperature curve falls

into a pseudo-plateau while this plateau cannot be observed for the other three higher temperatures. The downward slope gets steeper with the increasing of temperatures. Limited researches have been conducted on the role of mechanic twinning on the low temperature plastic deformation. The twinning process is believed to be controlled by the width of Shockley partial. The wider Shockley partial inhibits the dislocation mobility and promotes twining process. And the width of Shockley partial determines the value of stacking fault energy. So the critical twinning stress which triggers the activation of twinning process must be highly dependent of the stacking fault energy. SFE is a positive function of temperature for 316L stainless steel; therefore, the critical twinning stress has strong temperature dependence. In an earlier study, Byun *et al.* [69] proposed a critical twinning stress expression in terms of the equivalent or uniaxial stress. The expression is revised here based on the current EBSD results as:

$$\sigma_T = \frac{2\gamma_{SF}}{b_p} \cdot \frac{1}{SF} = 4.3 \frac{\gamma_{SF}}{b_p}$$

Here the average Schmidt factor is about 0.465. The Stacking Fault Energy values are taken from literatures [114-116]. The value of <112> type partial dislocation Burgers vector b_p is equivalent to 0.145 nm [69]. The curves for the calculated critical twinning stress, critical stress, yield strength for unirradiated materials and yield strength bands for irradiated materials up to 250°C versus test temperatures are plotted in Figure 5-7. The meanings of letter symbols are same as the ones in other figures and present the different interrupting positions for each temperature. The true stress for test B is less than the critical twinning stress for room temperature, so the twinning system is still not yet initiated as expected. However, the stress for test C is larger than the critical twinning stress, and then the twinning can be clearly identified. It means that once the true stress is larger than the critical twinning stress, the activation of twinning system will be

triggered and continues to develop until the plastic instability. For the materials tested at 100°C, because even the true stress at moderate strain level F is smaller than the critical twinning stress for 100°C, therefore no twinning systems can be identified in samples E and F. However the twinning system is clearly evident in sample G with the true stress larger than the critical stress. In addition, since even the critical stress is smaller than the critical twinning stress for 200°C, the twinning is completely absent as shown in Figure 5-6. From the above analysis, it can be concluded that the EBSD patterns for the microstructure evolution are consistent with the argument of critical twinning stress shown in Figure 5-7.
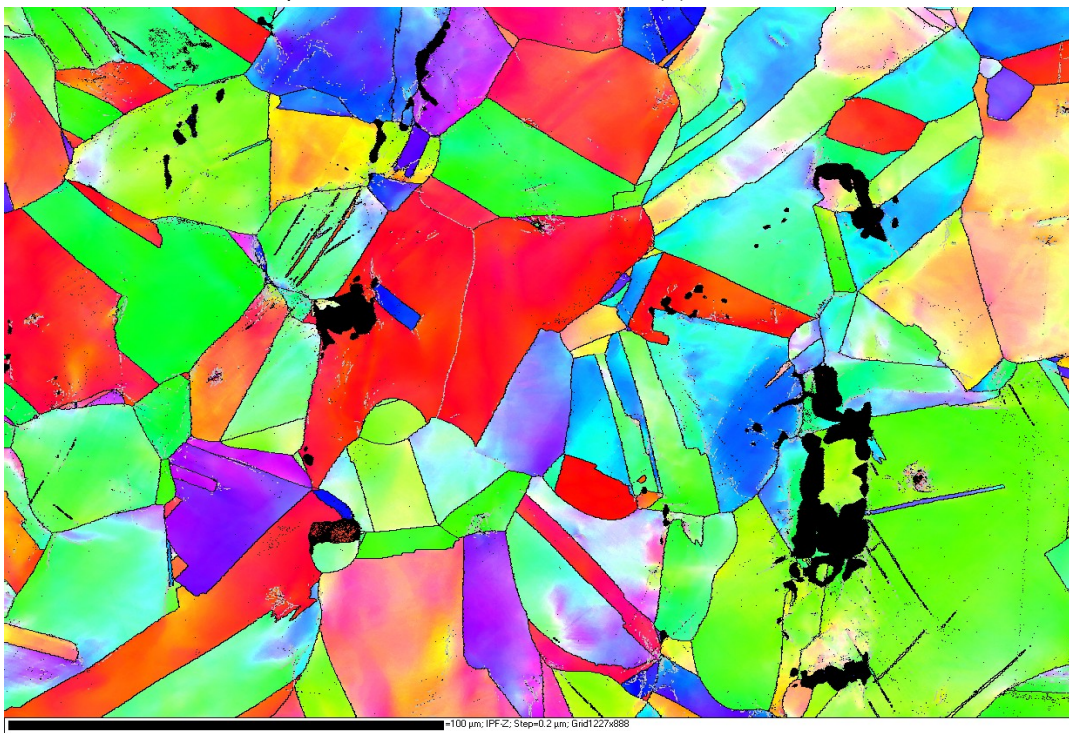

$100 \mu m$

(a)

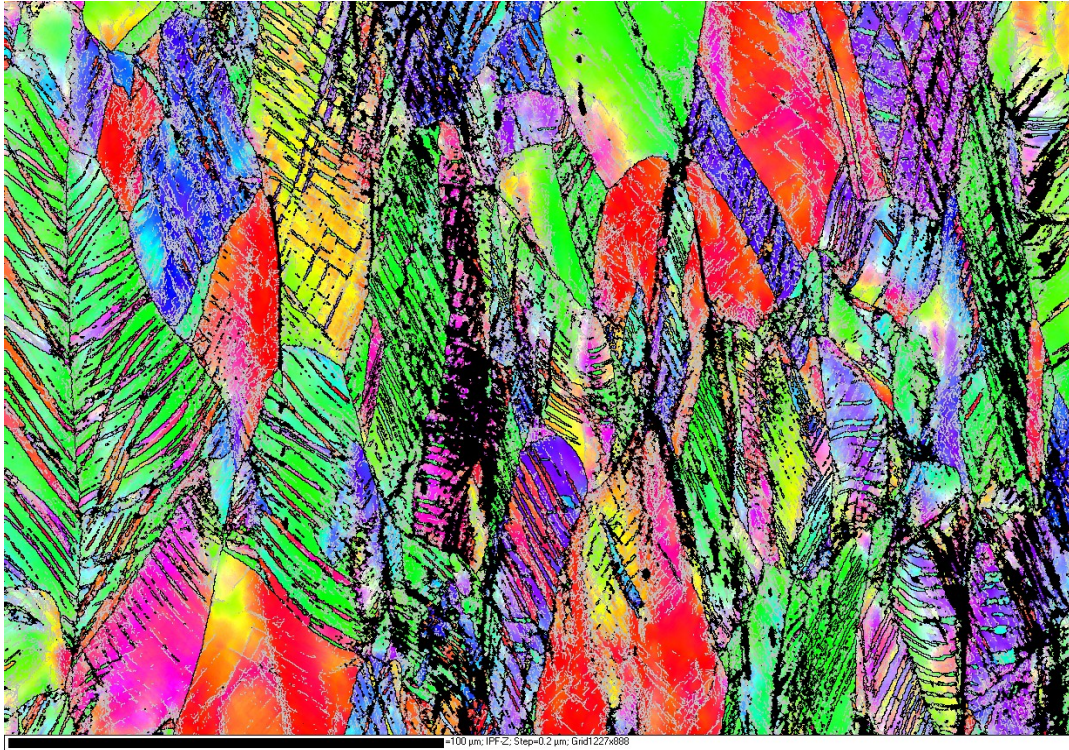$100\mu m$ (b)
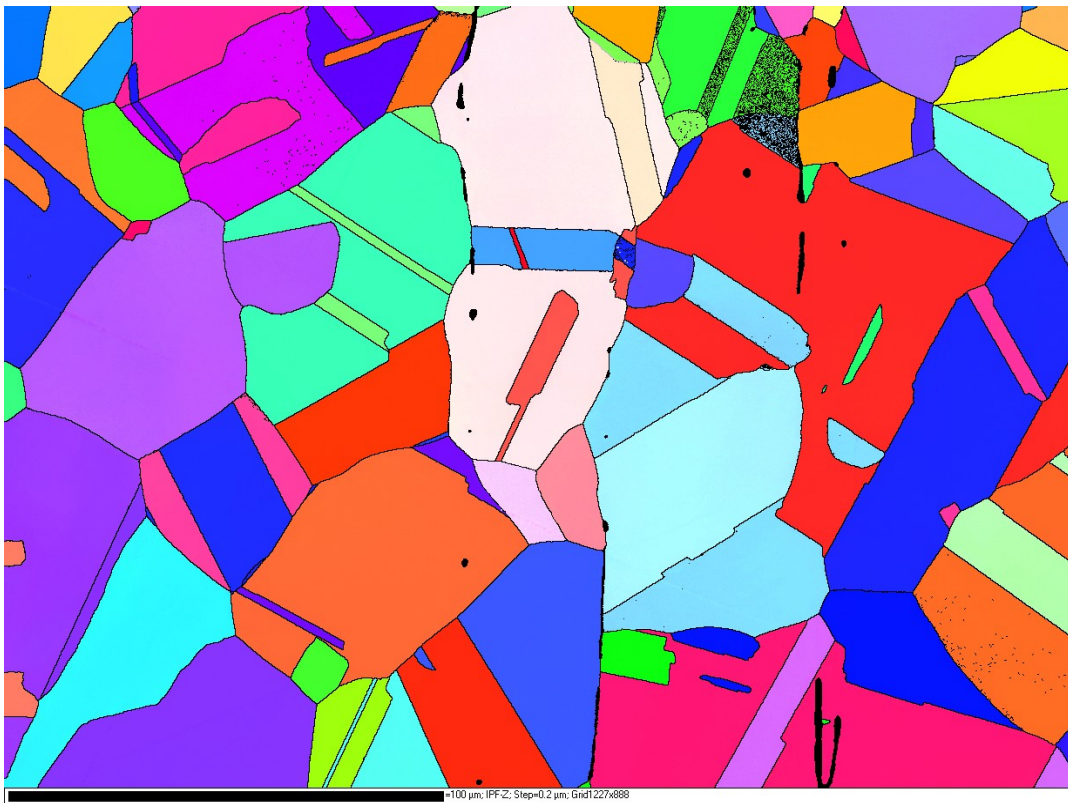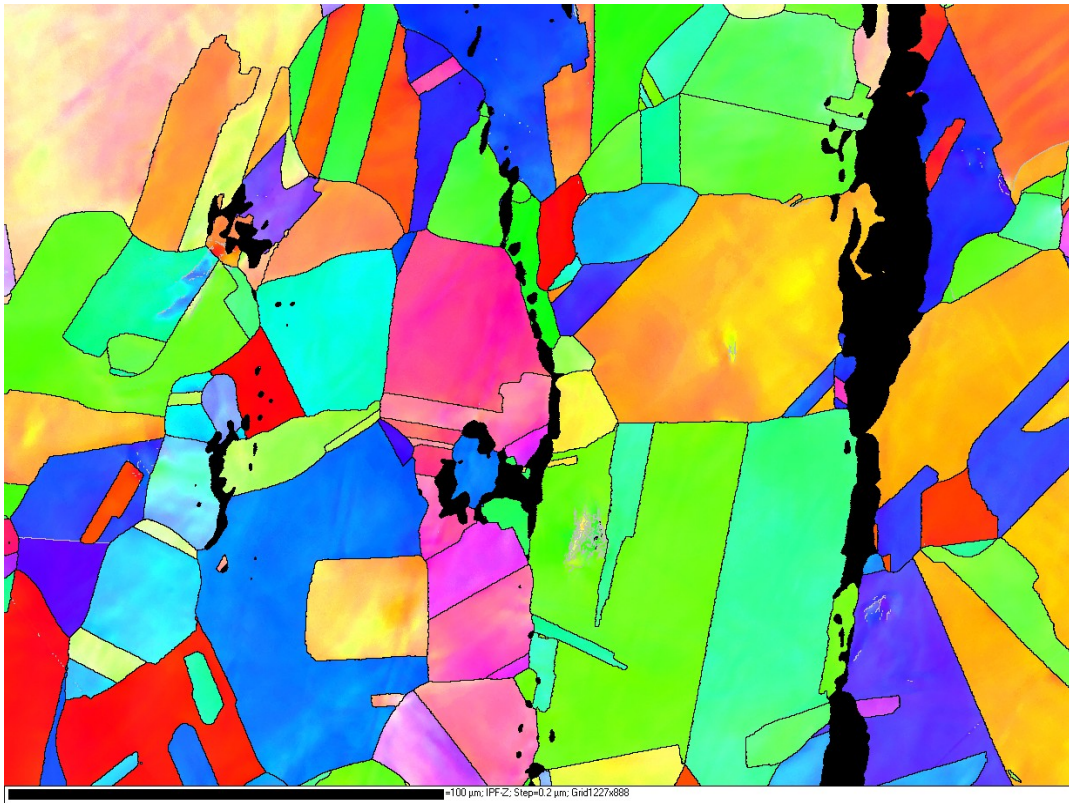
$100\mu m$ (c)

$100 \mu m$ (d)

Figure 5-4　SEM with EBSD pictures show the microstructure evolution, crystal orientation and misorientation for materials tested at room temperature: (a) undeformed, (b) interrupted at low strain level, (c) interrupted at intermediate strain level and (d) strained to uniform elongation

83

100μm (f)

$100\,\mu m$ (g)

Figure 5-5   SEM with EBSD pictures show the microstructure evolution, crystal orientation and misorientation for materials tested at 100°C: (a) undeformed, (e) interrupted at low strain level, (f) interrupted at intermediate strain level and (g) strained to uniform elongation.

$100\mu m$ (a)

$100\mu m$ (h)

86

100μm   (i)
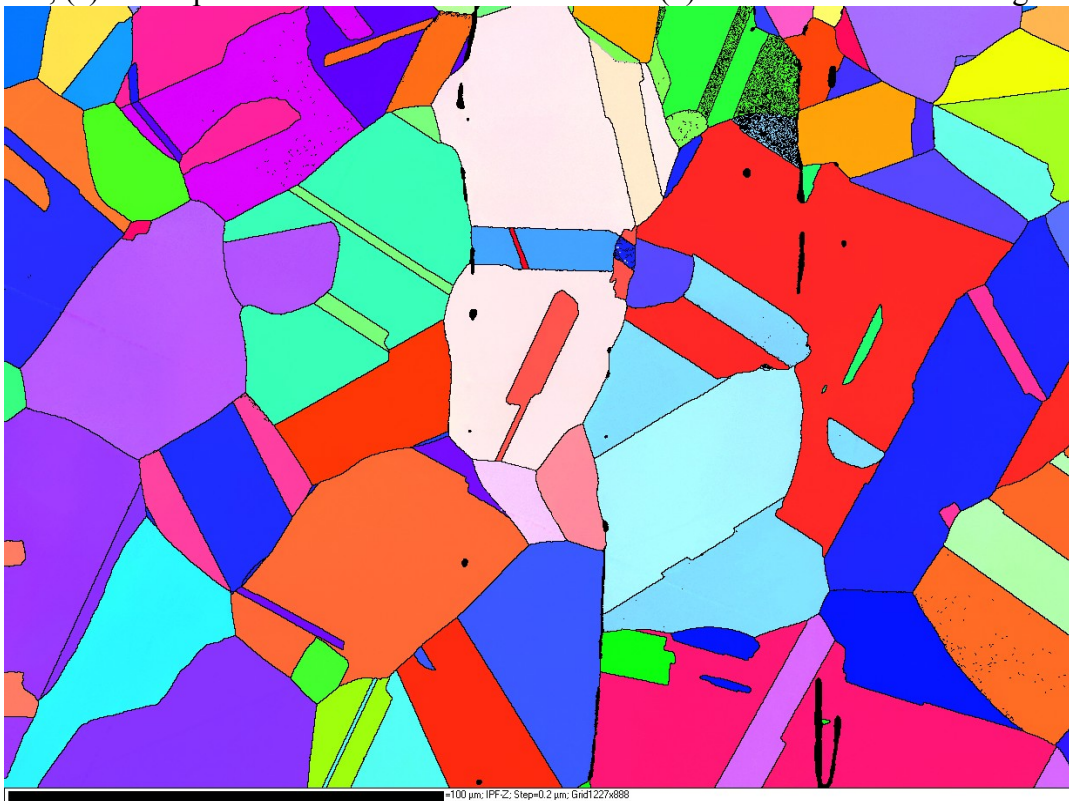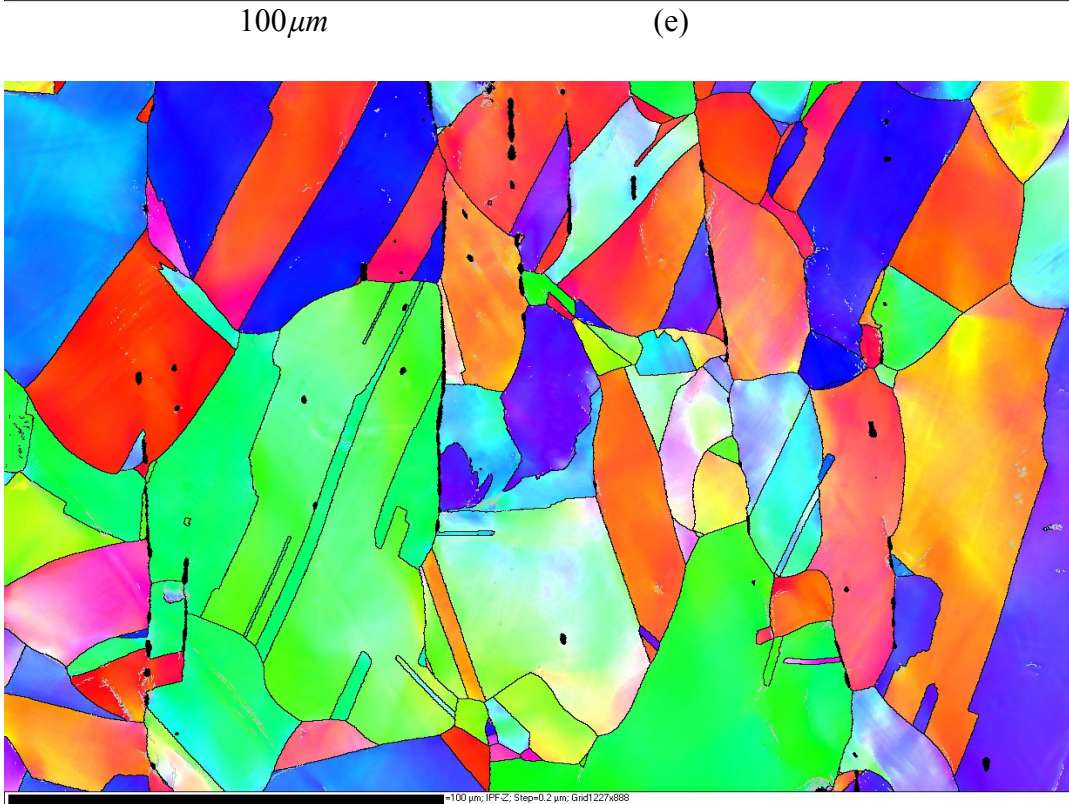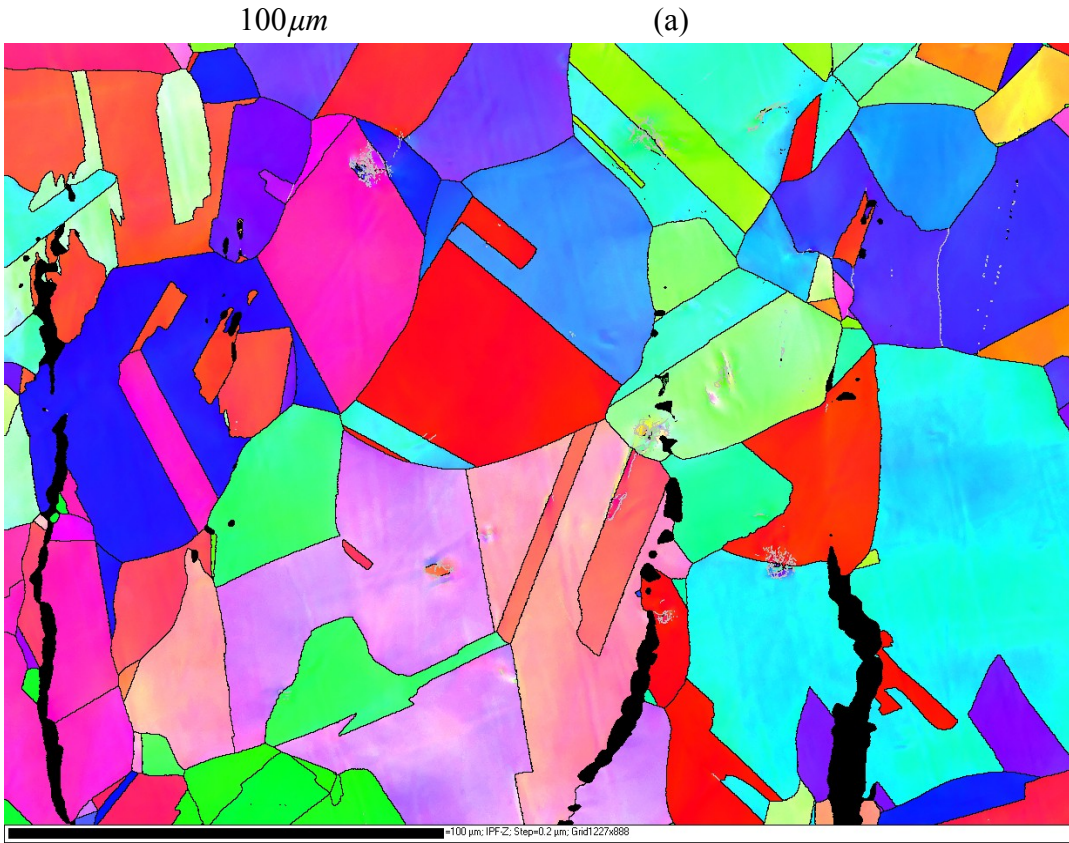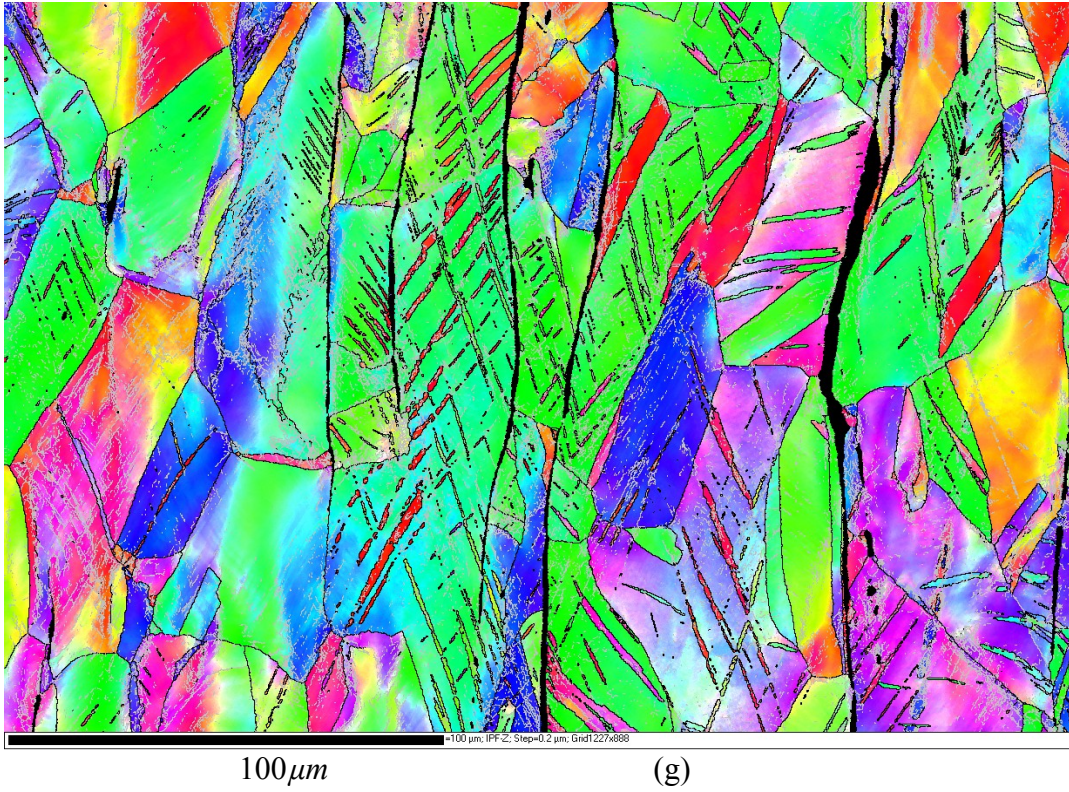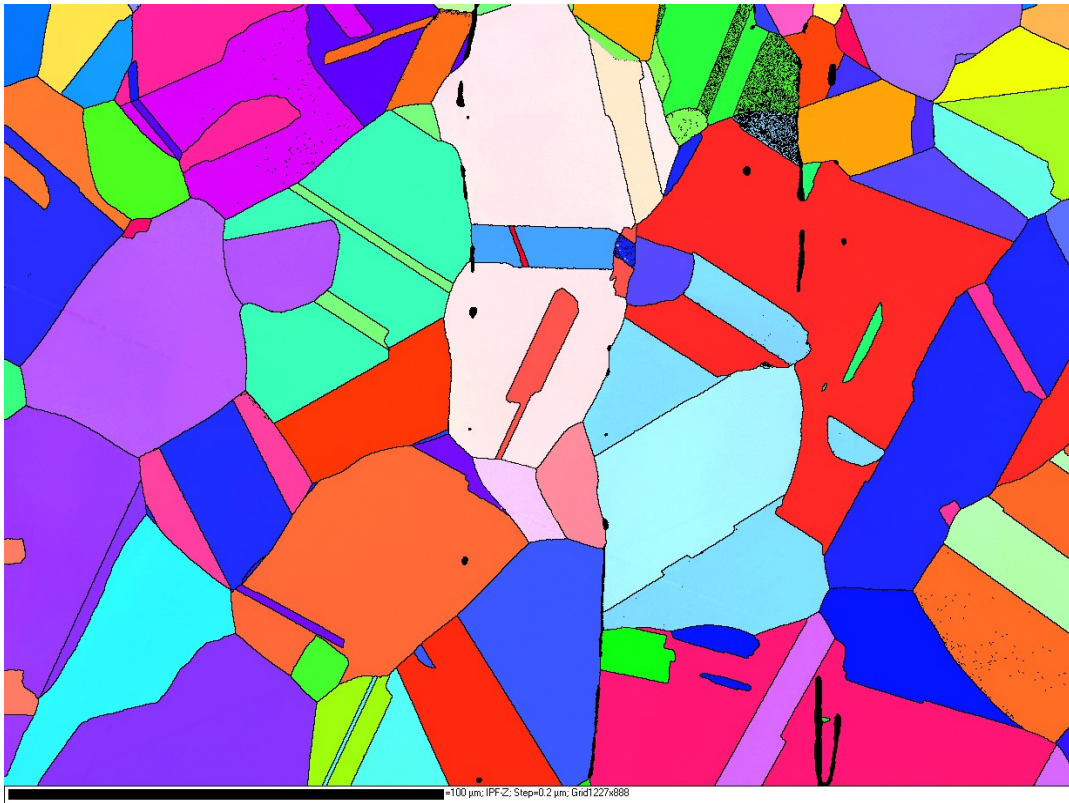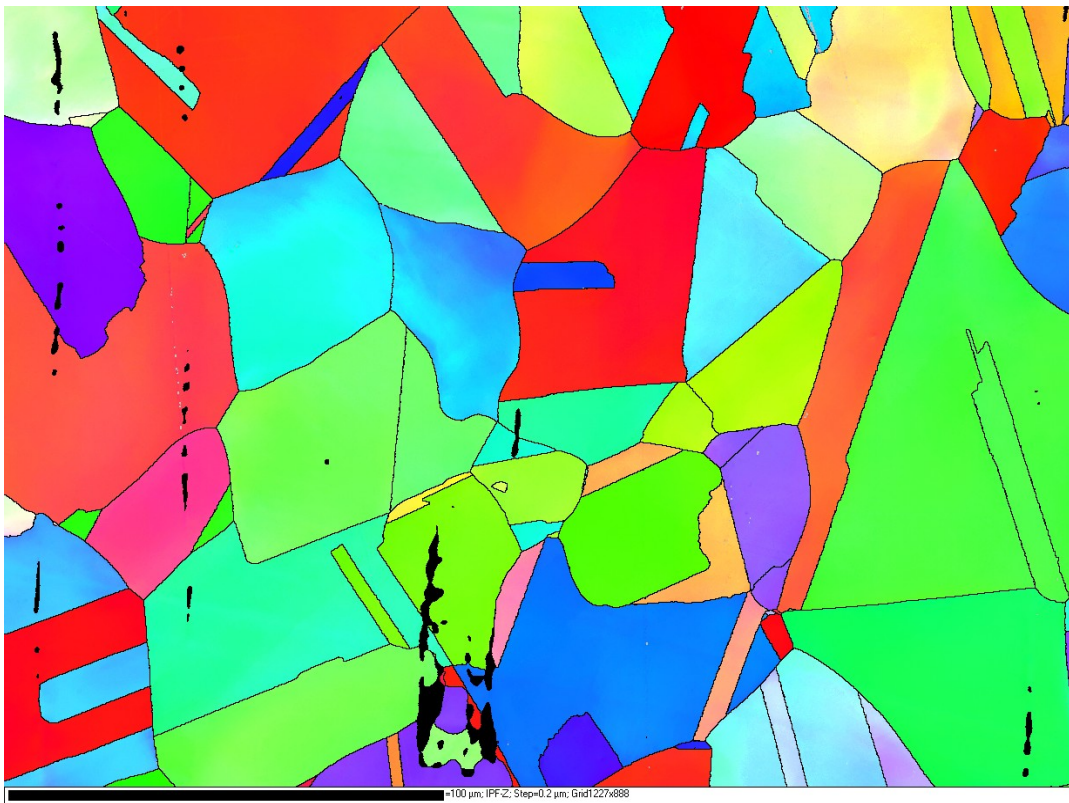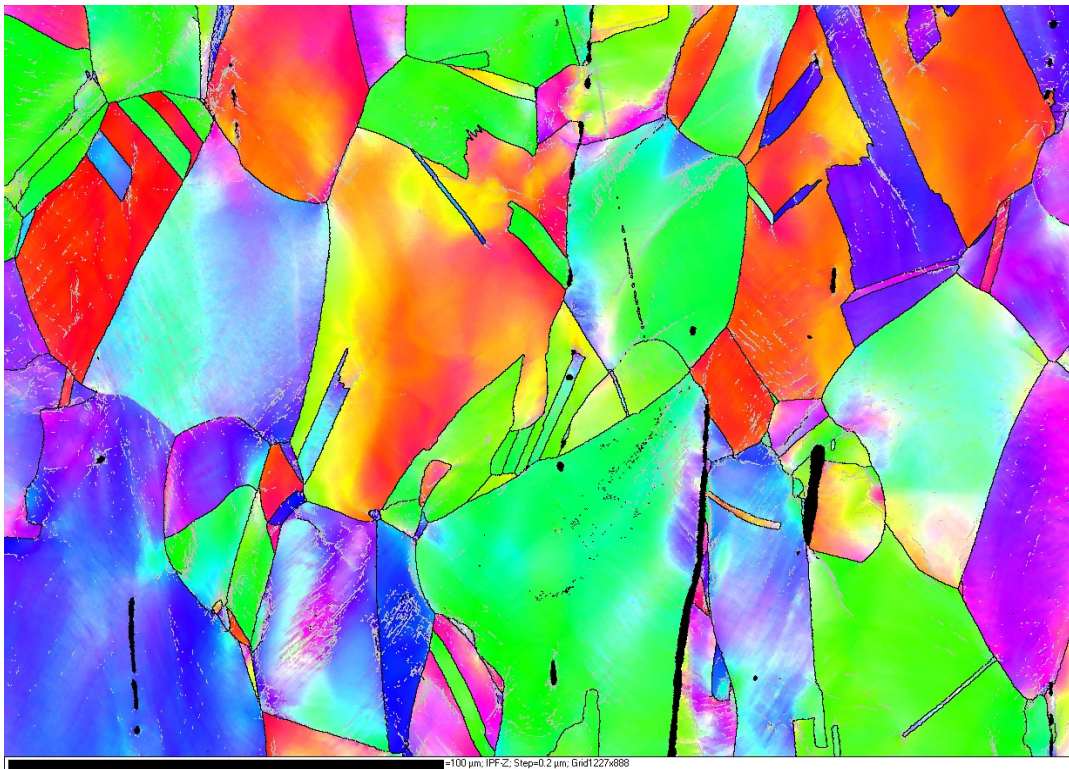

100μm   (i)

Figure 5-6   SEM with EBSD pictures show the microstructure evolution, crystal orientation and misorientation for materials tested at 200°C: (h) interrupted at low strain level, (i) interrupted at intermediate strain level and (j) strained to uniform elongation.

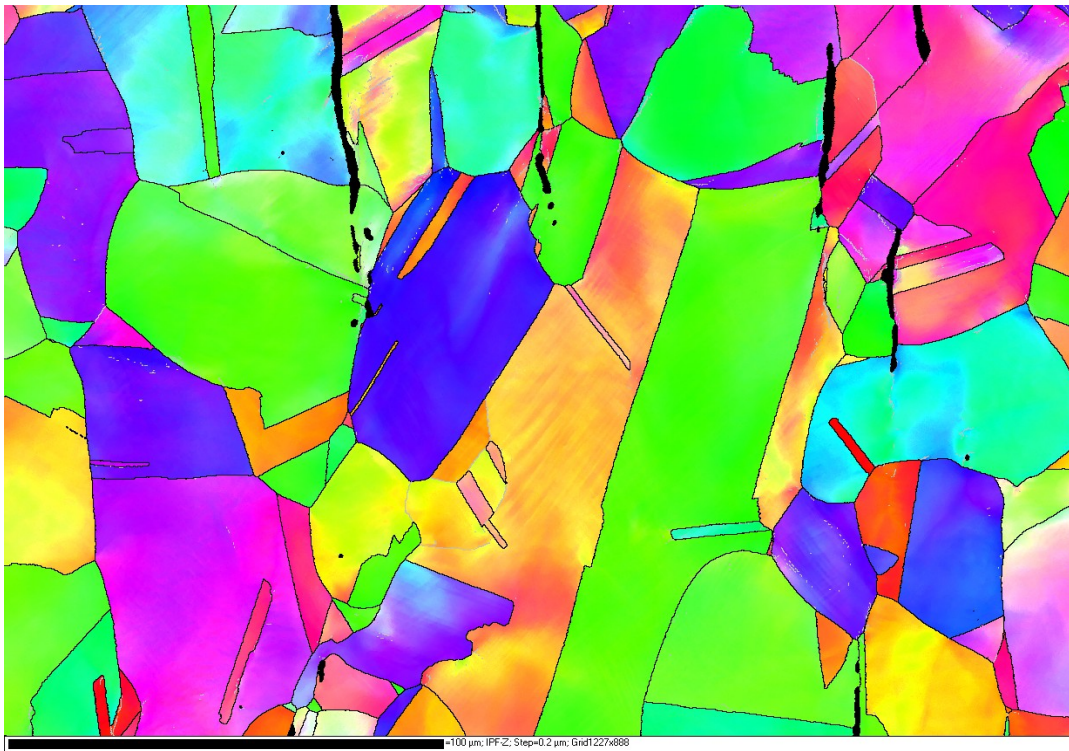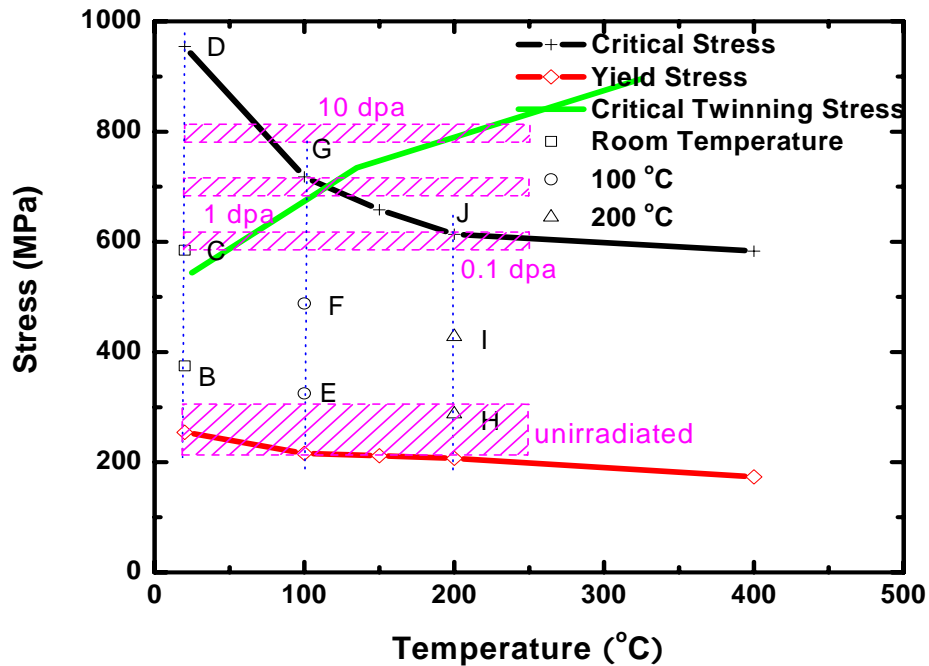Figure 5-7   Temperature dependence of critical stress, critical twinning stress, yield strength of unirradiated materials and yield strength band of irradiated materials for annealed type 316L SS; the interrupted points are also indicated.

5.6   Texture evolution and grain rotation during the plastic deformation of 316L stainless steel

The texture evolution for 316L stainless steel tested at room temperatures and strained to different strain levels are shown in Figure 5-8. For underformed materials, almost no texture can be observed except the annealing twinning. However, from 3% engineering strain to uniform elongation, the texture is more and more evident at the vicinity of {110}. Vercammen et al. [117] and Chowdhury et al. [118] proposed that brass-type ({110} <112>) and Goss-type ({110} <001>) textures are typical face centered cubic materials texture with low stacking fault energy. It is clearly evident that the brass-type fiber is enhanced. The rotation inside grain and indication of 60° twinning bands are also shown in Figure 5-8. The misorientation angle is shown

accumulatively to the line starting point and it is evident that even inside the grain, the misorientation could be as high as 17°.

(a)
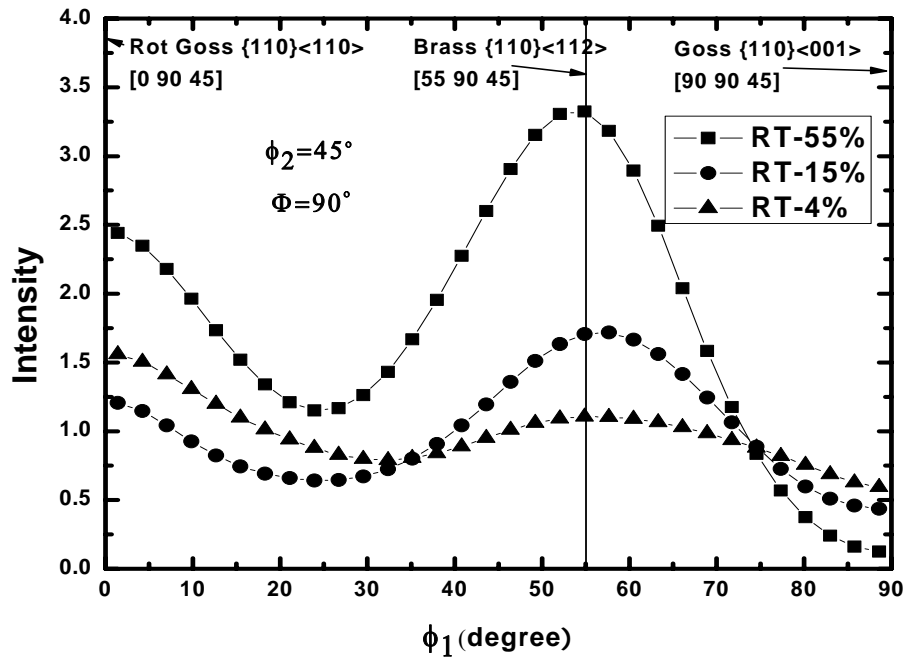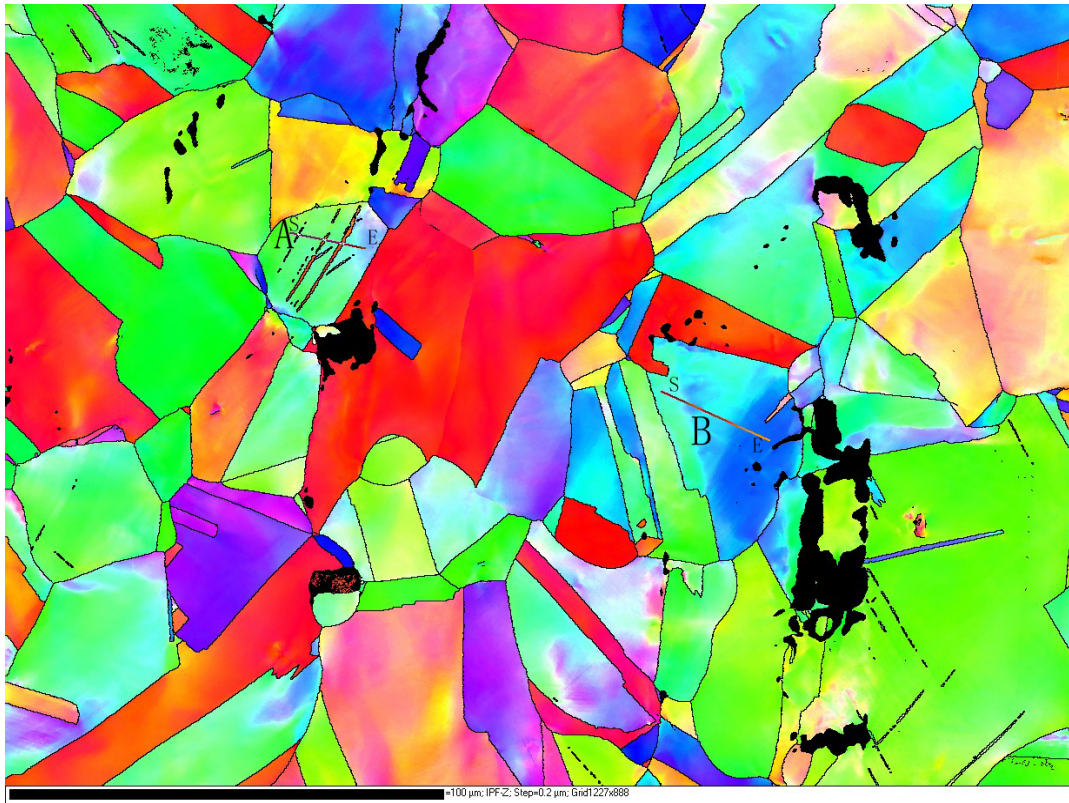
$100\mu m$ (b)
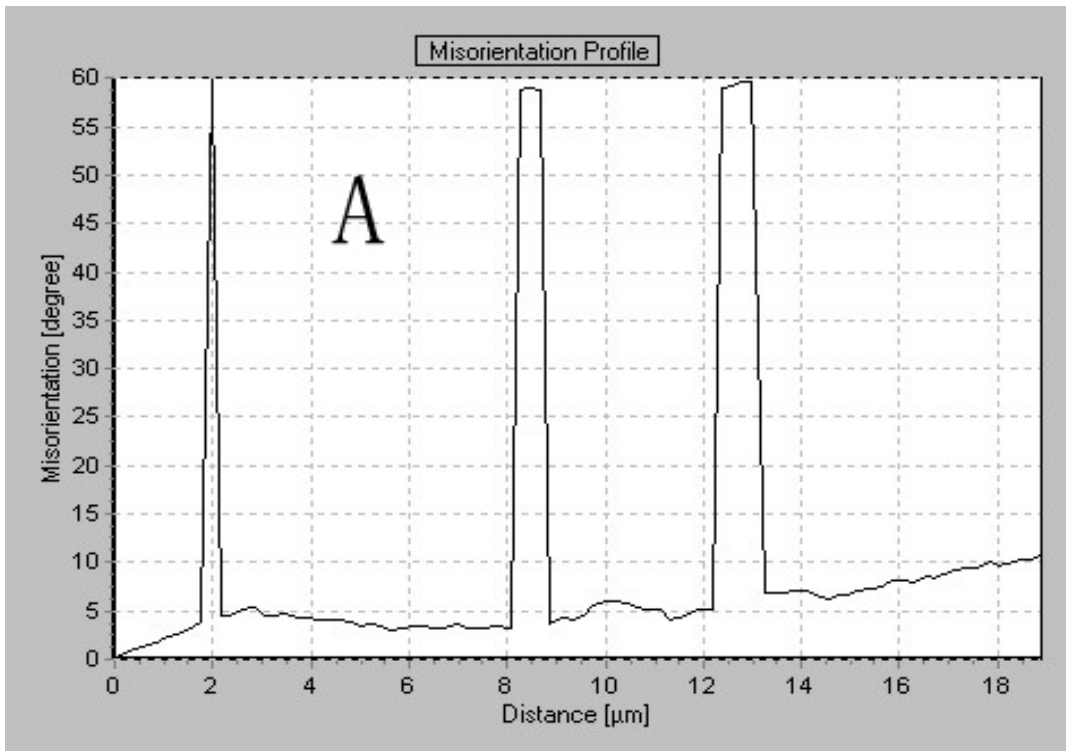
(c)
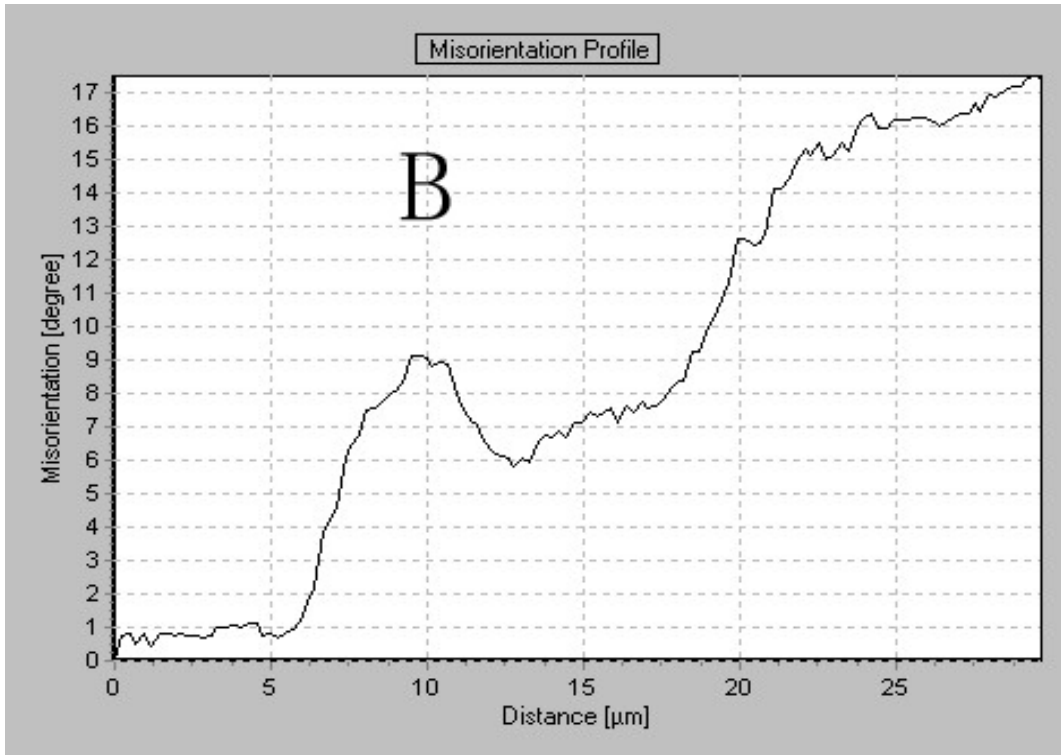
(d)

Figure 5-8   Texture evolution for 316L stainless steel deformed at room temperature is shown in (a); the grain rotation is shown in (b), misorientation profiles are measured for grains A and B and shown in (c) and (d), the angle is shown relatively to starting point at the left of the line (labeled as "S"); (c) shows the 60° twinning bands and (d) shows inside grain rotation.

CHAPTER 6   NOTCH STRENGTHENING OF FLOW LOCALIZATION

6.1   Overview

The limitation on structural components in large, engineered systems is often set by intended or unintended stress concentrators, including cracks, notches, bends or holes due to the manufacturing process, service applications or damaged developed during service. These stress concentrators require that the local stresses not exceed certain stress limits which are typically well below those that would acceptable in uniform dimension components. Much attention has been paid to notch and crack effects in reactor structural components due to the embrittlement caused by the irradiating environments.

It is important to understand the implications of these observations for the flow and fracture of notched components. The influence of various deformation modes on the notch strengthening of 316L stainless steel will be examined in this study. Four different notch configurations are considered. Electron backscattered diffraction (EBSD) scanning electron microscopy (SEM) was used to analyze the dominant plastic deformation modes and to estimate the deformation zone size. Crystal misorientation in the vicinity of the notch tips was also analyzed by EBSD. Stress contours were deterimined using FEM, and the results are compared with experiments. FEM analysis was also performed for irradiated material at 50°C to predict the tensile response and plastic deformation for notched samples.

6.2   Experiments and simulations

The material studied in this investigation was annealed 316L stainless steel, with the nominal composition given in Table 1. Four types of notches were machined at the center of the gauge area: two sharp V-Notches with different depths, and two semi-circular notches with different depths,

labeled V-Notch-L, V-Notch-S, C-Notch-L and C-Notch-S, respectively. For the V notches, the notch angle was fixed at 30°. Both V-Notch-L and C-Notch-L have the same notch depths, with ratios of notch depth to specimen diameter (denoted as *a/w*) of 0.214, while the V-Notch-S and C-Notch-S have a depth-to-diameter (*a/w*) ratio of 0.129. The specimen geometries are also shown in the FEM contours. Tensile tests were carried out at the room temperature with a strain rate of 0.005mm/s in position control.   The specimens were examined using a JEOL 7000F SEM with EBSD operated at 30 kV, after they were sliced symmetrically from the centerline and vibratory polished using 20 nm silicon carbide solution. The crystallography, misorientation, twinning and slip systems were studied using SEM. The details will be discussed in the following sections. The FEM analysis was performed using ABAQUS. The irradiated material tensile data were obtained from Los Alamos National Laboratory [12].

6.3   Notch strengthening and its microstructure analysis

The notch specimens were deformed at room temperature to the onset of necking in the deeper notches. The engineering stress-strain curves for the specimens with and without notches are shown in Figure 6-1. Compared to the un-notched specimen, the introduction of notches reduces the ductility of the material due to the fact that the notch structure confines the plastic deformation to the vicinity of the notch tip. It is evident that the both the V notch and C notch with a larger notch depth (labeled as L) have less overall strength and uniform elongation. For the two specimens with an *a/w* ratio of 0.214, the semi-circular notch shows a larger impact on the mechanical property degradation than the V-shape notch. However, for the specimens with an *a/w* ratio of 0.129 that is, the smaller notch depth, the V-shape notch has a larger effect. This will be discussed in more detail later.
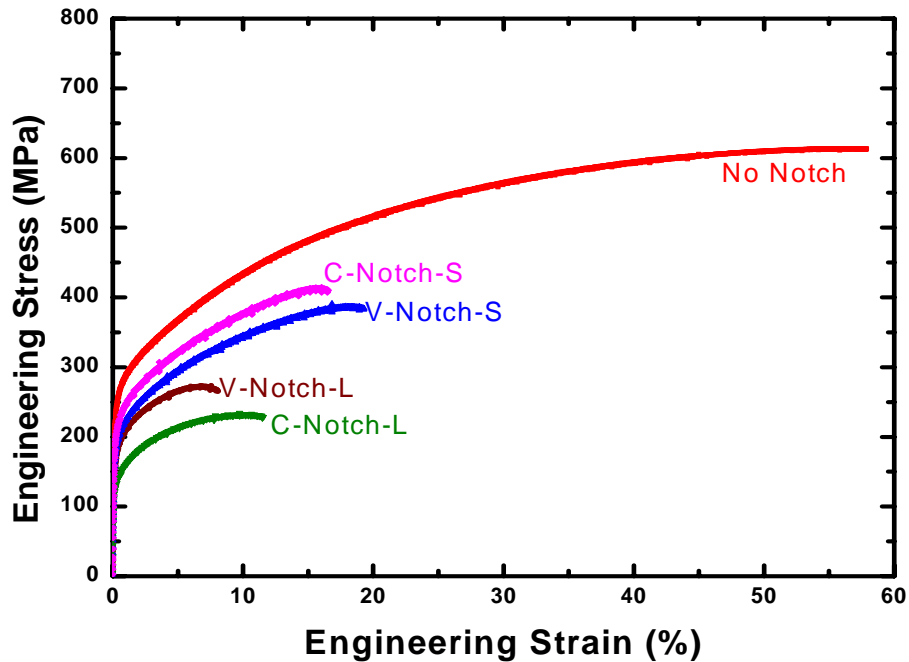
Figure 6-1   Engineering stress *vs* strain curves for 316L stainless steel tested at room temperature with and without notches

The EBSD orientation maps are shown in Figure 6-2. The integrated picture represents the grain structures from the centerline of the specimen to the notch tip, and the grain orientations are differentiated by colors. Twinning is activated in grains where the true stress is larger than the critical twinning stress of about 500 MPa. The details of the definition of critical twinning stress were discussed in the previous sections. The size of the twinning zone is a good indicator of the degree of stress concentration. Figure 6-2a shows the EBSD map for the specimen with the deep V-shape notch. It appears that the grains at the notch tip have undergone a large amount of deformation. In addition, micro-shear bands are formed and twinning is extensive. The influence of the sharper notch is concentrated near the notch tip. It was found that twinning systems are only activated in the vicinity (within several grains) of the notch tip, and no propagation was seen in the transverse direction toward the centerline of the specimen. In general, the twinning area has a

kidney shape around the notch, as expected for plane strain-like conditions. Figure 6-2b shows the EBSD pattern for the specimen with the small V notch. The twinning zone size in the transverse direction from the notch tip is increased to approximately 700 μm, which indicates that this specimen has a larger area with the true stress above the critical twinning stress at the onset of necking. By comparing the microstructures for the two V-notch depths, it can be concluded that the notch effect is more pronounced for the larger *a/w* ratio. Plastic blunting was also observed for this condition. The fracture mode remains ductile fracture instead of brittle fracture.

Figures 6-2c and 6-2d show the EBSD orientation maps for the specimens with semi-circular notches. The propagation of twins in semi-circular notches indicates the presence of a more uniform stress distribution than for the V-notch specimens. The notch shape and the tensile-induced hydrostatic stress are believed to produce an elliptical notch strengthening zone, where the true stress is greater than critical twinning stress throughout the zone, activating extensive twinning. In companion tests it was also observed that twins are not observed beyond the notch strengthening zone.
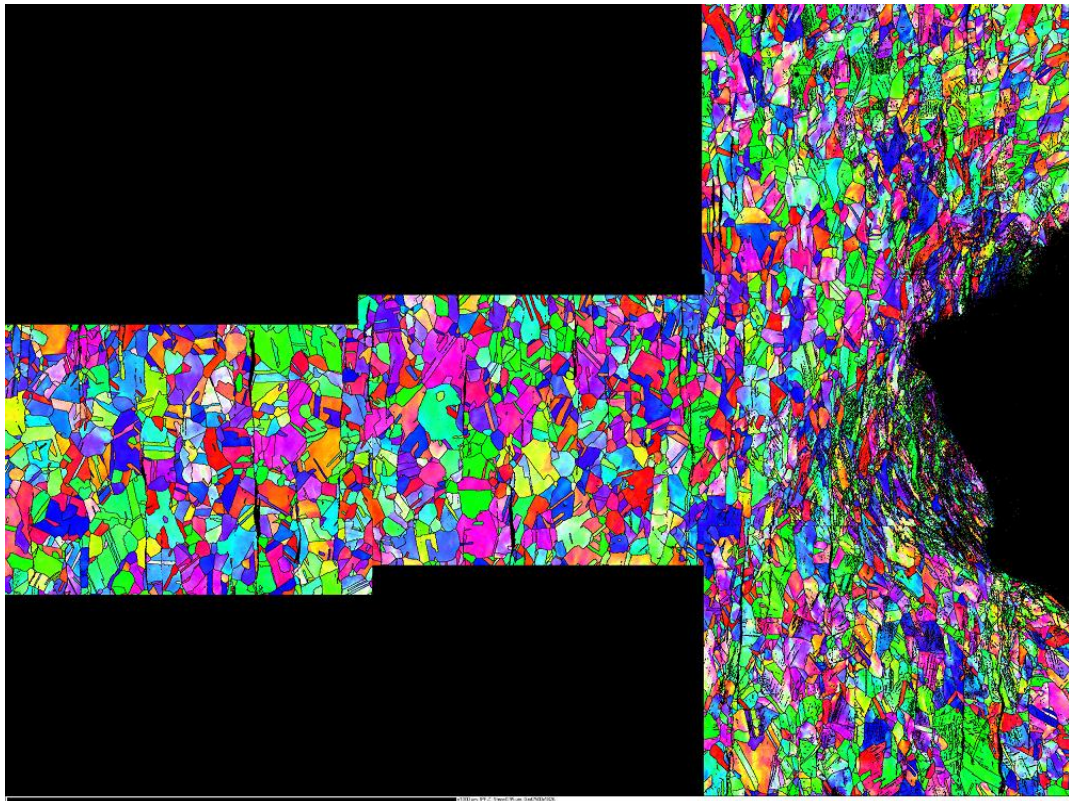
1000*um*   (a)
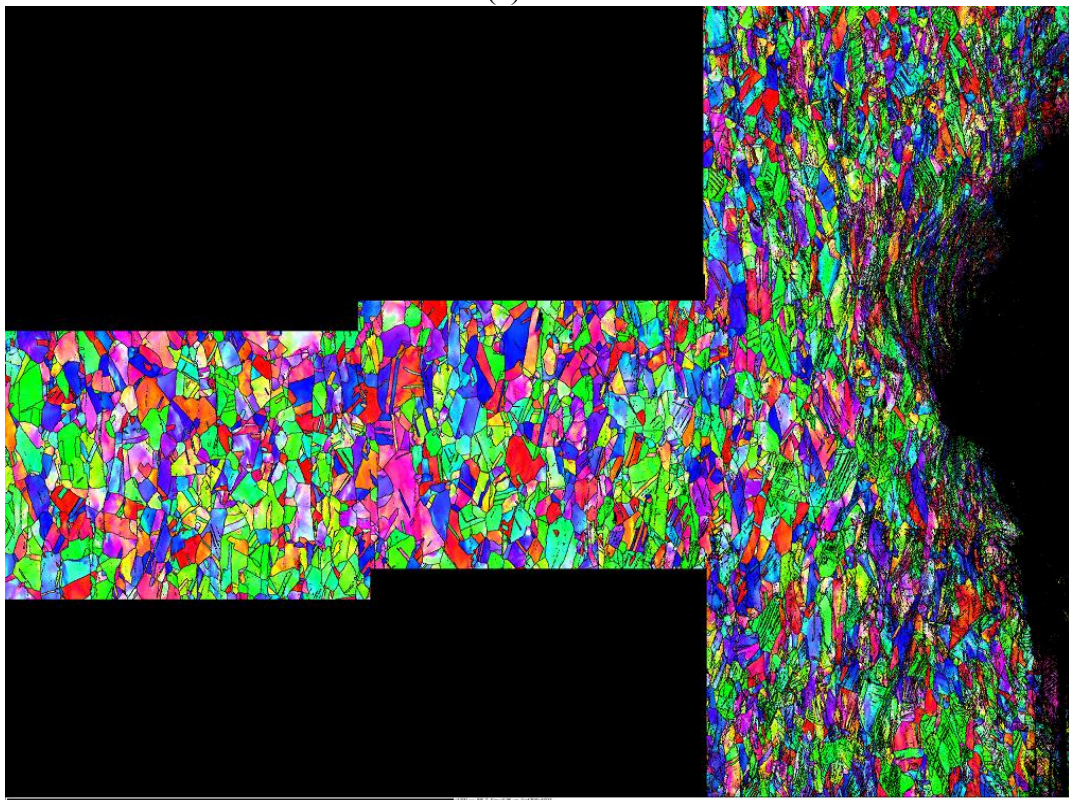
1000*um*   (b)

1000um (c)

1000um (d)

Figure 6-2   EBSD orientation maps of 316L stainless steel tested at room temperature for (a)
V-Notch-L-1, (b) V-Notch-S-1, (c) C-Notch-L-1 and (d) C-Notch-S-1

The local average misorientation maps are shown in Figure 6-3. The misorientation angles are calculated from the difference between the local orientation and the average orientation of several neighboring pixels [119]. The misorientation angles highlight the degree of plastic deformation in the materials. Figure 6-3a shows the EBSD misorientation map for th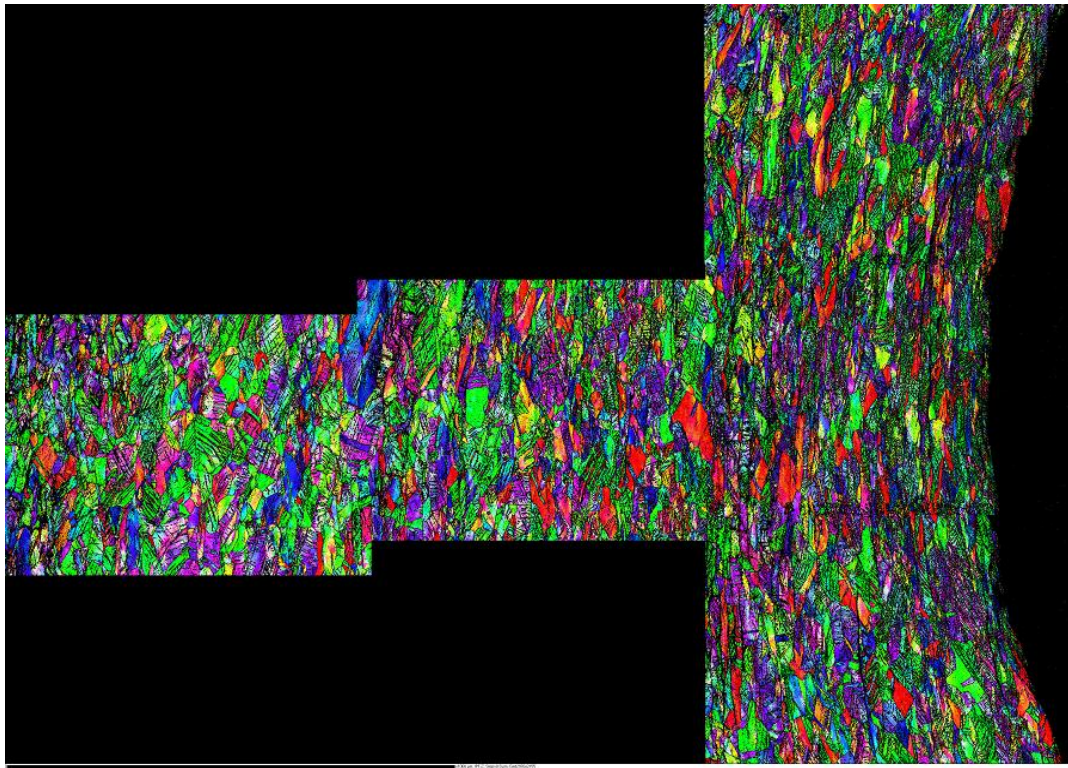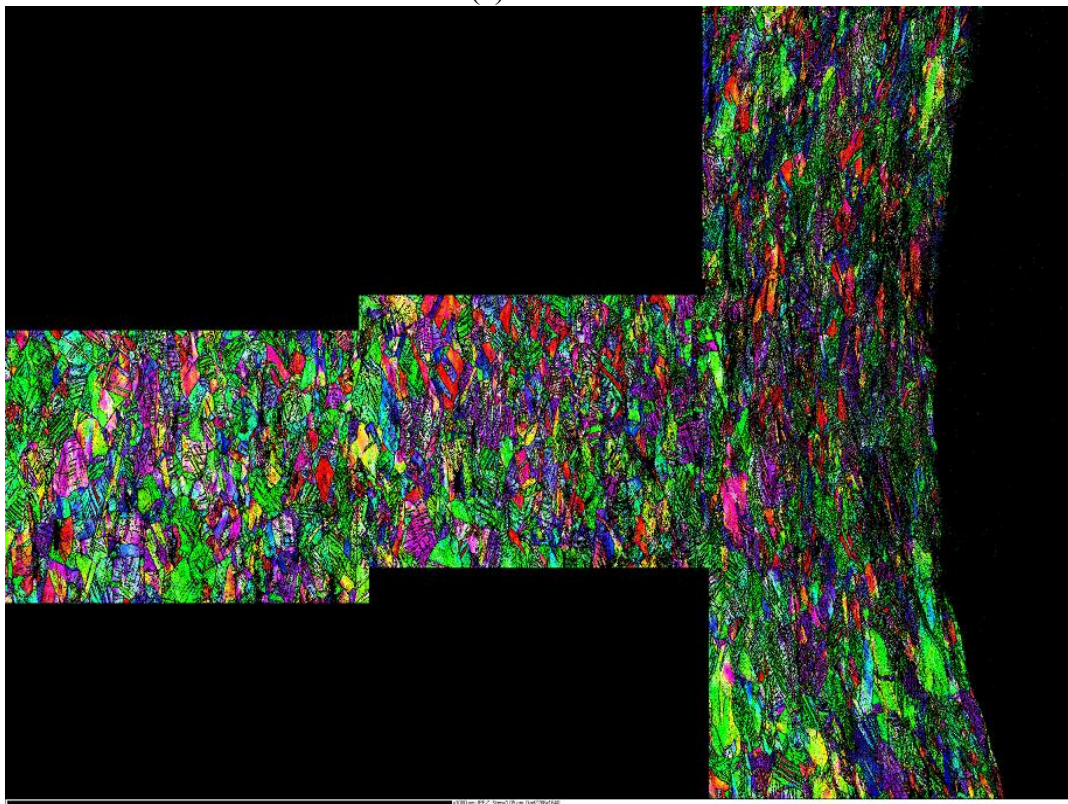e specimen with deep V notch. Due to the notch strengthening effect, it is again found that the plastic deformation is concentrated in the vicinity of the notch. The notch tip is plastically blunted and heavily deformed. The largest misorientation angle shown in Figure 6-3 is 10 degrees around the tip. (Above 10 degrees, lines are identified as grain and twinning boundary.) The zone with the larger misorientation in Figure 6-3 also has a kidney shape as described before in the discussion of the twinning zone. No misorientation can be detected beyond this elliptical deformation zone. Thus, the plastic deformation is confined to the local vicinity of the notch. The size of the deformation zone around the notch tip in the transverse direction is approximately 500 μm. The misorientation map for the specimen with the shallow V notch is shown in Figure 6-3b. The misorientation zone in the shallow V notch is larger than in the deep V notch. Even in the area away from the notch tip, some misorientation is observed. This is consistent with the discussion of the twinning zone in the previous section: the notch strengthening effect is weaker than in the case of the deep V notch due to the more localized stress concentration. Figures 6-3c and 6-3d indicate the misorientation maps for the specimens with semi-circular notches. For the semicircular notches, the stress is spread throughout the entire area surrounding the notch, so the volume with high plastic deformation is larger than in the specimens with V notches. The misorientation angles in the specimen with the shallow semicircular notch are more evenly distributed than in the specimen with the deep semi-circular notchindicating that shallow notches result in a larger plastic deformation zone. This, in turn, produces plastic blunting of notch tips, which, delays fracture to

larger strains. Since twinning is activated in the earlier stages of strain hardening adding to the dislocation flow deformation mechanisms, the enhanced plastic deformation and blunting explain the improved ductility and strength of the specimens with shallow notches.
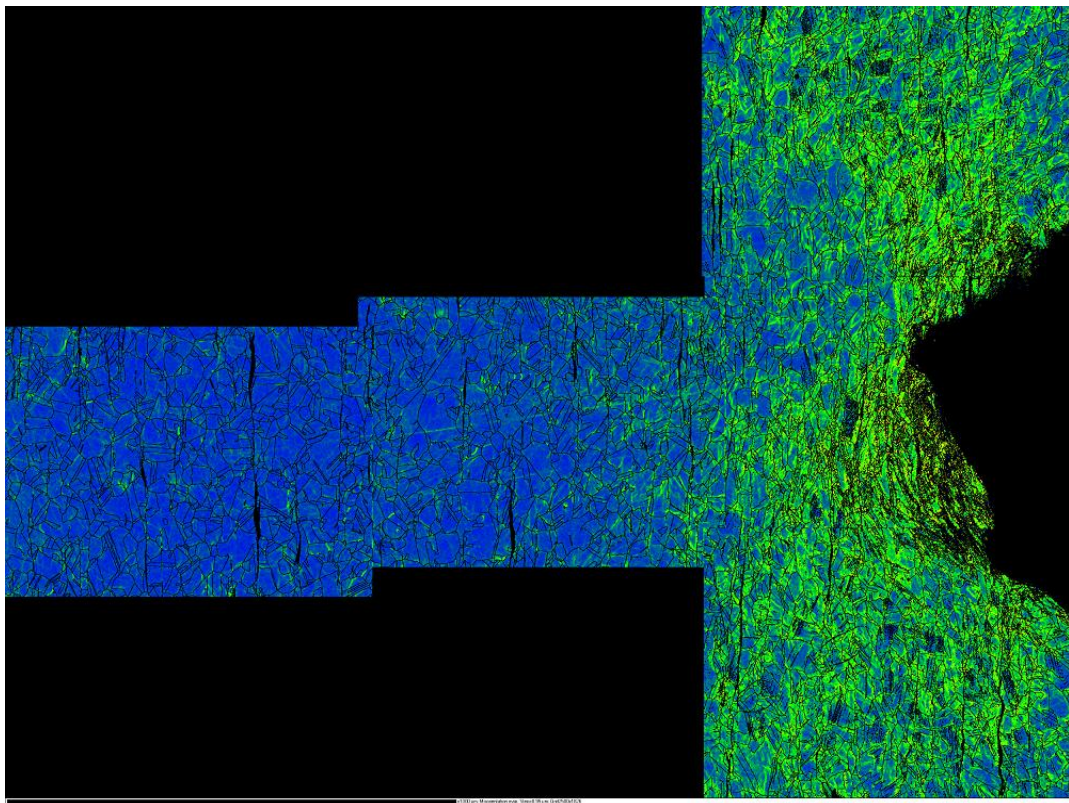
(a)

(b)

(c)

(d)

Figure 6-3   EBSD misorientation maps of 316L stainless steel tested at room temperature for (a) V-Notch-L-1, (b) V-Notch-S-1, (c) C-Notch-L-1 and (d) C-Notch-S-1
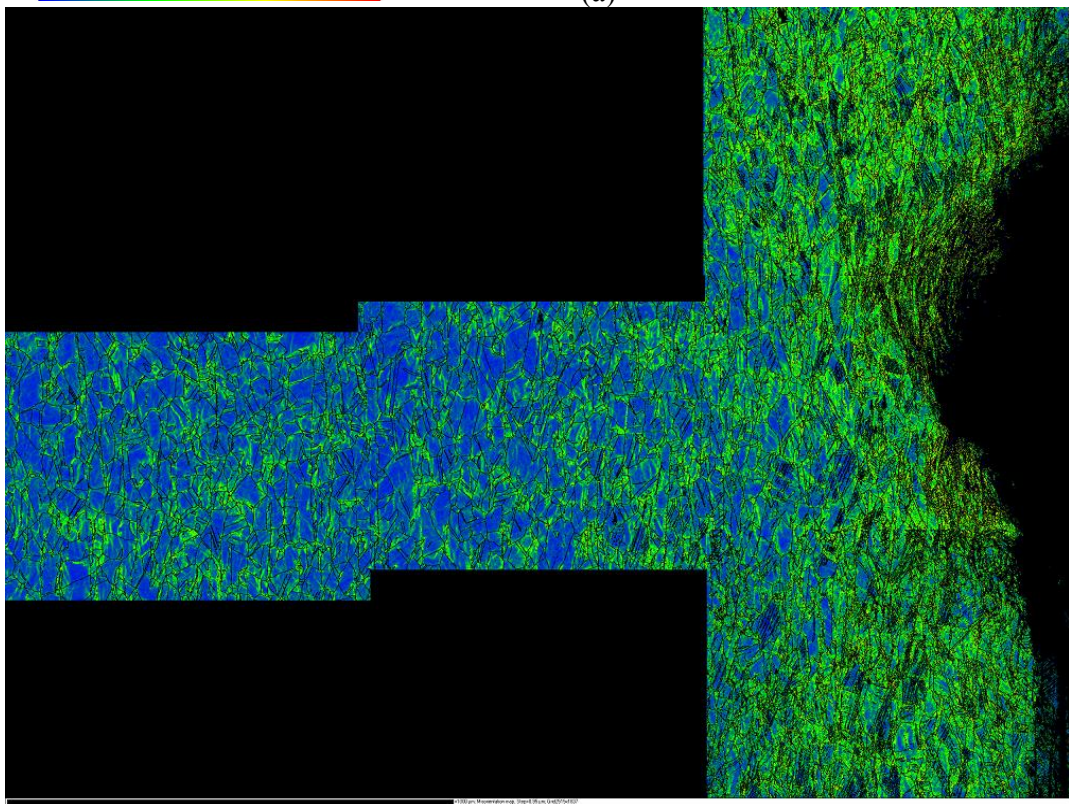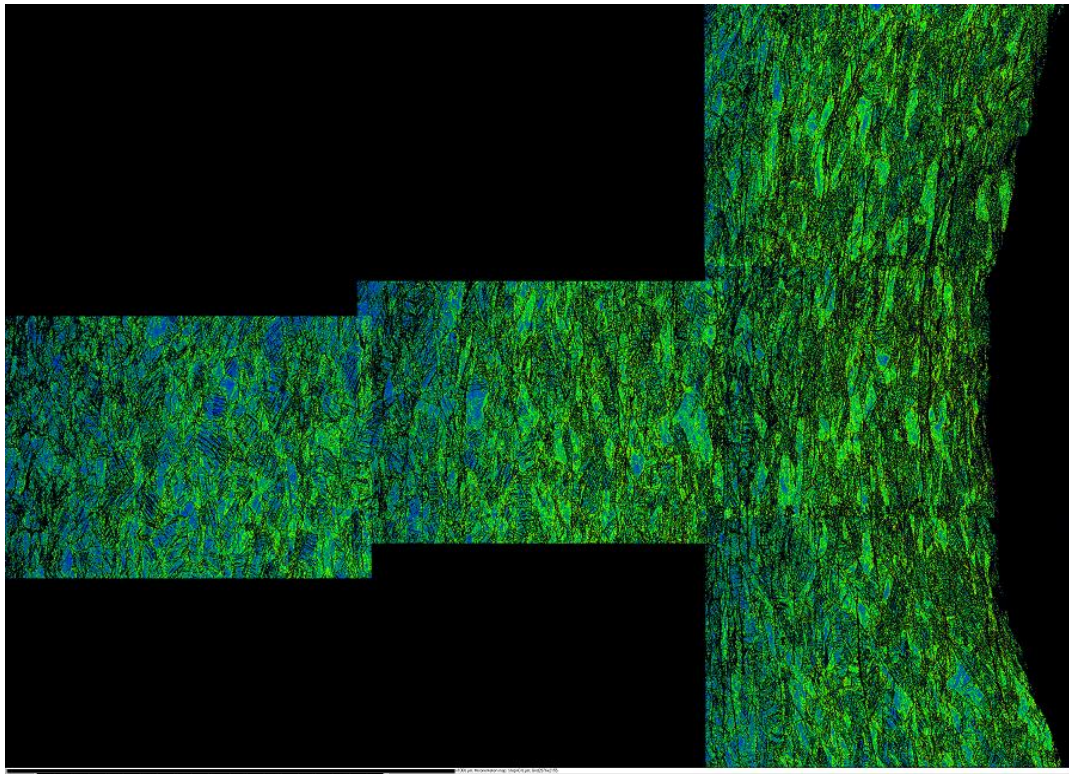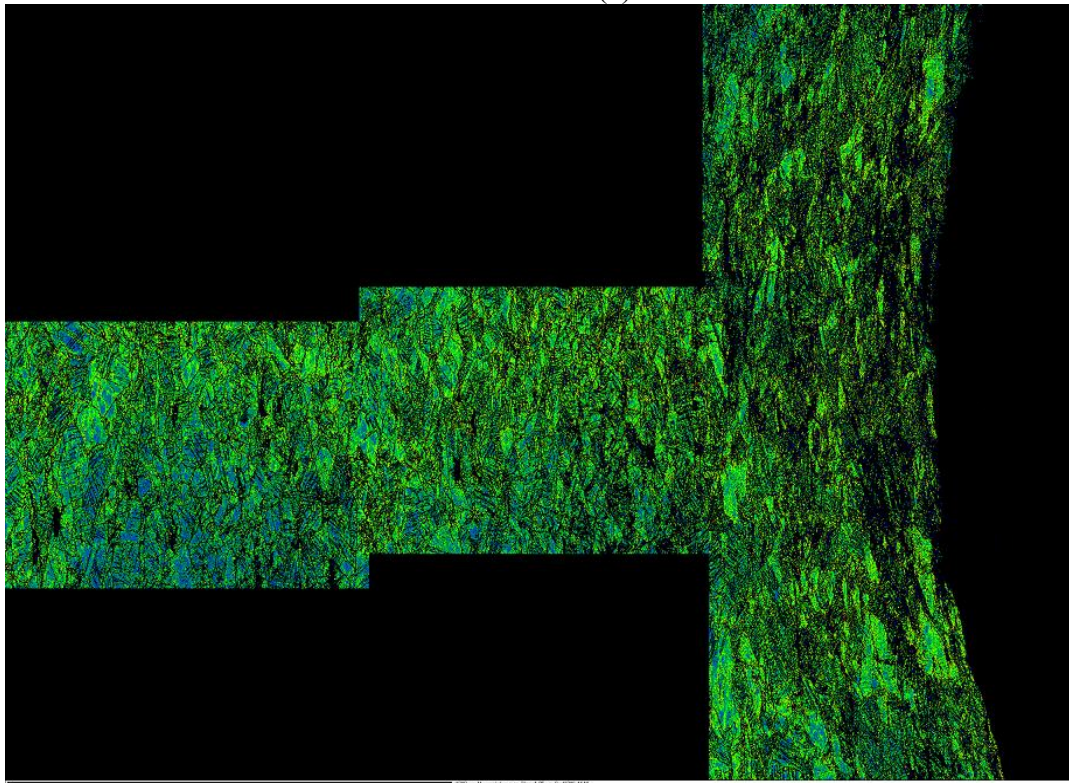
6.4 Temperature dependence of notch strengthening

In order to investigate the notch deformation evolution and its temperature dependence, the specimens with multiple notches were employed. Each specimen has three V-shape notches with different notch depths and the notch opening angle is fixed as 30o. The distance between each notch tip is 11.5 mm to avoid interference between notches. Three notches with various depths in the same specimen were used to show the notch strengthening microstructure evolution during tensile loading: from near yielding to the onset of necking. The ratios of notch depth versus specimen diameter are 0.15, 0.425 and 0.3 respectively.

The specimens with three V notches were tensile loaded to the onset of necking at room temperature and 200°C respectively. In this circumstance, when the element at the tip of the deepest notch reaches the necking initiating point, the other two notches were still in the middle of plastic deformation process. The notch depths are purposely designed using ABAQUS so that when the deepest notch starts to suffer the plastic instability, the smallest notch is still near the yielding point and the third one is in the middle of strain hardening. Figure 6-4 shows the EBSD orientation maps for the large V notch tested at room temperature and 200°C. It is evident that the notch tip is heavily deformed and plastic blunted. Micro-shear bands are formed in both cases. The difference is the activation of mechanic twinning system. Previous discussion indicates that the activation of mechanic twinning system is determined by the critical twinning stress and this stress has strong temperature dependence. The critical twinning stress for room temperature is about 500~550 MPa. The notch induced stress concentration makes the true stress around the notch tip larger than the critical twinning stress thus activates the mechanic twining system. However, when the testing temperature increases to 200°C, the critical twining stress increases dramatically and even is larger than the corresponding critical stress. In this situation, the

mechanic twinning is not able to be activated. From Figure 6-4, it is clearly evident that the mechanic twinning system is activated in the specimen tested at room temperature and spread throughout to form a kidney shape deformation twining zone around the notch while the twins are completely absent in the specimen tested at 200°C. The mechanic twinning is also not activated beyond that deformation zone in the room temperature specimen. This could be explained that the notch causes stress concentration around the notch tip thus in other area, the true stress is still not large enough to activate the twinning system.

The plastic deformation could be highlighted by the EBSD misorientation map. The misorientation maps for the three notches in the same specimen tested at room temperature are shown in Figure 6-5. Figure 6-5a shows the misorientation map for the deepest notch. The element in the vicinity of notch tip is heavily deformed and the plastic blunting is clearly evident at the notch tip. In general, the deformation zone shows a feature of kidney shape around the notch. Very few deformations could be observed beyond this zone because of the notch induced stress concentration. The plastic deformation for the middle notch is exhibited in Figure 6-5b. Very little plastic blunting could be noticed and the kidney shape plastic deformation zone is greatly shrunken. When the deepest notch reaches the onset of necking, the middle notch is still in the middle of strain hardening. It is reasonable that the middle notch has much less deformation than the deepest notch, but the kidney plastic deformation zone is still clearly evident. Figure 6-5c shows the deformation characteristic of smallest notch. Only at the notch tip, very little deformation could be observed. According to the above observations, the notches in the same specimen but with different depths actually exhibit the mechanical and microstructure evolution for the notch strengthening. When the notch was deformed to near yielding point, only the elements in the vicinity of notch tip is plastic deformed due to notch induced stress concentration.

Then after the notch is continued to be loaded to certain middle point of strain hardening, the plastic deformation is enlarged and shows a feature of kidney shape around the notch tip. Finally as soon as the elements in the vicinity of notch tip reach the onset of necking point, the material starts to failure although other parts of material may be still far from necking point. Similar characteristic of notch strengthening could be observed from the 316L stainless steel V-notched specimen tested at 200^oC shown in Figure 6-6. Specimen deformed at 200^oC could not have the twinning system activated due to the high critical twinning stress. The microstructure evolution is also pretty similar as room temperature test. The temperature dependence of the notch strengthening would be discussed in the following finite element modeling sections.

The EBSD misorientation maps exhibit the important impact of notch on the materials mechanic property degradation. The microstructure analysis indicates the existence of a kidney shape deformation zone. Recently the finite element analysis has been extensively applied to analyze the tensile response of uniaxial testing. A commercial finite element package, ABAQUS, was utilized to exhibit the stress distribution around the notch tip and investigate the stress evolution during the notch tensile test. The mesh is specially refined in the vicinity of notch tip to make the size of each element nearly equivalent to the grain size. Modified Gurson's model [98-100] was applied to simulate the post yield especially post necking process. Figures 6-7 and 6-8 indicate the stress distribution contours for 316L stainless steel V-notched specimens tested at room temperature and 200^oC. Both simulations were interrupted at the onset of necking to match the experiments conditions. The scales are set up as the same for more convenient comparison. The un-yielded area is marked as black. The yield stress for room temperature is about 250Mpa and for 200^oC, it is 200Mpa. Figure 4a shows the stress contour for the deepest notch of 316L stainless steel tested at room temperature. The elements in the vicinity of notch tip were heavily

deformed and the notch tip plastic blunting is clearly evident. The deformation zone shows a kidney shape characteristic. All of these features are consistent with the experimental EBSD misorientation map. Figures 6-7b and 6-7c indicate the simulations for the middle and small notches respectively. In general, they have a good agreement with the experiments. Then it should be a reasonably good prediction of the tensile performance for irradiated, notched specimens. Figure 6-8 shows the stress distribution for the specimen tested at 200°C. It is clearly evident that the deformation is much less in the high temperature tests. For the middle and small notches, the un-yielded zone is more pronounced, which indicates less deformation.
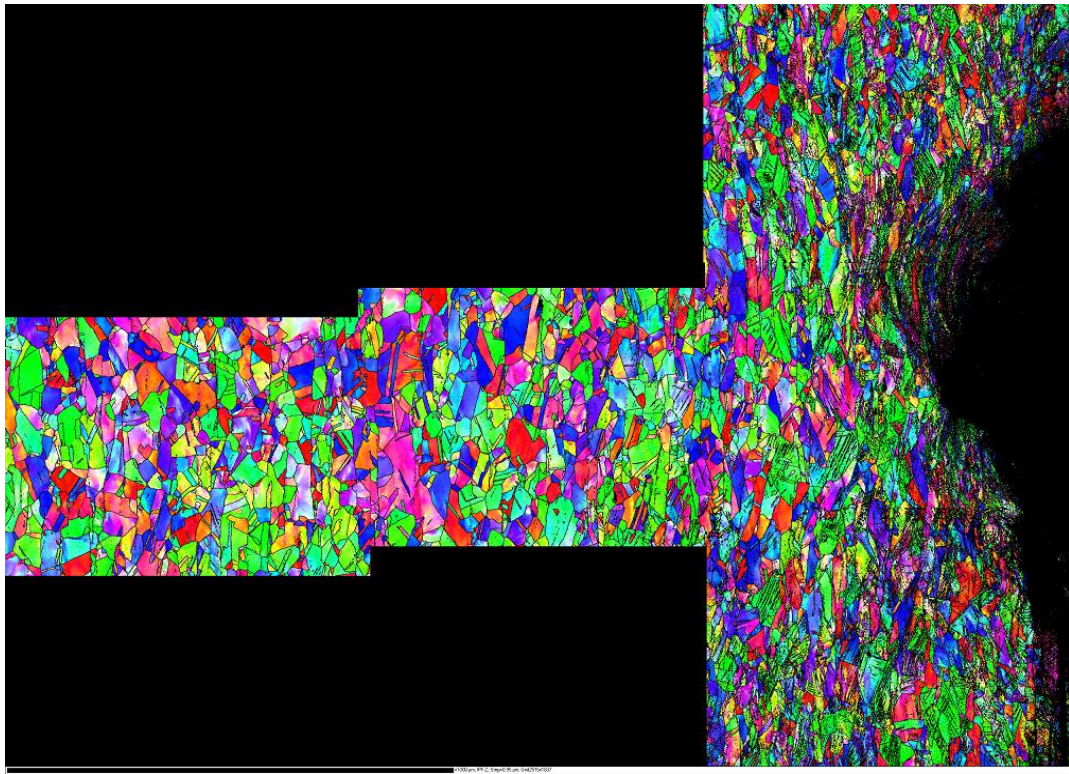
1000*um*   (a)
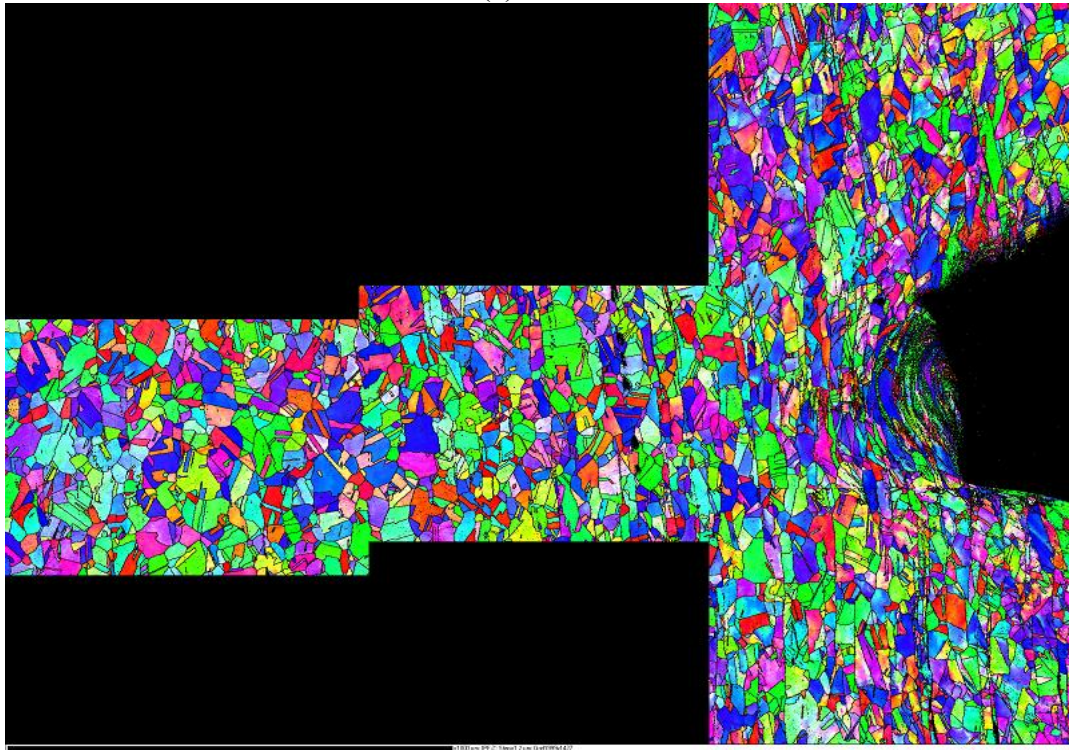
1000*um*   (b)

Figure 6-4 EBSD orientation maps for V-Notch tested at (a) room temperature and (b) 200°C; the twinning system is evidently activated in the test of room temperature while completely absent in (b)

(a)

(b)

1000*um*   (c)
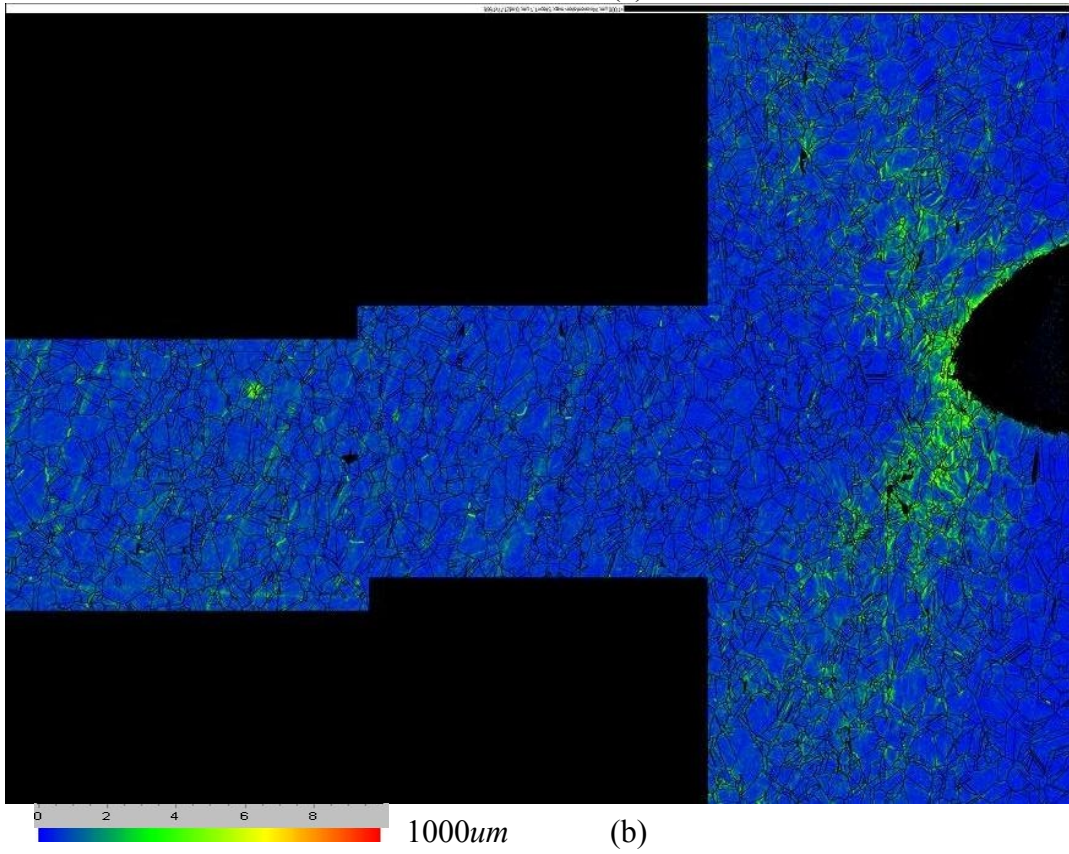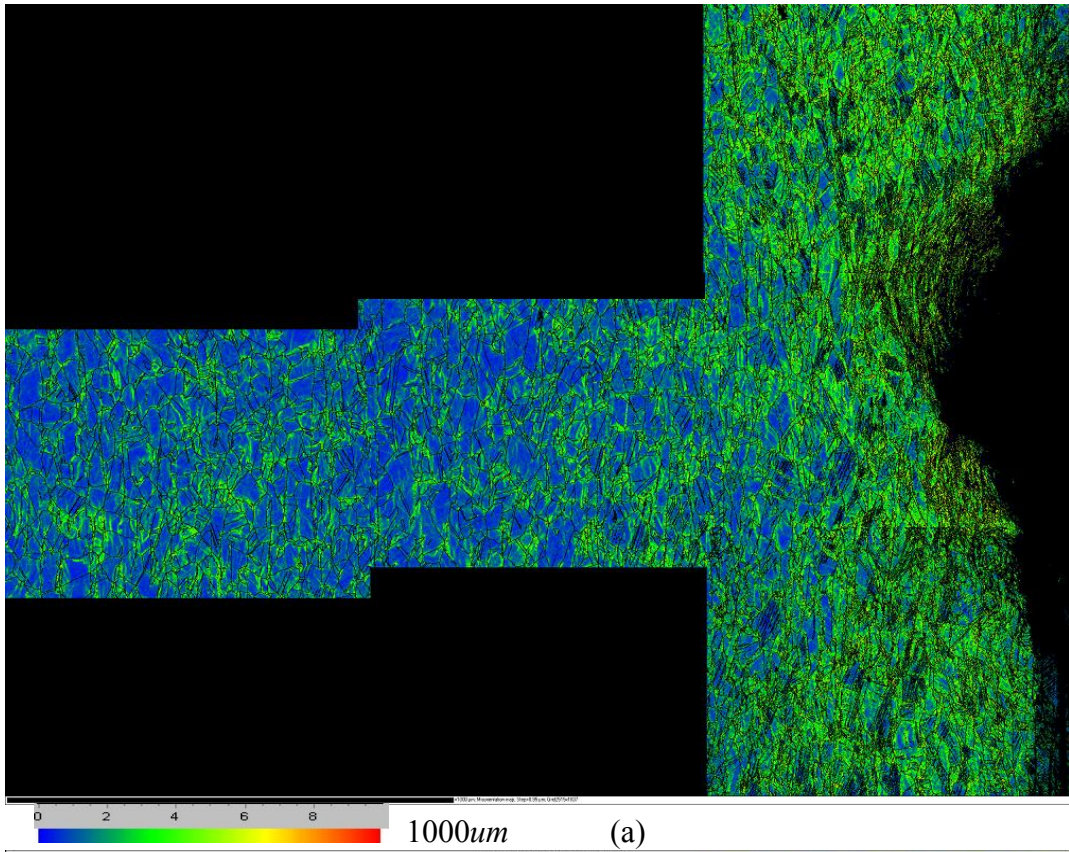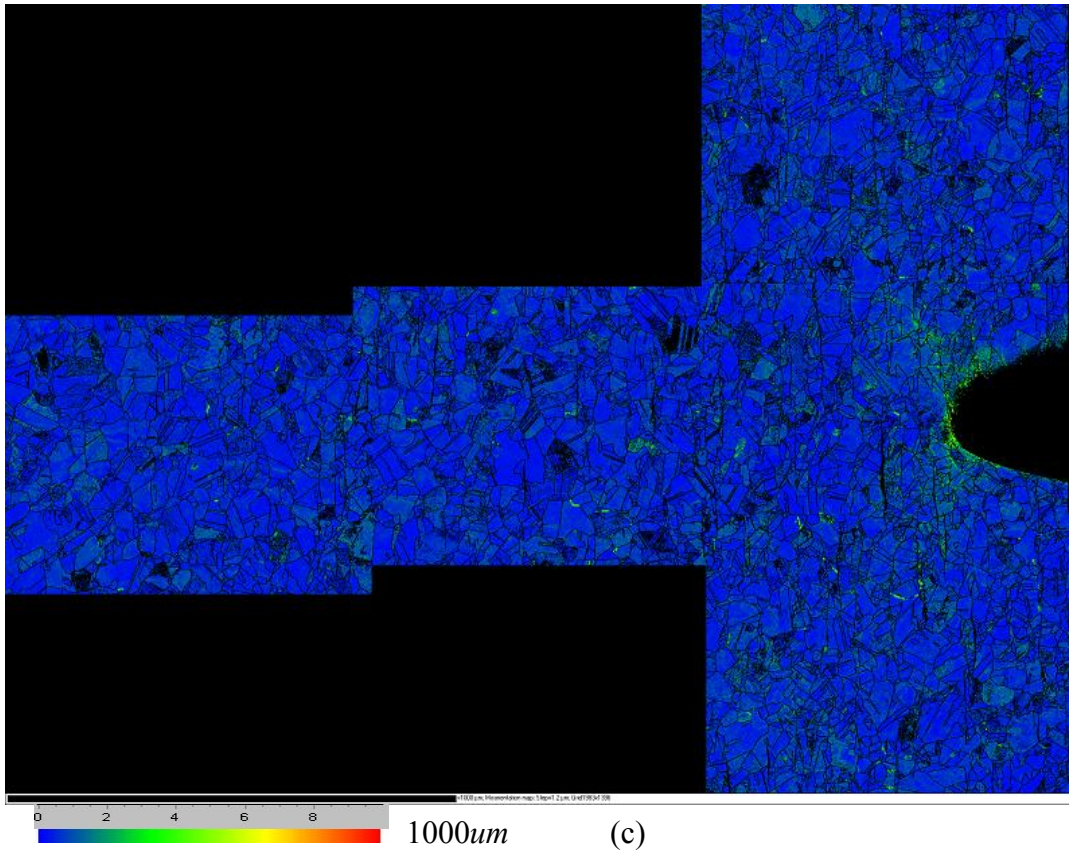
Figure 6-5 EBSD misorientation maps for 316L stainless steel notched samples tested at room temperature; (a), (b) and (c) stand for samples with different notch depths: (a)>(b)>(c)

(a)

1000*um*

1000*um*

(b)

109
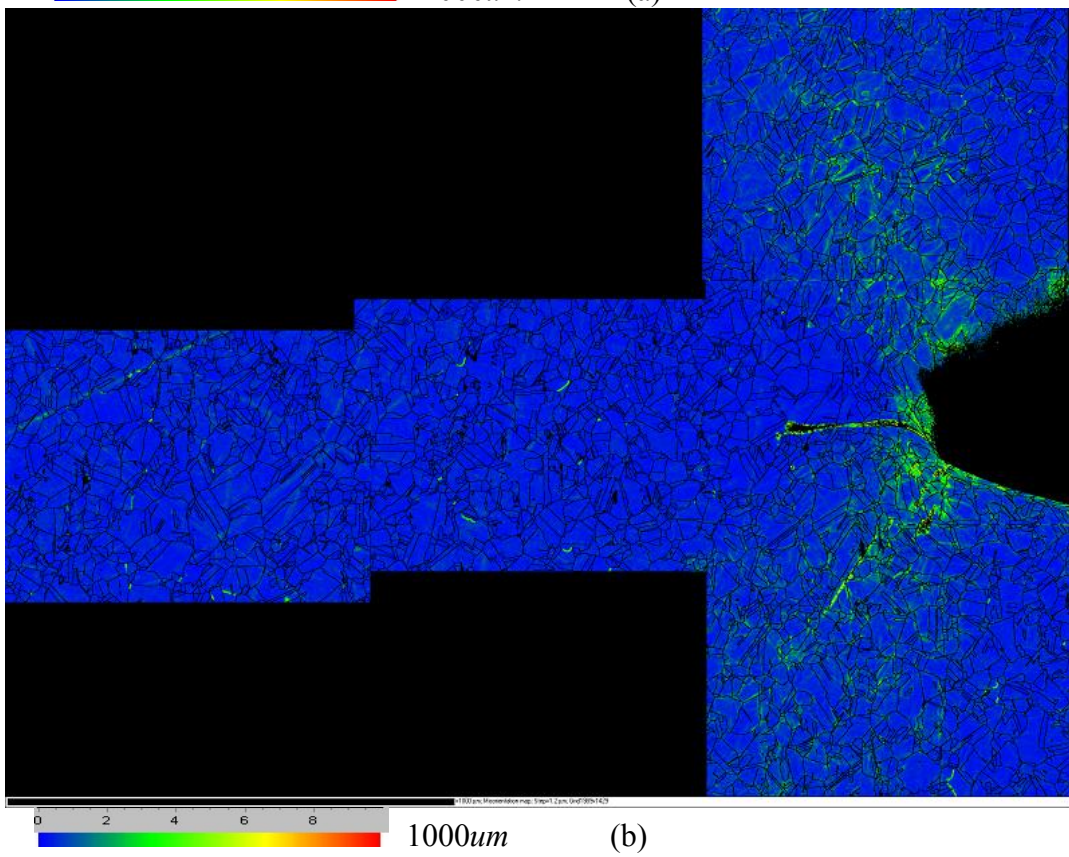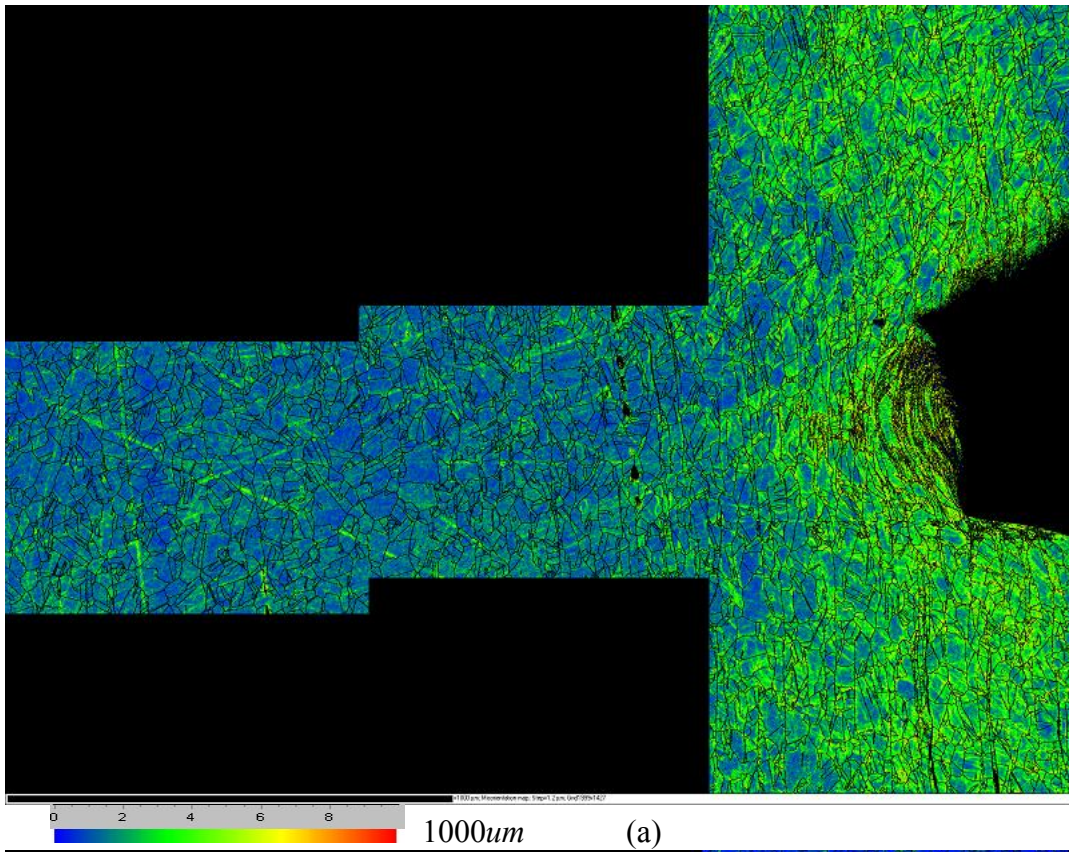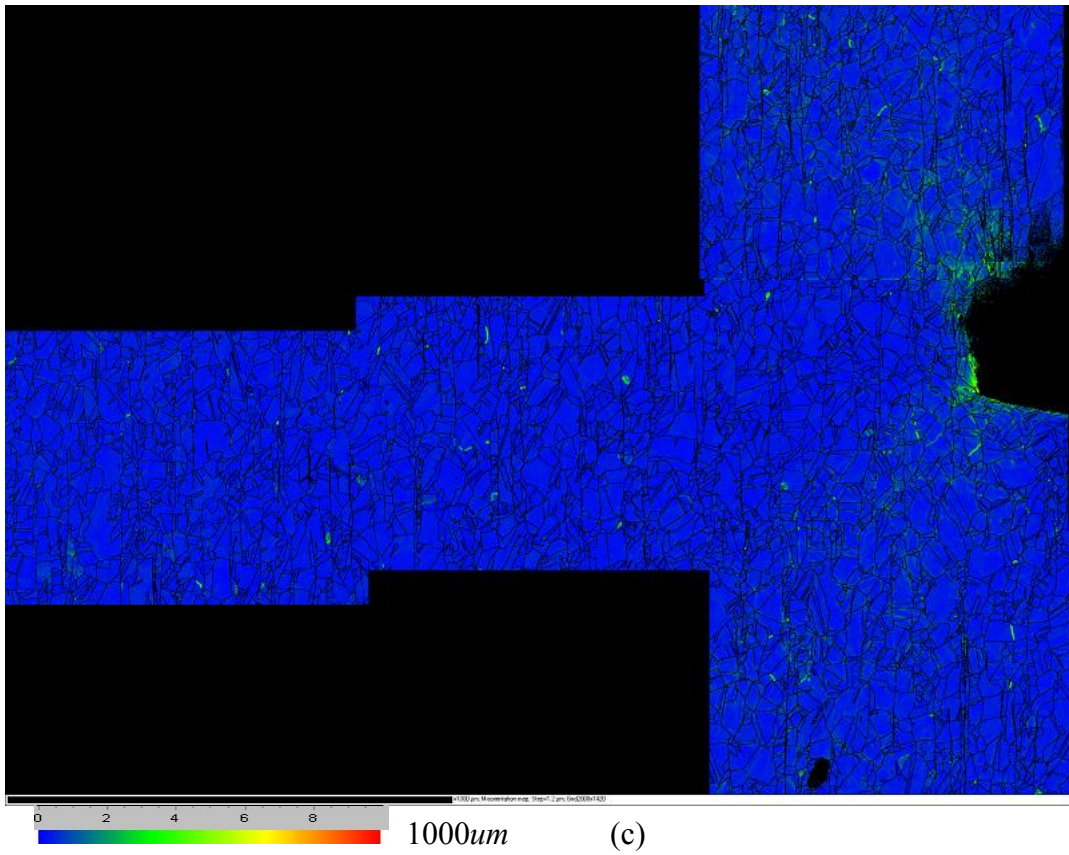
Figure 6-6 EBSD misorientation maps for 316L stainless steel notched samples tested at 200°C; (a), (b) and (c) stand for samples with different notch depths: (a)>(b)>(c)
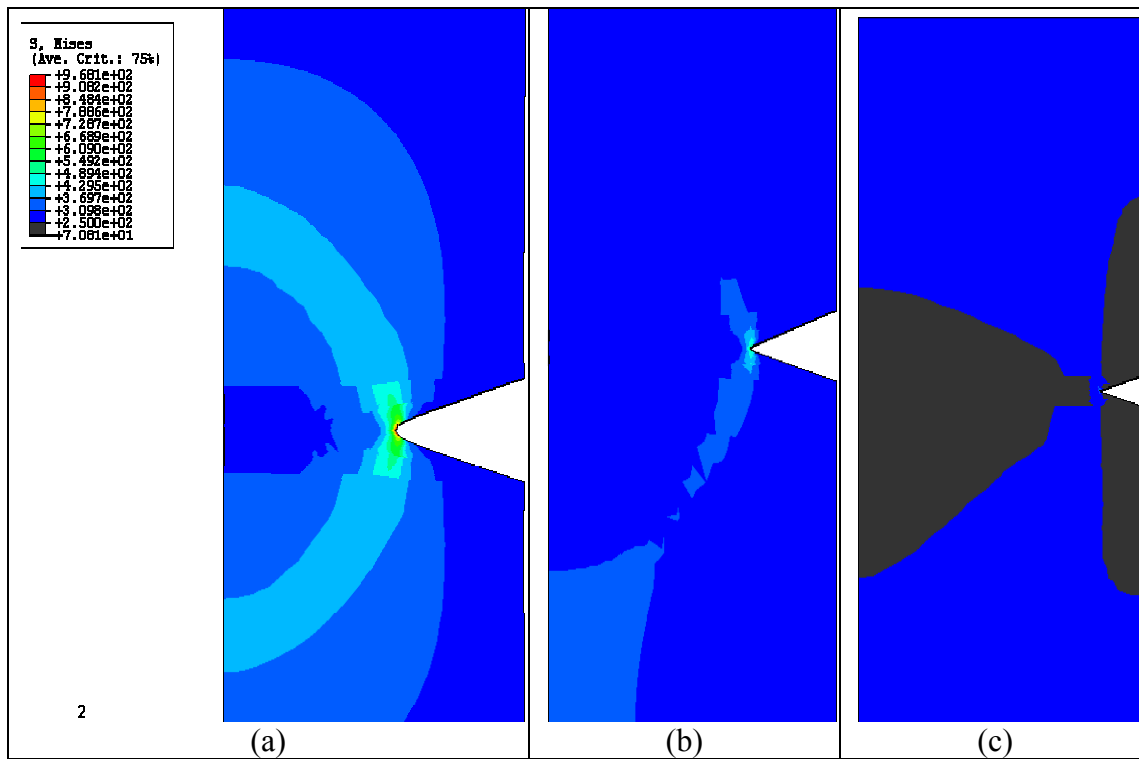
Figure 6-7 Stress distribution for 316L SS notched specimen tested at room temperature and interrupted at the onset of necking. (a) for large notch, (b) for middle notch and (c) for small notch.
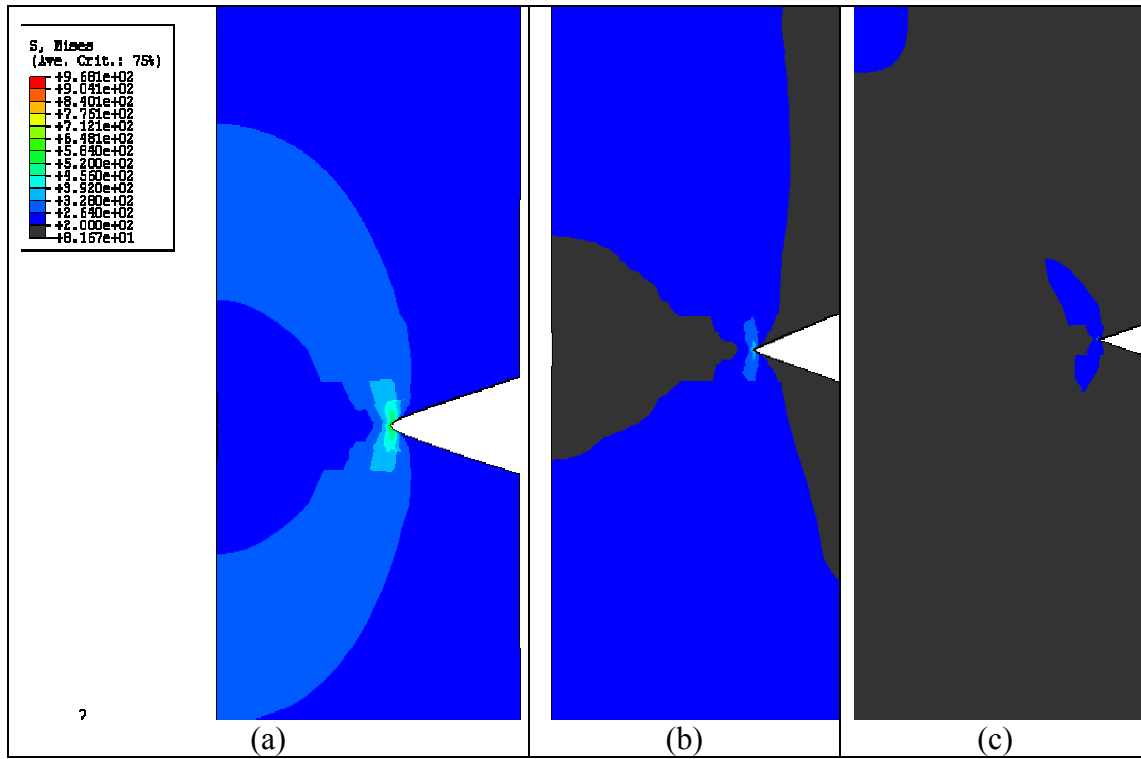
Figure 6-8 Stress distribution for 316L SS notched specimen tested at 200°C and interrupted at the onset of necking. (a) for large notch, (b) for middle notch and (c) for small notch.

CHAPTER 7   DISCUSSION

This study shows that there is the strong correlation between material yield strength and uniform elongation, which is independent of irradiation condition. The relationship, however, seems to have a very strong temperature dependence for 316 stainless steel, particularly between the temperatures of 20 and 150ºC. This relationship has a number of consequences, but perhaps the important consequence for assessing flow localization in irradiated 316 stainless steel is that the mode of deformation which affects the yield point and the post-yield strain hardening, has little influence on the onset of necking. Once the critical stress is reached, regardless of the operating flow mechanisms, the material will suffer plastic instability. Irradiation-induce hardening can increase the yield strength so that only a small amount of plastic flow occurs before necking, but the necking process itself seems to be controlled by other mechanisms.

A second important finding is that the true stress to failure is a material property and not a function of radiation-induced defect microstructure, dislocation multiplication mechanisms or strain hardening behavior. From the preceding discussion, it is apparent that the flow properties and the point of plastic instability, i.e. the critical stress, are not affected by irradiation exposure. This means that the same microstructural properties control plastic instability regardless of radiation damage microstructure. This is associated with the nucleation, growth and coalescence of plasticity-induced voids. These processes have received considerable attention in the literature (see for example ref. [102, 104, 120]) where plasticity-induced void formation processes have been modeled following Gurson [98, 99]. The least well characterized of these processes is the plasticity-induced void nucleation process. In much of the work to characterize the plasticity-induced void nucleation process, a highly stress or strain dependent functional relationship is assumed, see ref. [104, 120]. The functional form, however, is not related directly

to easily accessible materials parameters. The nucleation process should be dependent on the type and distribution of nucleation sites and surface energies required to form new internal surfaces. Nucleation processes which depend on a distribution of particles or inclusions have been reviewed by Goods and Brown [121]. Their review suggests that particle-matrix interfacial strengths are the controlling factor. The current findings indicate that the distribution plastic void nucleation cites is affected by radiation exposure for the conditions examined in this study.

An interesting point of comparison is the influence of cold work on the critical stress.   The studies of Pawel-Robertson et al. [20] included specimens with 20% cold work. The uniform elongation versus yield strength behavior is shown in Figure 8-1 for these conditions and compared to the values for solution annealed 316L stainless steel. It can be seen that cold working lowers the critical stress for plastic instability to a value of about 850 MPa compared to an extrapolated value of around 1100 MPa in the solution annealed material at 25ºC. The uniform elongation values for cold worked 316 stainless steel tensile tested at 200, 330 and 400°C are all low, but seem to approach zero by 700 MPa or perhaps lower stress levels. The drastic reduction in critical stress, at least at lower temperatures, would seem to indicate that the initial strength advantages that would derive from cold working have a detrimental effect on flow localization and fracture properties.
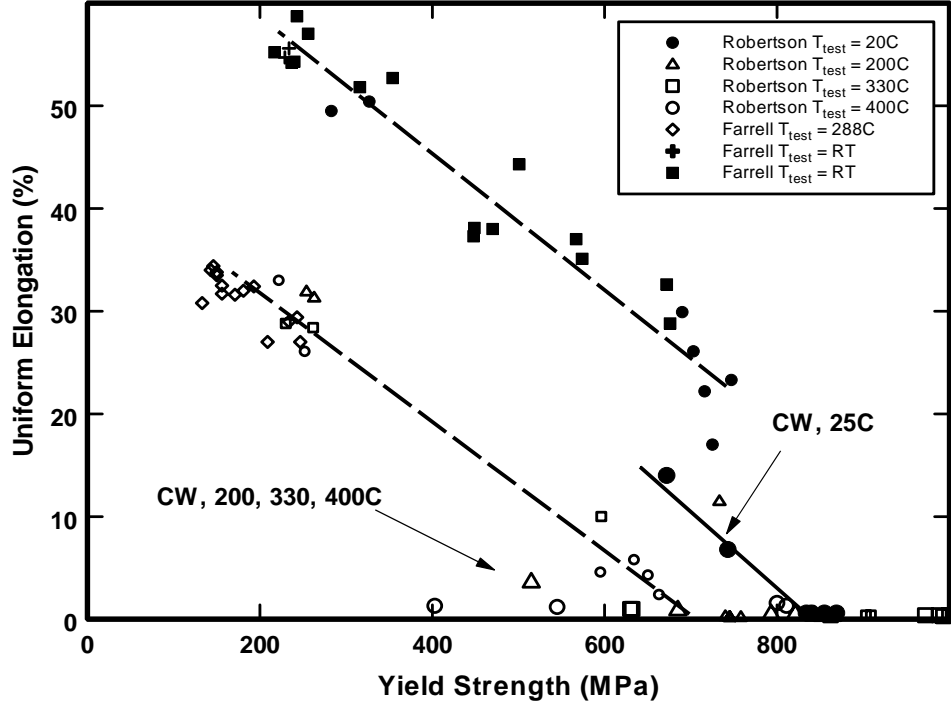
Figure 8-1 The influence of cold work on the uniform elongation versus yield strength behavior of 316SS [20]. Cold worked materials are shown with the larger size symbols compared to the annealed 316SS data from Pawel-Robertson [20] and the data from Farrell *et al.* [6].

The very strong linear relationship between uniform elongation and yield strength suggests a simple model for predicting uniform elongation or plastic instability based on materials yield strength. The level of uniform elongation, ε_u, can be predicted by equations of the form

$$\varepsilon_u = \varepsilon_u^0 - m \cdot \sigma_{ys} \qquad \text{for } \sigma < \sigma_{crit}$$
$$\varepsilon_u \sim 0 \qquad \text{for } \sigma \geq \sigma_{crit}$$

Where ε_u^0 is the intercept on the uniform elongation axis and *m* is the slope of the trend line. This approach is limited more by the variation in material yield strength than in the critical stress. A comparison of the data for Maloy *et al.* [11] and the group of studies by Pawel-Roberson, Farrell *et al.* [6, 20], indicate that, while the initial material yield strengths are different, the critical stress levels are very nearly the same. Thus the slope values, *m*, in the equations would vary drastically

115

depending on the starting material properties. This can be seen by comparing the slopes and intercepts shown in Figure 3-4.

A final point of this topic is the influence of He and H to dpa ratios on the tensile response. The current analysis would indicate that He and H have little influence on flow localization of plastic instability response in the materials studied here. The data represent a wide range of He to dpa and H to dpa ratios, He/dpa range from as low as 1 appm He/dpa to a value between of more than 50 appm He/dpa, but little differences are found in the tensile properties related to necking and plastic instability. This conclusion is consistent with other studies of these influences, and confirms that He and H have relatively little impact on flow instability for the conditions discussed above.

A major issue with the use of Type 316 stainless steel in irradiation environments is the strong drop in uniform elongation with irradiation exposure between 150 and 400ºC. This drop is perplexing since the rate of irradiation hardening is reasonably similar at temperatures from room temperature to nearly 400ºC. Nevertheless, the loss of ductility is most extreme in the intermediate temperature range. This strong temperature dependence is also highly evident in earlier studies of correlations between yield strength and uniform elongation values [17]. A strong drop in uniform elongation is found between room temperature and 150ºC, and a reasonably flat plateau is found up to 400ºC. In addition, it is observed [17] that the tensile test temperature, and not the irradiation temperature, is the most important parameter for describing uniform elongation levels. Results show that materials irradiated at higher temperatures and tested at lower temperatures, or vise versa, show a tensile response which is characteristic of the test temperature [17].

This observation, which has been a central focus of research for a numbers of years, can be reconciled in the following way. First, it should be noted that in each case, the material exhibits a critical stress at which uniform elongation ends and flow localization begins. The critical stress level is independent of irradiation exposure, and appears to be a material property, though it may depend on the test specimen configuration. Second, this critical stress can be obtained from tensile tests performed on unirradiated or irradiated material since it does not seen to depend directly on irradiation conditions. In the interests of resolving the temperature dependence of the critical stress in Type 316 stainless steel, a number of tensile tests were performed on unirradiated 316L stainless steel standard tensile specimens. The yield strengths were found to be uniformly higher than those from either the Byun [6] material or the material tested by Maloy [11, 12] because of the cold work. However, the strain hardening behavior is similar. In Figure 8-2, the true stress-strain curves from the 316L stainless steel tested in this study are shown plotted on the trend curves for the Byun [6] and Maloy [11, 12] curves. The data has been shifted to align with the curves to account for the higher yield strength of the current material. In addition, the 304L stainless steel data from Maloy [11, 12] at 50C has been shifted to match the 50C 316L stainless curves. Figure 8-2 shows that the critical stresses are similar between our material and those of the other studies, with only some slight differences in final strain hardening slope compared to the Maloy [11, 12] materials. Thus, good indications of the temperature response of the critical stress for flow localization in Type 316 stainless steel can be obtain from the series of tensile tests performed here. These tests were performed at room temperature up to 600ºC.

(a)

(b)

The plot shows true stress-strain curves with the following labels:
- y=1041.03x+387.55
- 1, 2, 3, 4 curves
- Y-axis: True Stress(MPa), 0 to 1000
- X-axis: True Strain, 0.0 to 0.6

Legend:
1: unirradiated
2: unirradiated -[JFS]-150
3: 2.9dpa
4: 4.1dpa
— Linear Fit
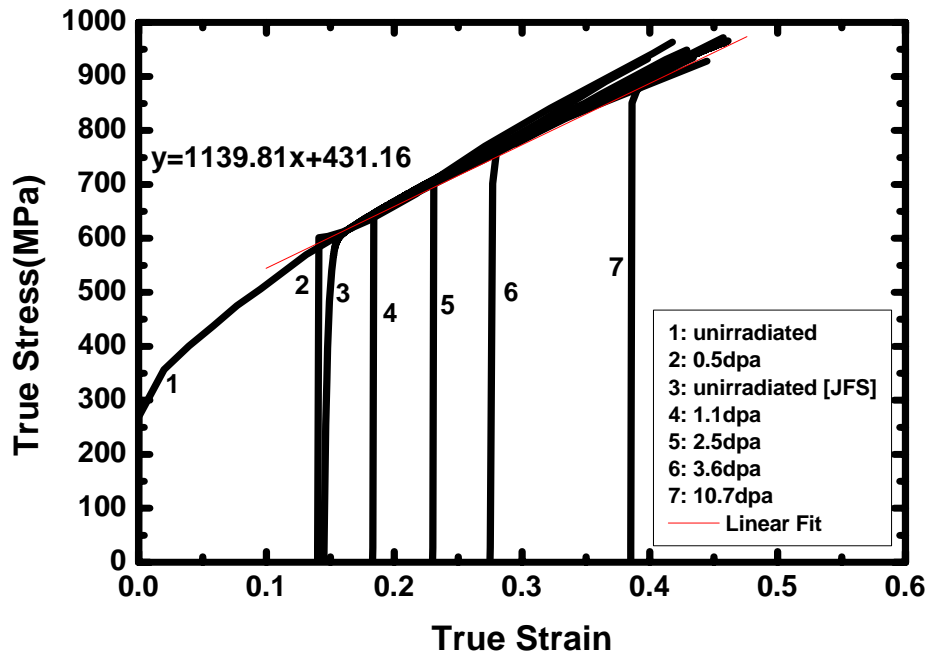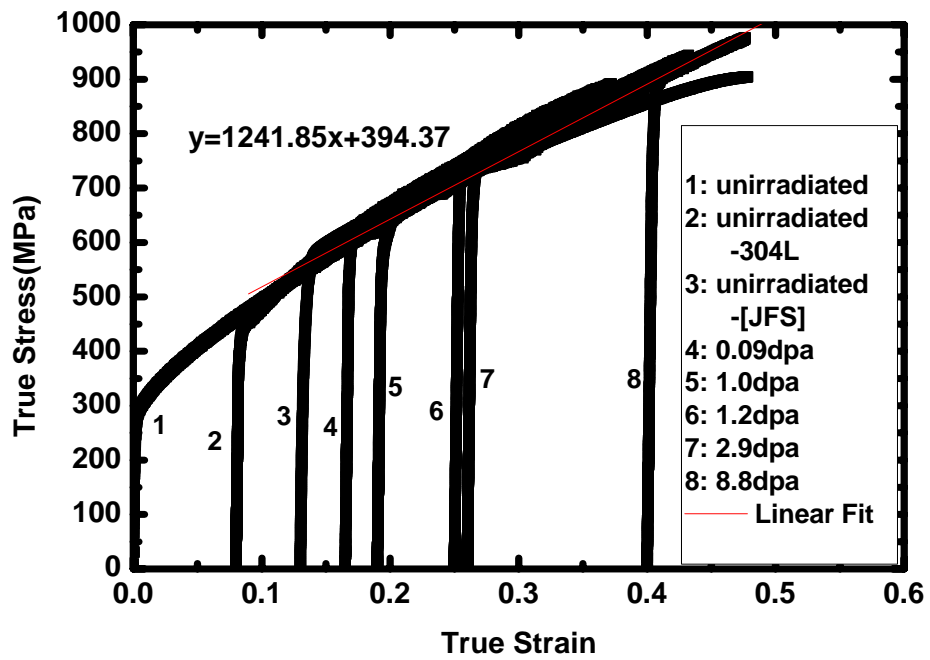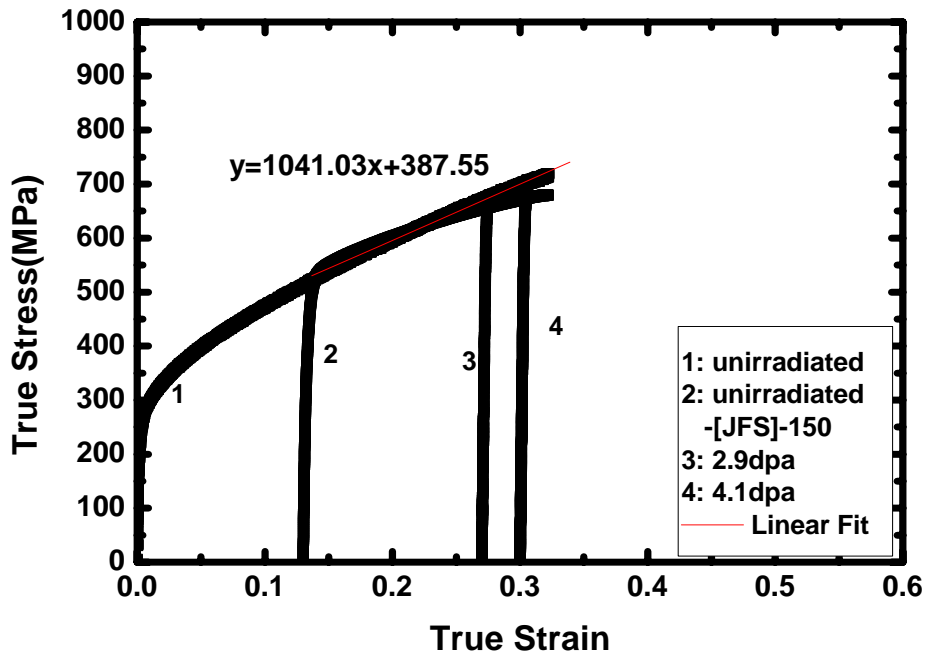
(c)

Figure 8-2   The true stress-strain tensile curves are shown for (a) EC 316LN SS tested at room temperature [51], (b) 316L SS tested at 50ºC [11, 12], and (c) 316L SS tested at 164ºC [11, 12] with the curves shifted proportional to the irradiation-induced increases in yield strength. Tensile data from unirradiated 316L SS from this study at test temperatures of 20, 50 and 150ºC are superimposed on the curves. In addition, tensile data for unirradiated 304 SS tested at 50ºC is superimposed on curve (b).

Figure 8-3 indicates the strong temperature dependence of the critical stress in Type 316L stainless steel and the relatively weak temperature dependence of the yield strength. The uniform elongations are shown as a function of test temperature and follow a trend which is similar to, but with somewhat less temperature dependence as, the critical stress. The band between the yield strength and the critical stress level indicates the amount of irradiation-induced hardening that the material can withstand before undergoing flow localization upon loading. It is clear that much higher hardening levels can be tolerated at room temperature than between 200 and 400ºC. While

the current material has somewhat higher yield strength than the other versions of 316L stainless

steel examined here because of cold work, the strong temperature difference of the critical stress

accounts for the observed low ductility in this alloy following irradiation between 150 and 400ºC.

It is also noteworthy that the difference between the yield strength and the critical stress is nearly

uniform in the temperature range between 150 and 400ºC, consistent with the observed tendency

for flow localization in this temperature range [20].

Figure 8-3   The critical stress for the onset of necking in 316 SS is shown as a function of temperature. The temperature dependence of yield strength and uniform elongation are also shown.

Another set of experiments were also performed on the full annealed 316L stainless steel to

correct the cold wok effect in the previous tests. Figure 8-4 indicates that the critical stress

decreases quickly between RT and 200°C and reaches a plateau thereafter. The average value for

the yield strength irradiated at different irradiation levels are also plotted in this graph. Once the radiation-induced hardening brings the yield strength to the level of the critical stress, the material will tolerate little or no plastic deformation prior to plastic instability, reducing the uniform elongation to critically low levels, below 1%. It is clear that much higher hardening levels can be tolerated at low temperatures than between 200 and 400°C. Therefore, materials deformed at low temperature, even after high irradiation exposure levels still maintain a large difference between the critical stress and the average yield strength and are able to undergo large amounts of plastic flow and strain hardening after yield and prior to plastic instability. However, for the materials tested at intermediate temperatures from 200 to 400°C, even at low doses, the difference between the irradiation-induced hardening and the critical stress is relatively small so that the materials suffer necking immediately after yielding. This observation is consistent with the previous investigation by Robertson *et al.* [20]. It is also noteworthy that the difference between the yield strength and the critical stress is nearly uniform in the temperature range between 200 and 400°C, consistent with the observed plateau in the tendency for flow localization in this temperature range.
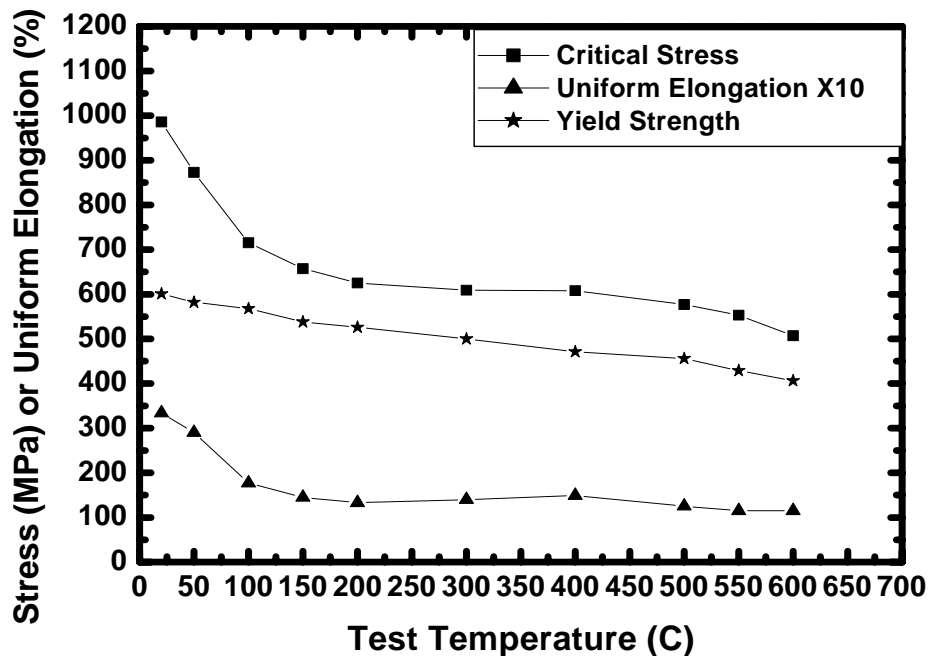
Figure 8-4 Temperature dependence of critical stress and yield strength

This study shows that the deformation mode of 316L stainless steel demonstrates a strong temperature dependence of the critical stress, while the yield strength is relatively temperature insensitive. Figure 8-4 indicates that the critical stress decreases quickly between RT and 200°C and reaches a plateau thereafter. The average value for the yield strength irradiated at different irradiation levels are also plotted in this graph. The band between the yield strength and the critical stress indicates the amount of irradiation-induced hardening that the material can withstand before undergoing flow localization at yield. Once the radiation-induced hardening brings the yield strength to the level of the critical stress, the material will tolerate little or no plastic deformation prior to plastic instability, reducing the uniform elongation to critically low levels, below 1%. It is clear that much higher hardening levels can be tolerated at low

temperatures than between 200 and 400°C. Therefore, materials deformed at low temperature, even after high irradiation exposure levels still maintain a large difference between the critical stress and the average yield strength and are able to undergo large amounts of plastic flow and strain hardening after yield and prior to plastic instability. However, for the materials tested at intermediate temperatures from 200 to 400°C, even at low doses, the difference between the irradiation-induced hardening and the critical stress is relatively small so that the materials suffer necking immediately after yielding. This observation is consistent with the previous investigation by Robertson *et al.* [20]. It is also noteworthy that the difference between the yield strength and the critical stress is nearly uniform in the temperature range between 200 and 400°C, consistent with the observed plateau in the tendency for flow localization in this temperature range.
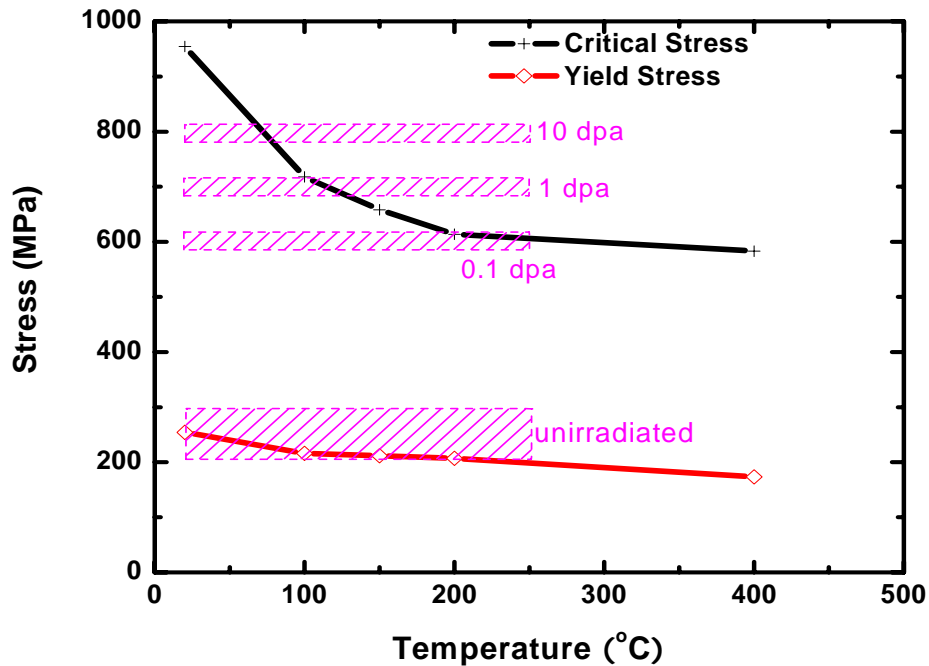
The twinning process is believed to be a major contributing mechanism to strain hardening for FCC materials. The trigger for the activation of twinning system is determined by the critical twinning stress. In an earlier study, Byun *et al.* [8] proposed a critical twinning stress expression in terms of the equivalent or uniaxial stress from the critical resolved shear stress. The expression is revised here based on the current EBSD results as:

$$\sigma_T = \frac{2\gamma_{SFE}}{b_p} \cdot \frac{1}{SF} = 4.3 \frac{\gamma_{SFE}}{b_p}$$

The critical twinning stress is proportional to the stacking fault energy which has a strong compositional and temperature dependence in FCC materials including 316L SS. The critical twinning stress increases with increasing temperature and intercepts with the critical stress for necking at a temperature just above 100°C. For the specimens tested below this temperature, the twinning process will be activated during the strain hardening process. It can be noted that the difference between the yield strength and critical twinning stress is smaller at low temperatures

than that at higher temperatures, and consequently the twinning process will be activated soon after yield at lower temperatures. However, for materials tested above the temperature at which the critical twinning stress is equal to critical stress, the twinning mechanism cannot be triggered during the hardening process because the true stress is smaller than the critical twinning stress. This observation is consistent with the SEM analysis shown in Figure 5-3.

Schmidt factor has an important impact on the deformation mechanism. The critical resolved stress for twinning is proportional to the Schmidt factor as $\tau = SF \cdot \sigma_{uniaxial}$. The EBSD patterns with Schmidt factor are included in Figure 8-5 to Figure 8-7 for room temperature, 100 and 200°C respectively. For the specimens tested at room temperature, twinning system is only activated after certain level of dislocation-based hardening. It is interesting to point out that the even in the {110} grains, the twinning system can only be activated if the Schmidt factor is below about 0.485 as shown in Figure 8-5. For the grains or partial of certain grain with Schmidt factor above 0.485, no twinning can be observed; however, the dislocation-based planar slip is clearly evident from these grains from the identification of misorientation lines and band contrast bands. The slip bands are shown in the Figure 8-8 for room temperature study. The marked grain has a Schmidt factor larger than about 0.485, no twinning can be observed, the planar slip dominates the plastic deformation. It is believed that the mechanic twinning and planar slip are competing mechanisms for plastic deformation. The grains with higher Schmidt factor can easily satisfy the threshold requirement for planar slip at early stage and even after the specimen is strained to certain level with higher uniaxial stress than critical twinning stress, the grain has already been dominated by the planar slip and no twinning system can be activated anymore. In general, the mechanic twinning dominated the deformation process of room temperature tensile loading of 316L stainless steel. However, the situations for the other two temperatures are totally different. In these

two situations, most of the grains are dominated by slip mechanism. The complete domination of slip mechanism in 200°C test causes earlier plastic instability than that in 100°C. The inability of the activation of mechanic twinning mechanism to be triggered at higher temperatures effectively limits the materials ability to deform, substantially reducing levels of uniform elongation. This explains the major tendency of 316L austenitic stainless steel to exhibit flow localization and very low uniform elongations following irradiation exposure between 200 and 400°C.
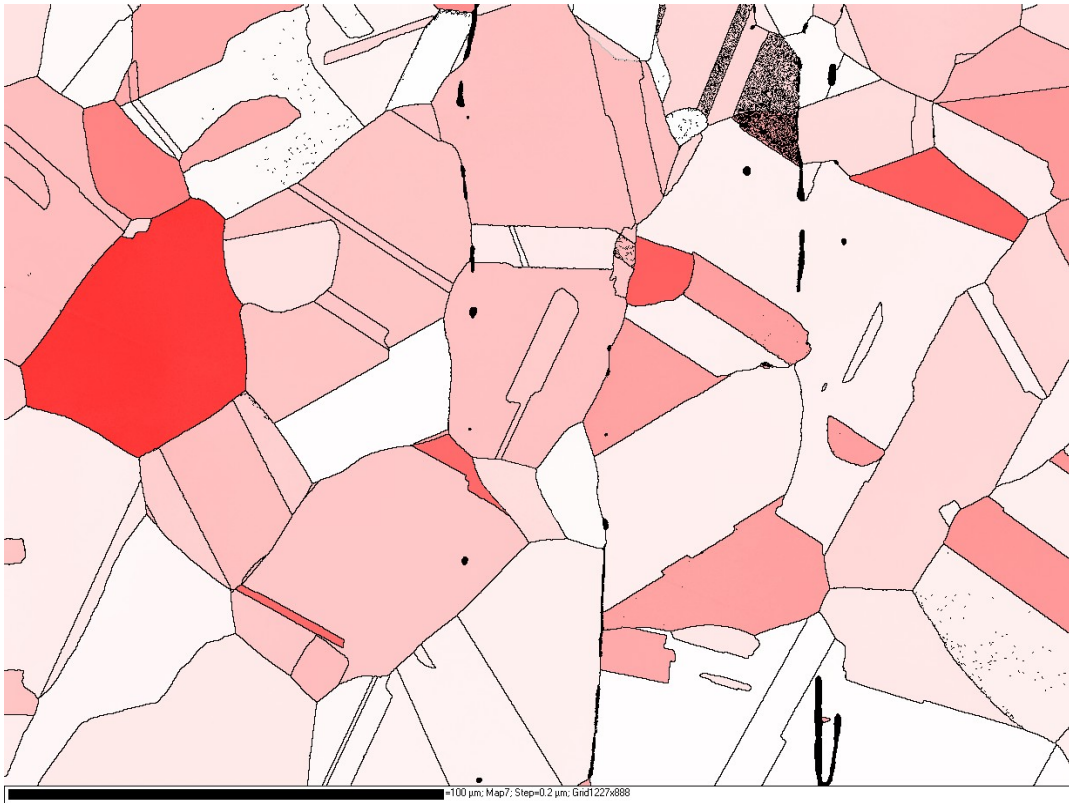
$100 \mu m$

Schmid Factor .... Iron fcc [99%]

(a)

$100 \mu m$

(b)
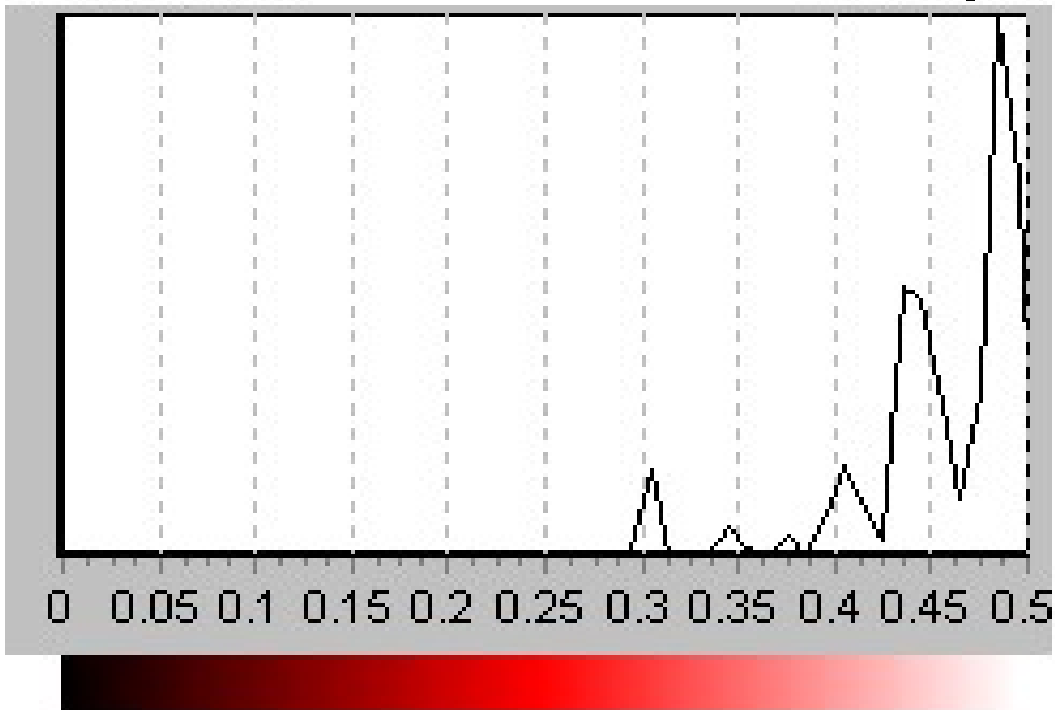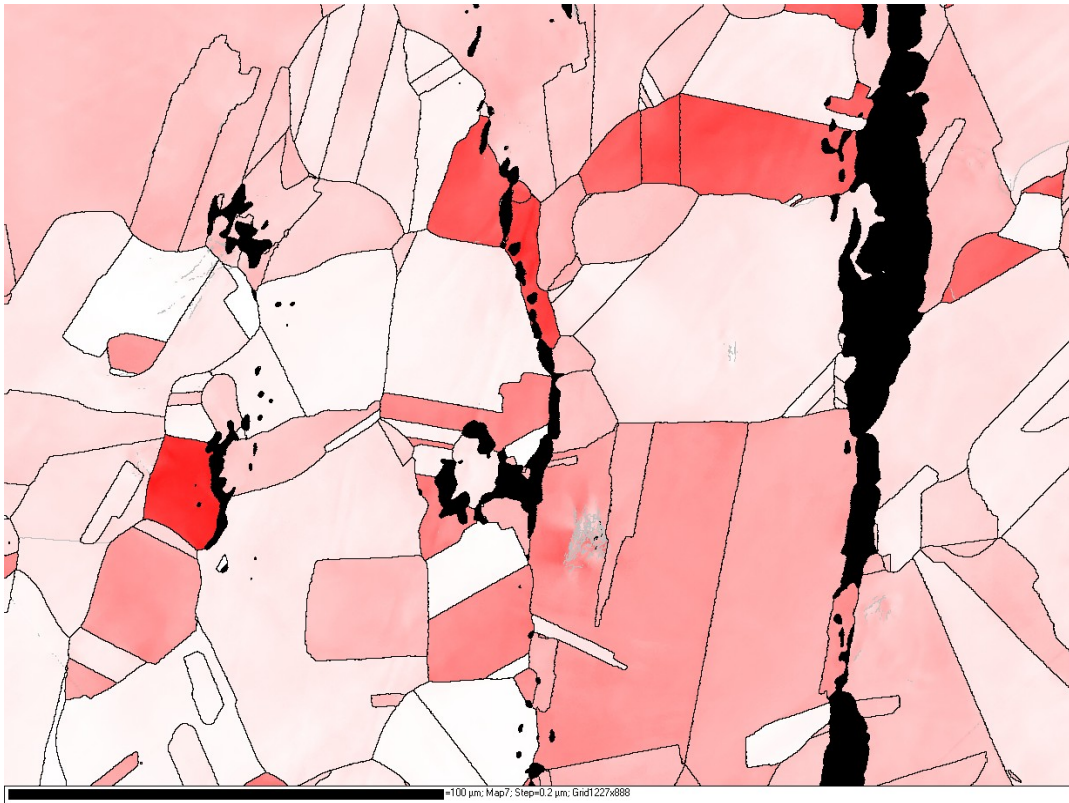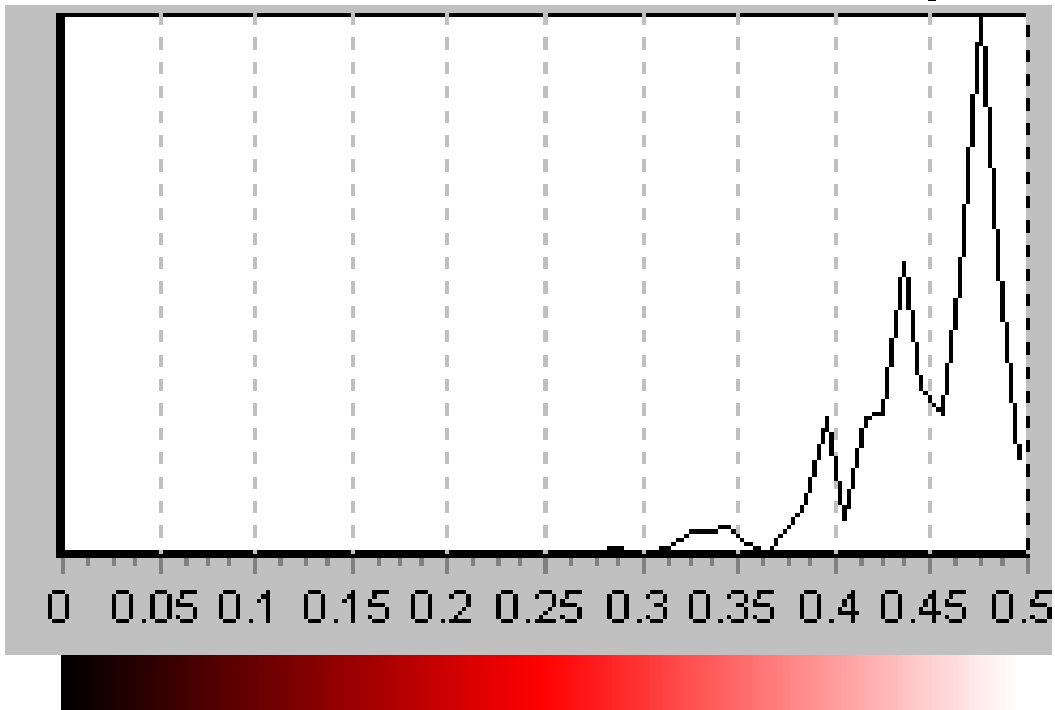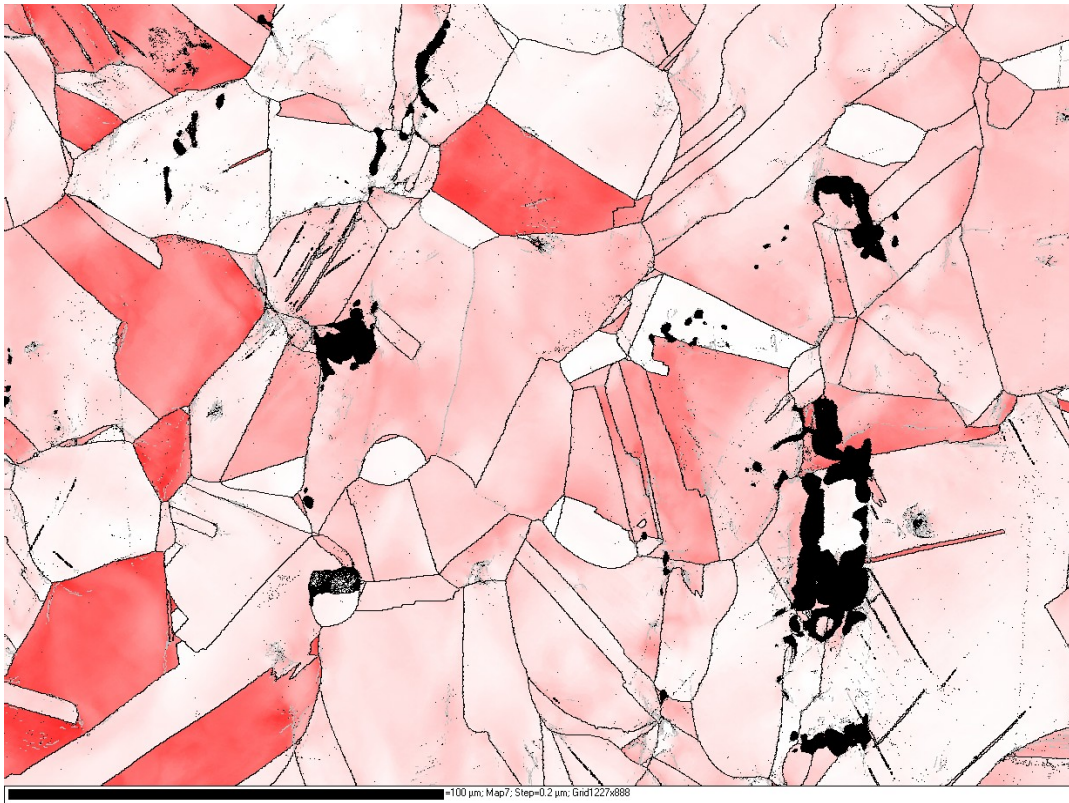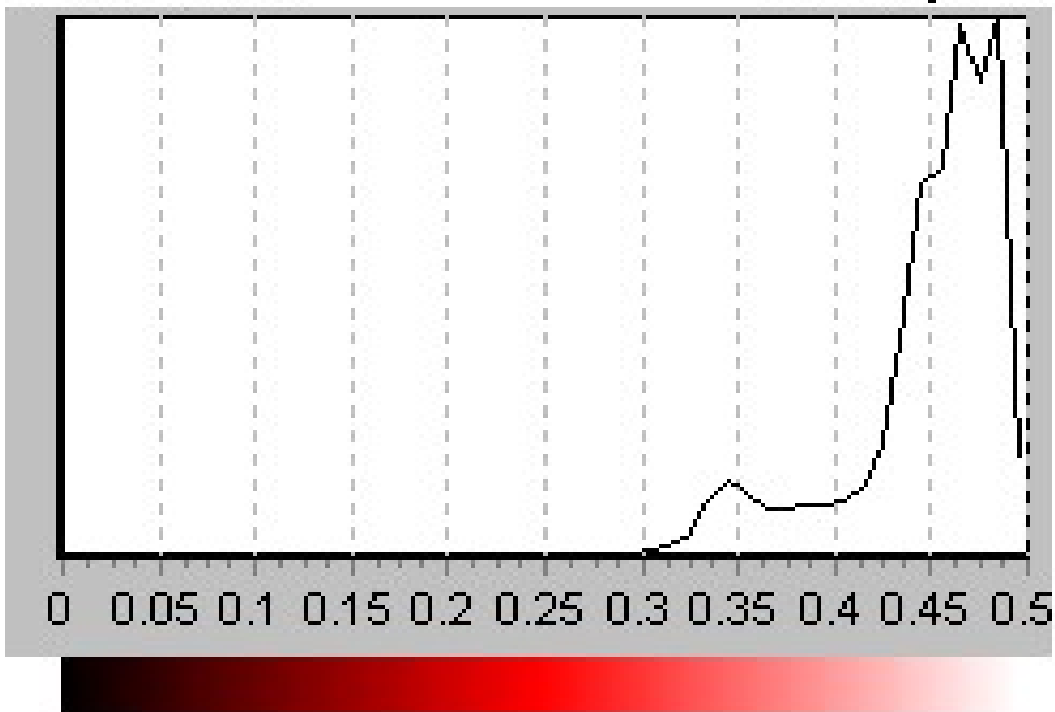
$100\mu m$

(c)
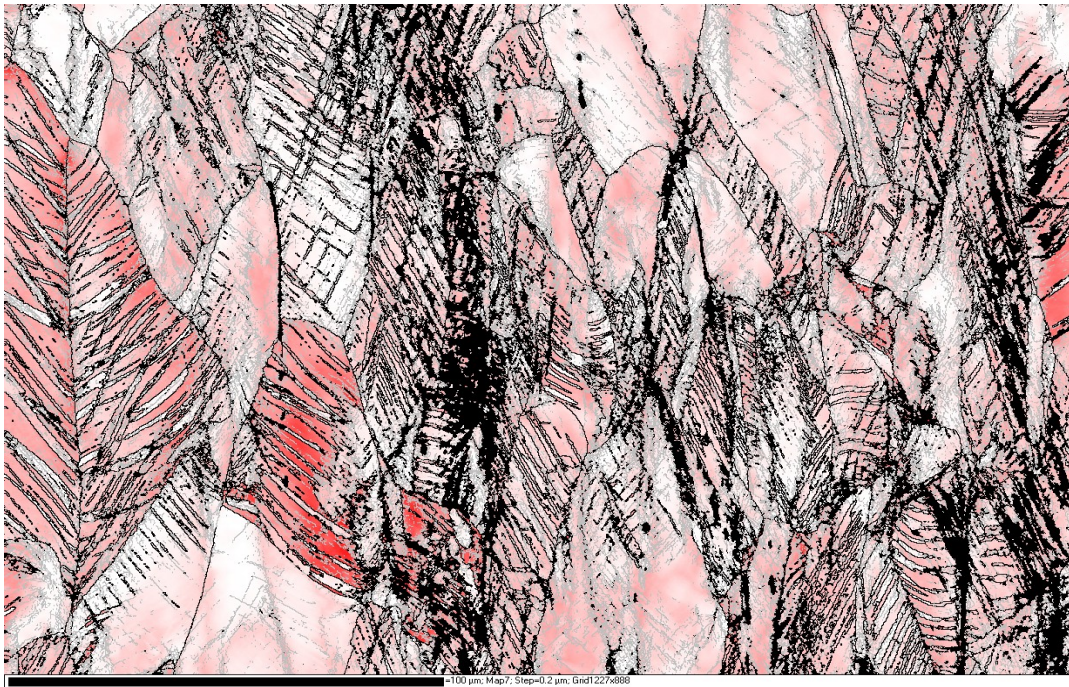
$100\mu m$
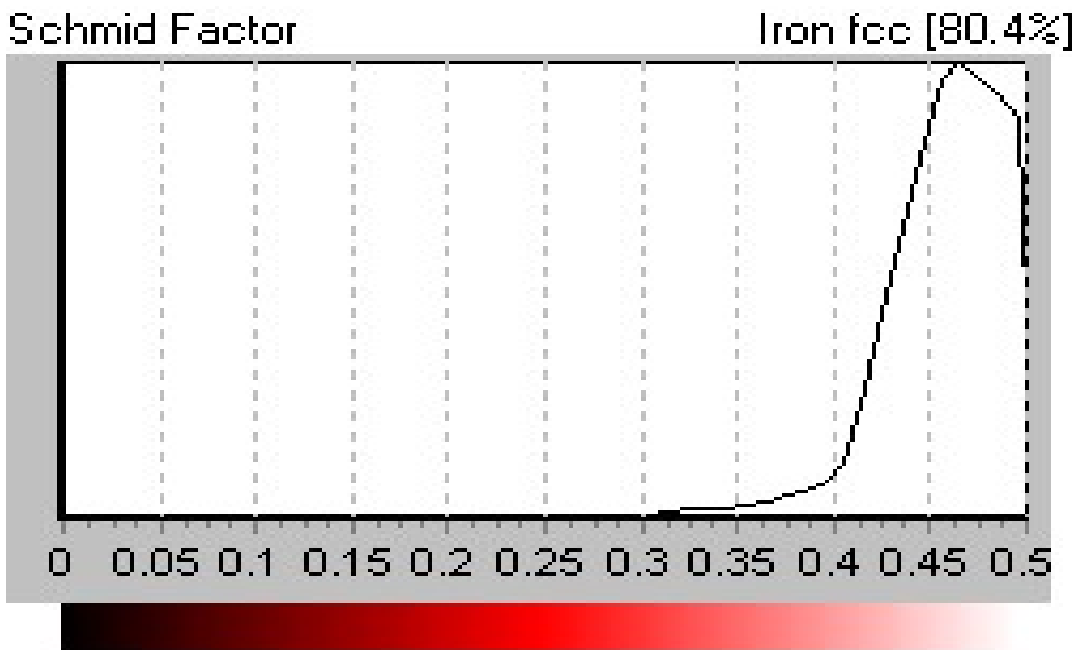
(d)

Figure 8-5   Electron backscattered diffraction (EBSD) patterns incorporating with Schmidt factor for materials tested at room temperature: (a) undeformed, (b) interrupted at low strain level, (c) interrupted at intermediate strain level and (d) strained to uniform elongation; the left two columns indicate the major differences in the amount of twinning and the distribution of Schmidt factors and the right column shows the planar slip band formation for grains with high Schmidt factor.

$100\mu m$

Schmid Factor   Iron fcc [80.4%]

0   0.05 0.1 0.15 0.2 0.25 0.3 0.35 0.4 0.45 0.5

(e)

$100\mu m$

Schmid Factor   Iron fcc [97.5%]

| 0 | 0.05 | 0.1 | 0.15 | 0.2 | 0.25 | 0.3 | 0.35 | 0.4 | 0.45 | 0.5 |

(f)
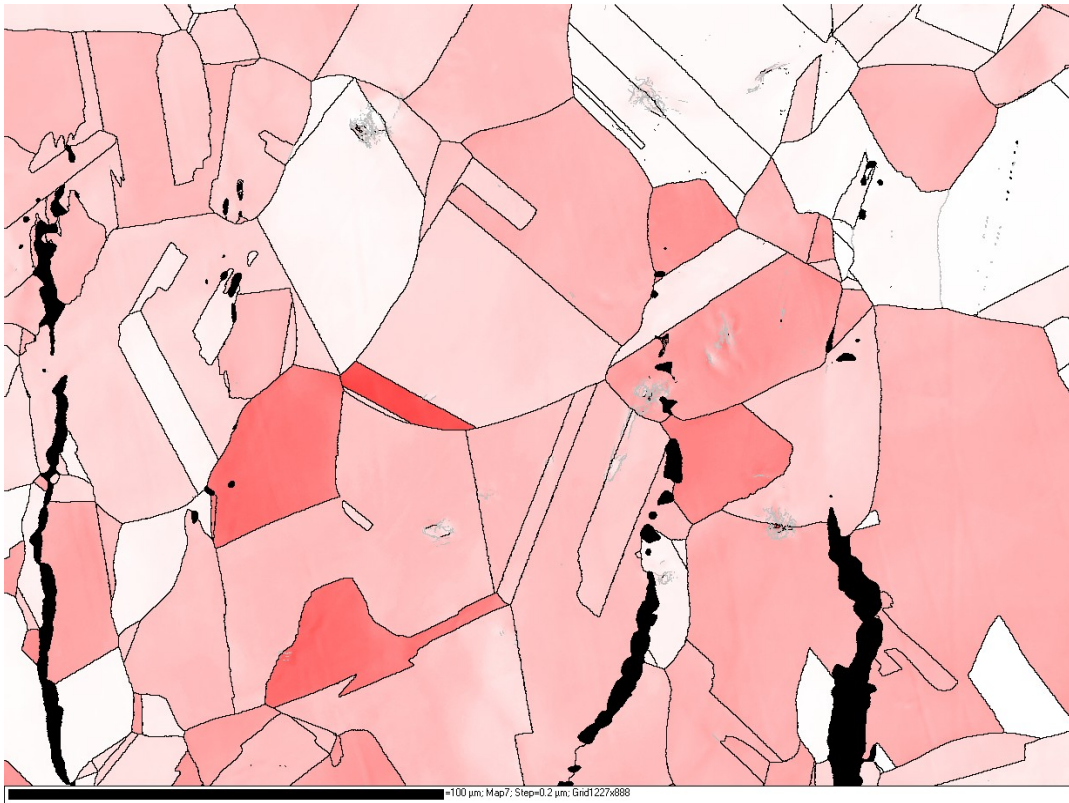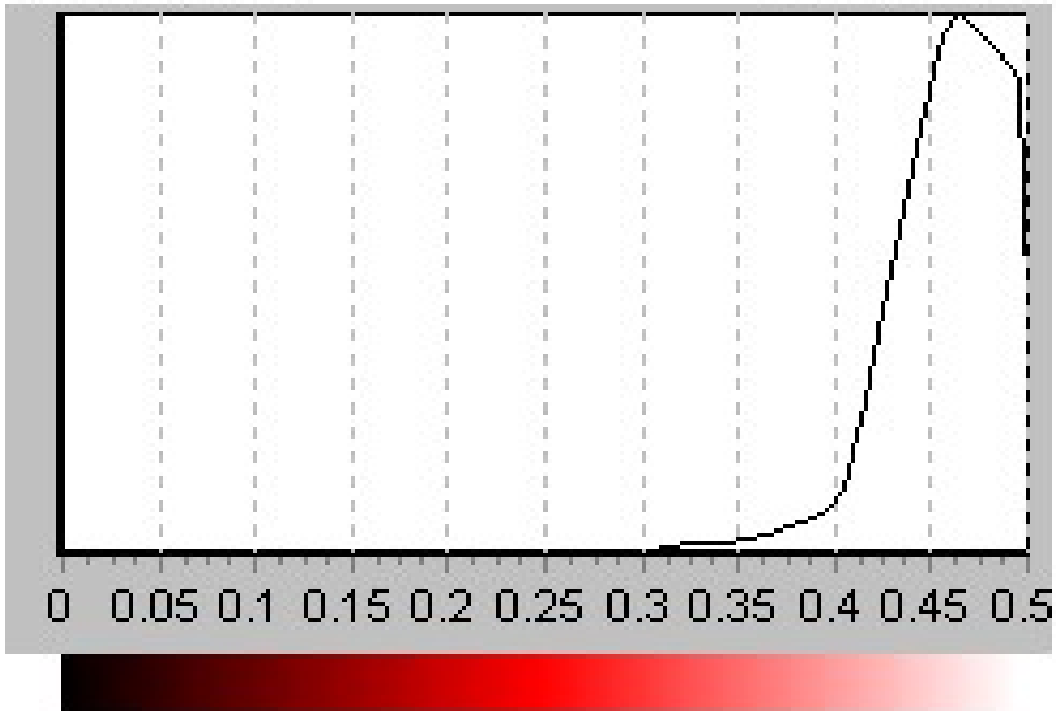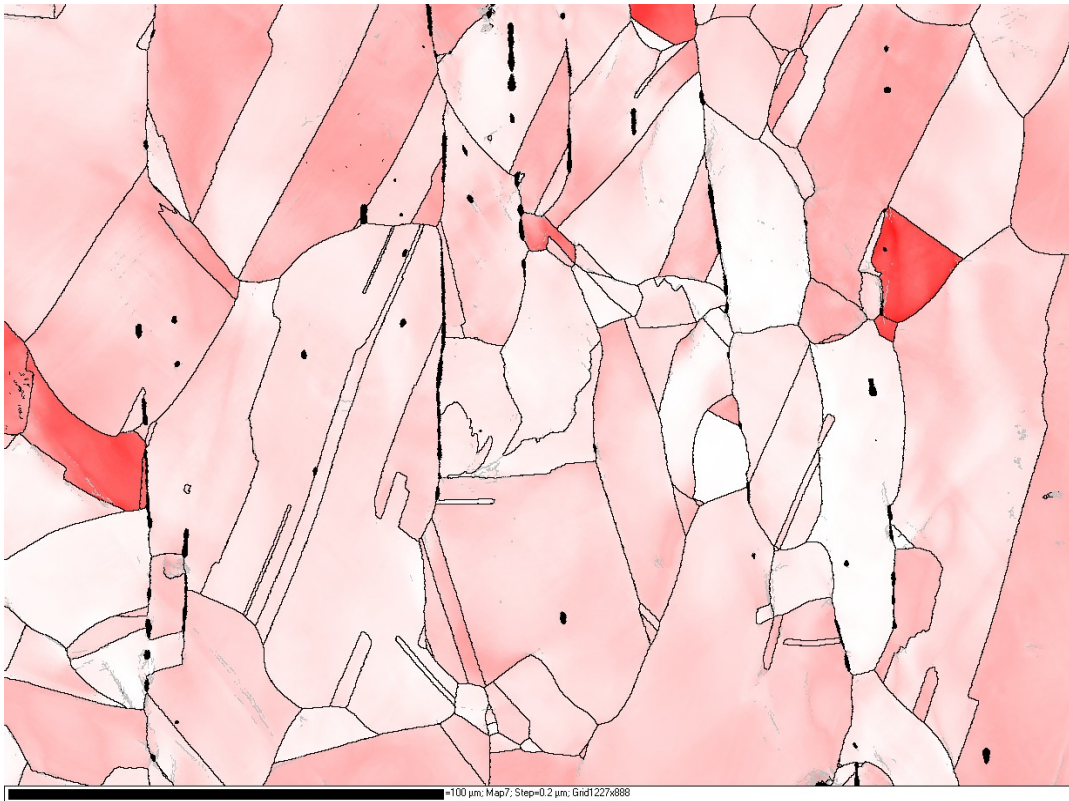
Schmid Factor   Iron fcc [99.3%]
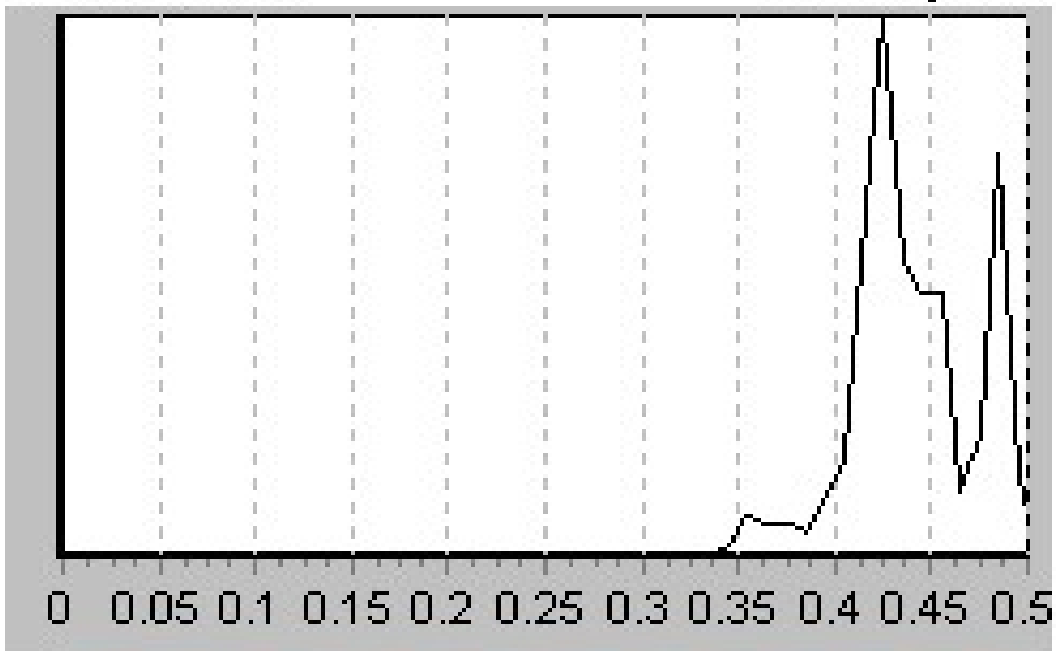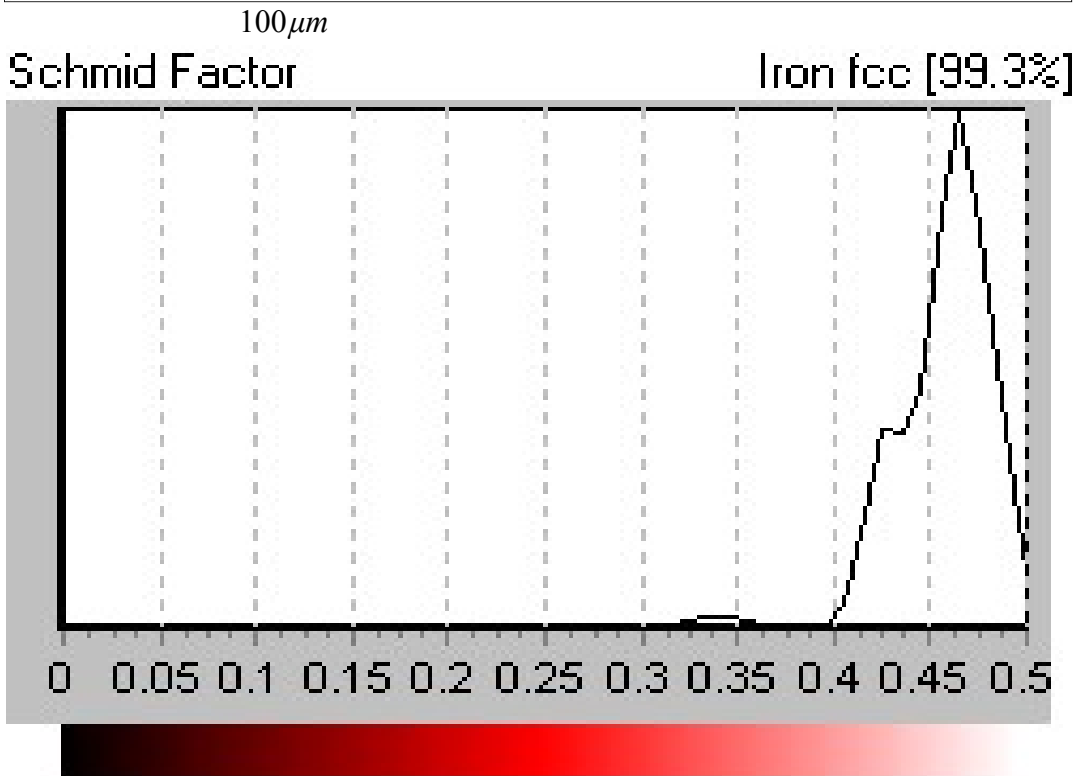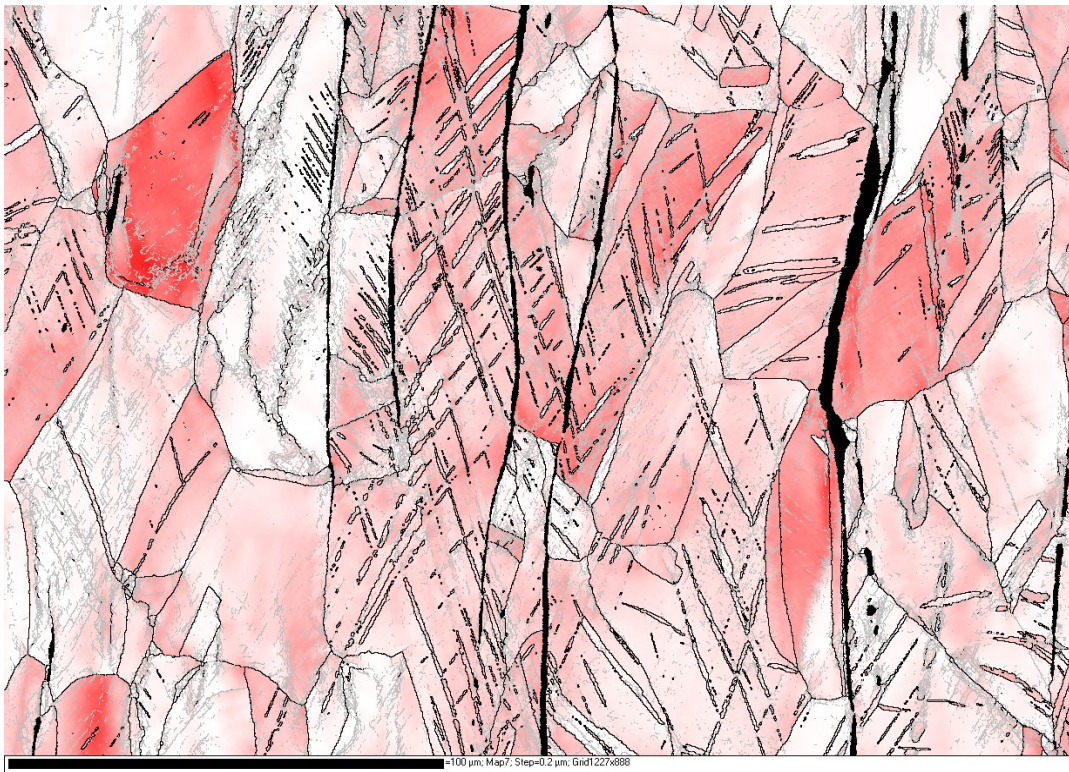
(g)

Figure 8-6 Electron backscattered diffraction (EBSD) patterns incorporating with Schmidt factor for materials tested at 100°C: (e) interrupted at low strain level, (f) interrupted at intermediate strain level and (g) strained to uniform elongation

$100\mu m$

Schmid Factor   Iron fcc [99.2%]

| 0 | 0.05 | 0.1 | 0.15 | 0.2 | 0.25 | 0.3 | 0.35 | 0.4 | 0.45 | 0.5 |

(h)

$100 \mu m$

Schmid Factor   Iron fcc [99.2%]

0   0.05 0.1 0.15 0.2 0.25 0.3 0.35 0.4 0.45 0.5
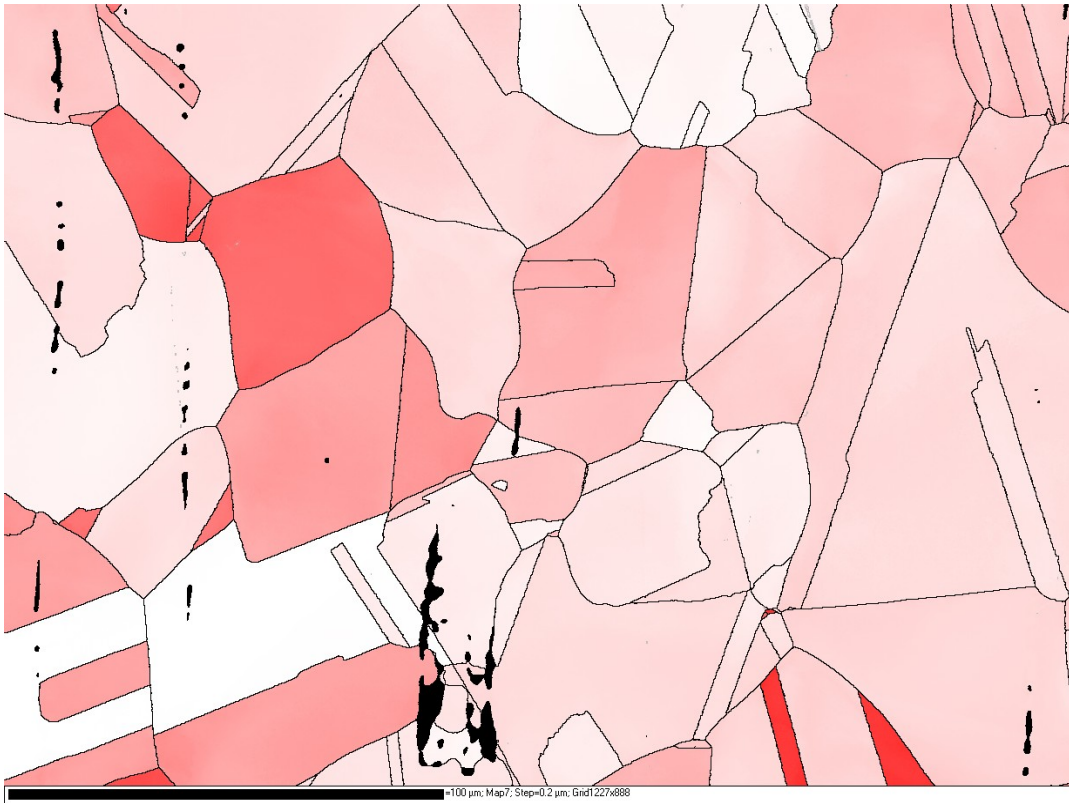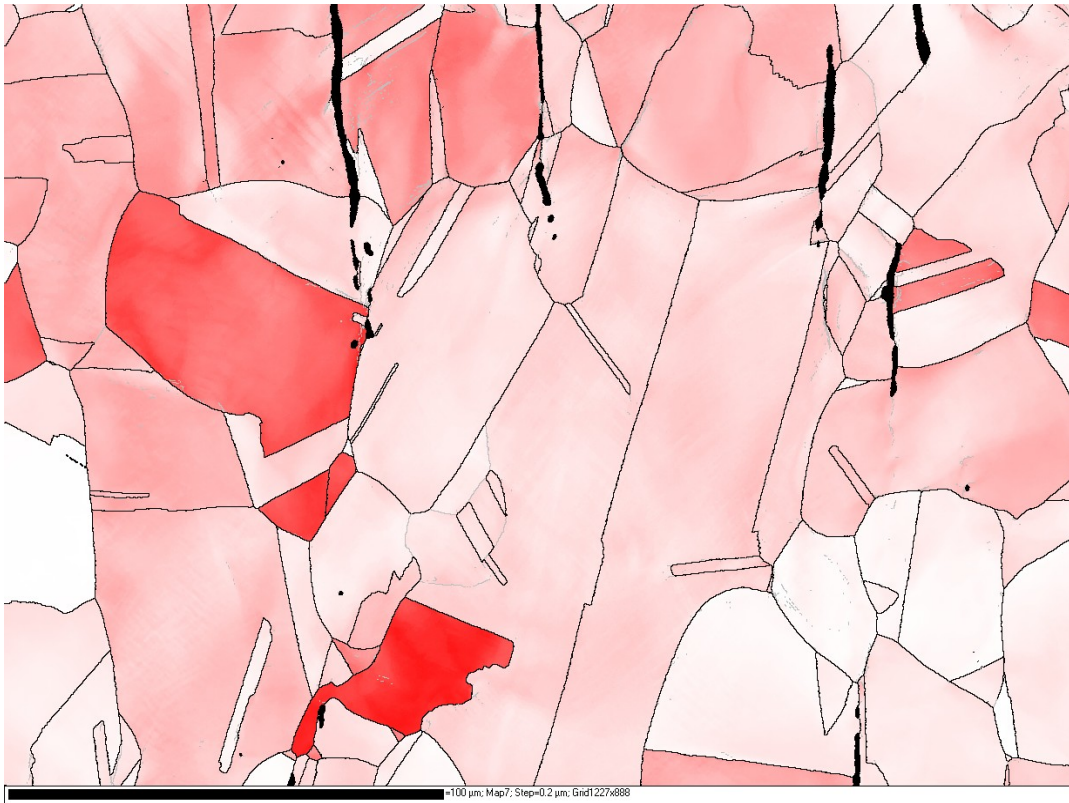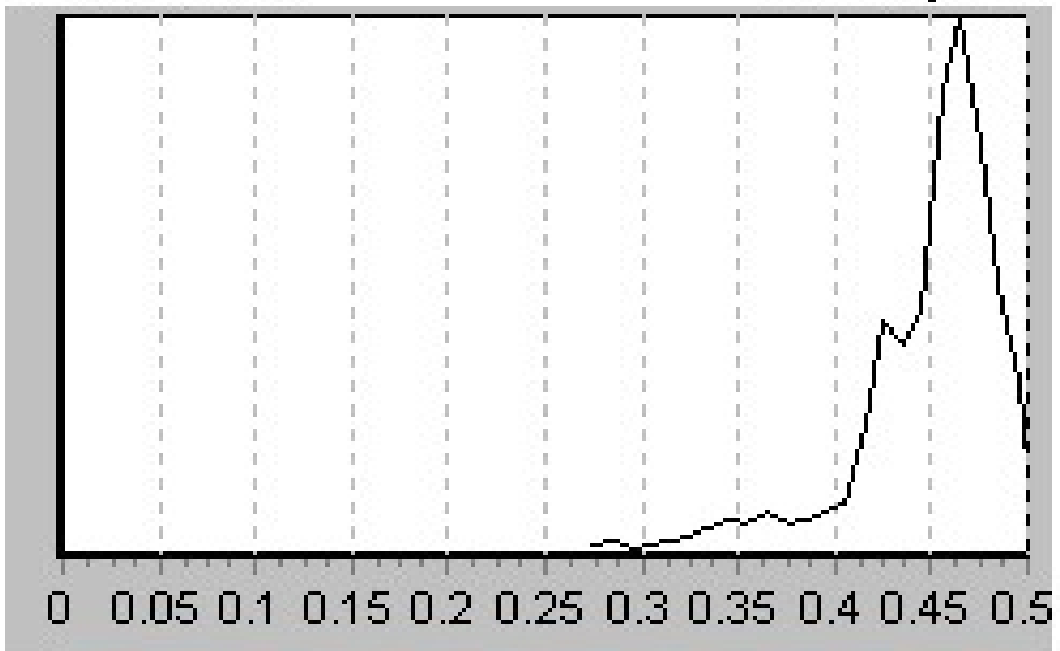
(i)
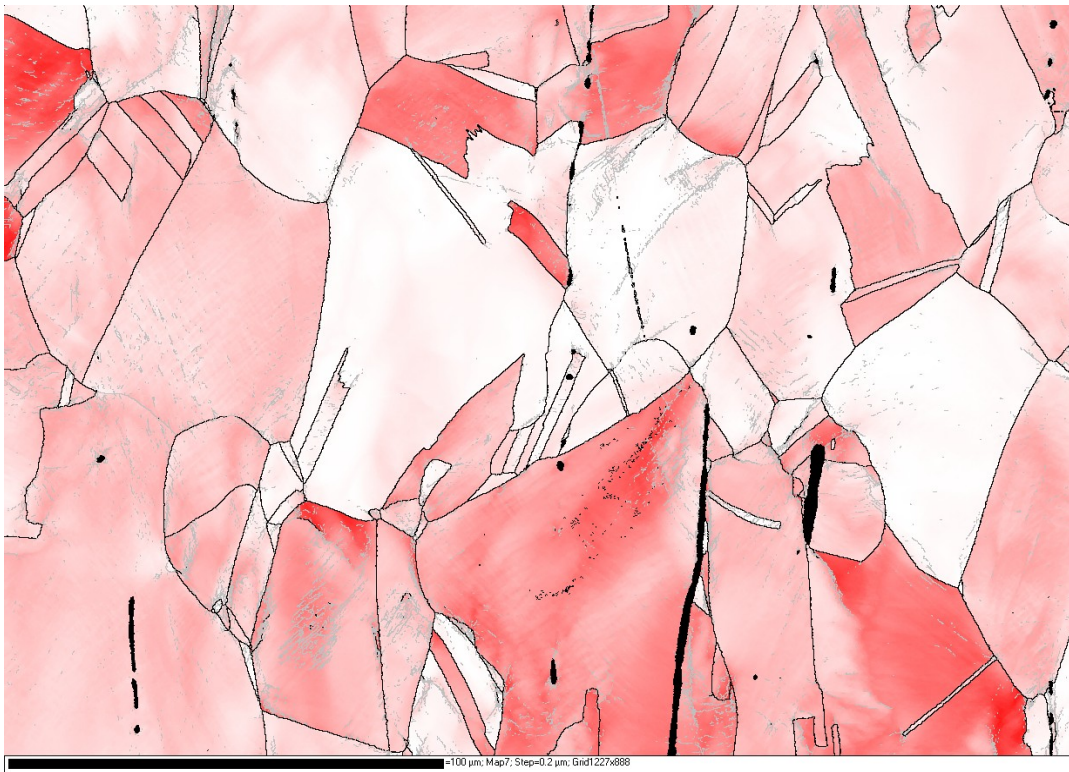
$100\mu m$

Schmid Factor　　　　　　　　　Iron fcc [99.3%]
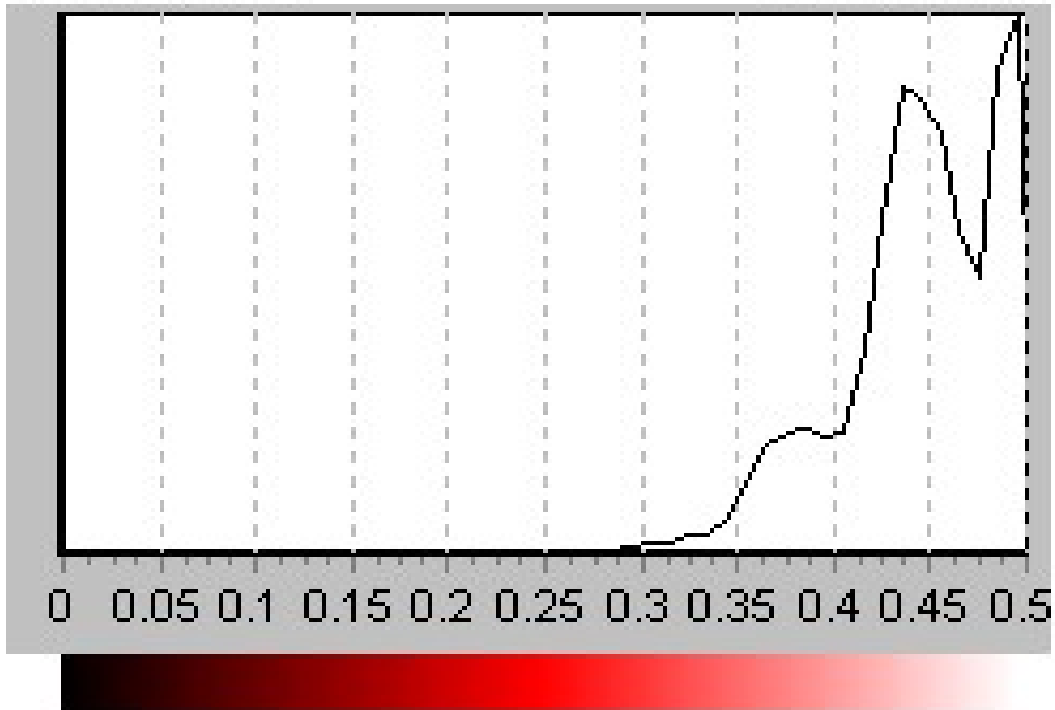
(j)

Figure 8-7 Electron backscattered diffraction (EBSD) patterns incorporating with Schmidt factor for materials tested at 200°C: (h) interrupted at low strain level, (i) interrupted at intermediate strain level and (j) strained to uniform elongation.
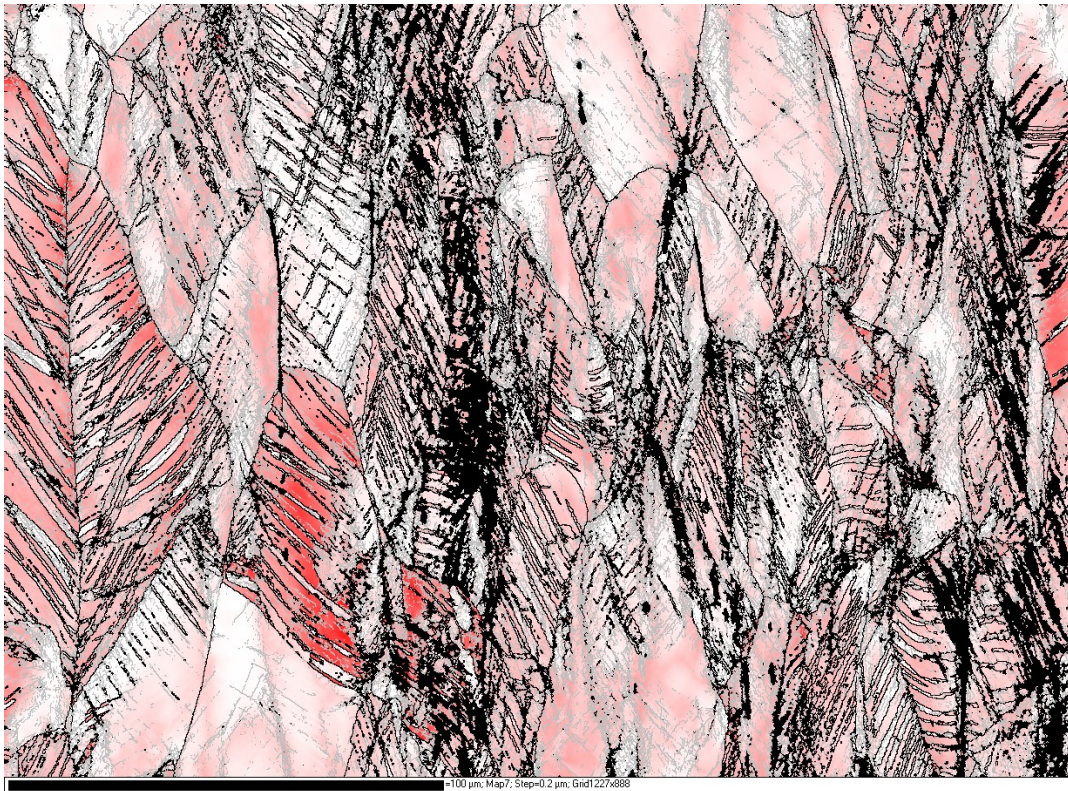
(a)
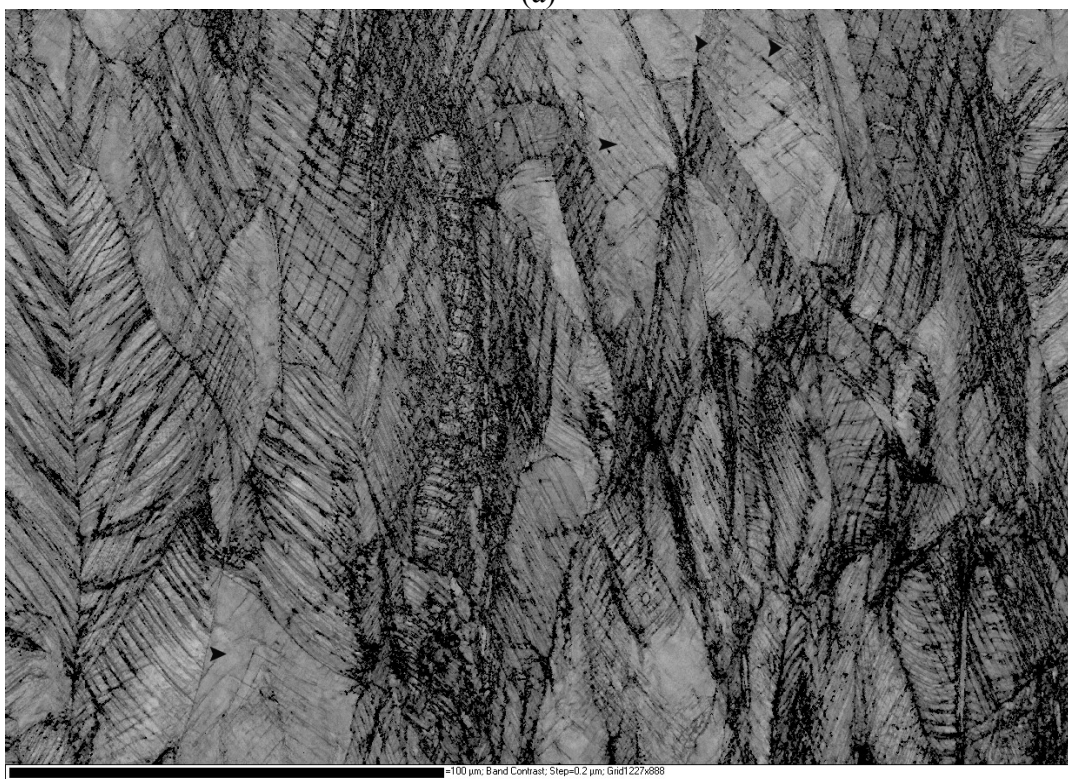
(b)

Figure 8-8 The slip bands are shown in the grains with Schmidt factor larger than 0.485 in (b); the grain by grain Schmidt factor value can be evaluated from (a)

The EBSD orientation and misorientation maps indicate the importance of notch depth, shape and plastic deformation to mechanical properties degradation and notch strengthening for unirradiated 316L stainless steel at room temperature. In recent years, finite element simulation has been extensively employed to analyze tensile response during uniaxial loading. In this study, a commercial finite element code, ABAQUS, was employed to analyze the stress distribution around the notch tip. The mesh is refined in the vicinity of notch tip so that the size of each element is nearly equivalent to the grain size. The simulations were interrupted at the onset of necking to compare with the experimental results. Two additional simulations were interrupted at the initiation of fracture. Gurson's model [98-100] with Tvergaard's modification [101, 102] was employed to simulate void nucleation, growth and coalescence. The simulated engineering stress-strain curves for unirradiated 316L stainless steel are shown in Figure 6-1. The predicted tensile responses are similar to experimental results. The ABAQUS simulation of the specimen without a notch shows a high degree of accuracy. The major differences seen in the experimental versus simulated deformation behavior in the notched specimens may result from the machining and from more localized plastic flow mechanisms which are not directly captured in the FEM approach. Nevertheless, the simulation is in good agreement with the general behavior of tensile responses for unirradiated, notched specimens, and should be a reasonably good prediction of the tensile performance for irradiated, notched specimens.

Deformation and fracture have been a long term concern for nuclear materials. Reactor component structure materials may experience stress corrosion cracking. The fracture may occur after the co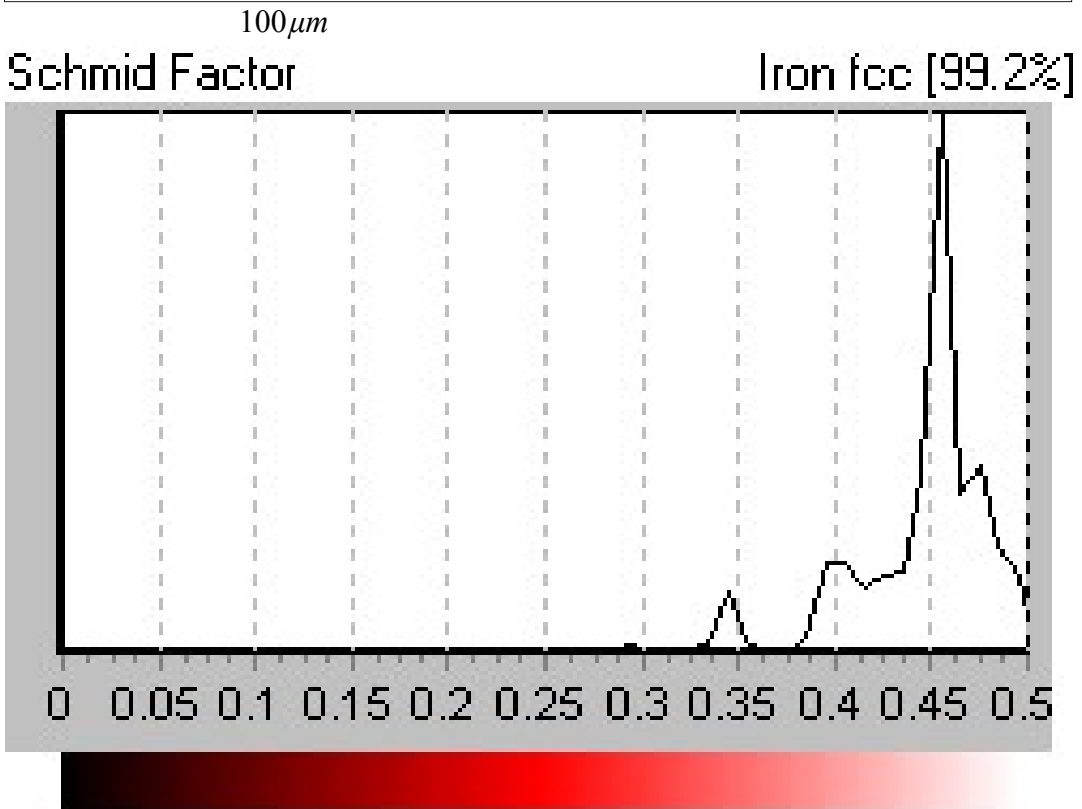mponent suffers the cracks and notches. It will be valuable to simulate the deformation process from tensile to sharp notch specimen. Three geometries are designed as: tensile specimen with a tiny imperfection to induce necking, which is required by ABAQUS, specimen with

semi-circular notch and specimen with sharp V notch. The ratio of depth-to-width is the same as 0.125. Figure 8-9 shows the finite element analysis for specimen tensile loaded to yielding point. For the tensile specimen, the whole specimen is uniformly yielded. However, for the specimens with notches, the notch strengthening is clearly evident. The elements in the vicinity of notch tip are yielded while the materials in other areas are still un-yielded which is indicated as black. The notch strengthening effect is more pronounced in the V-notched specimen, the yielding zone is even smaller than that of C-notched specimen. The fracture pattern evolution is shown in Figure 8-10. The small color difference indicates the load drop initiating the fracture process. For the tensile and C-notched specimens as shown in Figures 8-10a and 8-10b, the fracture pattern still remains ductile fracture mode. The fracture initiates from the inner of the specimen and form the cup-cone fracture structure. However, for the V-notched specimen, the fracture initiates from the notch tip. The difference in the fracture initiation location could be explained by the notch strengthening. The notch strengthening effect is more pronounced in the sharp V-notched specimen, which causes a ductile-to-brittle fracture mode transition. Figure 8-11 shows the finite element analysis for the specimens near final fracture. It is evident that the cup-cone pattern formed in the tensile and C-notched specimen.

Tensile data for irradiated 316 stainless steel tested at 50°C are used to perform finite element simulation and predict the tensile response of irradiated materials. The material was irradiated to 8.8 dpa in the spallation neutron source of Los Alamos national laboratory. Figure 8-12 shows the stress contour for the specimens loaded to the yielding point. The tensile specimen was deformed uniformly. The small variance in the stress is due to the tiny imperfection and could be ignored. Notch strengthening is still clearly evident in the irradiated notched specimen. Comparing to the unirradiated materials, the yielding zone at the notch tip is even smaller. Figure 8-13 shows the

fracture initiation location for the irradiation materials. No plastic blunting could be observed in the V-notched specimen and the fracture mode is transited from ductile to brittle. The near final fracture stress analysis for three geometries are shown in Figure 8-14. It is noteworthy to point out that the final hardening process for unirradiated and irradiated tensile specimens are nearly the same.
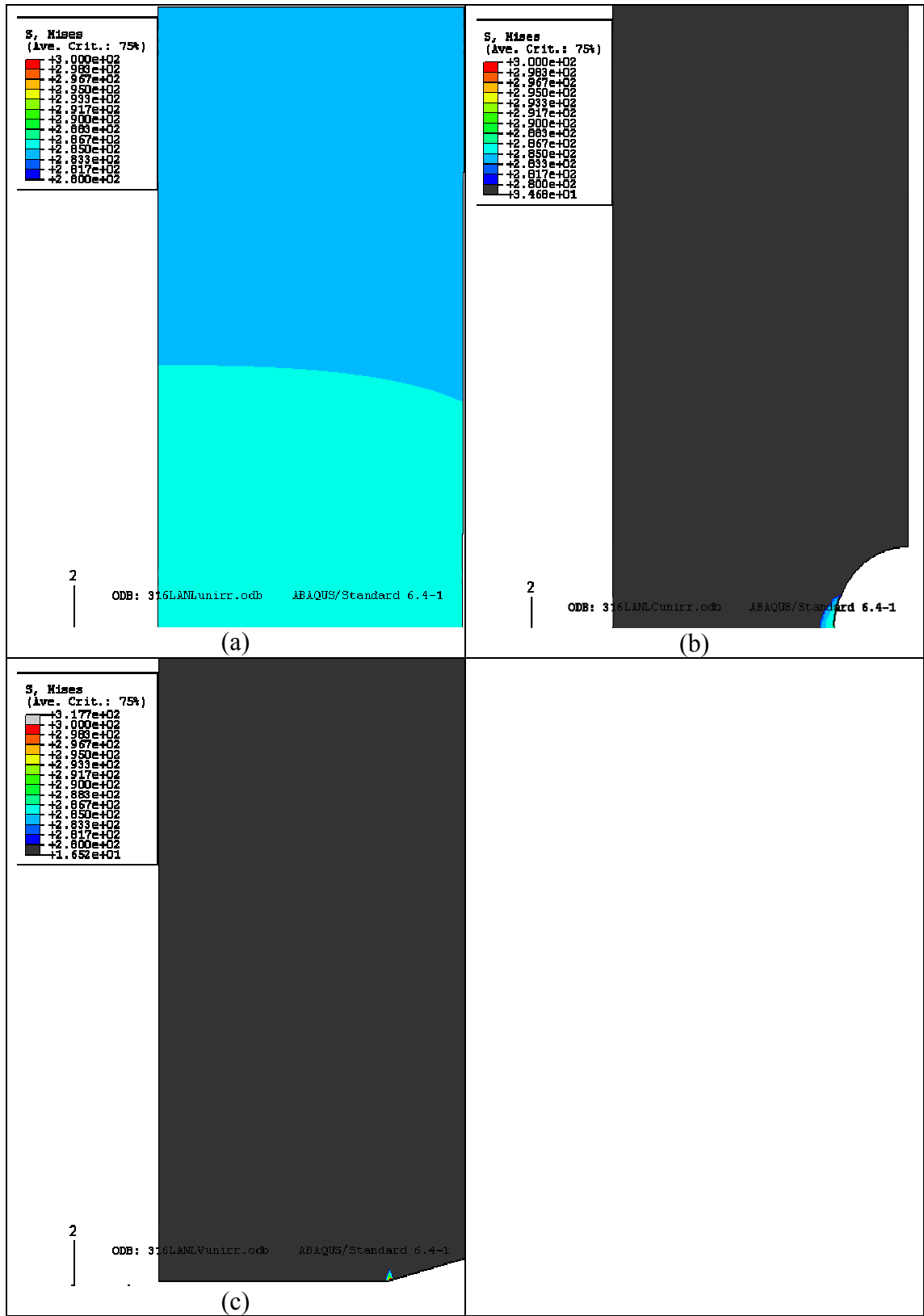
Figure 8-9 Finite element analysis for unirradiated 316L stainless steel tested at 50°C and interrupted at yield point with different geometries: (a) tensile, (b) C-Notch and (c) V-Notch
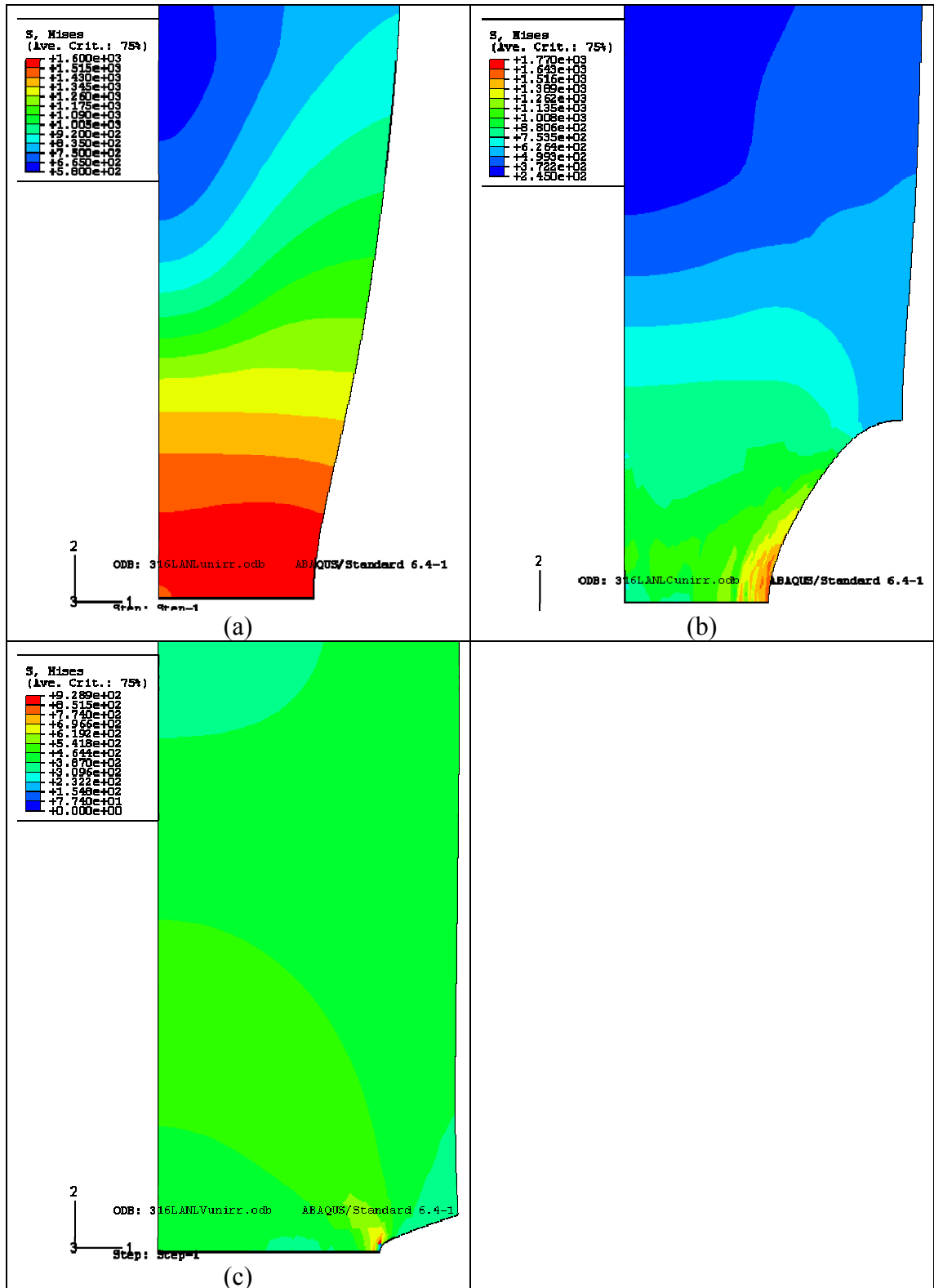
Figure 8-10 Finite element analysis for unirradiated 316L stainless steel tested at 50°C and interrupted at fracture initiation point with different geometries: (a) tensile, (b) C-Notch and (c) V-Notch
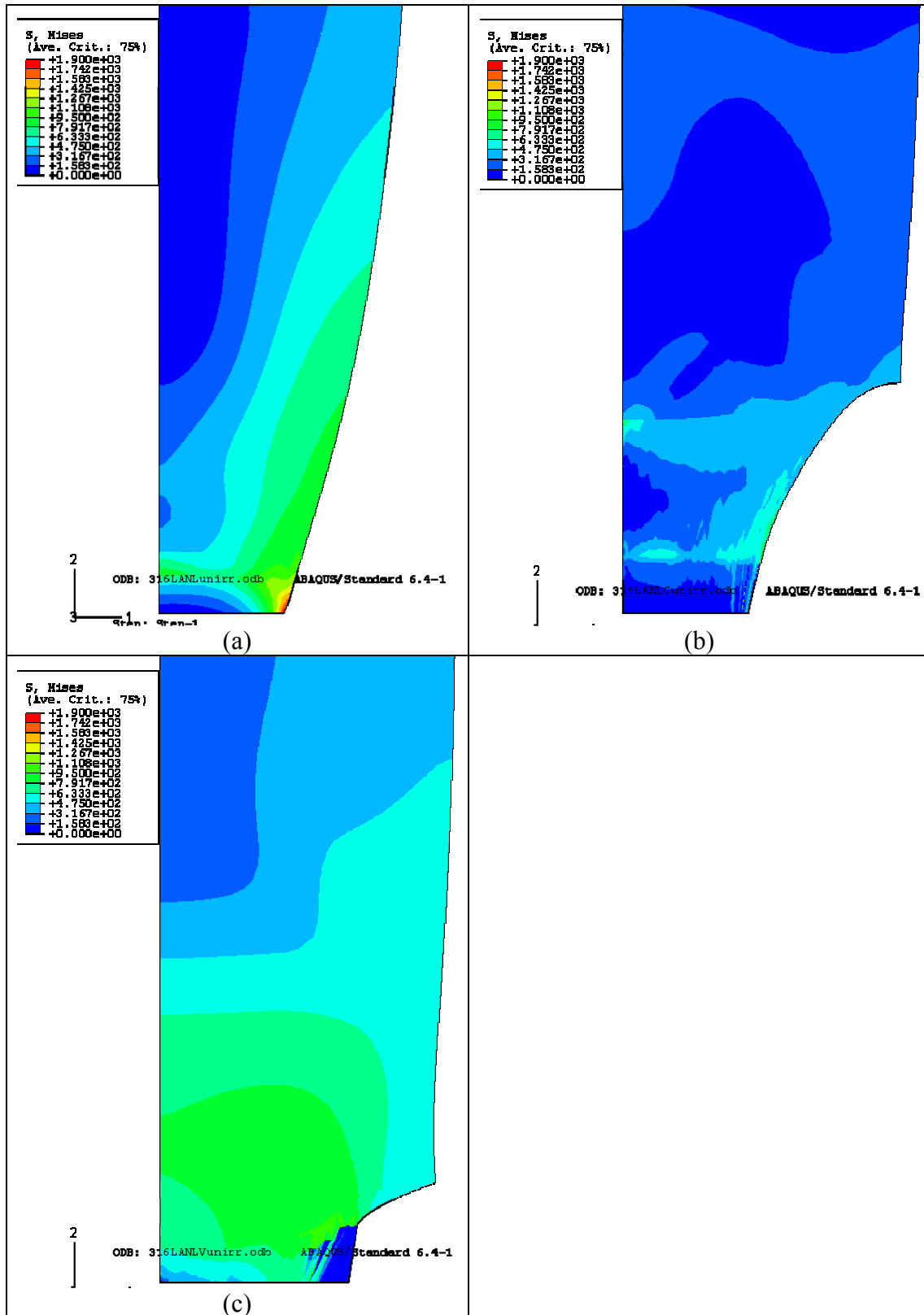
Figure 8-11 Finite element analysis for unirradiated 316L stainless steel tested at 50°C and interrupted at fracture point with different geometries: (a) tensile, (b) C-Notch and (c) V-Notch
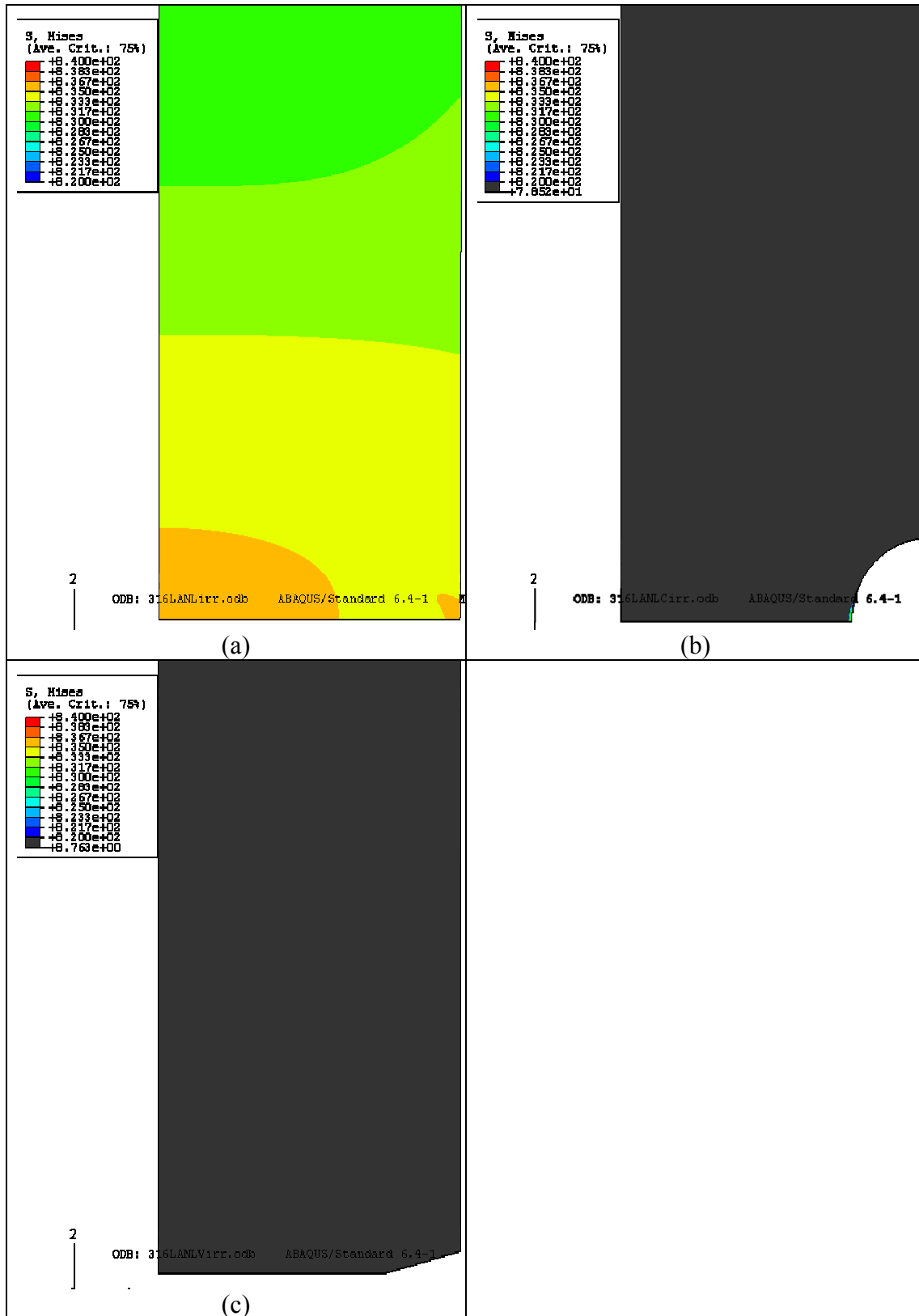
Figure 8-12 Finite element analysis for irradiated (8.8dpa) 316L stainless steel tested at 50°C and interrupted at yield point with different geometries: (a) tensile, (b) C-Notch and (c) V-Notch
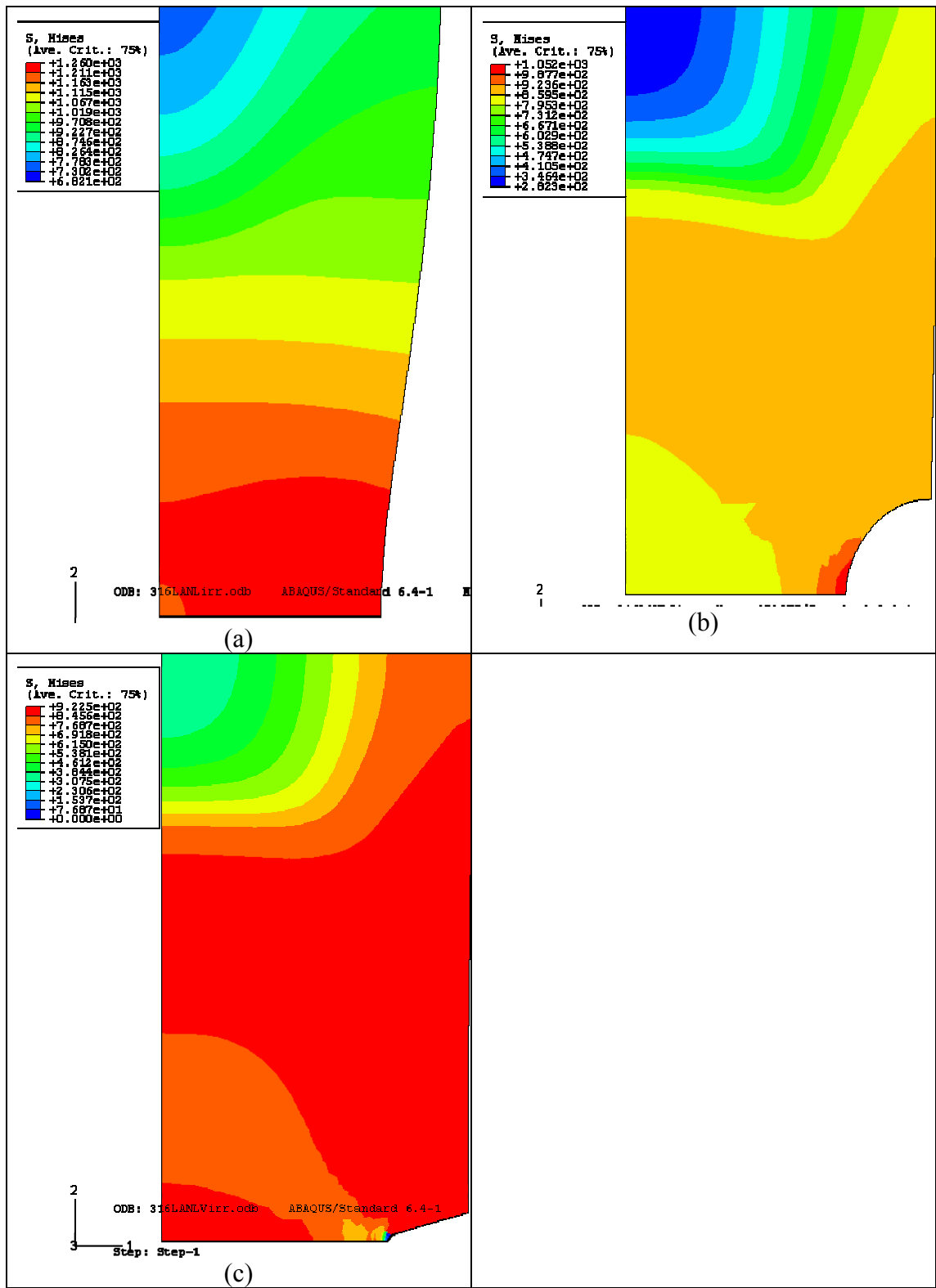
Figure 8-13 Finite element analysis for irradiated (8.8dpa) 316L stainless steel tested at 50°C and interrupted at fracture initiation point with different geometries: (a) tensile, (b) C-Notch and (c) V-Notch
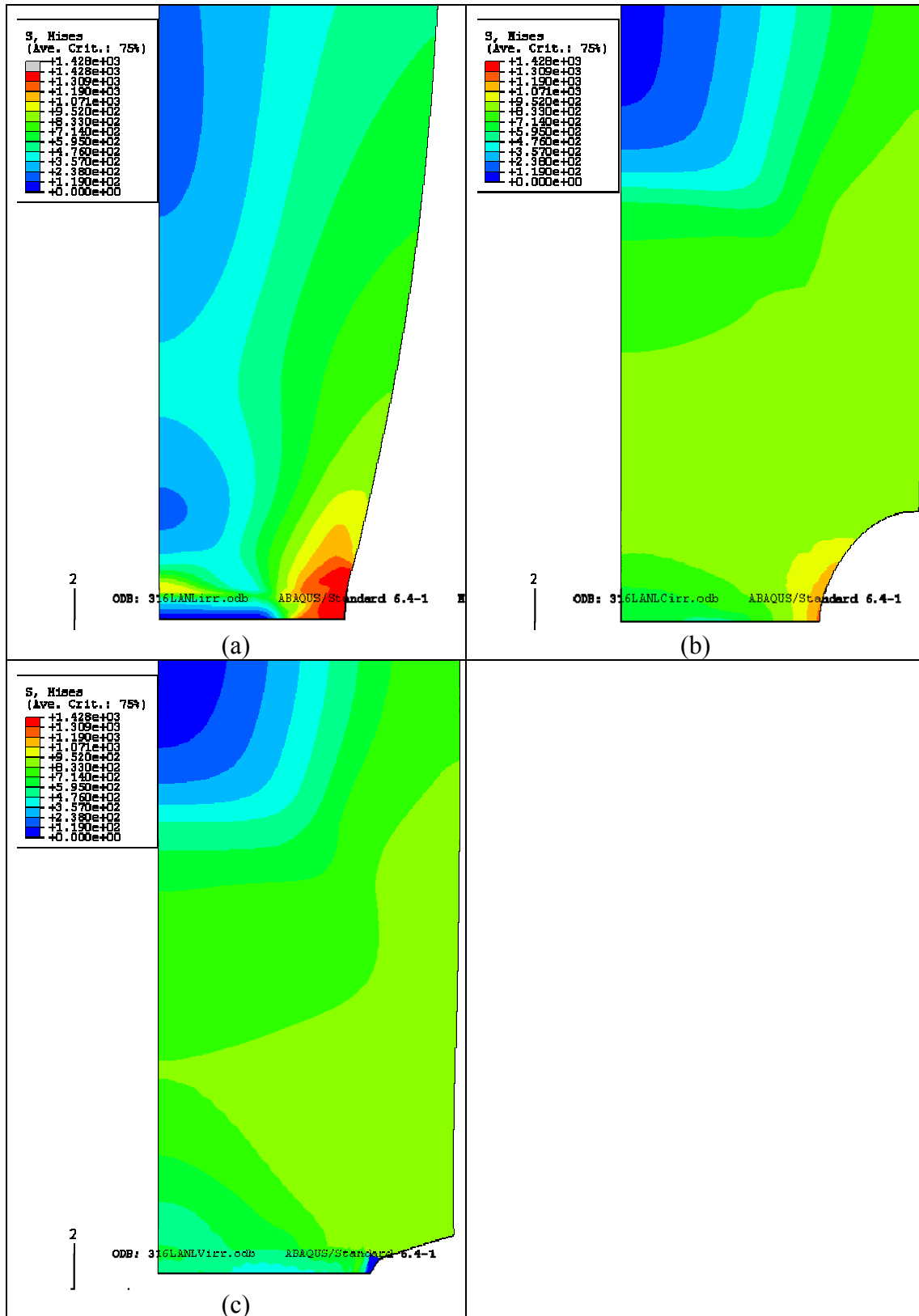
Figure 8-14 Finite element analysis for irradiated (8.8dpa) 316L stainless steel tested at 50°C and interrupted at fracture point with different geometries: (a) tensile, (b) C-Notch and (c) V-Notch

A direct comparison between the FEM and EBSD results are made in Figure 9-15 for the shallow V notch specimen. The deformation pattern observed from EBSD follows the general pattern found in the FEM simulations. This can be verified by comparing the extent and shape of the twinning surrounding the notch tip. The extent of the twinning zone conforms to the critical local stress for the initiation of twinning, about 500-550 MPa. The kidney strain distribution patter is evident from both the EBSD results and from the FEM calculations. Some distortions in the notch tip shape are a consequence of the 70° tilting angle necessary to perform the EBSD analysis.
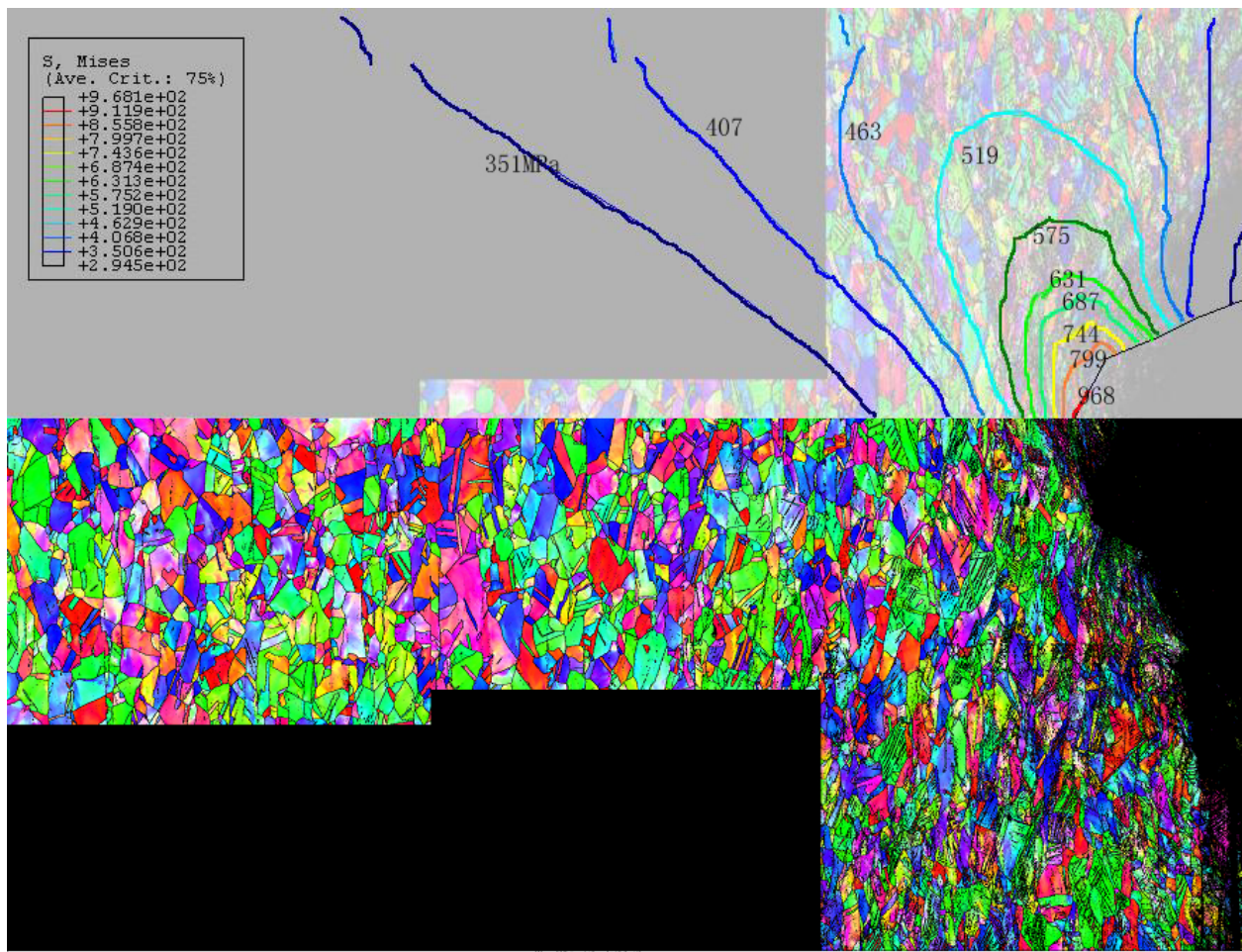
Figure 8-15 Superposition of EBSD orientation map and stress contour lines for V-Notch-S.

CHAPTER 8   CONCLUSION

Analysis of the tensile response of selected series of unirradiated and irradiated type 316 stainless steel tests was carried out to establish their tendency for plastic instability and flow localization. The interrupted tensile tests and microstructure evolution of selected series of unirradiated and irradiated type 316L austenitic stainless steel tested at different temperatures from room temperature to 400°C was carried out to establish the concept of critical stress and its temperature dependence, critical twinning stress for plastic instability and identify the controlling mechanism of flow localization. The notch strengthening and flow localization analysis were carried out by finite element methods. The following conclusions could be drawn:

1. Unirradiated and irradiated type 316L austenitic stainless steels experience flow localization, or extreme loss of ductility, when the irradiation-induced hardening increases the yield strength to the level of the critical stress; the critical stress level is a material inherent property and not sensitive to external irradiation environment;

2. The capacity of strain hardening after yielding is determined by the difference between critical stress and yield strength; and this capacity is highly dose and temperature dependent;

3. The 316L stainless steel strain hardening process is controlled by dislocation-induced hardening mechanisms and, to some extent, by mechanic twinning at low temperatures and planar slip at high temperature; the extent of twinning is highly dependent on test temperature and it causes the temperature dependence of flow localization;

4. There exists a phase transform from FCC to BCC during the plastic deformation of materials; It largely applies to the necking process;

5. Brass and Goss type textures are believed to be the typical face centered cubic materials texture by twinning induced orientation transformation;

6. The ability of the material to twin depends on a critical twinning stress for the activation of deformation which is directly proportional to stacking fault energy which also has a strong positive temperature and compositional dependence; The interrupted tests show that only after the critical twinning stress is overcame, the twinning system can be activated;

7. Schmidt factor plays an important role in the activation of twinning process and in the competing mechanism of twinning and slip. In cases here, some plastic, dislocation-based deformation occurs prior to the onset of twinning, also consistent with the need to reach a critical stress to activate twinning.

8. The strong temperature dependence of the stress to activate twinning in 316L austenitic stainless steel means that it is not possible to induce twinning during plastic deformation at temperatures above about 100°C; in this case, the planar slip dominates the plastic deformation process. This limits plastic deformation to lower levels of uniform elongation of this material above that temperature.

9. For conditions where irradiation-induced hardening occurs, the limitation in ductility is due to the convergence of the elevated yield strength and the critical stress for plastic instability. This explains the minimum ductility in the temperature range of 200 to 400°C for irradiated 316L stainless steel.

10. The notch depth was found to play an important role in the mechanical response in both unirradiated and irradiated materials. Deep notches degrade the mechanical properties of the material significantly due to their greater ability to localize the stress concentration.

The variation in the notch depth and shape has a strong impact on the sizes of the plastic deformation and twinning zone.

11. For shallow notches or notches with lower stress concentration factors, the large plastic deformation area and severe tip blunting enhances strain hardening capacity

12. A fracture mode transition from ductile fracture to brittle fracture was identified after the material has been exposed to an irradiative environment. In irradiated materials, the combination of high yield strength and highly localized stress concentrations at notches provide conditions that lead to brittle fracture.

13. The fracture initiates from the inner specimen for tensile and C-notched specimens while from the notch tip for sharp V-notched specimen;

14. The final strain hardening process is the same for both the unirradiated and irradiated materials.

PUBLICATIONS

- **Peer-reviewed journal articles**

  - Papers published and accepted
  1. Xiao Pan, Xianglin Wu, Meimei Li and James F. Stubbins, "Modeling Tensile Response and Flow Localization Effects in Selected Copper Alloys," Journal of Nuclear Materials, 329-333 (2004) 1088-1092

  2. Xianglin Wu, Xiao Pan, Meimei Li and James F. Stubbins, "Modeling Tensile Response and Flow Localization Effects in 316SS after Exposure to Spallation and Fission Irradiation Environments," Journal of Nuclear Materials, 343 (2005) 302-307

  3. Xianglin Wu, Xiao Pan, Meimei Li and James F. Stubbins, "Flow Localization Process in Austenitic Alloys," Journal of ASTM international, 3 (1) (2006)

  4. Xianglin Wu, Xiao Pan, James C. Mabon, Meimei Li and James F. Stubbins, "The Role of Deformation Mechanisms in Flow Localization of 316 Stainless Steel," Journal of Nuclear Materials 356 (2006) 70-77

  5. Xianglin Wu, Xiao Pan, Bachu N. Singh, Meimei Li and James F. Stubbins, "Hold-Time Effects on the Fatigue Life of Copper and Copper alloys for Fusion Applications," accepted by the Journal of Nuclear Materials

  6. Xianglin Wu, Xiao Pan, James C Mabon, Meimei Li and James F. Stubbins, "An EBSD Investigation of Flow Localization and Microstructure Evolution of 316L Stainless Steel for Gen IV Reactor Applications," accepted by the Journal of Nuclear Materials

  7. Xianglin Wu, Xiao Pan, and James F. Stubbins, "Analysis of Notch Strengthening of 316L Stainless Steel with and without Irradiation-induced hardening using EBSD and FEM," accepted by the Journal of Nuclear Materials

  - Papers in preparation and editing
  8. Xianglin Wu, Xiao Pan and James F. Stubbins, "Notch Strengthening and its Impact on the Deformation and Fracture of 316L Stainless Steel," in editing

  9. Xianglin Wu, Xiao Pan and James F. Stubbins, "Temperature Dependence of Deformation Mechanism Controlling Flow Localization of Polycrystalline 316L Austenitic Stainless Steel," in editing

  10. Xianglin Wu, Xiao Pan, and James F. Stubbins, "An EBSD Study on the Influence of Stacking Fault Energy on the Microstructure Evolution and Flow Localization of 316L Stainless Steel and OFHC Copper," in editing

  11. Xianglin Wu, Xiao Pan and James F. Stubbins, "EBSD and FEM Analysis on Notch Strengthening and its Temperature Dependence for OFHC Copper," in editing

  12. Xianglin Wu, Xiao Pan and James F. Stubbins, "Flow Localization and Textural Evolution in Structural Alloys for Accelerator Driven Systems," in preparation

  13. Xianglin Wu, Xiao Pan, Bachu N. Singh, Meimei Li and James F. Stubbins, "Microstructure Analysis of Hold-Time Effect on the Fatigue Life of CuCrZr for Fusion Application," in preparation

14. Xianglin Wu, Xiao Pan and James F. Stubbins, "In-Situ EBSD Investigation of Tensile Response for Miniature Specimen of Stainless Steel," in preparation

- **Conference proceedings and oral presentations**

15. Xianglin Wu, Xiao Pan, Meimei Li and James F. Stubbins, "Flow Localization Modeling in FCC alloys after Exposure to Irradiation," Transactions of the American Nuclear Society, Nov. 2004, 918-919
16. Xianglin Wu, Xiao Pan and James F. Stubbins, "Flow Localization and Fracture in Irradiated FCC Materials," TMS annual meeting, San Antonio, Texas, March 12-16, 2006
17. Xianglin Wu, Xiao Pan, James C. Mabon, Meimei Li and James F. Stubbins, "An EBSD Investigation on Flow Localization of 316L Stainless Steel," ANS annual meeting, Reno, Nevada, June 4-9, 2006
18. Xianglin Wu, Xiao Pan, James C. Mabon and James F. Stubbins, "EBSD Study of the Role and Activation of Mechanic Twinning in Plastic Deformation of 316L Stainless Steel," summary accepted by the Microscopy and Microanalysis 2006

REFERENCES

1. M. Aghaie-Khafri, R.M., *Flow Localization and Plastic Instability During the Tensile Deformation of Al Alloy Sheet.* JOM-JOURNAL OF THE MINERALS METALS & MATERIALS SOCIETY, 1998. **50**(11): p. 50-52.
2. K. Farrell, T.S.B., N. Hashimoto, *Deformation Mode Maps for Tensile Deformation of Neutron-Irradiated Structural Alloys.* Journal of Nuclear Materials, 2004. **335**: p. 471-486.
3. K. Farrell, T.S.B., *Tensile properties of ferritic/martensitic steels irradiated in HFIR, and comparison with spallation irradiation data.* Journal of Nuclear Materials, 2003. **318**: p. 274-282.
4. T.S. Byun, K.F., N. Hashimoto, *Plastic instability behavior of bcc and hcp metals after low temperature neutron irradiation.* Journal of Nuclear Materials, 2004. **329-333**: p. 998-1002.
5. T.S. Byun, K.F., *Plastic instability in polycrystalline metals after low temperature irradiation.* Acta Materialia, 2004. **52**(6): p. 1597-1608.
6. T.S. Byun, K.F., E.H. Lee, J.D. Hunn, L.K. Mansur, *Strain Hardening and Plastic Instability Properties of Austenitic Stainless Steels after Proton and Neutron Irradiation.* Journal of Nuclear Materials, 2001. **298**: p. 269-279.
7. T.S. Byun, K.F., *Irradiation Hardening Behavior of Polycrystalline Metals after Low Temperature Irradiation.* Journal of Nuclear Materials, 2004. **326**(2-3): p. 86-96.
8. Y. Dai, X.J.J., K. Farrell, *Mechanical properties of modified 9Cr–1Mo (T91) irradiated at < 300 °C in SINQ Target-3.* Journal of Nuclear Materials, 2003. **318**: p. 192-199.
9. B.H. Sencer, F.A.G., D.S. Gelles, G.M. Bond, S.A. Maloy, *Microstructural evolution in modified 9Cr–1Mo ferritic/martensitic steel irradiated with mixed high-energy proton and neutron spectra at low temperatures* Journal of Nuclear Materials, 2002. **307-311**: p. 266-271.
10. M. B. Toloczko, M.L.H., S. A. Maloy, *High temperature tensile testing of modified 9Cr–1Mo after irradiation with high energy protons* Journal of Nuclear Materials, 2003. **318**: p. 200-206.
11. S.A. Maloy, M.R.J., G Willcutt, W.F. Sommer, M Sokolov, L.L. Snead, M.L. Hamilton, F.A. Garner, *The Mechanical Properties of 316L/304L Stainless Steels, Alloy 718 and Mod 9Cr–1Mo after Irradiation in a Spallation Environment.* Journal of Nuclear Materials, 2001. **296**: p. 119-128.
12. S.A. Maloy, M.R.J., W.R. Johnson, T.S. Byun, K. Farrell, M.B. Toloczko, *Comparison of Fission Neutron and Proton/Spallation Neutron Irradiation Effects on the Tensile Behavior of Type 316 and 304 Stainless Steel.* Journal of Nuclear Materials, 2003. **318**: p. 283-291.
13. M.L. Grossbeck M.L. Pjmaziasz, A.F.R., *Modeling of Strengthening Mechanism in Irradiated Fusion-Reactor 1ST Wall Alloys.* Journal of Nuclear Materials, 1992 **191**: p. 808-812.
14. G.R. Odette, D.F., *Development of Mechanical Property Correlation Methodology for Fusion Environments.* Journal of Nuclear Materials, 1979. **85**(6): p. 817-822.
15. F. Garner, M.H., N. Panayotou, G. Johnson, *The Microstructual Origins of Yield Strength Changes in AISI-316 during Fission or Fusion Irradiation.* Journal of Nuclear Materials, 1982. **104** (1-3): p. 803-807.

16.   X. Pan, X.W., M. Li, J.F. Stubbins, *Modeling tensile response and flow localization effects in selected copper alloys.* Journal of Nuclear Materials, 2004. **329-333** p. 1088-1092.

17.   X. Wu, X.P., M. Li, J.F. Stubbins, *Modeling Tensile Response and Flow Localization Effects in 316SS after Exposure to Spallation and Fission Irradiation Environments.* Journal of Nuclear Materials, 2005. **343**(1-3): p. 302-307.

18.   X. Wu, X.P., M. Li, J.F. Stubbins, *Flow Localization Processes in Austenitic Alloys.* Journal of ASTM International, 2006. **3**(1).

19.   X. Wu, X.P., M. Li, J.F. Stubbins, *Flow Localization Modeling in FCC alloys after Exposure to Irradiation.* Transactions of the American Nuclear Society, 2004. **94**: p. 918-919.

20.   J.E. Pawel, A.F.R., G.E. Lucas, S.J. Zinkle, *Irradiation Performance of Stainess Steels for ITER Application.* Journal of Nuclear Materials, 1996. **1996**: p. 126-131.

21.   *http://www.iter.org/.*

22.   L.K. Mansur, J.R.H., *Status of the Spallation Neutron Source with Focus on Target Materials.* The Seventh International Workshop on Spallation Materials Technology, 2005.

23.   Askeland, D.R., *The Science and Engineering of Materials.* 3 ed. 1994: PWS Publishing Company.

24.   S.J. Zinkle, P.J.M., R.E. Stoller, *Dose Dependence of the Microstructural Evolution in Neutron-Irradiated Austenitic Stainless-Steel.* Journal of Nuclear Materials, 1993. **206**: p. 266-286.

25.   Lucas, G.E., *The Evolution of Mechanical Property Change in Irradiated Austenitic Stainless Steels.* Journal of Nuclear Materials, 1993. **206**: p. 287-305.

26.   G.E. Lucas, M.B., J.E. Pawel, M.L. Hamilton, *Implications of Irradiation-Induced Reductions in Ductility to the Design of Austenitic Stainless Steel Structures.* Journal of Nuclear Materials, 1996. **233-237**: p. 207-212.

27.   G.R. Odette, G.E.L., *The Effects of Intermediate Temperature Irradiation on the Mechanic Behavior of 300-series Austenitic Stainless Steels.* Journal of Nuclear Materials, 1991. **179-181**: p. 572-576.

28.   J.E. Powel, A.F.R., G.E. Lucas, S.J. Zinkle, *Irradiation Performance of Stainless Steels for ITER Application.* Journal of Nuclear Materials, 1996. **239**: p. 126-131.

29.   E.H. Lee, T.S.B., J.D. Hunn, K. Farrell, L.K. Mansur, *Origin of Hardening and Deformation Mechanisms in Irradiated 316 LN Austenitic Stainless Steel.* Journal of Nuclear Materials, 2001. **296**: p. 183-191.

30.   E.H. Lee, T.S.B., J.D. Hunn, M.H. Yoo, K. Farrell, L.K. Mansur, *On the Origin of Deformation Microstructures in Austenitic Stainless Steel: Part I - Microstructures.* Acta Materialia, 2001. **49**: p. 3269-3276.

31.   N. Hashimoto, T.S.B., K. Farrell, S.J. Zinkle, *Deformation Microstructure of Neutron-Irradiated Pure Polycrystalline Metals.* Journal of Nuclear Materials, 2004. **329-333**: p. 947-952.

32.   L.L. Snead, R.E.S., M.A. Sokolov, S. Maloy, *Experimental Determination of the Effect of Helium on the Fracture Toughness of Steel.* Journal of Nuclear Materials, 2002. **307-311**: p. 187-191.

33.   Stoller, R. 1987, UCSB.

34.   Y. Katoh, T.M., A. Kohyama, R.E. Stoller, C. Namba, *Rate Theory Modeling of Defect Evolution under Cascade Damage Condition: the Influence of Vacancy-Type Cascade*

Remnants on Defect Evolution. Journal of Nuclear Materials, 1996. **233-237**: p. 1022-1028.

35. Yoshida, N., *Microstructure Formatoin and Its Role on Yield Stengthen in AISI-316-SS Irradiated by Fission and Fusion Neutrons.* Journal of Nuclear Materials, 1990. **174**: p. 220-228.

36. Gelles, D.S., *Dislocation Modeling of Physical Systems.* Vol. 158. 1981, New York: Pergamon.

37. Maziasz, P.J., *Temperature-Dependence of the Dislocation Microstructure of PCA Austenitic Stainless-Steel Irradiated in ORR Spectrally-Tailored Experiments* Journal of Nuclear Materials, 1992. **191-195**: p. 701-705.

38. G.R. Odette, G.E.L., *Deformation and Fracture in Irradiated Austenitic Stainless Steels.* Journal of Nuclear Materials, 1992. **191-194**: p. 50-57.

39. G.R. Odette, G.E.L., *The Effects of Intermediate Temperature Irradiation the Mechanical-Behavior of 300-Series Austenitic Stainless-Steels.* Journal of Nuclear Materials, 1991. **179-181**: p. 572-576.

40. J.D. Elen, P.F., *Fast-Neutron Irradiation Hardening of Austenitic Stainless-Steel at 250-Degrees-C* Journal of Nuclear Materials, 1992. **191-194**: p. 766-770.

41. M.L. Hamilton, A.O., F.A. Garner, *Tensile Behavior and Swelling of Ternary Austenitic Alloys Irradiated in Different Neutron-Spectra.* Journal of Nuclear Materials, 1991. **179**: p. 558-562.

42. M. Grossbeck, P.J.M., A. Rowcliffe, *Modeling of Strengthening Mechanism in Irradiated Fusion-Reactor 1ST Wall Alloys.* Journal of Nuclear Materials, 1992. **191-194**: p. 808-812

43. Friedel, J., *Electron Microscopy and Strength of Crystals.* Vol. 605. 1963, New York: Interscience.

44. Kocks, U.F., *Physics of Strength and Plasticity.* Vol. 143. 1969, Cambridge: MIT Press.

45. Taylor, G.I., *Plasticity Strain in Metals.* J. Inst. Metals, 1938. **62**: p. 307-325.

46. F.A. Garner, D.S.G., *Irradiation Creep Mechanisms - An Experimental Perspective.* Journal of Nuclear Materials, 1988. **159**(286-309).

47. J.L. Strudel, J.W., *Direct Observations of Interactions Between Imperfect Loops and Moving Dislocations in Aluminum.* Philosophical Magazine, 1964. **9**: p. 491-506.

48. A.J.E. Forman, J.V.S., *Mechanism for the Sweeping-Up of Loops by Glide Dislocations During Deformation.* Philosophical Magazine, 1969. **19**: p. 931-938.

49. Wechsler, M., *Inhomogeneity of Plastic Deformation.* 1973, Metal Park, Ohio: ASM.

50. Bloom, E., *Radiation Damage in Metals.* Vol. 317. 1975, Metal Park, Ohio: ASM.

51. T.S. Byun, E.H.L., J.D. Hunn, *Plastic Deformation in 316LN Stainless Steel-Characterization of Deformation Microstructures.* Journal of Nuclear Materials, 2003. **321**: p. 29-39.

52. T.S. Byun, E.H.L., J.D. Hunn, K. Farrell, L.K. Mansur, *A Method to Study Deformation Mechanism in Ion-Irradiated Steels Using a Disk Bend Technique.* Small Specimen Test Techniques: Fourth Volume, ASTM STP 1418, M.A. Sokolov, J.D. Landes, G.E. Lucas, Eds., ASTM International, West Conshohocken, PA, 2002, 2002: p. 267-282.

53. S.A. Maloy, M.R.J., T.J. Romero, M.B. Toloczko, R.J. Kurtz, A. Kimura, *Tensile properties of the NLF reduced activation ferritic/martensitic steels after irradiation in a fast reactor spectrum to a maximum dose of 67 dpa* Journal of Nuclear Materials, 2005. **341**: p. 141-147.

54.   J. Henry, X.A., Y. Dai, P. Lamagnère, J. P. Pizzanelli, J. J. Espinas, P. Wident, *Tensile properties of 9Cr–1Mo martensitic steel irradiated with high energy protons and neutrons.* Journal of Nuclear Materials, 2003. **318**: p. 215-227.

55.   Y. Dai, X.J., S.A. Maloy, *Annealing effects on mechanical properties and microstructure of F82H irradiated at < 60 °C with 800 MeV protons.* Journal of Nuclear Materials, 2005. **343**: p. 241-246.

56.   D. Hamaquchi, Y.D., *Microstructural Study of EC316LN and its Welds Irradiated in SINQ Target-3.* Journal of Nuclear Materials, 2005. **343**(1-3): p. 262-266.

57.   M. Victoria, N.B., C. Bailat, Y. Dai, M.I. Luppo, R. Schaublin, B.N. Singh, *The Microstructure and Associated Tensile Properties of Irradiated FCC and BCC Metals.* Journal of Nuclear Materials, 2000. **276**: p. 114-122.

58.   S. Saito, K.K., K. Usami, A. Ishikawa, Y. Nishino, M. Kawai, Y. Dai, *Tensile Properties of Austenitic Stainless Steels Irradiated at SINQ Target 3.* Journal of Nuclear Materials, 2005. **343**(1-3): p. 253-261.

59.   Y. Dai, X.J., J.C. Chen, W.F. Sommer, M. Victoria, G.S. Bauer, *Microstructure of Both As-Irraiated and Deformed 304L Stainless Steel Irradiated with 800 Mev Protons.* Journal of Nuclear Materials, 2001. **296**: p. 174-182.

60.   A. Lind, U.B., *Mechanical Properties of Hot Isostatic Pressed Type 316LN Steel after Irradiation.* Journal of Nuclear Materials, 2000. **283**: p. 451-454.

61.   A. Lind, U.B., *Mechanical Properties of Hot Isostatic Pressed Type 316LN Steel after Irradiation to 2.5 dpa.* Fusion Engineering and Design, 2001. **58**(9): p. 713-717.

62.   G. Furutani, N.N., T. Konishi, M. Kodama, *Stress Corrosion Cracking on Irradiated 316 Stainless Steel.* Journal of Nuclear Materials, 2001. **288**: p. 179-186.

63.   H. Nishi, T.A., *Mechanical-Properties of Brazing Joints of Alumina Dispersion-Strengthened Copper to 316 Stainess-Steel for Fusion-Reactor Divertor.* Journal of the Atomic Energy Society of Japan, 1994. **36**(10): p. 948-966.

64.   S. Jitsukawa, P.J.M., T. Ishiyama, L.T. Gibson, A. Hishinuma, *Tensile Properties of Austenitic Stainless-Steels and Their Weld Joints after Irradiation by the Orr-Spectrally-Tailoring Experiment.* Journal of Nuclear Materials, 1992. **191**: p. 771-775.

65.   A. Kohyama, M.L.G., G. Piatti, *The Application of Austenitic Stainless-Steels in Advanced Fusion Systems-Current Limitations and Future-Prospects.* Journal of Nuclear Materials, 1992. **191**: p. 37-44.

66.   Boutard, J.L., *Structural Materials Requirements and Related R-and D for ITER Plasma-Facing Components.* Journal of Nuclear Materials, 1991. **179**: p. 1179-1184.

67.   M. F. Ashby, D.R.H.J., *Engineering Materials 1.* 1996: Butterworth-Heinemann.

68.   A.W. Thompson, M.I.B., W.F. Flanagan, *The Dependence of Polycrystal Work Hardening on Grain Size.* Acta Metallugica, 1973. **21**: p. 1017-1028.

69.   Byun, T.S., *On the Stress Dependence of Partial Dislocation Separation and Deformation Microstructure in Austenitic Stainless Steels.* Acta Materialia, 2003. **51**: p. 3063-3071.

70.   S. Asgari, E.E.-D., S.R. Kalidindi, R.D. Doherty, *Strain Hardening Regimes and Microstructural Evolution During Large Strain Compression of Low Stacking Fault Energy FCC Alloys That FOrm Deformation Twins.* Metallurgical and Materials Transactions A, 1997. **28A**: p. 1781-1795.

71.   S.M. Copley, B.H.K., *The Dependence of The Width of A Dissociated Dislocation on Dislocation Velocity.* Acta Metallugica, 1968. **16**: p. 227-231.

72.   Kalidindi, S.R., *Modeling the Strain Hardening Response of Low SFE FCC Alloys.* International Journal of Plasticity, 1998. **14**(2): p. 1265-1277.

73.   Cuitino, A.M., *Effect of Temperature and Stacking Fault Energy on The Hardening of FCC Crystals.* Materials Science and Engineering A, 1996. **216**: p. 104-116.

74.   E.I. Samuel, B.K.C., K.B.S. Rao, *Influence of Temperature and Strain Rate on Tensile Work Hardening Behaviour of Type 316 LN Austenitic Stainless Steel.* Scripta Materialia, 2002. **46**: p. 507-512.

75.   G.R. Johnson, W.H.C. *A Consititutive Model and Data for Metals Subjected to Large Strains, High Strain Rates and High Temperatures.* in *Proceedings of the Seventh International Symposium on Ballistic.* 1983. The Hague, The Netherlands.

76.   R.W. Armstrong, V.R., F.J. Zerilli, *Advances in Materials and Their Applications*: Wiley Eastern Ltd.

77.   S.R. Bodner, Y.P., *Consititutive Equations for Elastic-Viscoplastic Strain-Hardening materials.* Journal of Applied Mechanics, 1975: p. 385-395.

78.   S. Huang, A.S.K., *Modeling the Mechanic Behavior of 1100-0 Aluminum at Different Strain Rates by the Bodner-Partom model.* International Journal of Plasticity, 1992. **8**: p. 501-517.

79.   T. S. Byun, K.F., E. H. Lee, L. K. Mansur, S. A. Maloy, M. R. James, W. R. Johnson, *Temperature effects on the mechanical properties of candidate SNS target container materials after proton and neutron irradiation* Journal of Nuclear Materials, 2002. **303**: p. 34-43.

80.   J.P. Robertson, I.I., A. F. Rowcliffe, M. L. Grossbeck, S. Jitsukawa, *Temperature Dependence of The Deformation Behavior of Type 316 Stainless Steel after Low Temperature Neutron Irradiation.* Effects of Radiation on Materials: 18th International Symposium, ASTM STP 1325, R.K. Nanstad, M.L. Hamilton, F.A. Garner, A.S. Kumar, Eds., American Society for Testing and Materials, West Conshohocken, PA, 1999, 1999: p. 671-688.

81.   J.E. Powel, A.F.R., D.J. Alexander, M.L. Grossbeck, K. Shiba, *Effects of Low Temperature Neutron Irradiation on Deformation Behavior of Austenitic Stainless Steels.* Journal of Nuclear Materials, 1996. **233-237**: p. 202-206.

82.   Hertzberg, R.W., *Deformation and Fracture Mechanics of Engineering Materials.* 4 ed. 1995, New York: John Wiley & Sons, Inc.

83.   D. Hull, D.J.B., *Introduction to Dislocations.* 3 ed. 1984, New York: Pergamon Press Ltd.

84.   A. Staroselsky, L.A., *Inelastic Deformation of Polycrystalline Face Centered Cubic Materials by Slip and Twinning.* J. Mech. Phys. Solids, 1998. **46**(4): p. 671-696.

85.   C.N. Tome, G.C.K., *Modeling Texture, Twinning and Hardenging Evolution During Deformation of Hexagonal Materials.* Materials Science Forum, 2005. **495-497**: p. 1001-1006.

86.   C.N. Tome, S.R.A., W.R. Blumenthal, M.A.M. Bourke, D.W. Brown, G.C. Kaschner, P. Rangaswamy, *The Relation between Texture, Twinning and Mechanical Propertie in Hexagonal Aggregates.* Materials Science Forum, 2002. **408-412**: p. 263-268.

87.   D.W. Brown, S.R.A., S.P. Abeln, W.R. Blumenthal, M.A.M. Bourke, M.C. Mataya, C.N. Tome, S.C. Vogel, *The Role of Texture, Temperature, and Strain Rate in The Activity of Deformation Twinning.* Materials Science Forum, 2005. **495-497**: p. 1037-1042.

88. E. El-Danaf, S.R.K., R.D. Doherty, *Influence of Grain Size and Stacking-Fault Energy on Deformation Twinning in FCC Metals.* Metallurgical and Materials Transactions A, 1999. **30A**: p. 1223-1233.

89. G.G. Yapici, I.K., Z.P. Luo, H.J. Maier, Y.I. Chumlyakov, *Microstructural Refinement and Deformation Twinning During Severe Plastic Deformation of 316L Stainless Steel at High Temperature.* Journal of Materials Research, 2004. **19**(8): p. 2268-2278.

90. I.V. Kireeva, Y.I.C., N.V. Luzginova, *Slip and Twinning in Single Crystals of Austenitic Stainless Steels with Nitrogen.* The Physics of Metals and Metallography, 2002. **94**(5): p. 508-519.

91. J.F. Bingert, T.A.M., G.C. Kaschner, P.J. Maudlin, G.T. Gray, III, *Deformation Twinning in Polycrystalline Zr: Insight from Electron Backscattered Diffraction Characterization.* Metallurgical and Materials Transactions A, 2002. **33A**: p. 955-963.

92. M.A. Meyers, O.V., V.A. Lubarda, *The onset of Twinning in Metals: A Constitutive Description.* Acta Materialia, 2001. **49**: p. 4025-4039.

93. M.S. Szczerba, T.B., T. Tokarski, *Is There a Critical Resolved Shear Stress for Twinning in Face-Centered Cubic Crystal?* Philosophical Magazine, 2004. **84**(3-5): p. 481-502.

94. S. Allain, J.P.C., O. Bouaziz, *A Physical Model of The Twinning-Induced Plasticity Effects in a High Maganese Austenitic Steel.* Materials Science and Engineering A, 2004. **387-389**: p. 143-147.

95. S. Mahajan, D.F.W., *Deformation Twinning in Metals and Alloys.* International Metallurgical Reviews, 1973. **18**: p. 43-61.

96. S.G. Song, G.T.G.I., *Influence of Temperature and Strain Rate on Slip and Twinning Behavior of Zr.* Metallurgical and Materials Transactions A, 1995. **26A**: p. 2665-2675.

97. H.L. Ewalds, R.J.H.W., *Fracture Mechanics.* 1985, London Delft: Delftse U. M.

98. Gurson, A.L., *Continuum Theory of Ductile Rupture by Void Nucleation and Growth: Part I-Yield Criteria and Flow Rules for Porus Ductile Media.* Journal of Engineering Materials and Technology, 1977: p. 2-12.

99. Gurson, A.L., *Porous Rigid-Plastic Materials Containing Rigid Inclusions-Yield Function, Plastic Potential, and Void Nucleation.* Fracture, 1977. **2**: p. 357-364.

100. Gurson, A.L., in *Division of Engineering.* 1975, Brown University.

101. Tvergaard, V., *On Localization in Ductile Materials Containing Spherical Voids.* International Journal of Fracture, 1982. **18**(4): p. 237-252.

102. Tvergaard, V., *Necking in Tensile Bars with Rectangular Cross-Section.* Computer Methods in Applied Mechanics and Engineering, 1993. **103**: p. 273-290.

103. A.S. Argon, J.I., A. Needleman, *Distribution of Plastic Strain and Negative Pressure in Necked Steel and Copper Bars.* Metallurgical Transactions A, 1975. **6A**: p. 815-824.

104. C.C. Chu, A.N., *Void Nucleation Effects in Biaxially Stretched Sheets.* Journal of Engineering Materials and Technology, 1980. **102**: p. 249-256.

105. M.N. Shabrov, E.S., S. Kim, D.H. Sherman, L. Chuzhoy, C.L. Briant, A. Needleman, *Void Nucleation by Inclusion Cracking.* Metallurgical and Materials Transactions A, 2004. **35A**: p. 1745-1755.

106. Needleman, A., *A Numerical Study of Necking in Circular Cylindrical Bars.* J. Mech. Phys. Solids, 1972. **20**: p. 111-127.

107. Z.L. Zhang, E.N., *A New Failure Criterion for the Gurson-Tvergaard Dilational Constitutive Model.* International Journal of Fracture, 1995. **70**: p. 321-334.

108. M.H. Barnett, M.S.W., D.J. Dudziak, L.K. Mansur, B.D. Murphy, *Radiation damage to the 316 stainless steel target container vessel at SNS.* Journal of Nuclear Materials, 2001. **296**: p. 54-60.

109. F.A. Garner, B.M.O., L.R. Greenwood, M.R. James P.D. Ferguson, S.A. Maloy, W.F. Sommer, *Determination of helium and hydrogen yields from measurements on pure metals and alloys irradiated by mixed high energy proton and spallation neutron spectra in LANSCE.* Journal of Nuclear Materials, 2001. **296**: p. 66-82.

110. F.A. Garner, B.M.O., L.R. Greenwood, D.J. Edwards, S.M. Bruemmer, M.L. Grossbeck. *Generation and retention of helium and hydrogen in austenitic steels irradiated in a variety of LWR and test reactor spectral environments.* in *10th International Conference on Environmental Degradation of Materials in Nuclear Power Systems – Water Reactors.* 2001.

111. A. Okada, K.K., T. Yoshiie, S. Kojima, *Transition of Deformation Structure in Ni and Au by D-T Neutron Irradiation.* Materials Transactions, JIM, 1989. **30**(4): p. 265-272.

112. D. Edwards, B.S., P. Toft, *US DOE Fusion Materials Semiannual Progress Report*, in *DOE/ER-0313/30.* 2001. p. 99.

113. E. El-Danaf, S.R.K., R.D. Doherty, *Influence of Deformation Path on The Strain Hardenging Behavior and Microstructure Evolution in Low SFE FCC Metals.* International Journal of Plasticity, 2001. **17**: p. 1245-1265.

114. Ruff, R.L.A., *The Temperature Dependence of Stacking Fault Energy in Fe-Cr-Ni Alloys.* Metallurgical Transactions, 1971. **2** p. 505-509.

115. Pineau, L.R.A., *Temperature Dependence of Stacking Fault Energy in Close-Packed Metals and Alloys.* Materials Science and Engineering, 1978. **36** p. 47-63.

116. Abrassart, F., *Stress-Induced Martensitic Transformation in Two Carbon Stainless Steels. Application to Trip Steels.* Metallurgical Transactions, 1973. **4**: p. 2205-2216.

117. S. Vercammen, B.B., B.C.D. Cooman, P. Wollants, *Cold Rolling Behavior of an Austenitic Fe-30Mn-3Al-3Si TWIP-Steel: the Importance of Deformation Twinning.* Acta Materialia, 2004. **52**: p. 2005-2012.

118. S.G. Chowdhury, S.D., P.K. De, *Cold Rolling Behavior and Textural Evolution in AISI 316L Austenitic Stainless Steel.* Acta Materialia, 2005. **53**: p. 3951-3959.

119. L.N. Brewer, M.A.O., L.M. Young, T.M. Angeliu, *Misorientation Mapping for Visualization of Plastic Deformation via Electron Back-Scattered Diffraction.* Microscopy and Microanalysis, 2006. **12**(1): p. 85-91.

120. A.S. Argon, J.I., R. Safoglu, *Cavity Formation from Inclusions in Ductile Fracture.* Metallurgical Transactions A, 1975. **6A**: p. 825-837.

121. S.H. Goods, L.M.B., *The Nucleation of Cavities by Plastic Deformation.* Acta Materialia, 1979. **27**: p. 1-15.